九州大学学術情報リポジトリ
Kyushu University Institutional Repository

Geometric design principle for active ordering: From bacterial turbulence to cytoskeletons

別府, 航早

https://hdl.handle.net/2324/4784404

出版情報：Kyushu University, 2021, 博士（理学）, 課程博士
バージョン：
権利関係：

PhD Dissertation

Geometric design principle for active ordering: From bacterial turbulence to cytoskeletons

Department of Physics, Kyushu University

BEPPU Kazusa

February 25th, 2022

Abstract

In nature, the collection of motile elements self-organizes beautiful ordered structures such as bacterial swarms, school of fish, and flocking of birds over a wide range of scales. Such motile agents that transduce local internal energy into mechanical motions are named "active matter", which has been extensively studied in the context of nonequilibrium physics. The discovery of universality behind active matter is one of the greatest challenges ranging from biophysics to condensed matter physics. In Chapter 1, we review the development of this research field with a focus on the Vicsek model that is a flying XY model devised by Vicsek (1995). The Vicsek model not only can reproduce polar flocks like flocking of birds but also exhibits true long-range order despite two dimensions, which has been analytically proven by its continuum theory proposed by Toner and Tu (1995). Moreover, the Vicsek-style model with nematic interactions, proposed by Ginelli *et al.* (2010), also shows true long-range nematic order in a two-dimensional plane despite the different symmetry. Recent experimental studies using synthetic particles and swimming bacteria have demonstrated the emergence of true long-range order for both symmetries of interaction and its statistical properties, corroborating the existence of the Vicsek universality class across various active matter systems. However, in natural systems, dense active matter tends to create much more complex collective motions such as active turbulence rather than long-range orientational order observed in the simplified systems. Wensink and Dunkel *et al.* (2012) put forward a Swift-Hohenberg-type Toner-Tu equation to quantitatively describe bacterial turbulence, which successfully captures its statistical properties such as energy spectrum. This suggested that many transient and recurring vortices emerge with a characteristic length in chaotic active turbulence due to the destabilization mechanism. The presence of ordered vortices

behind active turbulence motivated many physicists to study its intrinsic geometrical nature. Using fabricated devices to impose boundary conditions, several studies revealed that inherently ordered vortices prefer either a ferromagnetic state or an anti-ferromagnetic state depending on a geometrical constraint. However, physical rules based on geometry remain unclear, and exploiting further possibilities for controlling active turbulence is also challenging. Furthermore, as with the discovery of the Vicsek universality class, elucidating a common geometric rule across different systems would provide a better understanding of universality in a broad class of active matter. To address the above issues, we study geometric rules in a confined active matter based on symmetries of individual units.

In Chapter 2, we firstly reveal geometric constraints ruling the appearance of ferromagnetic vortices (FMV) and anti-ferromagnetic vortices (AFMV) inherent in bacterial turbulence by simply focusing on two physical quantities: the radius of vortex R and the inter-center distance of vortices Δ. In a fabricated polydimethylsiloxane (PDMS) microwell with two overlapping circles, we found the transition from FMV to AFMV occurs around the ratio $\Delta/R = 1.4$. A mean-field Vicsek model with polar particles that collide at a tip whose shape is characterized by Δ/R gives an equal probability between FMV and AFMV at $\Delta/R = \sqrt{2}$, suggesting the presence of the geometric rule determined by polar interactions of ordered vortices in active turbulence.

In Chapter 3, to gain a further understanding of the design principle for active turbulence, we investigate the role of chirality, which has been overlooked in previous works, in collective bacterial motions. By developing a new device that enables one to induce the intrinsic chirality of swimming bacteria, we uncovered robust chiral edge currents near boundary walls, capable of producing larger-scale flows. To clarify how chiral edge currents control active turbulence, we applied our geometric approach for interacting vortices. As a result, the chiral edge current stabilized FMV pairing order and altered the transition point. The mean-field Vicsek model including alignment by a chiral edge current yields a quantitative agreement with the experiment, leading to an extended geometric rule to control active turbulence by the microscopic chirality.

In Chapter 4, we investigate geometric rules in an assembly of gliding microtubules whose symmetry of interaction is different from swimming bacteria to explore geometric universality. In this system, geometric confinements of overlapping circles drove the self-organization of two distinct aligned patterns: a protruding bundle and a bridge pattern. According to the mean-field Vicsek model with nematic interactions, the transition between these patterns can be also ruled by $\Delta/R = \sqrt{2}$, implying the presence of the common geometric rule across different systems.

Finally, we discuss future perspectives for our geometric approach to active matter physics. In Chapter 5, we introduce geometric features of frustrated vortices induced in a triplet circular confinement. Geometric frustration also induces co-rotational FMV pairing, which cannot be explained by our existing model. The simplified Toner-Tu model implies that the geometrical positioning of vortices may determine pairing order. In Chapter 6, we conclude with a comprehensive potential argument for the geometric rule that governs all the active matter systems we studied in this dissertation. Our findings will bring new insights into a universal framework based on geometry for active turbulence and even different kinds of active matter.

Contents

1 Introduction **7**

1.1 Active matter and collective motion 7

1.2 Mathematical model for collective motion 8

1.2.1 Vicsek model 8

1.2.2 Self-propelled rods model 15

1.2.3 Mean-field model 16

1.2.4 Toner-Tu model 20

1.2.5 Experimental demonstration of the Vicsek universality class 22

1.3 Classification of active matter 27

1.4 Active turbulence 28

1.4.1 Active turbulence model for polar fluids 30

1.4.2 Energy spectrum in active polar turbulence 32

1.4.3 Active nematics 36

1.5 Bacterial turbulence and geometry 38

1.5.1 Vortical motion under a circular comfinement 39

1.5.2 Multiple interacting vortices 40

1.6 Research aim 44

2 Geometric control of interacting bacterial vortices **45**

2.1 Experimental setup 45

2.1.1 *Escherichia coli* bacteria 45

2.1.2 Confinement by fabricated polydimethylsiloxane microwells . 46

2.2 Bacterial turbulence in a quasi-2D system 47

2.3 Single vortex stabilized in a circular miocrowell 49
2.3.1 Vortex Order Parameter 51
2.4 Vortex pairing order in doublet circular microwells 53
2.4.1 Geometric design of doublet circular boundary 53
2.4.2 Two distinct vortex pairing and its geometry dependence . . 54
2.5 Theoretical analysis for pairing order transition 56
2.5.1 Vicsek model 57
2.5.2 Fokker-Planck equation 58
2.5.3 Mean-field model 61
2.6 Vortex pairing order in quadruplet circular microwells 66
2.6.1 Geometric design of quadruplet circular boundary 66
2.6.2 Various patterns of vortex pairing in a quadruplet microwell 66
2.7 Summary of Chapter 2 68

3 Chiral edge current and pairing order transition 69
3.1 Introduction 69
3.2 Experimental setup 71
3.3 Chiral bacterial vortex 72
3.4 Chiral edge current 75
3.5 Origin of chiral edge current 77
3.5.1 Individual bacterial motions in a dilute suspension inside a microwell 78
3.5.2 Individual bacterial motions and fluid flows in a dense suspension inside a microwell 80
3.5.3 Interplay between chiral collective motions at top and bottom 83
3.5.4 Density distribution inside microwells 85
3.5.5 Effect of bacterial density on chiral edge current 86
3.5.6 Effect of physical properties of interfaces on chirality selection 88
3.5.7 Numerical simulation of chirality selection 90
3.6 Fast material transport in chiral bacterial vortices 96
3.7 Edge-current-induced pairing order transition of chiral vortices . . . 97
3.7.1 Theoretical analysis for chirality-induced pairing order . . . 98

3.7.2 Edge-current-induced co-rotational order 102
3.8 Summary of Chapter 3 106

4 Geometric control of a confined active cytoskeleton system 108
4.1 Experimental setup 109
4.2 Unconfined motile microtubules 110
4.3 Emergent patterns in confined motile microtubules 111
4.4 Theory for self-propelled rods 117
4.4.1 Numerical simulation 118
4.4.2 Theoretical analysis 121
4.5 Compartmentalization in channels by bundled patterns 127
4.6 Summary of Chapter 4 129

5 Future perspective: frustrated vortices 130
5.1 Vortex pairing order in triplet circular microwells 132
5.2 Simulation based on a simple Toner-Tu model 134
5.2.1 Numerical method 134
5.2.2 Geometry dependence of confined Toner-Tu fluids 135

6 Conclusion and outlook 138

Appendix A 141

Appendix B 146

Appendix C 154

Appendix D 160

References 169

Acknowledgements 182

Publications 184

Chapter 1

Introduction

“ The whole is greater than the sum of its parts. ” by Aristoteles

1.1 Active matter and collective motion

Autonomous motile elements or their entities that consume internal energy or energy of the surrounding environment and convert it into kinetic ones are termed active matter. This system is far from passive systems in that the detailed balance is broken at a single particle level. In nature, active matter is ubiquitous across scales from motor proteins at a nanoscopic scale, motor-protein-driven cytoskeletons [1, 2], sperm cells [3], and swimming bacteria to animals such as fish, birds, and human (Fig. 1.1) [4, 5]. Intriguingly, even though motile elements disorderly move at low density, as highly concentrated, grown interactions among them often give rise to beautiful collective motions such as swarming, swirling, and flocking. Such vivid examples of collective behaviors are seen not only in biological systems but also in non-biological systems such as colloidal particles under external fields [6, 7], vibrated disks [8], and active camphor disks [9]. This active ordering in nonequilibrium systems has been extensively studied in the context of hydrodynamics and nonequilibrium statistical physics. Despite different scales and species including biological and non-biological ones, common physical features are found in various active matter systems. Such ubiquity hints at the existence of some

universal features, irrespective of details at the individual level. Thus, exploring the universality behind collective motions is a pivotal challenge in active matter physics. That is why great attention has been paid by many scientists all over the world.

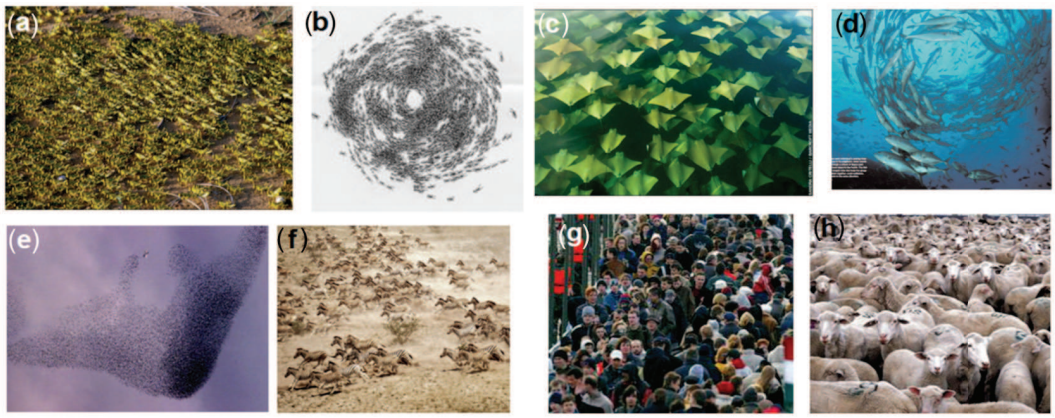

Figure 1.1: Examples of collective motions in nature. (a) A flock of Wingless Locusts in the field. (b) A rotating colony of army ants. (c) An array of golden rays. (d) A vortex of fish. (e) A flock of thousands of starlings. (f) A herd of zebra. (g) Traffic lanes of people. (h) Sheep coherently moving. Images are adapted from Ref. [4].

1.2 Mathematical model for collective motion

Many theoretical studies have been devoted to understanding the underlying mechanism of collective motions and their statistical features. In this section, we introduce some representative physical models to explain a variety of collective behaviors and their nontrivial nature unique to nonequilibrium systems.

1.2.1 Vicsek model

Recent developments of theoretical works about active matter were unquestionably triggered by the pioneering work of Tamás Vicsek *et al.* (1995), which was done to study collective behaviors such as flocking of birds and school of fish [10]. The Vicsek model is a minimal mathematical model to describe a transition to collective motion, similar to the XY model for equilibrium ferromagnetism in condensed matter physics. Unlike the XY model, however, it is an off-lattice model where

the constituents have motility. The essence of the Vicsek model is that particles spontaneously move (named self-propelled particles, SPPs), and their orientations are changed through ferromagnetic interactions among surrounding particles while being perturbed by a noise (Fig. 1.2). The overdamping dynamics of a collection of N SPPs with their off-lattice position $\boldsymbol{x_i}$ and the orientation θ_i is governed by the following equations:

$$\boldsymbol{x_i}(t+1) = \boldsymbol{x_i}(t) + \boldsymbol{v_i}(t)\Delta t \tag{1.1}$$

where $\boldsymbol{v_i} = v_0(\cos\theta_i, \sin\theta_i)$, and

$$\theta_i(t+1) = \langle\theta_i(t)\rangle_r + \Delta\theta, \tag{1.2}$$

where $\langle\theta_i(t)\rangle_r$ denotes an ensemble average over the particles inside a range r and is given by

$$\langle\theta_i(t)\rangle_r = \arctan[\langle\sin(\theta_i(t))\rangle_r / \langle\cos(\theta_i(t))\rangle_r], \tag{1.3}$$

and $\Delta\theta$ represents a random number chosen with a uniform probability from the range $[-\eta/2, \eta/2]$. The simulations were performed under a periodic boundary condition for various number densities $\rho = N/L^2$ (N: total number of particles, L: system size) and strengths of noise η corresponding to the thermal fluctuation of spins in the XY model. Fig. 1.3 presents snapshots displaying a collection of SPPs at steady state under four different conditions. At low density and low noise, SPPs disorderly move. As the noise strength is reduced while keeping the density small, a flocking behavior emerges, whereas at high density and strong noise, SPPs display disordered but locally correlated motions. Most importantly, when the density and the noise become high and low, respectively, the collective motions where the directions of particles' motion are highly correlated throughout the system are coordinated, named long-range order.

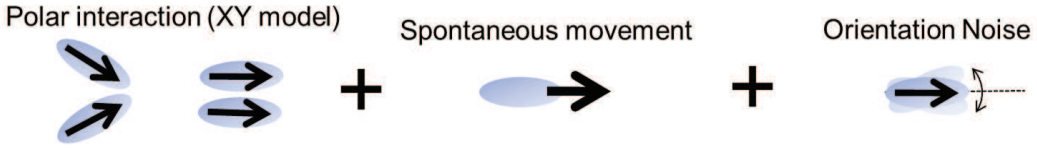

Figure 1.2: Essence of the Vicsek model. The orientation of particles is aligned through ferromagnetic interactions with neighbors and perturbed while spontaneously moving.

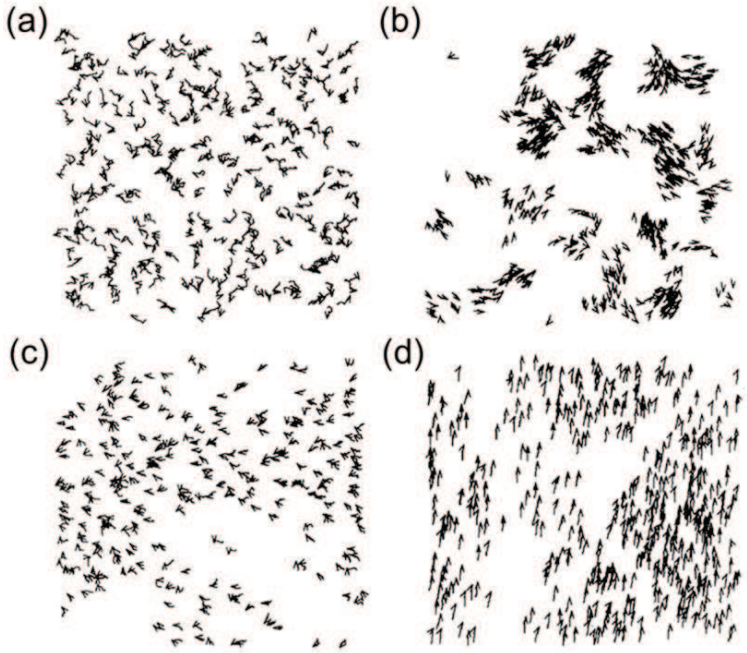

Figure 1.3: Snapshots of simulations based on the Vicsek model at various densities and noises. The particle's number density is fixed to $N = 300$. (a) Disordered phase. $t = 0,\ L = 7,\ \eta = 2.0$. (b) Flocking behaviors. $L = 25,\ \eta = 0.1$. (c) Locally correlated random motions. $L = 7,\ \eta = 2.0$. (d) Highly directed ordered phase. $L = 5,\ \eta = 0.1$. Images are adapted from Ref. [10].

To quantify the extent to which a collection of SPPs is aligned in some direction, the order parameter is defined as the mean normalized velocity in the following equation:

$$\phi(t) = |\boldsymbol{\varphi}(t)|,\ \boldsymbol{\varphi}(t) = \frac{1}{v_0}\langle \boldsymbol{v_i}(t)\rangle_t, \tag{1.4}$$

where v_0 is a constant speed of individual particles. In Figs. 1.4 (a) and (b), the order parameter is plotted as a function of η and ρ, respectively. The transition from disordered phase ($\phi(t) \sim 0$) to ordered one ($\phi(t) \sim 1$) occurs with a decrease of the

noise or an increase of the density. In this kind of computation, it is imperative to confirm the system-size dependence of the transition behavior. Hence, Chaté *et al.* (2008) [11] conducted large-scale simulations based on the Vicsek model. Remarkably, they found that the larger the system size becomes, the more sharply the disorder-order transition occurs (Fig. 1.4 (c)). In addition to the discontinuous transition, they found the coexistence phase of a high-density propagating band and a disordered region near the transition point, named "Vicsek wave" (Fig. 1.4 (d)). These properties of the phase transition are indeed hallmarks of a first-order transition, although Vicsek regarded the phase transition as being second-order because of the small system size when he proposed his model in 1995.

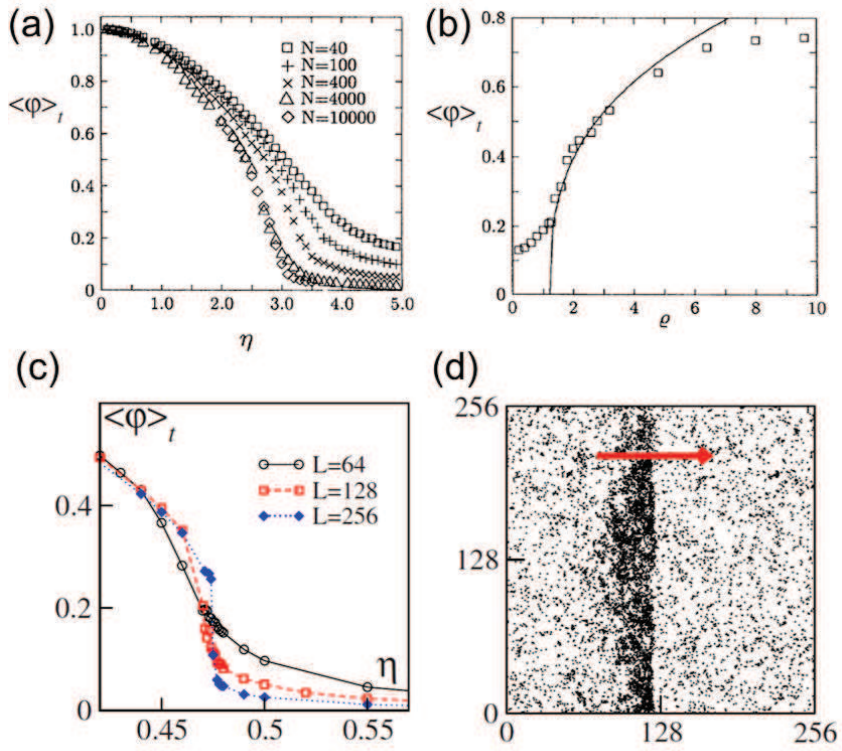

Figure 1.4: Order parameter and large-scale computation. (a) Noise-dependence of polar order. The system size is varied while maintaining a constant number density ρ. (b) Density-dependence of polar order. The umber density is varied while keeping $L = 20$ and a constant noise. (c) Noise-dependence of polar order at different system sizes. $\rho = 2, v_0 = 0.3$, time averages are carried over 10^7 time steps. (d) A typical snapshot of *Vicsek wave*. $\rho = 1/2, v_0 = 0.5, \eta = 0.3, L = 256$. Images in (a) and (b) are adapted from Ref. [4]. Images in (c) and (d) are adapted from Ref. [11].

Giant Number Fluctuation

One of the most important properties in the Vicsek model is giant number fluctuations (GNF). In what follows, the number fluctuations are defined. We consider the number of particles inside an observation area at time t, $n(t)$, and its time average $\langle n \rangle$. The number fluctuations are defined as the standard deviation, $\Delta n = \sqrt{\langle (n - \langle n \rangle)^2 \rangle}$, where $\langle \cdot \rangle$ denotes time average over sufficiently long period. (Note that in the above calculation of $\langle \cdot \rangle$, spatial averages can be also used, but temporal averages are experimentally more accessible.) As depicted in Fig. 1.5 (a), both $\langle n \rangle$ and Δn increase with the observation area. When the observation area is sufficiently large, the fluctuation Δn scales asymptotically as $\Delta n \propto \langle n \rangle^{\alpha}$. In equilibrium systems (or random systems), the exponent α goes to 0.5, that is, the normal fluctuations because the fluctuations must obey the central limit theorem. In the Vicsek model, on the other hand, the homogeneous ordered state far from the transition point exhibits anomalous number fluctuations with the exponent larger than $\alpha = 0.5$. The large-scale computation implemented by Chaté *et al.* [11] found the exponent $\alpha \sim 0.8$ (Fig. 1.5 (a)), which was also analytically derived from the hydrodynamic continuum theory for the Vicsek model under some approximations, constructed by Toner and Tu. (We will detail the Toner-Tu model later.) As easily expected, the fluctuations in the disordered phase are normal with exponent $\alpha = 0.5$.

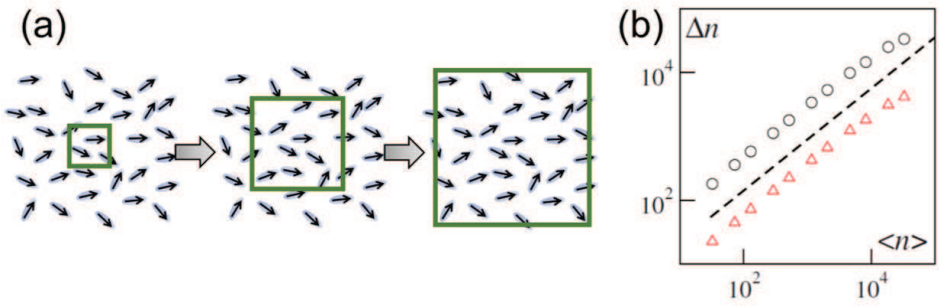

Figure 1.5: Giant number fluctuations. (a) Calculation of number fluctuations. The number of particles and its standard deviation are calculated at different observation areas. (b) Number fluctuations vs mean particle's number. Δn scales approximately as $\Delta n \propto \langle n \rangle^{0.8}$ both in two dimensions (black circles, $\rho = 2, v_0 = 0.5, \eta = 0.25, L = 256$) and in three dimensions (red triangles, $\rho = 1/2, v_0 = 0.5, \eta = 0.1, L = 64$). The image in (b) is adapted from Ref. [11].

Interpretation of GNF

In the transition from the disordered phase to the long-range order in the Vicsek model, the spontaneous breaking of rotational symmetry of the system takes place. Thus, why GNF can be observed in the ordered phase of the Vicsek model can be intuitively interpreted by the Nambu-Goldstone mode (NG mode). The NG mode is a gapless excitation mode that appears when a continuous symmetry is spontaneously broken in a system, allowing for long-wavelength fluctuations without any energy costs. This can be often understood using a wine bottle potential (Fig. 1.6). In the regime where a collection of SPPs exhibits the long-range order, a point standing for an isotropic (disordered) phase becomes unstable, and in turn points in the bottom of the potential become stable, resulting in the spontaneous symmetry breaking whose direction corresponds to the global direction of the long-range order. Once the state falls to the valley of the potential, even infinitesimal perturbations can turn the global polar order to any direction due to the same level of the potential valley.

The occurrence of GNF can be also roughly understood in a mathematical manner using the continuity equation of the density field. Although the details of the equation will be described later, the coarse-grained fields of the density and the velocity, ρ and $\boldsymbol{v}$, can be governed by the number conservation of particles in the system,

$$\frac{\partial \rho}{\partial t} + \nabla \cdot (\boldsymbol{v}\rho) = 0. \tag{1.5}$$

Taking the Lagrangian derivative $\frac{D}{Dt} = \frac{\partial}{\partial t} + \boldsymbol{v} \cdot \nabla$ into account, Eq. (1.5) readily reads

$$\frac{D\rho}{Dt} = -\rho \nabla \cdot \boldsymbol{v}. \tag{1.6}$$

As shown in Eq. (1.6) above, the density change in time is coupled with div $\boldsymbol{v}$ that corresponds to splay instability considered in liquid crystals, meaning that the density in the next time step can be affected by the velocity orientation in the previous time step. This is how the coupling between the density fluctuations and the velocity (orientational) fluctuations causes GNF larger than the normal one.

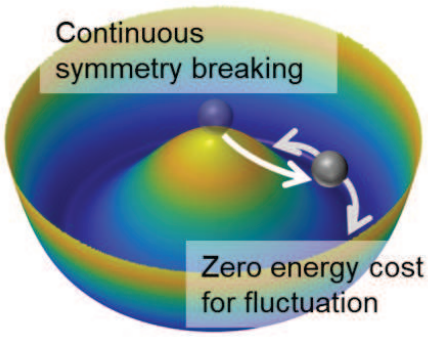

Figure 1.6: A schematic illustration showing spontaneous breaking of rotational symmetry and the occurrence of the Nambu-Goldstone mode.

Superdiffusion

Superdiffusion is also one of the important physical properties in the Vicsek model. SSPs in the symmetry-broken ordered phase show anomalous diffusion in the transverse direction of the polar order. Because of the self-propulsion of particles, the observation of anomalous diffusion seems to be trivial. However, even if we focus only on components of displacement transverse to the mean velocity of the polar order, superdiffusion can be found. This is discussed in the following. Considering the transverse components of the particle's position at time t, $\boldsymbol{r}_\perp(t)$, the mean square displacement (MSD) in the transverse direction is defined as

$$\Delta \boldsymbol{r}_\perp^2 \equiv \langle [\boldsymbol{r}_\perp(t) - \boldsymbol{r}_\perp(0)]^2 \rangle \tag{1.7}$$

where $\langle \cdot \rangle$ denotes ensemble average. In the long time limit, as for Brownian motion, $\Delta \boldsymbol{r}_\perp^2$ scales asymptotically as $\Delta \boldsymbol{r}_\perp^2 \sim t^\nu$ with $\nu = 1$. On the other hand, each particle in the ordered phase of the Vicsek model exhibits superdiffusion with the exponent $\nu = 4/3$ in the two-dimensional system, which is derived by the theoretical analysis of the Toner-Tu model [11, 12]. This originates from strong diffusions induced by advection.

1.2.2 Self-propelled rods model

The understanding of the Vicsek model has been further developed by considering the different symmetry in orientatinal interactions. Ginelli *et al.* proposed another type of the Vicsek model (Vicsek-style model), the so-called self-propelled rod (SPR) model, where particles align not their moving direction but the long axis of the orientation, resulting in either parallel alignment or anti-parallel alignment (Fig. 1.7) [13]. This kind of apolar orientational interaction is called nematic interaction in the same sense as liquid crystals. The dynamics of the position and the orientation of SPRs is described by the following equations:

$$\boldsymbol{r}_j^{t+1} = \boldsymbol{r}_j^t + v_0 e^{i\theta_j^{t+1}} \tag{1.8}$$

$$\theta_j^{t+1} = arg\left[\sum_{k\sim j} sign[\cos(\theta_k^t - \theta_j^t)]e^{i\theta_j^t}\right] + \eta\xi_j^t, \tag{1.9}$$

where the summation runs over all particles k within unit distance from the j-th particle, and ξ represents a white noise uniformly distributed in the interval $[-\pi/2, \pi/2]$.

Figure 1.7: Nematic alignment among self-propelled rods. The collision between rod-shaped particles allows for either parallel alignment or anti-parallel alignment.

Some ordered phases were found by simulating the SPR model above at various noise values η under periodic boundary conditions while fixing the number density $\rho = 1/8$ and the velocity $v_0 = 1/2$. At low noise, long-range nematic order where SPRs are uniformly distributed and align not their polarity but their orientational long axis arises (Fig. 1.8 (a), phase I). When the noise value exceeds $\eta \simeq 0.098$, a low-density disordered region emerges, and a high-density ordered band appears in the steady state (Fig. 1.8 (b) and (c), phase II). As the noise further increases, unstable thinner bands that show spatiotemporal chaotic behaviors appear at $\eta \simeq$

0.163 (Fig. 1.8 (d), phase III). Of course, at strong enough noise, the state becomes completely disordered (Fig. 1.8 (e), phase IV).

The phase III is considered to be the coexistence phase that appears close to the transition point from disordered phase to ordered one, and its transition behavior is classified into discontinuous first-order phase transitions, as with the original Vicsek model. In addition, SPRs in long-range nematic order (phase I) exhibit GNF with the exponent larger than 0.5, compatible to that measured for polarly ordered phases in the Vicsek model, $\alpha = 0.8$.

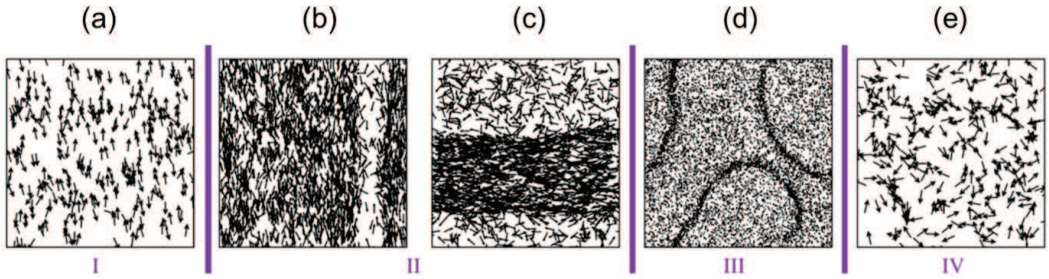

Figure 1.8: Representative snapshots in the steady state at different noise values (linear system size L = 2048). (a) $\eta = 0.08$. (b) $\eta = 0.10$. (c) $\eta = 0.13$. (d) $\eta = 0.168$. (e) $\eta = 0.20$. Arrows shows orientations of SPRs. Images are adapted from Ref. [13].

1.2.3 Mean-field model

We next review the mean-field approach to understand the mechanism of the order-disorder transition using the Vicsek model and the SPR model [14]. Peruani *et al.* described continuous-time versions of these models as follows:

$$\dot{\boldsymbol{x}}_i = v_0 \boldsymbol{v}(\theta_i) \tag{1.10}$$

$$\dot{\theta}_i = -\gamma \frac{\partial U(\boldsymbol{x}_i, \theta_i)}{\partial \theta_i} + \tilde{\eta}_i(t) \tag{1.11}$$

where the state of the i-th particle at time t is given by its position $\boldsymbol{x}_i$ and its orientation θ_i, $\boldsymbol{v}(\theta_i)$ is defined as $\boldsymbol{v}(\theta_i) = (\cos\theta_i, \sin\theta_i)$, and γ is the strengh of orientational interaction. U is the interaction potential among particles, and hence $\frac{\partial U(\boldsymbol{x}_i, \theta_i)}{\partial \theta_i}$ is the rotational force for the velocity alignment. $\tilde{\eta}_i(t)$ works as the white gaussian noise that obeys $\langle \tilde{\eta}_i(t) \rangle = 0$ and $\langle \tilde{\eta}_i(t) \tilde{\eta}_i(t') \rangle = \tilde{\Gamma} \delta_{i,j} \delta(t - t')$, where $\delta_{i,j}$ and

$\delta(t-t')$ are a Kronecker-delta function and a Dirac-delta function, respectively.

In what follows, Peruani *et al.* introduced interaction potentials of polar and apolar alignments. The polar interaction potential $U_p(\boldsymbol{x}_i, \theta_i)$ is given by

$$U_p(\boldsymbol{x}_i, \theta_i) = -\sum_{|\boldsymbol{r}_{ij}|<\epsilon} \cos(\theta_i - \theta_j) \tag{1.12}$$

where $\boldsymbol{r}_{ij} = \boldsymbol{x}_i - \boldsymbol{x}_j$, and ϵ is the radius of polar interaction, which is the same spirit as the ferromagnetic alignment mechanism in spin systems. According to the liquid-crystal alignment mechanism, the nematic interaction potential can be described by

$$U_n(\boldsymbol{x}_i, \theta_i) = -\sum_{|\boldsymbol{r}_{ij}|<\epsilon} \cos^2(\theta_i - \theta_j). \tag{1.13}$$

Figs. 1.9 (a) and (b) show time evolutions of orientation distributions of the agent-based simulations, where each particle obeys Eqs. (1.10) and (1.11), for polar interactions and nematic interactions, respectively. For the polar alignment, the distribution is characterized by a single peak, whereas that for the nematic alignment has two peaks separated by π.

Introducing a density field $\psi(\boldsymbol{x}, \theta, t)$, the particle density at a position $\boldsymbol{x}$ and the orientation distribution can be expressed in the following, respectively:

$$\rho(\boldsymbol{x}, t) = \int_0^{2\pi} \psi(\boldsymbol{x}, \theta, t) d\theta, \tag{1.14}$$

$$C(\theta, t) = \int_\Omega \psi(\boldsymbol{x}, \theta, t) d\boldsymbol{x}, \tag{1.15}$$

where $\psi(\boldsymbol{x}, \theta, t)$ is integrated over the area Ω.

From the conservation of the number of particles, the evolution equation of $\psi(\boldsymbol{x}, \theta, t)$ is obtained as

$$\partial\psi = D_\theta \partial_{\theta\theta}\psi - \partial_\theta \left[F_\theta \psi\right] - \nabla \cdot \left[\boldsymbol{F}_x \psi\right] \tag{1.16}$$

where D_θ is the rotational diffusion coefficient, $F_\theta\psi$ is a deterministic flux for the local alignment mechanism, and $\boldsymbol{F}_x\psi$ is the flux by active migration.

The specific expressions for D_θ, F_θ, and $\boldsymbol{F}_x$ can be derived in what follows. D_θ is associated with the noise amplitude. In the agent-based simulations, the updating rule is written as Eq. (1.2), whose noise amplitude is uniformly distributed in the interval $[-\eta/2, \eta/2]$. Taking into account such a homogeneous distribution centered around 0 with the width η, D_θ can be written as $D_\theta = \eta^2 \Delta t/24$, where Δt is the temporal time step. Next, the interaction of particles, F_θ, can take the following form:

$$F_\theta = -\gamma \int_{R(\boldsymbol{x})} d\boldsymbol{x}' \int_0^{2\pi} d\theta' \frac{\partial U(\boldsymbol{x}, \theta, \boldsymbol{x}', \theta')}{\partial \theta} \psi(\boldsymbol{x}', \theta', t), \tag{1.17}$$

where $U(\boldsymbol{x}, \theta, \boldsymbol{x}', \theta')$ is the pair potential, and the spatial integral is conducted in the interaction range around $\boldsymbol{x}$, $R(\boldsymbol{x})$. Finally, $\boldsymbol{F}_x$ takes the simple form:

$$\boldsymbol{F}_x = v_0 \boldsymbol{v}(\theta). \tag{1.18}$$

Assuming a homogeneous spatial distribution $\psi(\boldsymbol{x}, \theta, t) = C(\theta, t)\rho_0/N$ where $\rho_0 = N/L^2$ is the number density (L: the system size), the evolution equation of $C(\theta, t)$ is given by

$$\frac{\partial C(\theta, t)}{\partial t} = D_\theta \frac{\partial^2 C(\theta, t)}{\partial t^2} + \gamma \frac{\pi \epsilon^2}{L^2} \partial_\theta \left[\left\{ \int_0^{2\pi} d\theta' \frac{U(\theta, \theta')}{\partial \theta} C(\theta', t) \right\} \right]. \tag{1.19}$$

For both polar interactions and nematic interactions, Peruani *et al.* investigated the onset of ordered states by analyzing the linear stability. In doing so, they redefine the following parameters as $\tau = (\gamma \pi \epsilon^2/L^2)t$ and $D'_\theta = D_\theta/[\gamma \pi \epsilon/L^2]$, so that for the polar interaction Eq. (1.19) readily reads

$$\frac{\partial C(\theta, t)}{\partial \tau} = D'_\theta \frac{\partial^2 C(\theta, t)}{\partial t^2} + \partial_\theta \left[\left\{ \int_0^{2\pi} d\theta' \sin(\theta - \theta') C(\theta', t) \right\} \right]. \tag{1.20}$$

By substituting a weak perturbation of the homogeneous state $C(\theta, t) = C^* + C_0 e^{in\theta} e^{\lambda \tau}$, where $e^{in\theta}$ denotes eigenfunctions, into Eq. (1.20), one can obtain the real part of the eigenvalues, $Re(\lambda) = -D'_\theta n^2 + \pi C^* \delta_{n,1}$. This gives the condition

for the instability of the homogeneous pattern,

$$\rho_0 > \frac{2D_\theta}{\gamma\pi\epsilon^2}. \tag{1.21}$$

This analysis suggests that the homogeneous state is no longer stable above the critical number density of particles, leading to the appearance of the global polar order (Fig. 1.9 (c)).

In the same way, for nematic interactions, they obtain the following equation:

$$\frac{\partial C(\theta,t)}{\partial \tau} = D'_\theta \frac{\partial^2 C(\theta,t)}{\partial t^2} + \partial_\theta \left[\left\{ \int_0^{2\pi} d\theta' 2\cos(\theta-\theta')\sin(\theta-\theta')C(\theta',t) \right\} \right]. \tag{1.22}$$

Applying the same procedure yields the critical number density,

$$\rho_0 > \frac{4D_\theta}{\gamma\pi\epsilon^2}, \tag{1.23}$$

which is twice as high as that of polar interactions. This also suggests the presence of the ordered collective state, where the orientation distribution $C(\theta,t)$ has two sharp peaks separated by π, above the critical value (Fig. 1.9 (d)).

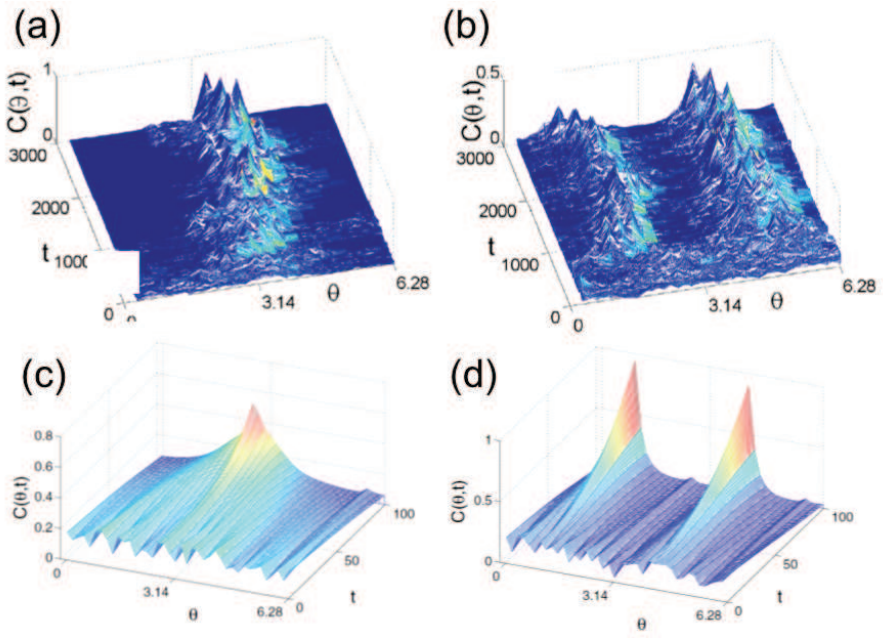

Figure 1.9: Temporal evolution of the orientation distribution, $C(\theta, t)$. (a) and (b) Agent-based simulations for polar alignment and nematic alignment under the conditions: $N = 100, \epsilon = 2, L = 42.4, \eta = 0.25$. (c) and (d) Numerical integrations of Eq. (1.20) with $D_\theta = 0.28$ for polar alignment and Eq. (1.22) with $D_\theta = 0.014$ for nematic alignment. For both (c) and (d), other parameters are set to $C^* = 0.3183, \Delta t = 0.001$, and $\Delta\theta = 0.16$. Images are adapted from Ref. [14].

1.2.4 Toner-Tu model

The Vicsek model exhibits intriguing collective behaviors, and its mean-field theory successfully demonstrates the order-disorder transition caused by the instability above the critical particle's number density. However, it is still hard to analytically discuss the appearance of long-range order and statistical features such as GNF and superdiffusion. We here review the hydrodynamic theory for the Vicsek model, proposed by Toner and Tu [12, 15, 16]. They focused only on the slow and long-wavelength dynamics and considered the coarse-grained velocity field $\boldsymbol{v}(\boldsymbol{r}, t)$ and the density field $\rho(\boldsymbol{r}, t)$.

They wrote down Navier-Stokes-like hydrodynamic equations purely on the symmetry argument that the equation of motion includes all of terms allowed by

the symmetry of the Vicsek model as follows:

$$\begin{aligned}
&\partial_t \boldsymbol{v} + \lambda_1(\boldsymbol{v}\cdot\nabla)\boldsymbol{v} + \lambda_2(\nabla\cdot\boldsymbol{v})\boldsymbol{v} + \lambda_3\nabla(|\boldsymbol{v}|^2) \\
&= \alpha\boldsymbol{v} - \beta|\boldsymbol{v}|^2\boldsymbol{v} - \nabla P_1 - \boldsymbol{v}(\boldsymbol{v}\cdot\nabla P_2) + D_B\nabla(\nabla\cdot\boldsymbol{v}) \\
&\quad + D_T\nabla^2\boldsymbol{v} + D_2(\boldsymbol{v}\cdot\nabla)^2\boldsymbol{v} + \boldsymbol{f},
\end{aligned} \tag{1.24}$$

$$\frac{\partial\rho}{\partial t} + \nabla\cdot(\boldsymbol{v}\rho) = 0, \tag{1.25}$$

$$P_1(\rho,|\boldsymbol{v}|) = \sum_{n=1}^{\infty}\sigma_n(|\boldsymbol{v}|)(\rho-\rho_0)^n, P_2(\rho,|\boldsymbol{v}|) = \sum_{n=1}^{\infty}\mu_n(|\boldsymbol{v}|)(\rho-\rho_0)^n, \tag{1.26}$$

where the phenomenological coefficients, $\lambda_1, \lambda_2, \lambda_3, \alpha, \beta, P_1, P_2, D_B, D_T$, and D_2 are, in general, allowed to depend on the density ρ and the amplitude of the velocity $|\boldsymbol{v}|$. β, D_B, D_T, and D_2 are all positive. P_1 and P_2 are the isotropic pressure and the anisotropic one, which are expressed by the Taylor expansions (Eq. (1.26)), respectively. Note that the anisotropic pressure P_2 is present for nonequilibrium systems like polar flocks, which is absent in equilibrium systems since Pascal's Law ensures that pressure is isotropic. The terms $\alpha\boldsymbol{v} - \beta|\boldsymbol{v}|^2\boldsymbol{v}$ correspond to the derivatives of a quartic Landau velocity potential $-\frac{\alpha}{2}|\boldsymbol{v}|^2 + \frac{\beta}{4}|\boldsymbol{v}|^4$ [17]. For $\alpha > 0$, the potential yields fixed points $|\boldsymbol{v}| = \sqrt{\frac{\alpha}{\beta}}$ that allow for global polar order, while for $\alpha < 0$, the disordered phase becomes stable. The terms of D_B, D_T, and D_2 are the diffusion constants that reflect the tendency of a localized fluctuation in the velocities via interaction among constituents. $\boldsymbol{f}$ is assumed as a white gaussian noise that satisfies the following relation:

$$\langle \boldsymbol{f}_i(\boldsymbol{r},t)\boldsymbol{f}_j(\boldsymbol{r}',t')\rangle = \Delta\delta_{ij}\delta^d(\boldsymbol{r}-\boldsymbol{r}')\delta(t-t') \tag{1.27}$$

where Δ is the noise amplitude, and δ denotes the delta functions.

The left-hand side of Eq. (1.24) has three kinds of advection terms with the coefficients λ_1, λ_2, and λ_3. In contrast to the Navier-Stokes equation for a simple fluid which must be Galilean invariant (i.e., $\lambda_1 = 1$ and $\lambda_2 = \lambda_3 = 0$), conservation of momentum does not hold in the nonequilibrium system we consider here due to the absence of Galilean invariance. This fact allows all three combinations of one

spatial gradient and two velocities with nonzero coefficients.

Eq. (1.25) is just a continuity equation for the conservation of particle number.

Importantly, as a result of the dynamical renormalization group analysis including nonlinear effects in the Toner-Tu theory, they found the velocity fluctuation with a finite magnitude in two dimensions, suggesting that despite two dimensional systems, the population of polar particles as defined in the Vicsek model exhibits true long-range order. In equilibrium spin systems, e.g., the XY model, since the Mermin-Wagner theorem ensures that there cannot be true long-range order in passive systems with less than three dimensions [18], the constituents exhibit quasi-long-range order with the appearance of topological defects of ± 1. Thus, the nontrivial nature of the emergence of true long-range order found in the Vicsek model is a consequence of the nonequilibrium nature of self-propulsion in active systems.

Besides, the Toner-Tu theory gave analytical predictions for some important exponents such as number fluctuations and mean square displacements. In particular, they found the number fluctuations to scale as $\Delta n \propto \langle n \rangle^{\alpha}$ with $\alpha = 4/5$ for two dimensions, i.e., GNF, which is in good agreement with the numerical simulation of the Vicsek model.

1.2.5 Experimental demonstration of the Vicsek universality class

As stated above, it has been reported that both of the Vicsek model and the SPR model, where self-propelled particles interact among nearby particles via polar alignment and nematic alignment, respectively, demonstrate the emergence of true long-range (polar or nematic) order and the presence of GNF in its ordered phase. Although these models are different in the symmetry of interactions, these common physical natures imply the presence of a universal class across different active matter systems. Above all, collective motions with physical properties unique to the Vicsek model (or Vicsek-style model) are regarded to belong to the Vicsek universality class. Although many theoretical works and numerical simulations have provided the evidence for such universality, experiments for its demonstration

have not been well-developed yet due to experimental difficulties. We here review some recent experimental demonstrations of the Vicsek universality class.

Self-propelled particles with polar interactions

Let us firstly report the experiments to realize long-range order of polar active matter in quasi-two-dimensional systems. Iwasawa *et al.* have developed an experimental system consisting of Janus particles of titanium and silica suspended in deionized water under an AC electric field (Fig. 1.10 (a)) [19]. The particles are driven by a surface force that arises from localized nonuniform electric field gradients produced between the asymmetric Janus particle and the surface of the electrode. The particles are thought to interact in a polar-alignment manner, resulting from the balance of electrostatic and hydrodynamic interactions among the particles, though its mechanism is still under discussion. As a result of the experiment, at high density, the population of Janus particles coordinated highly directed motions, leading to true long-range order (Fig. 1.10 (b)). Moreover, the measured number fluctuations in the ordered phase were anomalous and scaled approximately as the mean particle's number to the power of 0.8 (Fig. 1.10 (c)).

Besides, the Quincke rollers have been also widely used as a model system to study collective motion, in particular as active colloids with polar interactions [20, 21]. The experimental system is composed of methyl methacrylate colloids dispersed in an AOT/hexadecane solution. When an electric field is applied, free ion accumulates on the surface of the particles due to the difference of the conductivity and dielectric permittivity between the particle and the surrounding medium, which induces a dipole anti-parallel to the applied field. This unstable state results in the spontaneous rotation of the particles on the substrate, which is called the Quincke effect (Fig. 1.10 (d)). This self-propelled particle effectively shows the polar alignment among the others mediated by electrostatic and far-field hydrodynamic interactions. As with the Janus particles reported above, their population formed long-range polar order (Fig. 1.10 (e)). Note that in this system, the GNF is suppressed because the long-range hydrodynamic interactions damp the splay modes that couple orientation disturbances to density fluctuations.

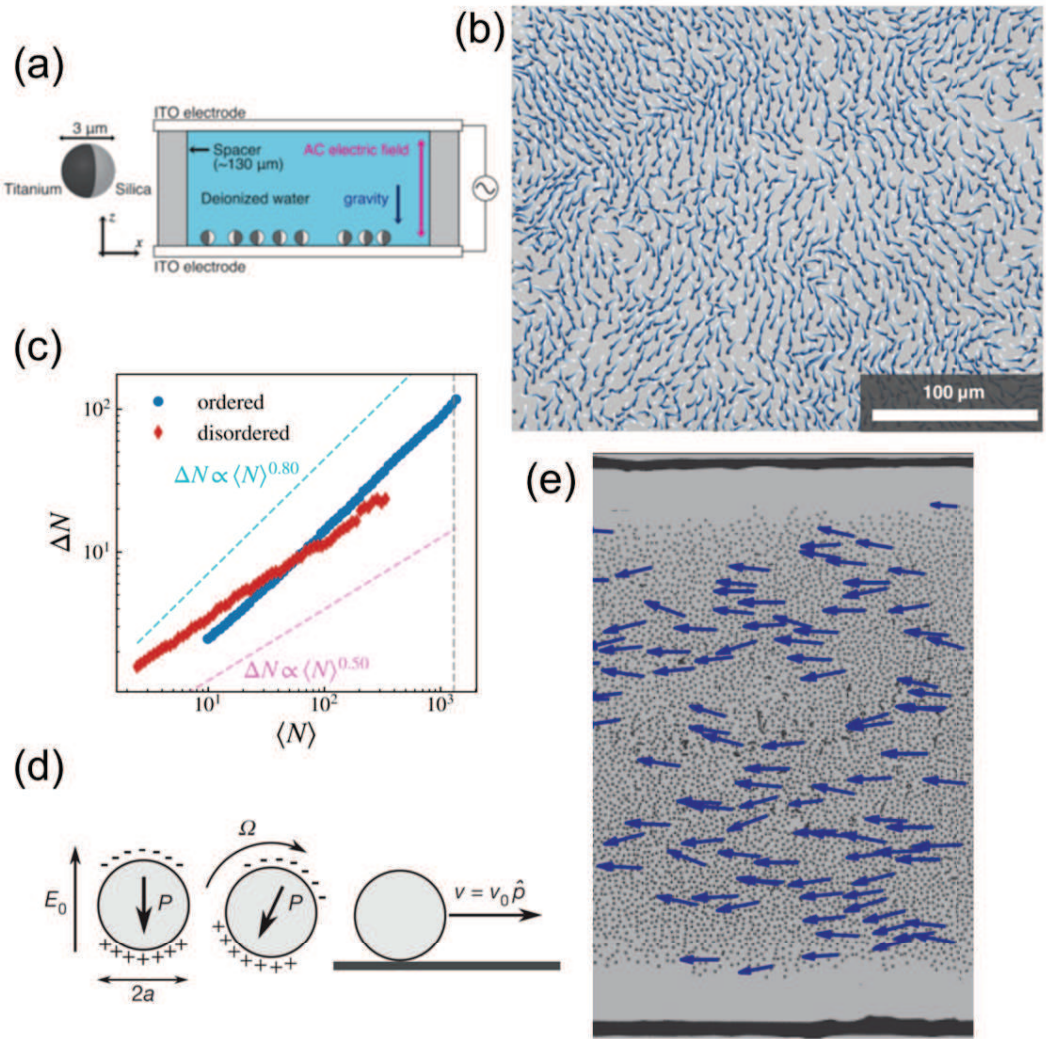

Figure 1.10: Long-range polar order of self-propelled particles. (a) Schematic illustration of the experimental system of Janus particles. (b) Trajectories of the particles in the ordered state. (c) Measurement of number fluctuations in the disordered state and the ordered state. Images in (a-c) are adapted from Ref. [19]. (d) Schematic illustration of the Quincke rotation and of the self-propulsion mechanisms of a colloidal roller. The induced dipole P is anti-parallel to the applied electric field E_0, and in turn, the instability induces the spontaneous rotation. (e) Homogeneous polar order of the Quincke rollers. The arrows denote the instantaneous displacements. Images in (d) and (e) are adapted from Ref. [20].

Self-propelled particles with nematic interactions

We next introduce recent experimental works corresponding to the SPR model. The nematic interactions purely come from the steric interactions between rod-shaped objects. Nishiguchi *et al.* have realized self-propelled rods in experiment by confining long filamentous nontumbling bacteria ($\sim 19 \pm 5\,\mu$m in body length) in a thin chamber ($\sim 2\,\mu$m in depth) [22]. Thanks to the thin enough confinement space and long body length of bacteria, the hydrodynamic interactions become negligible, and in turn, only the steric interactions predominantly work. They firstly observed binary collisions between swimming bacteria and found that the elongated bacteria are weakly oriented after the collisions in a nematic-alignment manner (Fig. 1.11 (a)). Despite the weakness of the alignment, at sufficiently high density of cells, their frequent collisions gave rise to global nematic order: true long-range nematic order (Fig. 1.11 (b)). They furthermore found that the number fluctuations ΔN in the homogeneous ordered state scale as $\Delta N \propto \langle N \rangle^{0.63}$ where $\langle N \rangle$ is an average of the number of cells counted in region of interest (Fig. 1.11 (c)), which is GNF predicted by the Vicsek-style model of polar particles with nematic alignment (SPR model). A slight deviation from $\Delta N \propto \langle N \rangle^{0.75}$ predicted in the numerical simulation is considered to be ascribed to the limited range of accessible statistically significant scales and/or excluded volume effects.

The experimental system of self-propelled rods is realized not only by elongated bacteria but also by active microtubules [23]. Scattered microtubules on a carpet of motor proteins (kinesin motors) where kinesin proteins are bound onto a glass substrate behave as self-propelled rods, which is called motility assay (Fig. 1.11 (d)). As microtubule's density sufficiently increases, nematic interactions between filamentous gliding microtubules give rise to true long-range nematic order (Fig. 1.11 (e)).

This agreement between the theory based on the Vicsek model of polar particles with polar or nematic interactions and the corresponding experiments implies the existence of the Vicsek universality class behind various active matter systems.

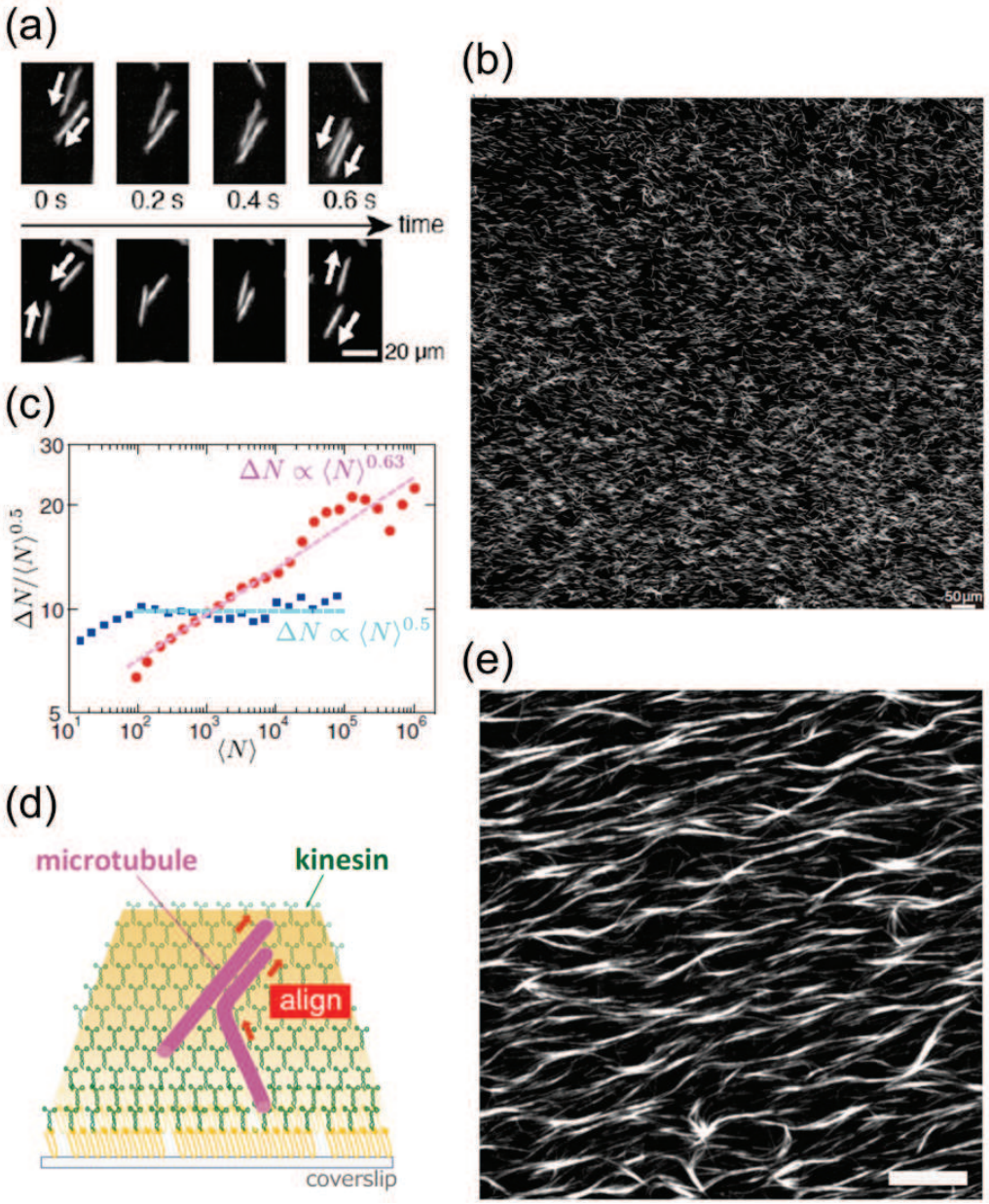

Figure 1.11: Long-range nematic order of self-propelled rods. (a) Binary collisions of elongated swimming bacteria. (b) True long-range nematic order of bacteria at large enough density. (c) Measurement of number fluctuations in the disordered state and the ordered state. Images in (a-c) are adapted from Ref. [22]. (d) Schematic illustration of the experimental system of motility assay. (e) Long-range nematic order of gliding microtubules at sufficiently high density. Scale bar, 20 μm. Images in (d) and (e) are adapted from Ref. [23].

1.3 Classification of active matter

Two types of active matter in terms of the symmetry of interactions have been so far discussed, but there are not only polar particles that move in their orientation but also apolar particles that do not have polarity in their motions in active matter systems. Taken together, on the basis of the symmetry of motions and interactions, active matter can be roughly classified into four types: polar particles with polar interactions (P-P), apolar particles with polar interactions (A-P), polar particles with nematic interactions (P-N), and apolar particles with nematic interactions (A-N) [24].

The P-P type, in general, includes swimming bacteria [25], Janus particles [19], Quincke rollers [20, 21], myosin-driven actin filaments [26], and so on, which is characterized by the emergence of polarly ordered motions such as polar flocks and vortices.

The P-N type includes elongated bacteria [22], gliding microtubules [2, 23], vibrated polar disks [8], and so on. The steric interactions between rods lead to nematic interactions, which give rise to orientational order.

A mixture of microtubules and kinesin motors [27], C2C12 cells [28], neural progenitor cells [29], shaken rods [30], and so on are assigned as the A-N type. These apolar particles stochastically change the direction of movement back and forth to move. This active matter system is often called active nematics that features the emergence of disclinations (topological defects) at which the orientation cannot be locally defined, in particular those of half-integer under densely packed conditions. Besides, the Vicsek-style model of apolar particles with nematic interactions has been argued in Ref. [31]. Ngo *et al.* have found that number fluctuations Δn in the numerical simulations of active nematics exhibit the scaling of $\Delta n \propto \langle n \rangle^{\alpha}$ with $\alpha \sim 0.8$, while its linearized theory yields the exponent $\alpha = 1$. Meanwhile, the number fluctuations with scaling $\Delta n \propto \langle n \rangle^{0.75}$ have been measured in the neural progenitor cells [29]. These imply that the existence of the Vicsek universality class in active nematics (A-N type) could be argued as well.

Finally, the A-P type active matter has been also theoretically studied in Ref. [32]. To the best of our knowledge, however, the corresponding experimental

system has not been found yet. Mahault *et al.* suggest that such an experimental system could be realized by shaken granular disks endowed with two identical legs and carrying magnets [32].

Capturing the essence of active matter in terms of the symmetry of motions and interactions would help us to explore the universality across a variety of active matter systems.

So far, collective motions that can be described by the Vicsek model or Vicsek-style models have been mainly discussed. They are called 'dry' active matter which is simple self-propelled particles without any complex interaction such as hydrodynamic interactions. In general, however, as active matter is immersed in a medium and is highly concentrated, local active stresses destabilize ordered structures via hydrodynamic interactions, often leading to more complex dynamics of collective behaviors. Such active matter is called 'wet' active matter [33].

1.4 Active turbulence

In nature, one of the most fascinating phenomena that the population of wet active matter exhibits is turbulent-like collective behaviors, named active turbulence, created by swimming bacteria [34–39], sperm cells [40], tissue cells [29, 41, 42], and mixtures of motor proteins and cytoskeletons [27, 43, 44]. Amusingly, such many active matter systems exhibit active turbulence reminiscent of the classical turbulent flows with high Reynolds number Re ($Re \gg 1$), although at small Reynolds numbers ($Re \sim 10^{-5}$), rendering the fluid inertia negligible. In this section, we review the theoretical works of active turbulence and hallmarks to discriminate between inertial turbulence and active turbulence.

Before proceeding, let us discuss the classification of active turbulence and intuitive interpretation for its occurrence. Active turbulence is also classified into two types on the basis of the symmetry of motions and interactions. One is active polar fluids composed of dense polar particles with polar interactions (Fig. 1.12 (a) and (b)). The other is active nematics composed of apolar particles with nematic interactions (Fig. 1.12 (c) and (d)). Their constituents are known to exert

extensile or contractile forces at the individual level. For example, microswimmers like swimming bacteria have two types: pusher-type (extensile) swimmers and puller-type (contractile) swimmers which exert a force dipole on a surrounding fluid (Fig. 1.13) [45–47]. In particular, as for dense active matter that exerts extensions, constituents locally align their orientations, but bending configurations are unstable to extensile forces, leading to the instability of aligned configurations in a long wavelength. Quantitatively, the kinetic theory has demonstrated that active turbulence of microswimmers originates from the hydrodynamic instability induced by force dipole of pusher swimmers [48].

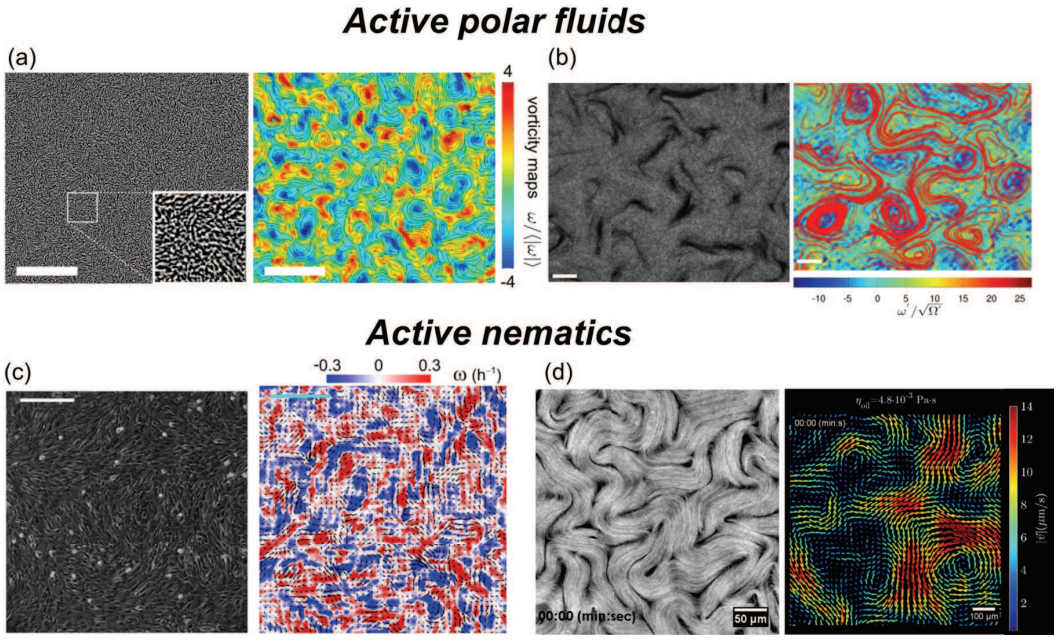

Figure 1.12: Active turbulence. (a) and (b) Active polar fluids. (c) and (d) Active nematics. For each experimental system, a left panel shows an image of the system, and a right panel shows a snapshot of the vorticity field overlapped with either streamlines or the velocity field (only the velocity field in (d) is colored with its magnitude). (a) Bacterial suspension (*B. subtilis*). Scale bars, 50 μm. The image is adapted from Ref. [39]. (b) Sperm cell suspension. The image is adapted from Ref. [40]. (c) C2C12 cell monolayer. Scale bar, 300 μm. The image is adapted from Ref. [42]. (d) Kinesin-driven microtubules suspension. The image is adapted from Ref. [27, 44].

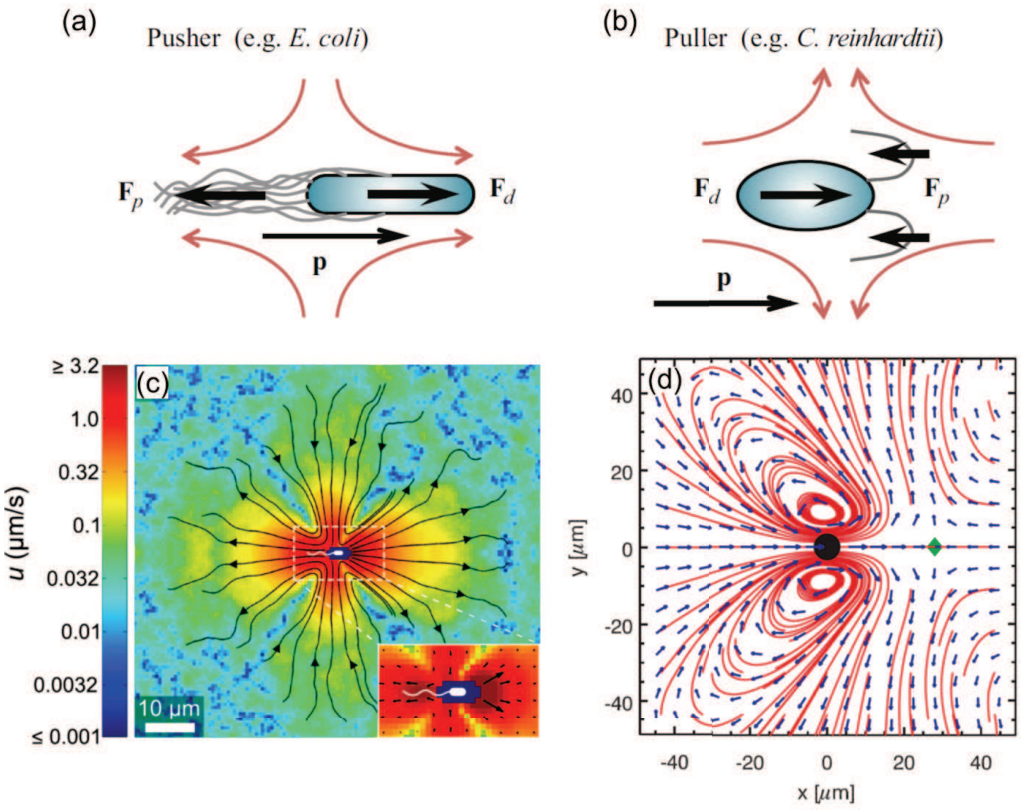

Figure 1.13: (a) and (b) Schematic illustrations of paradigmatic examples of pusher (e.g., *E. coli*) and puller microswimmers (e.g., *C. reinhardtii*). The microswimmer with the polarity $\boldsymbol{p}$ induces the fluid flow depicted by red arrows. Images are adapted from Ref. [47]. (c) Experimental measurement of the flow field near the single *E. coli* bacterium, which shows an extensile dipole flow. The image is adapted from Ref. [45]. (d) Experimental measurement of the flow field near the single *C. reinhardtii* bacterium, which shows a contractile dipole flow. The image is adapted from Ref. [46].

1.4.1 Active turbulence model for polar fluids

As shown above, active polar turbulence, in general, comprises dense microswimmers which are polar entities with head-tail asymmetry such as swimming bacteria, spermatozoa, and active colloids [49]. Early theoretical works proposed continuum models of microswimmer suspensions that comprise three coupled fields: microswimmer density, coarse-grained polarity, and the flow velocity of the surrounding fluid [48, 50, 51]. Although simulations based on these equations yielded turbulent-like flows similar to the experimental observations, these models are not

analytically tractable. Wensink and Dunkel *et al.* regarded motions of a dense bacterial suspension as a single velocity field and put forward a phenomenological description known as the Toner-Tu-Swift-Hohenberg (TTSH) equation [39, 52, 53]. We here review its details.

The TTSH equation is constructed by the Toner-Tu equations, supplemented with a Swift-Hohenberg-type fourth-order term. It assumes that the direction of motion coincides with that of particle's orientation and incompressibility, i.e., $\nabla \cdot \boldsymbol{v} = 0$ that should be a good approximation for very dense suspensions. Based on the structure of the Toner-Tu equation (Eq. (1.24)), the TTSH equation is given by

$$(\partial_t + \boldsymbol{v} \cdot \nabla)\boldsymbol{v} = \alpha \boldsymbol{v} - \beta |\boldsymbol{v}|^2 \boldsymbol{v} - \nabla P + \nabla \cdot E \tag{1.28}$$

where the pressure P is the Lagrange multiplier for the incompressibility constraint. As already discussed in the Toner-Tu equation, powers of the velocity, $\alpha \boldsymbol{v} - \beta |\boldsymbol{v}|^2 \boldsymbol{v}$, are terms coming from a quartic Landau velocity potential that allows the system to reach global polar order with velocity $v_0 = \sqrt{\frac{\alpha}{\beta}}$ in an arbitrary direction for $\alpha > 0$ and $\beta > 0$. From the fact that swimming bacteria locally align their moving directions, but their flow configurations are disturbed and hence leads to the occurrence of many vortices, other instability mechanisms must be at work. In this spirit, the effective stresses that ensure both stability and energy input are introduced in the stress tensor E in the following.

$$E_{ij} = (\Gamma_0 + \Gamma_2 \nabla^2)(\partial_i v_j + \partial_j v_i) + S\left(v_i v_j - \frac{\delta_{ij}}{d}|\boldsymbol{v}|^2\right) \tag{1.29}$$

where d denotes the space dimension, and δ_{ij} is a Kronecker-delta function denoting elements of the unit matrix $\boldsymbol{I}$. The second term corresponds to active nematic stresses due to swimming, and its strength S becomes $S < 0$ for pusher-swimmers like *B. subtilis* or *E. coli* [45] and $S > 0$ for puller-swimmers like *C. reinhardtii* [46].

Substituting Eq. (1.29) for Eq. (1.28), one can obtain

$$(\partial_t + \lambda_0 \boldsymbol{v} \cdot \nabla)\boldsymbol{v} = \alpha \boldsymbol{v} - \beta |\boldsymbol{v}|^2 \boldsymbol{v} - \nabla(P - \lambda_1 |\boldsymbol{v}|^2) + (\Gamma_0 \nabla^2 + \Gamma_2 \nabla^4)\boldsymbol{v} \tag{1.30}$$

where λ_0 and λ_1 are defined as $\lambda_0 = 1 - S$ and $\lambda_1 = -S/d$, respectively. For $\alpha = \beta = S = \Gamma_2 = 0$ and $\Gamma_0 > 0$, Eq. (1.30) readily reduces to the usual Navier-Stokes equation for a conventional fluid. However, in order to generate self-sustained turbulent-like flows, the effective viscosity Γ_0 needs to be negative for destabilization, and the coefficient Γ_2 in the higher-order term positive for stabilization at shorter wavelengths. According to microscopic models that derives the TTSH equation [54], an increase of activity leads to a decrease of the effective viscosity Γ_0, implying the possibility of turning negative.

Fig. 1.14 (d) is the vorticity field with streamlines, produced by the simulation of Eq. (1.30), which is similar to the experiment with a dense *B. subtilis* suspension confined in a quasi-two-dimensional chamber.

1.4.2 Energy spectrum in active polar turbulence

We next discuss a comparison between the active turbulence model and the experiment using energy spectrum that is one of the most important and informative analyses for turbulent dynamics so far. The energy spectrum is obtained from Fourier transformation of the equal-time two-point velocity correlation function (see Chapter 2 for the details of the calculation) (Figs. 1.14 (e) and (f)). As evident from the energy spectrum, the key difference between active turbulence and classical one lies in how the injected energy cascades over the scales. In inertial turbulence, the scale of the energy injection is determined by external driving, whereas in active turbulence, the energy injection is from its microscopic constituents, and they self-organize into correlated structures on larger scales. However, since there is a competition between energy input and dissipation, the energy spectrum is peaked out at similar scales, unlike the inertial turbulence. This leads to the presence of characteristics scales of the generated flows and simultaneously implies the limitation of cascading up towards much larger scales. The linear stability analysis of Eq. (1.30) yields a maximum growth rate at a finite wavenumber $q_c = \sqrt{-\Gamma_0/(2\Gamma_2)}$, which corresponds to a characteristic vortex size $\Lambda = 2\pi\sqrt{2\Gamma_2/(-\Gamma_0)}$ in diameter. This is consistent with the experiment (Fig. 1.14). The ratio of Γ_0 and Γ_2 also determines a characteristic velocity $V_\Gamma = \sqrt{|\Gamma_0|^3/\Gamma_2}$. These properties are

obviously different from classical turbulence. Note that in terms of energy input or dissipation, the negative friction α and the negative viscosity Γ_0 terms inject energy, while the cubic nonlinear term β and the higher-order derivative term Γ_2 are responsible for energy dissipation, and the self-advection term λ_0 transports energy across length scales.

The power law behaviors of $k^{5/3}$ at small wave numbers and $k^{-8/3}$ at large wavenumbers in the energy spectrum would be also an interesting point. This motivated some physicists to investigate whether they are universal exponents. Bratanov *et al.* have reported that exponents of the energy spectrum depend on parameter values because the cubic nonlinearity ($\beta|\boldsymbol{v}|^2\boldsymbol{v}$) in the Toner-Tu model, which is absent in the the normal Navier-Stokes equation, gives additional freedom other than the advective nonlinearity ($\boldsymbol{v}\cdot\nabla\boldsymbol{v}$) [55]. Thus, so far, it is believed that power laws of energy spectra observed in active polar turbulence have non-universal exponents, although there is no experimental evidence yet.

As a side note, another type of SPR model that only considers excluded volume effects of rods with an aspect ratio has been also proposed in Ref. [39]. Its simulation produced seemingly turbulent-like behaviors, but its statistical properties were different from both the experiment and the TTSH model (Figs. 1.14(c-f)).

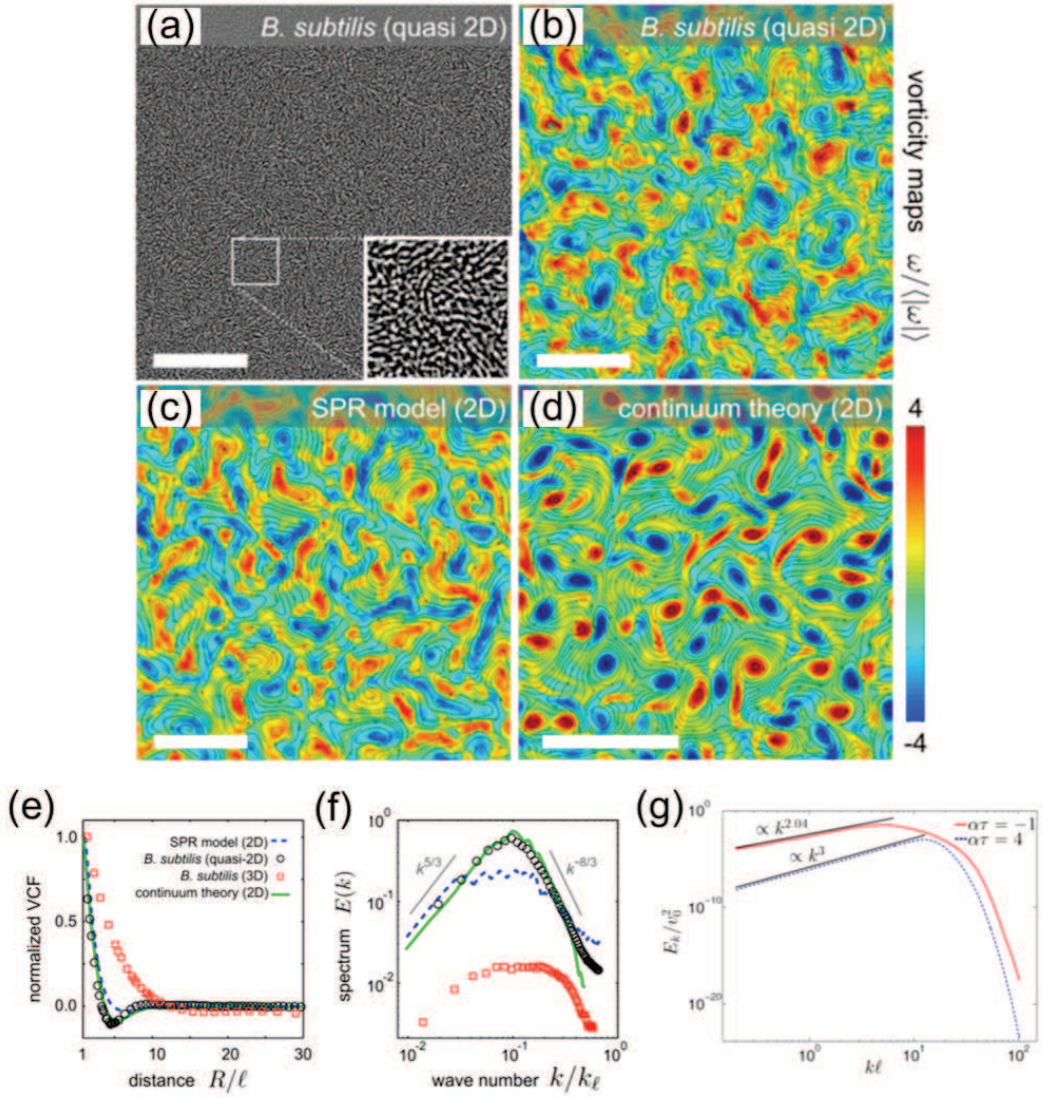

Figure 1.14: Bacterial turbulence and active turbulence model. Scale bars, 50 µm. (a) Image of a dense *B. subtilis* suspension confined in a quasi-two-dimensional chamber. (b-d) Vorticity with streamlines is analyzed for the experiment (b), the SPR model (c), and the TTSH model (d). (e) Normalized velocity correlation function. (f) Energy spectrum obtained from (e). Images in (a-e) are adapted from Ref. [39]. (g) Parameter dependence of energy spectrum. The image in (g) is adapted form Ref. [55].

To further understand the link between active turbulence and hydrodynamic classical turbulence, Linkmann *et al.* put forward a generalized Navier–Stokes model with a piecewise constant viscosity to seek the phase transition between

them [56]. Their model has demonstrated that, in the regime where the kinematic viscosity of the suspension is small (above its critical point), an inverse cascade to larger scales occurs, and condensate forms at the largest scale, which is analogous to 2D inertial turbulence. However, the feasibility of its experimental demonstrations remains an open question.

Although the TTSH model is obtained upon phenomenological assumptions, it can be also derived from the kinetic theory starting from microscopic descriptions like Langevin equations [54]. Applying a mean-field approximation to the microscopic model consisting of three equations for center-of-mass velocity, orientational velocity, and flow velocity of an ambient fluid yields the mean-field Fokker-Planck equations. They further give the coarse-grained field equations for polarization field and fluid velocity field. Importantly, since in the limit that the ratio of active force (pusher-swimmer) to viscous force is sufficiently small the Stokes equation for the solvent velocity becomes independent of the swimmer orientation, two-fields equations can reduce to the single-field TTSH equation. Note that another approach to derive the TTSH equation from a two-field model has been reported in Ref. [57].

As supposed in Ref. [54], in general, swimming bacteria should interact with their environment via long-range effective hydrodynamic interactions and short-range alignment interactions: nematic (passive) interactions and polar (active) interactions. The origin of polar interactions may be still elusive, while it is trivial that nematic interactions stem from steric interactions between rods. Li *et al.* have reported on hydrodynamic interactions between pusher swimmers [58]. Analyzing angular rotation of a rod induced by a force dipole flow, which follows Jeffery orbits, they found that the resulting angular rotation can be described by a function including the symmetry of polar alignments, although at a dilute condition. Therefore, polar interactions among microswimmers may be attributed to the near-field hydrodynamic interactions, e.g., re-orientation by force dipole flows.

1.4.3 Active nematics

Next, let us briefly review active nematics. Active polar turbulence and active nematics can be characterized by topological defects with ± 1 integer charges and $\pm\frac{1}{2}$ half-integer charges, respectively (Fig. 1.15 (a)). Fig. 1.15 (b) displays flow configurations induced by each of topological defects of $\pm\frac{1}{2}$, which are substantially different from the orientations of constituents. As is clear from the difference, equations to describe dynamics of active nematics certainly need two coupled fields, unlike active polar turbulence that is successfully described by the TTSH equation.

Intriguingly, scaling laws of the energy spectrum in a turbulent state of active nematics that appears in the limit of high activity have been predicted to be $E(q) \propto q^{-1}$ for $qR^* \ll 1$ and $E(q) \propto q^{-4}$ for $qR^* \gg 1$, where q is a wave number, and R^* denotes a characteristic vortex size (Fig. 1.15 (d)) [61, 62]. These predicted scaling laws have been confirmed in the experiment with active nematic microtubule films assembled at an oil-water interface (Fig. 1.15 (c)) [44]. This suggests that the scaling laws with universal exponents exist in the turbulent state of active nematics. Unlike the active polar turbulence, since a commonly used equation for flow field does not have an advection term, the energy in active nematic turbulence is transferred by other nonlinear effects such as flow alignment and elastic stresses.

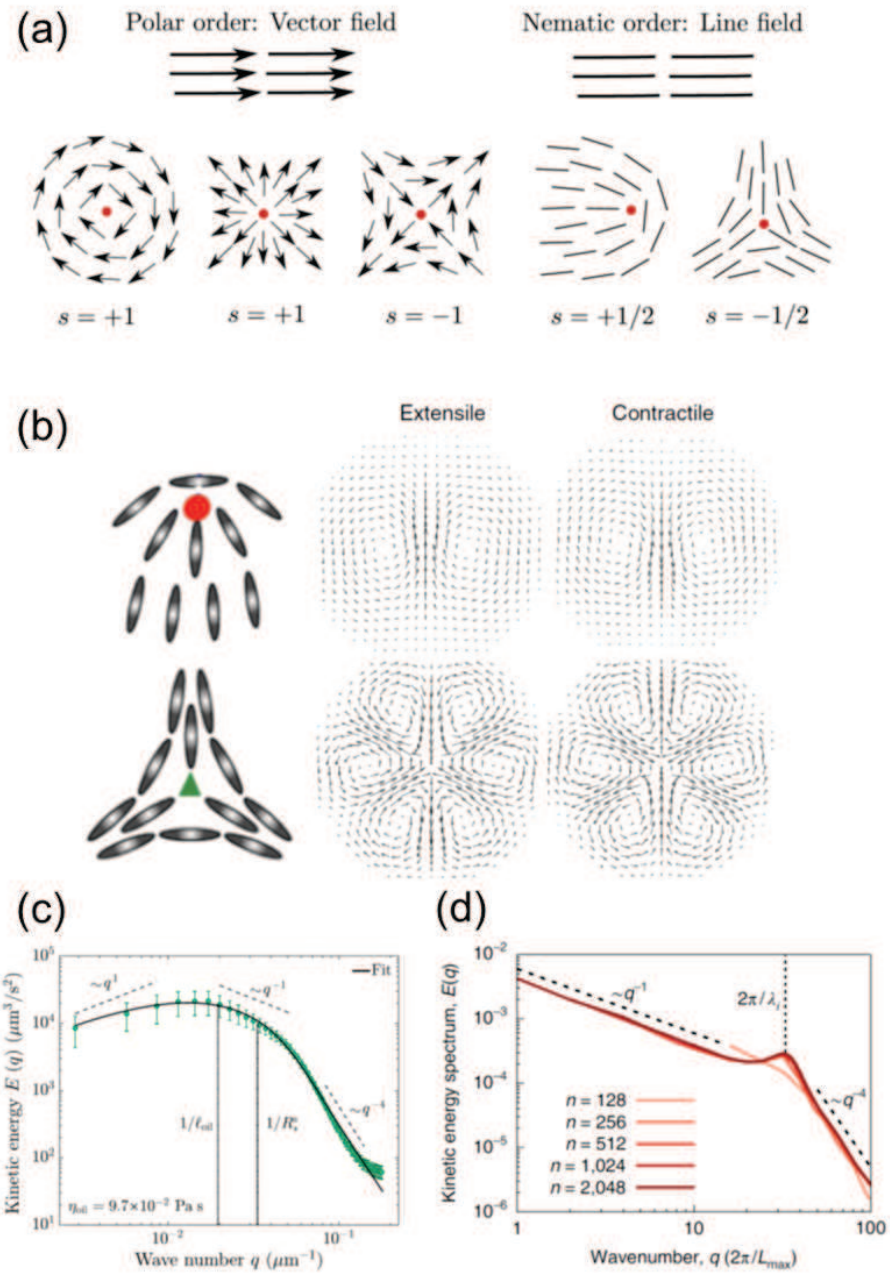

Figure 1.15: Topology and energy spectrum in active nematics. (a) Examples of topological defects. Their charges depend on the symmetry of particles. The image is adapted from Ref. [59]. (b) Flow configurations induced around half-integer topological defects. The image is adapted from Ref. [60]. (c) Energy spectrum measured in kinesin-driven microtubule films assembled at an oil-water interface. The image is adapted from Ref. [44]. (d) Energy spectrum obtained from theory. The image is adapted from Ref. [61].

1.5 Bacterial turbulence and geometry

As discussed above, collective states produced by a group of swimming bacteria are manifold, ranging from true long-range nematic order [22] to swarming [25], active polar turbulence [39], and even active nematic turbulence [63]. Due to such fascinating diverse phenomena and the tractability in experiments, a considerable number of studies have used them as a model experimental system. As for bacterial turbulence, its experimental study was sparked by Mendelson *et al.* (1999) about twenty years ago [34], which discovered that a thin film of dense *B. subtilis* on an agar plate exhibits turbulent-like collective motions composed of transient vortices and jets. Afterward, both experimental and theoretical intense efforts have been made to understand the underlying mechanism and physical properties, e.g., superdiffusion of suspended particles [35], energy spectrum [37, 39], the dependence of a characteristic length on concentration or swimming speed [64, 65], Lévy walk of individual bacteria [66], and transition kinetics of 3D bacterial turbulence [38].

Let us mention the pioneering work by Wu and Libchaber (2000) in more detail [35]. They have demonstrated through quantitative measurements that transient yet ordered vortical motions could be inherent in active turbulence of a dense bacterial suspension, although the disordered state seemingly appears to be chaotic. They suspended silica beads tracer particles of a few microns in a quasi-two-dimensional bacterial bath and analyzed their trajectories. Indeed, the suspended particles are stirred by bacterial swarming and hence the mean square displacement (MSD) or velocity correlation function of tracer beads can characterize the transient ordered state of bacterial collective motion. The measured MSD showed a rapid increase at a shorter timescale as t^2, whereas the MSD became proportional to t at a longer timescale. The crossover at the characteristic time indicates that ordered motion with coherent heading angle is present behind apparently chaotic motions of swarming bacteria.

Thanks to many previous works presented above, it has been revealed that chaotic active turbulence comprises locally ordered structures like vortices, implying the possibility of controlling it. Accordingly, considerable attention to controlling patterns has been paid due to its potential in exploiting the underlying mech-

anism behind the elusive dynamics of turbulent vortices. A simple yet promising means is to give a geometrical boundary condition. Recent experimental studies have shown that geometric constraints with a characteristic length scale unveil the geometrical nature of constituent vortices inherent in active turbulence. We here review some important previous works regarding collective bacterial motion under geometrical constraints.

1.5.1 Vortical motion under a circular comfinement

Wioland *et al.* have reported that a single bacterial vortex can be isolated by encapsulating a dense *B. subtilis* suspension in a water-in-oil droplet [67]. When bacteria are confined in a droplet with an appropriate size, the group of bacteria starts to align the heading angle and in turn form coherent rotational mode as a vortex-like structure (Figs. 1.16 (a) and (b)). To quantitatively investigate the dependence of the emergent vortex on compartment size, they defined a vortex order parameter that becomes 1 for a clear vortex (see Chapter 2 for details of the definition). As shown in Fig. 1.16 (c), a highly ordered vortex arose in drops of $30\,\mu\mathrm{m} < d < 70\,\mu\mathrm{m}$ which is comparable with the characteristic length in mesoscale turbulence of unconfined bacteria ($\sim 50\,\mu\mathrm{m}$). Since the bacteria themselves are rod-shaped, steric interaction with the boundary of the droplet aligns the direction of motion, leading to a stabilized vortex. Indeed, the flagella rotation, namely propelling helical tail, pushes ambient fluids at rest against the heading angle, meaning that bacteria also have hydrodynamic interactions with other bacteria or the boundary wall. The boundary of the water-in-oil droplet behaves like a solid wall, that is, a no-slip boundary because of the viscosity difference between the inner and outer medium. The induced shear stress acts on bacteria swimming close to the boundary and then turns their direction of motion opposite to the inside vortex rotation. The resulting counter-rotating layer close to the boundary generates backflows that further stabilize the inside vortex. Thus, it has been demonstrated that suitably designed boundaries can isolate a stable bacterial vortex from disordered bacterial turbulence.

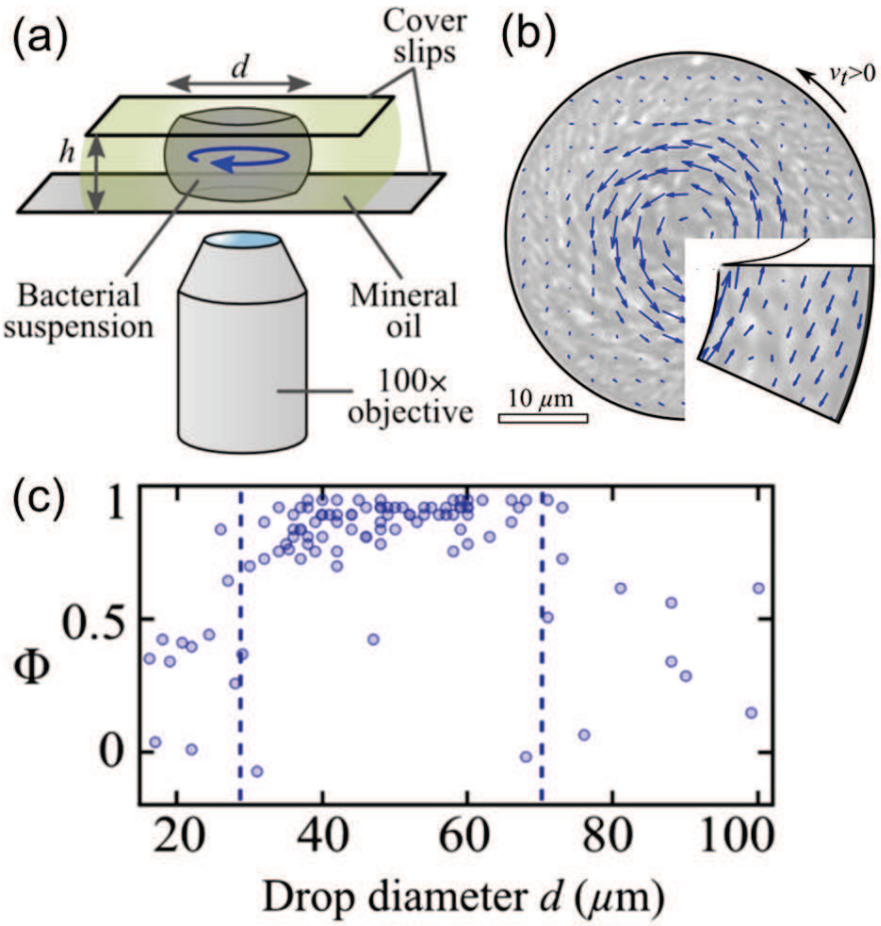

Figure 1.16: Single bacterial vortex stabilized in an emulsion. (a) Schematic of experimental setup. A dense *B. subtilis* suspension is confined in a cylindrical water-in-oil droplet with a diameter d and a height h. (b) Representative data of coarse-grained velocity field. (c) Vortex order parameter vs droplet diameter. Images are adapted from Ref. [67].

1.5.2 Multiple interacting vortices

Indeed, bacterial vortices with clockwise or counter-clockwise handedness composing active turbulence resemble interacting spins in condensed matter, where either spin up or spin down corresponds to a clockwise or a counter-clockwise bacterial vortex. Wioland *et al.* have extended circular geometries to lattices of circular cavities containing a dense bacterial suspension and connected by channels with width w by using microfluidic devices made of polydimethylsiloxane (PDMS) [68]. In such chambers, interacting vortices gave rise to two distinct ordered phases: the ferromagnetic order of bacterial vortices rotating in the identical direction

and the anti-ferromagnetic one of bacterial vortices rotating in opposite directions. Remarkably, the transition between them was governed by the width of the channel w such that the state shows the ferromagnetic order for large w and the anti-ferromagnetic for small w (Fig. 1.17). These results exhibited fundamental similarities with quantum systems, implying the potential to capture collective behavior in active matter systems on the basis of the theoretical concept to describe magnetism.

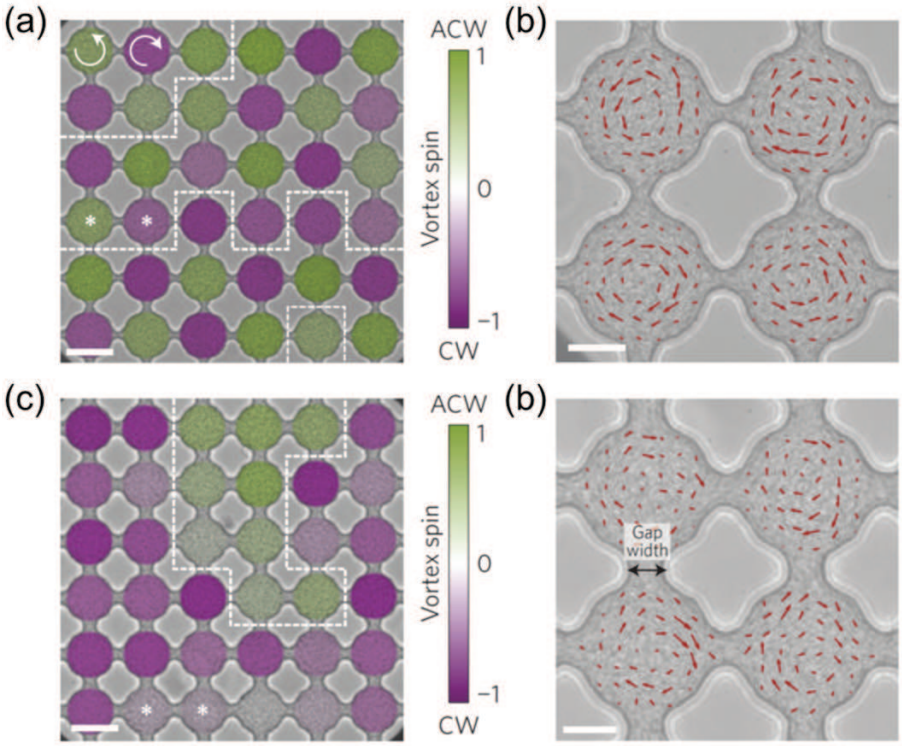

Figure 1.17: Ferromagnetic order (a,b) and anti-ferromagnetic order (c,d) in interacting vortices of bacteria. (a) Channel width $w = 6\,\mu\text{m}$. The three domains with the ferromagnetic order are separated by white broken lines. (b) Velocity field in a domain with the ferromagnetic order. (c) Channel width $w = 11\,\mu\text{m}$. The three domains with the anti-ferromagnetic order are separated by white broken lines. (d) Velocity field in a domain with the anti-ferromagnetic order. Scale bars, 50 µm for (a) and (c). Scale bars, 20 µm for (b) and (d). Images are adapted from Ref. [68].

Then, Nishiguchi *et al.* have investigated bacterial turbulence under geometrical constraints by periodic vertical pillars, without any enclosing outer boundary [69]. Putting square pillars at regular intervals with square lattice constant

L in a dense *B. subtilis* suspension, the population exhibited the tendency of the anti-ferromagnetic order in active turbulence, although the degree of order is dependent on L. To quantitatively capture the anti-ferromagnetic order against L, they defined a spin variable for each region of interest (ROI), which is set as a rectangular area surrounded by pillars, and an adjacent spin correlation as follows. The former is defined by

$$S_{i,L}(t) \equiv \frac{\hat{\boldsymbol{z}} \cdot \left[\sum_{\boldsymbol{r} \in ROI_L^i} (\boldsymbol{r} - \boldsymbol{r}_i) \times \boldsymbol{v}(\boldsymbol{r}, t)\right]}{\sum_{\boldsymbol{r} \in ROI_L^i} |\boldsymbol{r} - \boldsymbol{r}_i|} \tag{1.31}$$

where ROI_L^i is the i-th ROI in the lattice with period L, $\boldsymbol{r}_i$ is the center position of ROI_L^i, and $\hat{\boldsymbol{z}}$ is the vertical unit vector, which stands for rotational directions: negative for CW and positive for CCW. The latter is given by

$$\chi_L \equiv \frac{\sum_{ij} S_{i,L}(t) S_{j,L}(t)}{\sum_{ij} |S_{i,L}(t) S_{j,L}(t)|} \tag{1.32}$$

where the summation is taken over all adjacent pairs in a single lattice structure. As shown in Fig. 1.18 (c), for a pillars' spacing period of $L \sim 70\,\mu\text{m}$, which is comparable with intrinsic length of vortex, the stable anti-ferromagnetic order was organized in spite of a tiny amount of volume occupied by pillars, characterized by strong anti-correlation between adjacent vortices. Note that similar stabilization mechanism of bacterial flows in channels depending on confinement size has been reported in Ref. [70]. These results stress the importance of the characteristic scale for both fully enclosed (like lattice-like microfluidic device) and weakly confined (like pillars' spacing) systems in controlling active turbulence.

Moreover, simulations based on the TTSH equation (Eq. (1.30)) in the presence of geometrical pillar's constraints yielded results consistent with the experiment [71].

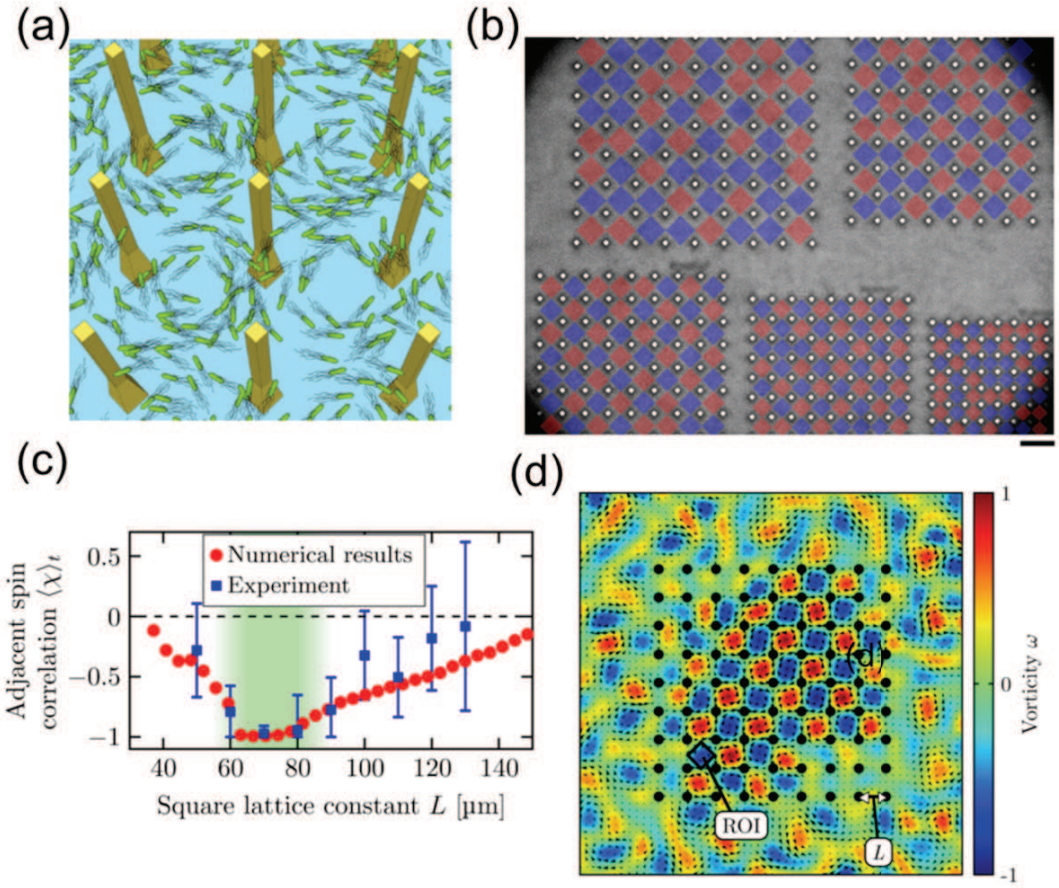

Figure 1.18: Bacterial turbulence under geometrical pillars' spacing. (a) Schematic of a dense *B. subtilis* suspension slightly confined by rectangular pillars. (b) Image of a dense bacterial suspension in the presence of pillars placed at various periods. Red colored region denotes CW circulation and blue CCW. (c) Dependence of anti-ferromagnetic order on a lattice constant L. (d) Snapshot of simulation based on the TTSH equation under a boundary condition of pillars' spacing. (a) and (b) Images are adapted from Ref. [69]. (c) and (d) Images are adapted from Ref. [71].

1.6 Research aim

Despite an exciting development in the field of active turbulence last two decades, the physical rule and the universality behind chaotic active turbulence, which is ubiquitous across various active matter systems, remain unclear. As discussed above, active turbulence comprises ordered vortical structures with a characteristic length. Indeed, the inherently ordered vortices can be characterized by ferromagnetic (co-rotating) order and anti-ferromagnetic (anti-rotating) order and controlled by geometrical constraints. This hints at the presence of geometric rule behind ordered bacterial vortices, but it remains uncovered. In Chapter 2, we aim to elucidate how ordered bacterial vortices can be ruled by simple geometric quantities.

Another important symmetry of active matter except for motion and interaction is chirality, i.e., the mirror-symmetry breaking. Swimming bacteria also have chirality in their swimming mechanism (we will detail later), but its role played in active turbulence is poorly understood. The aim of Chapter 3 is to clarify the effect of chirality on collective motion and a geometric rule including it.

Furthermore, the geometric approach is of importance not only for studying physical rule in active turbulence but also for exploring the geometric universality across various active systems. In Chapter 4, applying it to an assembly of gliding microtubules, that is, a self-propelled rods system, we aim to reveal a common geometric rule hidden in active matter with different symmetries.

Chapter 2

Geometric control of interacting bacterial vortices

2.1 Experimental setup

In order to reveal geometric features of ordered vortices behind bacterial turbulence, we use a confined dense suspension of *Escherichia coli* (*E. coli*) RP4979 strain that shows smooth-swimming known as one of the model systems in active matter physics. In this section, we describe the basic properties of *E. coli* bacteria and their RP4979 strain and how to impose a boundary condition on bacterial suspensions.

2.1.1 *Escherichia coli* bacteria

Many previous studies use *Batillus subtilis* (*B. subtilis*) that is also useful for experiments of active matter. The comparison between their wild-type strains is in what follows. Both bacteria swim with peritrichous flagella and have a rod-shaped body, but their aspect ratio is different. In regard to a typical size, the body length of *B. subtilis* is $4 \sim 10\,\mu\mathrm{m}$ and its width is $\sim 1\,\mu\mathrm{m}$ [72], while *E. coli* is $2 \sim 3\,\mu\mathrm{m}$ in length and $\sim 1\,\mu\mathrm{m}$ in width [73], and thus the aspect ratio of the body shape of *B. subtilis* is larger than that of *E. coli*. (Note that the *E. coli* RP4979 strain has the body length of $3.5 \pm 0.6\,\mu\mathrm{m}$, which is still shorter than *B. subtilis*.)

As for the bacterial motility, both typical swimming speeds are almost comparable that is $20 \sim 30\,\mu m/s$. In addition, these bacteria usually perform chemotaxis which is the movement in response to a chemical stimulus such as concentration gradients of some attractants and nutrients. Repeating the movement in the straight line (run) and the stochastic change of moving direction (tumble) while changing its rate depending on a chemical stimulus, they move in the preferred direction. In the run process, they swim like a screw with bundled flagella by rotating them in a counterclockwise (CCW) direction and their body in a clockwise (CW) direction (when viewed from behind). In the tumbling, they temporarily stop by rotating the flagella in CW and unwinding them (Fig. 2.1). However, an RP4979 strain of *E. coli* lacks the ability to tumble, resulting in smooth swimming (see Appendix A for the details). That is why the *E. coli* RP4979 strain is one of the simplest realizations of active matter due to its simplicity and tractability in experiments.

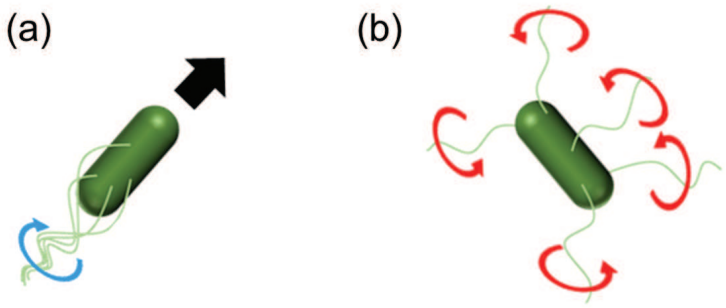

Figure 2.1: Two modes of *E. coli* motion. (a) Run mode: swimming in the straight line by rotating bacterial flagella in CCW. (b) Tumbling mode: randomly changing the direction of motion by rotating them in CW.

2.1.2 Confinement by fabricated polydimethylsiloxane microwells

To design boundaries for confinement, we fabricate polydimethylsiloxane (PDMS) microwells (see Fig. 6.6 (b) in Appendix B). Dense *E. coli* suspensions ($\sim$ 20 v/v%) are confined by designed PDMS microwells and a glass slide with a surface treatment to avoid unspecific adhesion of bacteria (Fig. 2.2 (a)), leading to symmetric confinement in that both top and bottom interfaces are solid (Fig. 2.2 (b))

(see Appendix A and B for details of methods).

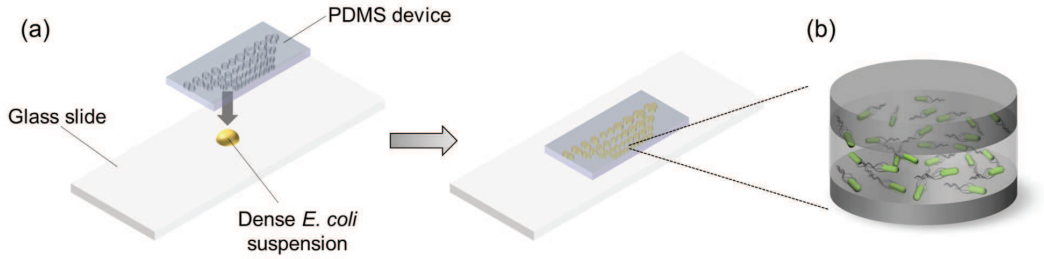

Figure 2.2: Schematic illustrations of the method of confinement. (a) Process of confining a dense bacterial suspension ($\sim$ 20 v/v%) in PDMS microwells. (b) The dense bacterial suspension is encapsulated by a PDMS microwell and a glass substrate.

2.2 Bacterial turbulence in a quasi-2D system

Before investigating the geometric rule of ordered interacting vortices, we first clarify the statistical features of laterally unconfined dense bacterial suspensions in a quasi-two-dimensional system.

We measured bacterial turbulence by sandwiching a 1 µL drop of a dense *E. coli* suspension ($\sim$ 20%v/v) with an MPC(2-Methacryloyloxyethyl phosphorylcholine)-polymer-coated glass slide and PDMS block whose surface is flat, which realizes a quasi-2D chamber with $\sim$ 10 µm in height. Fig. 2.3 (a) and (b) show the bright-field image of a dense *E. coli* suspension undergoing active turbulence and the velocity field calculated from the particle image velocimetry (PIV) analysis which is averaged over 1 s, respectively (see Appendix C for details). Taking the rotation of the velocity field, $\nabla \times \boldsymbol{v}$, we analyze the vorticity map (Fig. 2.3 (c)) where the domains of red and blue basically tell us CW and CCW vortices, respectively. As shown here, many interacting bacterial vortices coexist in bacterial turbulence.

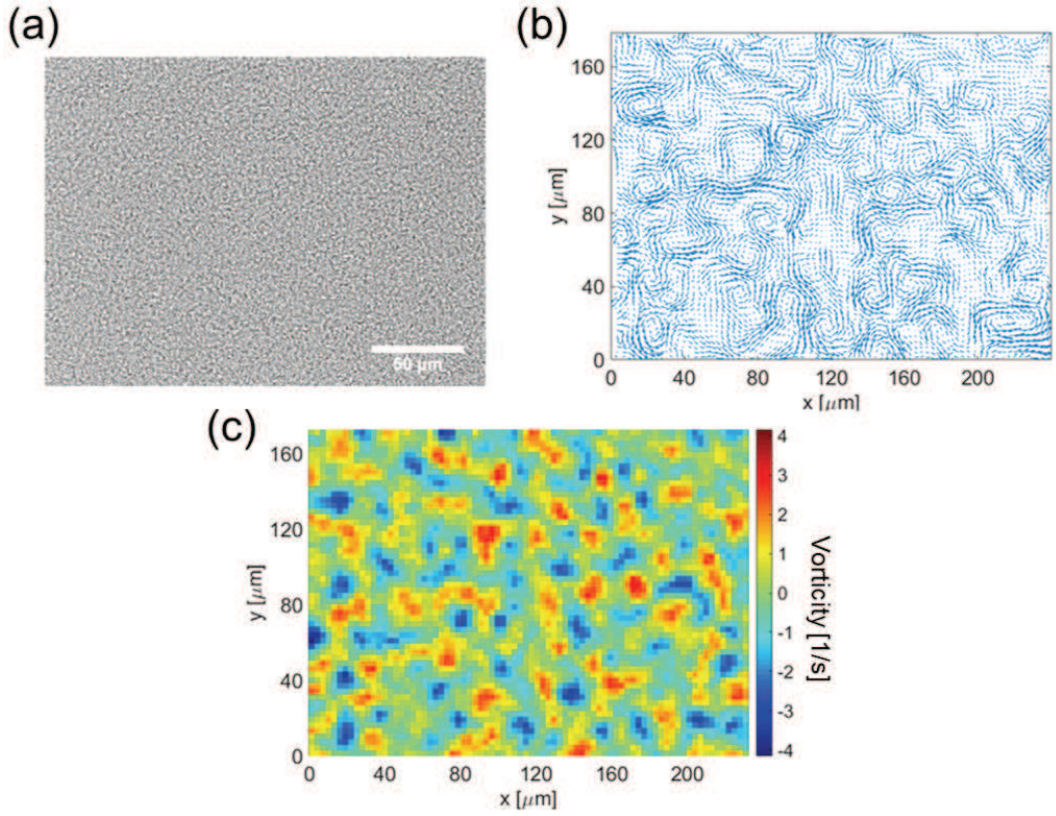

Figure 2.3: Bacterial turbulence in a quasi-2D chamber. (a) Bright-field image. (b)Velocity field. (c) Vorticity map. Colors represent the CW and CCW rotation of the flow for red and blue, respectively.

To quantitatively extract the length scales from such chaotic flow fields, we calculate the energy spectrum that is commonly used in the analysis of classical turbulence. The energy spectrum $E(k)$ is defined by Fourier transformation of the velocity correlation function in the following [39]:

$$E(k) = \frac{k}{2\pi} \int d^2r' e^{-i\boldsymbol{k}\cdot\boldsymbol{r}'} \langle \boldsymbol{v}(t,\boldsymbol{r}) \cdot \boldsymbol{v}(t,\boldsymbol{r}+\boldsymbol{r}') \rangle \tag{2.1}$$

where $\langle \boldsymbol{v}(t,\boldsymbol{r}) \cdot \boldsymbol{v}(t,\boldsymbol{r}+\boldsymbol{r}') \rangle$ denotes the equal-time two-point velocity correlation function for $\boldsymbol{r}'$. Fig. 2.4 shows the energy spectra for wild-type bacteria (Normal) and elongated bacteria with cephalexin (Elongated), which has a peak at a certain wavenumber k^*, the same as the previous work [39]. The characteristic diameter of the emergent vortices l^* can be estimated as $l^* = \pi/k^*$, yielding $l^* \approx 25.1\,\mu\mathrm{m}$

for 'Normal' and $l^* \approx 45.3\,\mu\mathrm{m}$ for 'Elongated'.

Moreover, the resulting correlation length increases with bacterial length, which is consistent with the previous work [74]. This is because enlarging aspect ratio of rod-shaped bacteria makes the local alignment interaction stronger, resulting in the emergence of longer correlated regions. This is also supported by previous theoretical studies for active turbulence that show the hydrodynamic instability occurs at a length scale characterized by cell aspect ratio, swimming speed, effective bulk viscosity, etc [51, 54].

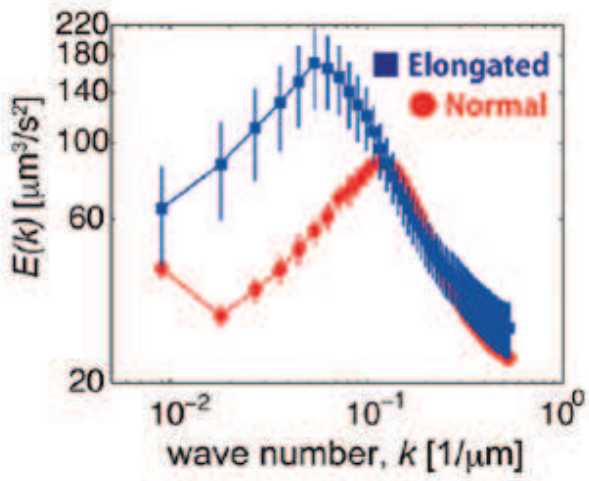

Figure 2.4: Energy spectra of bacterial turbulence. Red circles indicate data for wild-type (normal) bacteria and blue squares indicate data for elongated bacteria.

2.3 Single vortex stabilized in a circular miocrowell

Next, to clarify how to control a stable single vortex with circular confinement, we confine a dense *E. coli* bacterial suspension in circular microwells with a height $\sim 20\,\mu\mathrm{m}$. Fig. 2.5 represents representatives of the vorticity map overlapped by the velocity field and its orientation map. A stable single vortex emerges in a circular microwell, as well as in an emulsion [67].

To assess the extent to which the single vortex is stabilized in circular microw-

ells, we confine a dense bacterial suspension in circular microwells with various sizes (Fig. 2.6). Fig. 2.6 (a) indicates a stable single vortex inside a microwell of $R = 28\,\mu\text{m}$, as well as in the microwell of $R = 19\,\mu\text{m}$. As the radius is further increased to $R = 37\,\mu\text{m}$, $46\,\mu\text{m}$, and $55\,\mu\text{m}$, multiple vortices occur inside the microwells, resulting in turbulent-like motions in larger microwells.

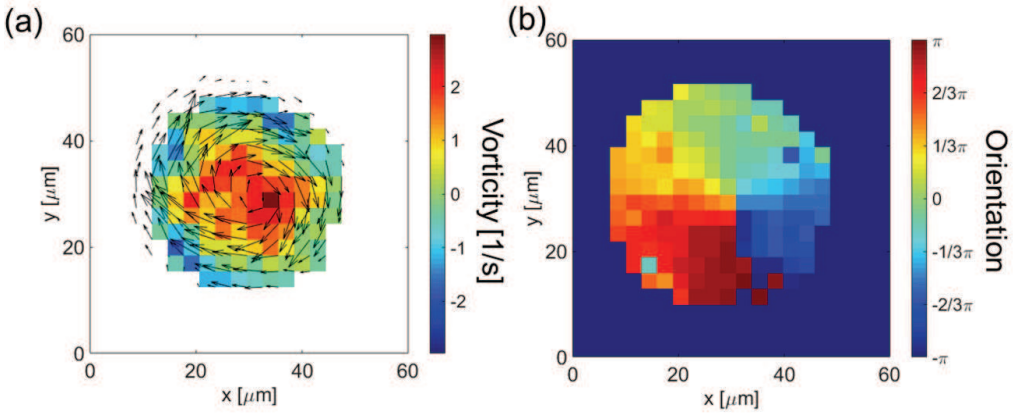

Figure 2.5: Single vortical motion in a circular microwell of $R = 19\,\mu\text{m}$. (a) Vorticity map overlapped by the velocity field. (b) Orientation map of the velocity field.

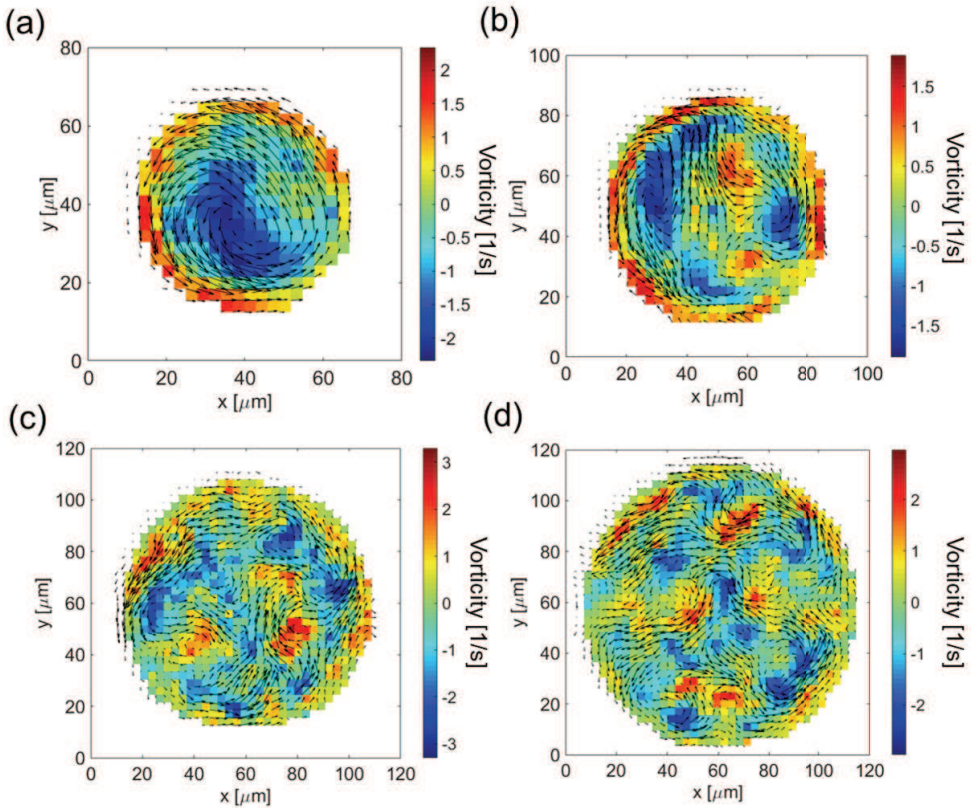

Figure 2.6: Vorticity maps in circular microwells with various radii R. Single vortex changes to disturbed patterns with an increase of radius R. (a) $R = 28\,\mu\text{m}$. (b) $R = 37\,\mu\text{m}$. (c) $R = 46\,\mu\text{m}$. (d) $R = 55\,\mu\text{m}$.

2.3.1 Vortex Order Parameter

To quantify collective vortical motions in circular microwells, we calculate the vortex order parameter (VOP) defined as [67]

$$\text{VOP} = \frac{1}{1-\frac{2}{\pi}}\left(\frac{\sum_i |\boldsymbol{v_i}\cdot\boldsymbol{t_i}|}{\sum_i |\boldsymbol{v_i}|} - \frac{2}{\pi}\right), \tag{2.2}$$

where $\boldsymbol{v_i}$ and $\boldsymbol{t_i}$ denote the velocity field and the azimuthal unit vector at a site of a grid position i in coarse-grained velocity fields, respectively (Fig. 2.7 (a)). VOP $= 1$ for steady azimuthal circulation, VOP $= 0$ for disordered motion, and VOP < 0 for radial flow configurations.

The VOP is plotted as a function of radius R in Fig. 2.7 (b). Once the

radius R of microwells exceeds the characteristic length in bacterial turbulence, l^*(Normal: $\sim 25\,\mu$m, Elongated: $\sim 45\,\mu$m), the VOP for suspensions of both wild-type bacteria (Normal) and elongated bacteria (Elongated) is attenuated rapidly. This is because the confinement with a size larger than the characteristic length allows multiple vortices to emerge and hence a single vortex becomes unstable, which also has been reported in Ref. [70]. The larger transition point to chaotic flows for elongated bacteria can be interpreted by the longer correlation length in active turbulence. This result suggests that a stable single vortex can be controlled by the confinement whose size is comparable to that of the intrinsic vortex in bacterial turbulence.

We note that apparent counter-rotating layers at lateral boundaries reported in Refs. [67, 68] do not form in a suspension of shorter *E. coli* bacteria, which has been also reported in Ref. [75].

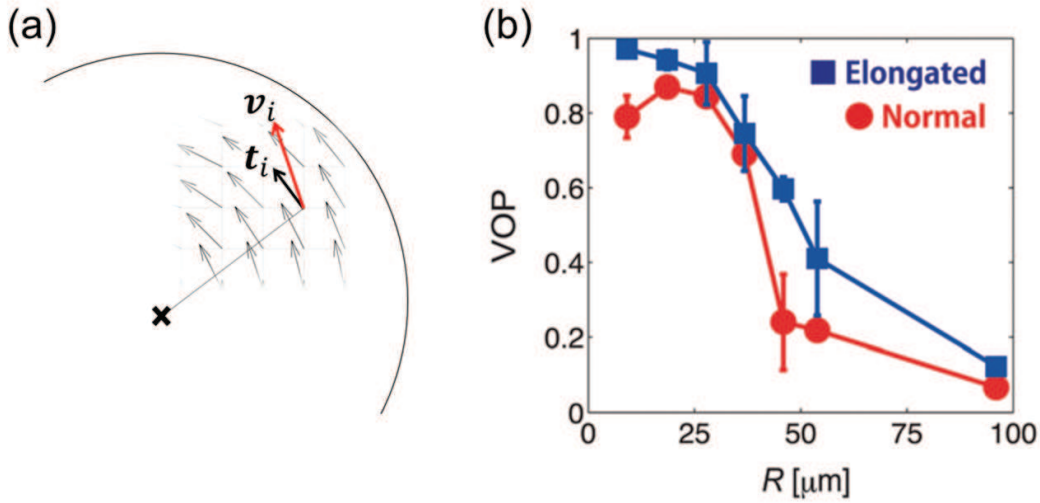

Figure 2.7: Vortex Order Parameter. (a) Schematic of variables, $\boldsymbol{v_i}$ and $\boldsymbol{t_i}$ at a certain grid position, in the definition of VOP. $\boldsymbol{v_i}$ is the velocity and $\boldsymbol{t_i}$ the azimuthal unit vector at a PIV grid point i. (b) The vortex order for both cases of wild-type bacteria (Normal) and elongated bacteria (Elongated) decays with increasing R.

2.4 Vortex pairing order in doublet circular microwells

The next question is whether or not geometric rule exists in interacting bacterial vortices inherent in bacterial turbulence. We both experimentally and theoretically demonstrate geometric features in vortex pairing order that is formed in microwells with various boundaries from doublet to quadruplet circles.

In the previous section, we found the characteristic length scales to control a stable bacterial vortex from bacterial turbulence: for example, radius $R = 19\,\mu m$ for normal *E. coli* and $R = 25\,\mu m$, $28\,\mu m$, or $37\,\mu m$ for elongated bacteria. Then, what kind of pattern is formed under a geometrical constraint that makes two bacterial vortices with a characteristic size collide?

2.4.1 Geometric design of doublet circular boundary

In order to simply capture the geometric nature in ordered bacterial vortices, we focus on two physical quantities of interacting vortices: a radius of vortex R and a distance between vortices Δ. We designed a doublet circular microwell such that two circles with radius R partially overlap and their centers are separated by a distance Δ. The geometry of this doublet circular boundary is also defined by an elevation angle Ψ that satisfies the geometric relation, $\cos\Psi = \Delta/(2R)$ (Fig. 2.8).

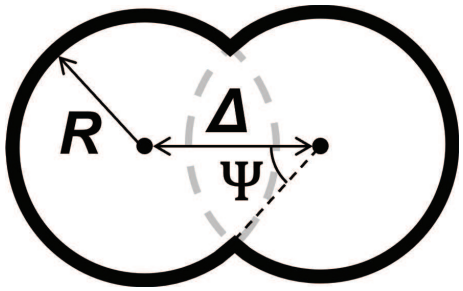

Figure 2.8: Geometry of a doublet circular microwell. The radius R, the distance between centers of circles Δ, and the elevation angle with respect to the horizontal line Ψ are defined.

2.4.2 Two distinct vortex pairing and its geometry dependence

Confining a dense bacterial suspension in doublet circular microwells, we found two distinct patterns of vortex pairing (Fig. 2.9): ferromagnetic vortices (FMV) pattern where two vortices rotate in an identical direction for a large overlap of two circular compartments (small Δ) and anti-ferromagnetic vortices (AFMV) one where two vortices rotate in opposite directions for small overlap of them (large Δ).

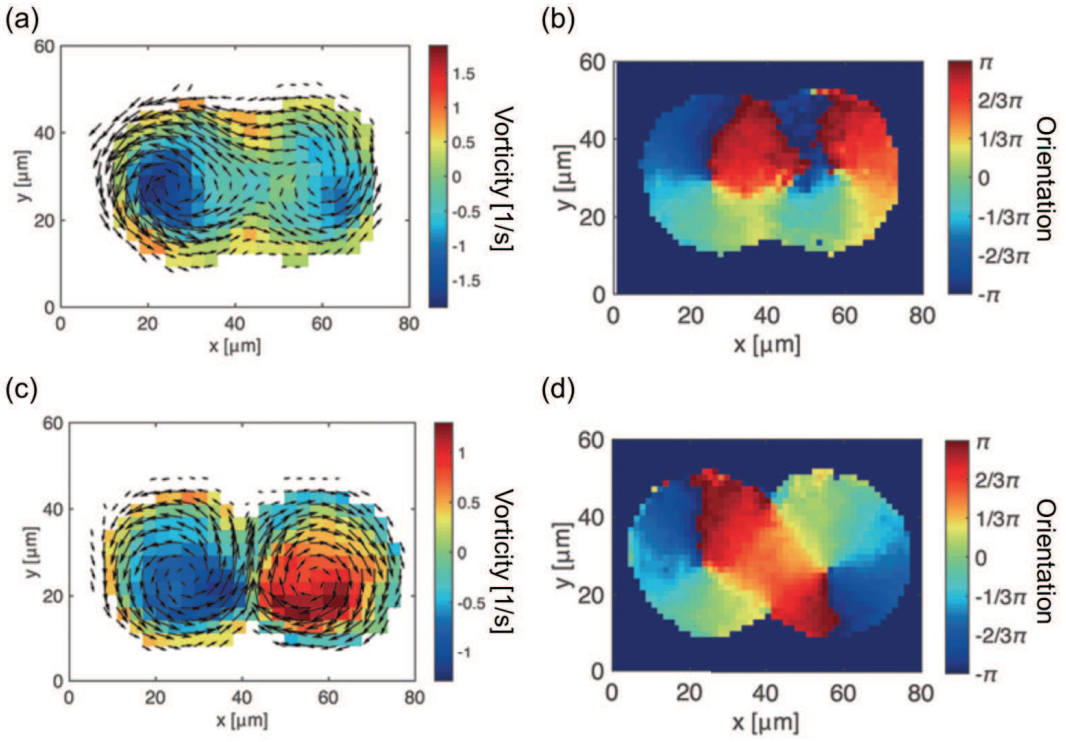

Figure 2.9: Two distinct patterns of vortex pairing in doublet circular microwells. (a) Vorticity map overlaid with velocity field measured in a microwell with $R = 19\,\mu\text{m}$ and $\Delta = 25\,\mu\text{m}$. (b) Velocity orientation map corresponding to (a). For clarity, the window size and the grid size in the PIV analysis are a half of those of (a). (c) Vorticity map overlaid with velocity field measured in a microwell with $R = 19\,\mu\text{m}$, $\Delta = 31\,\mu\text{m}$. (d) Velocity orientation map corresponding to (c).

We then investigate the geometry dependence of the emergent patterns by using various radii R and distances Δ. An array of vorticity maps overlaid with

velocity fields measured in microwells with $R = 19\,\mu m$ is shown in Fig. 2.10. the transition from FMV to AFMV takes place with an increase of Δ while keeping R constant. In addition, by varying R and taking a dimensionless parameter Δ/R, we examine the relationship between emergent patterns and Δ/R in more detail. Remarkably, from the resulting phase diagram (Fig. 2.11), the transition of the vortex pairing from FMV to AFMV was found at $\Delta/R = 1.3 \sim 1.4$ irrespective of the compartment size. This transition behavior can be quantitatively characterized by the vorticity averaged over the inside of a microwell. We will illustrate its details in the next chapter.

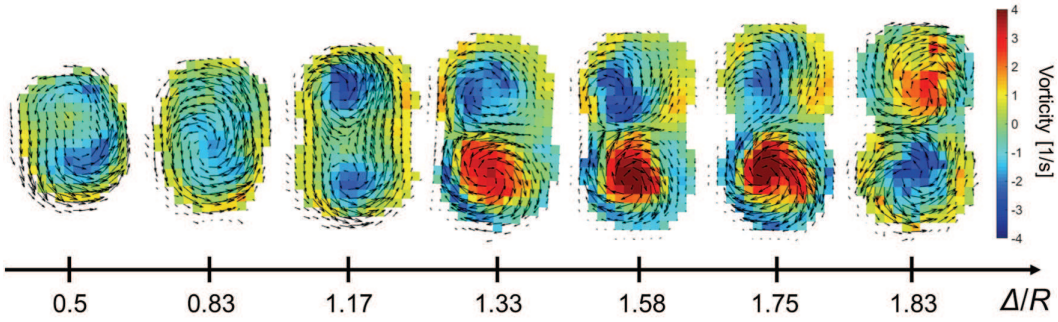

Figure 2.10: An array of vorticity maps at various values of Δ/R. As the distance between circles Δ increases while keeping radius $R = 19\,\mu m$, the transition from FMV to AFMV was observed.

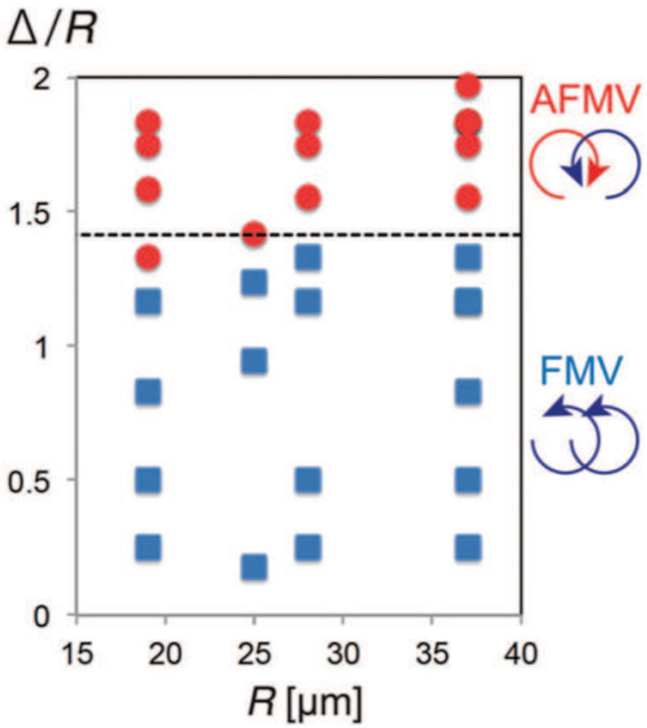

Figure 2.11: Phase diagram of pairing order at various radii R and the dimensionless quantity Δ/R. Blue squares present an FMV pairing, and red circles stand for an AFMV pairing.

2.5 Theoretical analysis for pairing order transition

To explain why the transition from an FMV pattern to an AFMV pattern takes place at $\Delta/R \approx 1.4$, we constructed a mean-field model based on the Vicsek model. In this theoretical model, we focus on the bacterial orientation at a representative point, '*tip*', where two circles intersect in a doublet circular microwell. As shown in Fig. 2.9, the bacterial orientation is considered to be aligned in the horizontal direction (along the wall) for an FMV pattern and in the vertical direction (tip-to-tip) for an AFMV pattern. Therefore, we assume that the orientation of bacteria at a tip determines global patterns when two vortices collide at an angle of a tip characterized by Ψ. In this section, we account for the pairing order transition

of interacting vortices depending on geometry by solving a Fokker-Planck equation of the probability equation of bacterial orientation derived from orientational dynamics of bacteria interacting in the vicinity of a tip.

2.5.1 Vicsek model

We here consider self-propelled particles interacting among neighboring particles through polar alignment. The state of an m-th particle at time t can be described by its position $\boldsymbol{x}_m(t)$ and its orientation $\theta_m(t)$. According to the Vicsek model in Ref. [14], $\boldsymbol{x}_m(t)$ and $\theta_m(t)$ are evolved by the following equations:

$$\dot{\boldsymbol{x}}_m = v_0 \boldsymbol{e}(\theta_m) \tag{2.3}$$

$$\dot{\theta}_m = -\gamma \frac{\partial U}{\partial \theta_m} + \eta_m(t) \tag{2.4}$$

where $\boldsymbol{e}(\theta_m)$ is a unit vector defined as $\boldsymbol{e}(\theta_m) = (\cos\theta_m, \sin\theta_m)$, v_0 is a constant particle speed, and γ represents the strength of polar interaction (i.e., relaxation of orientation). The last term of the RHS of (2.4), $\eta_m(t)$, denotes the white gaussian noise that satisfies

$$\begin{cases} \langle \eta_m(t) \rangle = 0 \\ \langle \eta_m(t) \eta_n(t') \rangle = 2D\delta_{mn}\delta(t-t') \end{cases} \tag{2.5}$$

where δ_{mn} and $\delta(t)$ represent the functions of Kronecker delta and Dirac delta, respectively, and D denotes the rotational diffusion coefficient. The polar interaction potential $U(\boldsymbol{x}_m, \theta_m)$ is defined by

$$U(\boldsymbol{x}_m, \theta_m) = -\sum_{|\boldsymbol{r}_{mn}|<\epsilon} \cos(\theta_m - \theta_n) \tag{2.6}$$

where $\boldsymbol{r}_{mn} = \boldsymbol{x}_m - \boldsymbol{x}_n$, and ϵ represents the effective radius of polar interaction.

2.5.2 Fokker-Planck equation

We next derive a Fokker-Planck equation that governs the probability distribution of the orientation of a particle from the Langevin Eq. (2.4). Let us first give the four important assumptions as follows.

Assumption 1 Eq. (2.5) holds.

Assumption 2 $\theta(t)$ and $\eta(t')$ are statistically independent at $t < t'$.

Assumption 3 $\eta(t)$ is in a Gaussian process.

Assumption 4 The probability distribution function $P(x,t)$ satisfies $P(x,t) \to 0$, $\frac{\partial P(x,t)}{\partial x} \to 0$ for $x \to \pm\infty$.

Taking the infinitesimal change in Eq. (2.4) (Let us omit the index m) and integrating Eq. (2.4) over time t in a range of $[t, t+\Delta t]$,

$$\int_t^{t+\Delta t} dt' \dot{\theta}(t') = \int_t^{t+\Delta t} dt' \left(-\gamma \frac{\partial U}{\partial \theta} \right) + \int_t^{t+\Delta t} dt' \eta(t'). \tag{2.7}$$

(LHS of Eq. (2.7)) $= \theta(t+\Delta t) - \theta(t) = \Delta\theta$, and (the second term of RHS in Eq. (2.7)) $\equiv \Delta W$. If Δt is small enough, Eq. (2.7) can be rewritten as

$$\Delta\theta = -\gamma \frac{\partial U}{\partial \theta} \Delta t + \Delta W. \tag{2.8}$$

Taking averages of first and second order of infinitestimal $\Delta x, \Delta y$, and ΔW, we obtain the following relations:

$$\Delta x = (v_0 \cos\theta)\Delta t, \quad \Delta y = (v_0 \sin\theta)\Delta t, \quad (\because \text{Eq.(2.3)}) \tag{2.9}$$

$$\langle \Delta W \rangle = 0, \tag{2.10}$$

$$\begin{aligned}\langle \Delta W^2 \rangle &= \int_t^{t+\Delta t} dt_1 \int_t^{t+\Delta t} dt_2 \langle \eta(t_1)\eta(t_2)\rangle \\ &= 2D \int_t^{t+\Delta t} dt_1 \int_t^{t+\Delta t} dt_2 \delta(t_1 - t_2), \\ &= 2D \int_t^{t+\Delta t} dt_1 = 2D\Delta t. \end{aligned} \tag{2.11}$$

An arbitary function $f(\boldsymbol{r}(t), \theta(t))$ can be approximated by the Taylor expansion with respect to $\Delta\boldsymbol{r}(t)$ and $\Delta\theta(t)$ as follows:

$$\begin{aligned} f(\boldsymbol{r}(t+\Delta t), \theta(t+\Delta t)) = f(\boldsymbol{r}(t), \theta(t)) &+ \frac{\partial f}{\partial x}\Delta x + \frac{\partial f}{\partial y}\Delta y + \frac{\partial f}{\partial \theta}\Delta\theta \\ &+ \frac{1}{2}\frac{\partial^2 f}{\partial x^2}(\Delta x)^2 + \frac{1}{2}\frac{\partial^2 f}{\partial y^2}(\Delta y)^2 + \frac{1}{2}\frac{\partial^2 f}{\partial \theta^2}(\Delta\theta)^2 \\ &+ \frac{\partial^2 f}{\partial x \partial y}\Delta x\Delta y + + \frac{\partial^2 f}{\partial y \partial \theta}\Delta y\Delta\theta + + \frac{\partial^2 f}{\partial \theta \partial x}\Delta\theta\Delta x + ... \end{aligned} \tag{2.12}$$

We substitute Eqs. (2.8) and (2.9) into Eq. (2.12) and take its averages. Note that we neglect the second or higher order of Δt due to the limit $\Delta t \to 0$, and from the assumption 3 the third or higher order terms of $\Delta\theta$ in Eq. (2.12) are negligible since taking their average leads to the second or higher order terms of Δt. Moreover, from the assumption 2, Eq. (2.10), Eq. (2.11), and Eq. (2.12) readily read

$$\begin{aligned} \langle f(\boldsymbol{r}(t+\Delta t), \theta(t+\Delta t))\rangle &= \langle f(\boldsymbol{r}(t), \theta(t))\rangle \\ &- \gamma \left\langle \frac{\partial f}{\partial \theta}\frac{\partial U}{\partial \theta} \right\rangle \Delta t + \frac{D}{2}\left\langle \frac{\partial^2 f}{\partial \theta^2} \right\rangle \Delta t \\ &+ v_0 \left(\left\langle \frac{\partial f}{\partial x}\cos\theta \right\rangle + \left\langle \frac{\partial f}{\partial y}\sin\theta \right\rangle \right) \Delta t \\ &+ O(\Delta t^2). \end{aligned} \tag{2.13}$$

Accordingly, by taking the limit $\Delta t \to 0$ in both sides of Eq. (2.13), the differential

equation of average of $f(\boldsymbol{r}(t), \theta(t))$ is given by

$$\begin{aligned}\frac{d}{dt}\langle f(\boldsymbol{r}(t),\theta(t))\rangle &= D\left\langle \frac{\partial^2 f}{\partial\theta^2}\right\rangle - \gamma\left\langle \frac{\partial f}{\partial\theta}\frac{\partial U}{\partial\theta}\right\rangle \\ &+ v_0\left(\left\langle \frac{\partial f}{\partial x}\cos\theta\right\rangle + \left\langle \frac{\partial f}{\partial y}\sin\theta\right\rangle\right). \end{aligned} \tag{2.14}$$

With the probability distribution $P(\boldsymbol{r}(t), \theta(t), t)$, we obtain the following relations with respect to the average of the arbitrary function to be satisfied for each corresponding term in Eq. (2.14):

$$[LHS] = \frac{d}{dt}\int_{-\infty}^{\infty} d\boldsymbol{r}\int_{-\pi}^{\pi} d\theta f(\boldsymbol{r},\theta)P(\boldsymbol{r},\theta,t), \tag{2.15}$$

$$\begin{aligned}[1st\ term\ in\ RHS] &= D\int_{-\infty}^{\infty} d\boldsymbol{r}\int_{-\pi}^{\pi} d\theta\frac{\partial^2 f}{\partial\theta^2}P(\boldsymbol{r},\theta,t) \\ &= D\int_{-\infty}^{\infty} d\boldsymbol{r}\left(\left[\frac{\partial f}{\partial\theta}P(\boldsymbol{r},\theta,t)\right]_{-\pi}^{\pi} - \int_{-\pi}^{\pi} d\theta\frac{\partial f}{\partial\theta}\frac{\partial P(\boldsymbol{r},\theta,t)}{\partial\theta}\right) \\ &= D\int_{-\infty}^{\infty} d\boldsymbol{r}\int_{-\pi}^{\pi} d\theta f(\boldsymbol{r},\theta)\frac{\partial^2 P}{\partial\theta^2}, \end{aligned} \tag{2.16}$$

$$\begin{aligned}[2nd\ term\ in\ RHS] &= -\gamma\int_{-\infty}^{\infty} d\boldsymbol{r}\int_{-\pi}^{\pi} d\theta\frac{\partial f}{\partial\theta}\frac{\partial U}{\partial\theta}P(\boldsymbol{r},\theta,t) \\ &= \gamma\int_{-\infty}^{\infty} d\boldsymbol{r}\int_{-\pi}^{\pi} d\theta f(\boldsymbol{r},\theta)\frac{\partial}{\partial\theta}\left(\frac{\partial U}{\partial\theta}P(\boldsymbol{r},\theta,t)\right), \end{aligned} \tag{2.17}$$

$$\begin{aligned}[3rd\ term\ in\ RHS] &= v_0\int_{-\infty}^{\infty} d\boldsymbol{r}\int_{-\pi}^{\pi} d\theta\left(\frac{\partial f}{\partial x}\cos\theta + \frac{\partial f}{\partial y}\sin\theta\right)P(\boldsymbol{r},\theta,t) \\ &= -v_0\int_{-\infty}^{\infty} d\boldsymbol{r}\int_{-\pi}^{\pi} d\theta f(\boldsymbol{r},\theta)\left(\cos\theta\frac{\partial P}{\partial x} + \sin\theta\frac{\partial P}{\partial y}\right). \end{aligned} \tag{2.18}$$

In order for above equations to hold for arbitrary f, the following Fokker-Planck

equation needs to be satisfie:

$$\frac{\partial P}{\partial t} = D\frac{\partial^2 P}{\partial \theta^2} + \gamma\frac{\partial}{\partial \theta}\left(\frac{\partial U}{\partial \theta}P\right) - v_0\left(\cos\theta\frac{\partial P}{\partial x} + \sin\theta\frac{\partial P}{\partial y}\right). \tag{2.19}$$

2.5.3 Mean-field model

We assume the spatial uniformity of the bacterial density in our experiment due to sufficiently high density ($\sim$ 20%v/v). Thus, Eq. (2.19) into which the polar interaction potential (Eq. (2.6)) is substituted can be rewritten as a continuum description based on a mean-field approximation by averaging over translational positions, in the same way as the mean-field theory proposed in Ref. [14].

$$\frac{\partial P}{\partial t} = D\frac{\partial^2 P}{\partial \theta^2} + \gamma\frac{\partial}{\partial \theta}\left(\int_{-\pi}^{\pi} d\theta' \sin(\theta - \theta')P(\theta', t)P(\theta, t)\right) \tag{2.20}$$

where $P(\theta, t)$ is the probability distribution of a particle heading θ at a given time t, and $P(\theta', t)$ is that of a particle heading θ' with which the particle heading θ interact.

Our focus of the theoretical analysis here is to account for the mechanism of the transition from FMV to AFMV as observed in the experiment. To do so, we consider the orientation distribution of a particle interacting with a particle coming from either left or right circle in the vicinity of a tip of a doublet circular boundary characterized by the geometric quantity Ψ. Hence, the corresponding Fokker-Planck equation can be described in the following:

$$\frac{\partial P}{\partial t} = D\frac{\partial^2 P}{\partial \theta^2} + \gamma\frac{\partial}{\partial \theta}\left(\int_{-\pi}^{\pi} d\theta' \sin(\theta - \theta')\bar{P}(\theta', t; \Psi)P(\theta, t; \Psi)\right) \tag{2.21}$$

where $\bar{P}(\theta', t; \Psi)$ represents the probability distribution of a particle heading θ' that comes from either left or right circle in the vicinity of a tip. To analytically solve Eq. (2.20), we need to get a concrete form of the distribution function $\bar{P}(\theta', t; \Psi)$ by considering the interaction between a particle and a boundary wall.

We assume the interaction between the m-th particle and a wall $\bar{n}$ to be apolar (nematic) because in general self-propelled objects are likely to move along the

wall in colliding it due to the steric interaction. The nematic interaction potential is given by

$$\bar{U}(\boldsymbol{x}_m, \theta_m) = -\sum_{|\boldsymbol{r}_{m\bar{n}}|<\epsilon} \cos(2(\theta_m - \theta_{\bar{n}})), \tag{2.22}$$

where Eq. (2.22) represents the nematic potential, $\boldsymbol{r}_{m\bar{n}} = \boldsymbol{x}_m - \boldsymbol{x}_{\bar{n}}$ denotes distance between the particle and the wall, and $\bar{\epsilon}$ is the effective radius of the interaction between them. Therefore, the Fokker-Planck equation for the particle heading θ constrained by the boundary is given by

$$\frac{\partial \bar{P}}{\partial t} = \bar{D}\frac{\partial^2 \bar{P}}{\partial \theta^2} + \bar{\gamma}\frac{\partial}{\partial \theta}\left(\int_{-\pi}^{\pi} d\theta' \sin(2(\theta - \theta'))\bar{P}(\theta', t; \Psi)\bar{P}(\theta, t; \Psi)\right). \tag{2.23}$$

Here, since the emergent vortical patterns including FMV and AFMV are stationary within the our observation time, at least 30 s, we consider the steady states of $\partial_t P = 0$ and $\partial_t \bar{P} = 0$. Eq. (2.23) in the steady state yields the following solution:

$$\bar{P}(\theta) = \frac{1}{2\pi I_0(\alpha\bar{\gamma}/\bar{D})}\exp\left[\frac{\alpha\bar{\gamma}}{\bar{D}}\cos 2(\theta - \theta_0)\right], \tag{2.24}$$

where $I_0(x)$ is the modified Bessel function of the first kind, $\alpha = \frac{1}{2}\int_{-\pi}^{\pi} d\theta' \cos(2\theta')\bar{P}(\theta')$, and θ_0 is the tangential angle at the boundary. In the vicinity of the boundary, the nematic interaction with it is strong enough, so that we can neglect the fluctuation of particle orientation and assume the small noise limit, $\bar{\gamma}/\bar{D} \to \infty$. This means $\bar{P}(\theta)$ is not constant, which leads to $\alpha \neq 0$, thus yielding the following form:

$$\lim_{\bar{\gamma}/\bar{D}\to\infty} \frac{\exp\left[\frac{\alpha\bar{\gamma}}{\bar{D}}\cos 2(\theta - \theta_0)\right]}{2\pi I_0(\alpha\bar{\gamma}/\bar{D})} = \delta(\theta - \theta_0 - l\pi) \tag{2.25}$$

where $\delta(\theta)$ denotes the Dirac delta function, and $l = 0, \pm 1, \pm 2, ...$ $\delta(\theta - \theta_0)$ or $\delta(\theta - \theta_0 - \pi)$ corresponds to CCW or CW direction of a moving particle near the boundary. In what follows, we can obtain the explicit forms of the distribution function $\bar{P}(\theta)$ by taking into account the tangential directions of the boundary at the tip.

We ought to consider possible contributions of motions of particles coming

both from a left circle (I, I* in Fig. 2.12 (a)) and from a right circle (II, II* in Fig. 2.12 (a)) in the vicinity of a tip of a doublet circular microwell, characterized by Ψ because a particle around the tip should interact with particles whose heading angle is constrained by the tip geometry. Since the tangential directions of a left circle and a right circle are defined as $\theta_0 + \Psi = \pm\pi/2$ and $\theta_0 - \Psi = \pm\pi/2$, respectively, the probability distributions of a particle heading θ', $\bar{P}(\theta'; \Psi)$, can be given as follows.

(I) Case for outgoing from a left circle

$$\bar{P}(\theta'; \Psi) = \delta(\theta' - \pi/2 + \Psi) \tag{2.26}$$

(I*) Case for coming into a left circle

$$\bar{P}(\theta'; \Psi) = \delta(\theta' + \pi/2 + \Psi) \tag{2.27}$$

(II) Case for outgoing from a right circle

$$\bar{P}(\theta'; \Psi) = \delta(\theta' - \pi/2 - \Psi) \tag{2.28}$$

(II*) Case for coming into a right circle

$$\bar{P}(\theta'; \Psi) = \delta(\theta' + \pi/2 - \Psi) \tag{2.29}$$

From Fig. 2.12 (a), we assume that when the interaction of either ((I) and (II)) or ((I*) and (II*)) is predominant, an AFMV pattern should be formed, whereas an FMV one should arise when that of either ((I) and (II*)) or ((I*) and (II)) is predominant. Using either of their combinations is enough to obtain the solution of the Fokker-Planck equation for FMV and AFMV because of the symmetry of the two tips in a doublet circular boundary. Accordingly, we can obtain the solutions of Eq. (2.21) for FMV and AFMV in the steady state as follows, respectively:

$$P^{FMV}(\theta; \Psi) = \frac{\exp\left(\frac{2\gamma}{D}\cos\theta\sin\Psi\right)}{2\pi I_0\left(\frac{\gamma}{D}\sin\Psi\right)}, \tag{2.30}$$

$$P^{AFMV}(\theta;\Psi) = \frac{\exp\left(\frac{2\gamma}{D}\sin\theta\cos\Psi\right)}{2\pi I_0\left(\frac{\gamma}{D}\cos\Psi\right)}. \tag{2.31}$$

The transition point between two distinct vortex patterns corresponds to the boundary condition (Ψ_c) at which their maximized probabilities are equal, $P^{FMV}(\theta = 0;\Psi) = P^{AFMV}(\theta = \pi/2;\Psi)$ (Fig.2.12 (b)). With the defined geometrical relationship, we can obtain a boundary condition $\sin\Psi_c = \cos\Psi_c$ of the transition point, yielding

$$\Psi_c = \frac{\pi}{4}, \tag{2.32}$$

$$\Delta_c/R = 2\cos(\Psi_c) = \sqrt{2} \approx 1.41, \tag{2.33}$$

which is in good agreement with the experimental result. This result implies that ordered interacting bacterial vortices inherent in active turbulence have the symmetry of polar interactions.

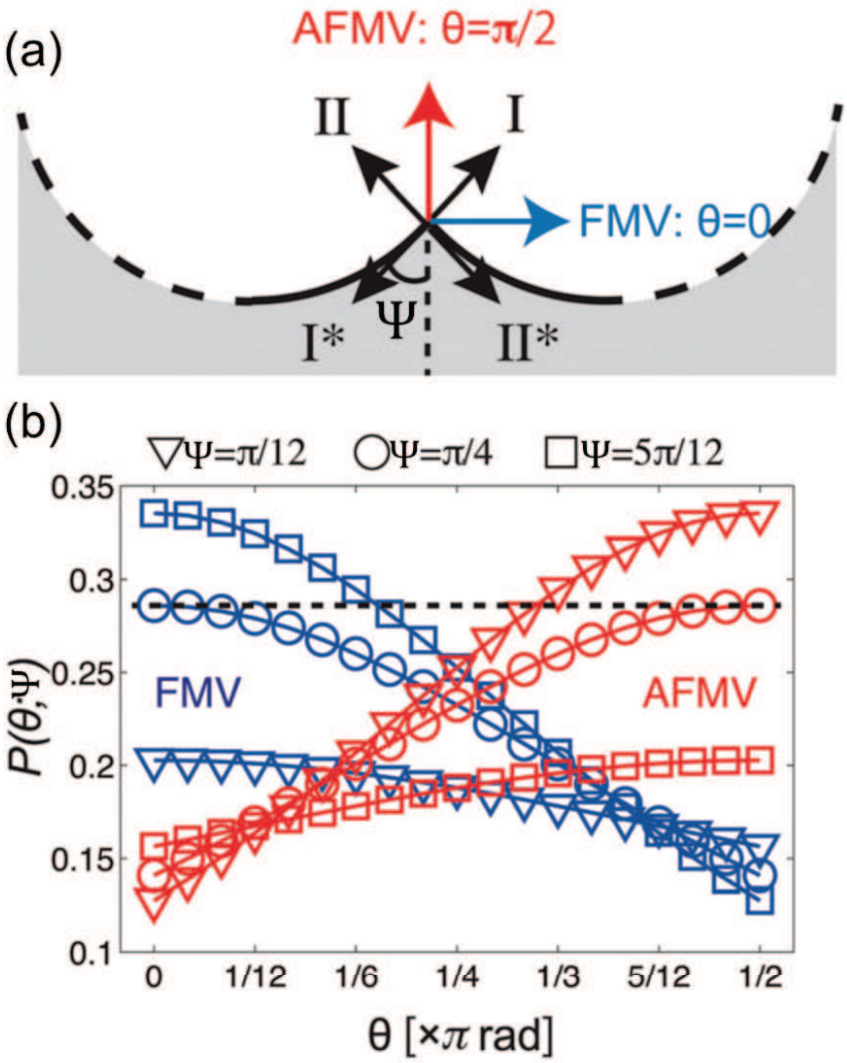

Figure 2.12: Theoretical model for FMV and AFMV patterns. (a) Schematic illustration of particles' motion in the vicinity of a tip. At the tip, the particle belonging to a left circle moves towards either I or I*, while the particle belonging to a right circle moves towards either II or II*. We assume that the orientation resulting from the interactions of particles at the tip determines the occurrence of either FMV or AFMV. (b) The probability distributions of P^{FMV} (blue) and P^{AFMV} (red) are plotted as a function of θ for constant $\Psi = \pi/12,\ \pi/4$, and $5\pi/12$, respectively. For simplicity, we here set $2\gamma/D = 1$. The dashed lines exhibit that both probabilities are the same at $\Psi = \pi/4$.

2.6 Vortex pairing order in quadruplet circular microwells

2.6.1 Geometric design of quadruplet circular boundary

In order to test the applicability of the geometric rule to a more complex geometrical boundary, we designed a quadruplet circular microwell that comprises four overlapping circles such that two distances (Δ_x and Δ_y) between circles are both horizontally and vertically controllable (Fig. 2.13).

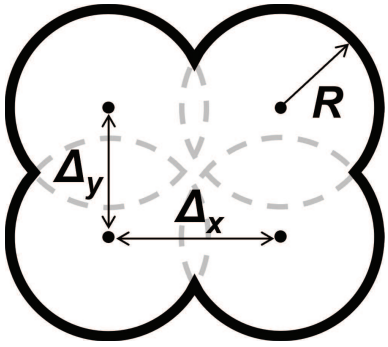

Figure 2.13: Geometry of a quadruplet circular microwell. Unlike the doublet geometry, distances between circles are defined as Δ_x in the horizontal direction and Δ_y in the vertical direction, respectively.

2.6.2 Various patterns of vortex pairing in a quadruplet microwell

The emergent patterns in quadruplet circular microwells defined by various combinations of Δ_x/R and Δ_y/R are presented in the phase diagram in Fig. 2.14. When $\Delta_x/R \leq \sqrt{2},\ \Delta_y/R \leq \sqrt{2}$, four bacterial vortices rotate in the identical direction (FMV), while all of pairs of adjacent vortices become AFMV when $\Delta_x/R \geq \sqrt{2},\ \Delta_y/R \geq \sqrt{2}$. On the other hand, by setting an asymmetric condition such as $\Delta_x/R \geq \sqrt{2},\ \Delta_y/R \leq \sqrt{2}$, only a pair of vortices in the direction where Δ/R exceeds the criterion $\sqrt{2}$ becomes AFMV, resulting in the mixed configuration of FMV and AFMV (Achiral mixed). More interestingly, in the region close to the transition point, i.e., at $\Delta_x/R = \Delta_y/R = 1.33$, despite the absence

of asymmetry in the geometrical boundary, we found the coexistence of FMV and AFMV (Fig. 2.15). Furthermore, a chiral pattern in which FMV and AFMV coexist (Chiral mixed) was also found around $\Delta_x/R = \Delta_y/R = \sqrt{2}$ (Fig. 2.15). According to our theoretical model, the probabilities of FMV and AFMV become equal near the transition point, indicating that the interaction among vortices no longer discriminates which is preferred, FMV or AFMV.

We thus conclude that the geometric rule derived from the theoretical analysis of the Vicsek model is applicable even to miscellaneous geometrical boundaries such as quadruplet overlapping circles, providing new insight into a design principle for active turbulence.

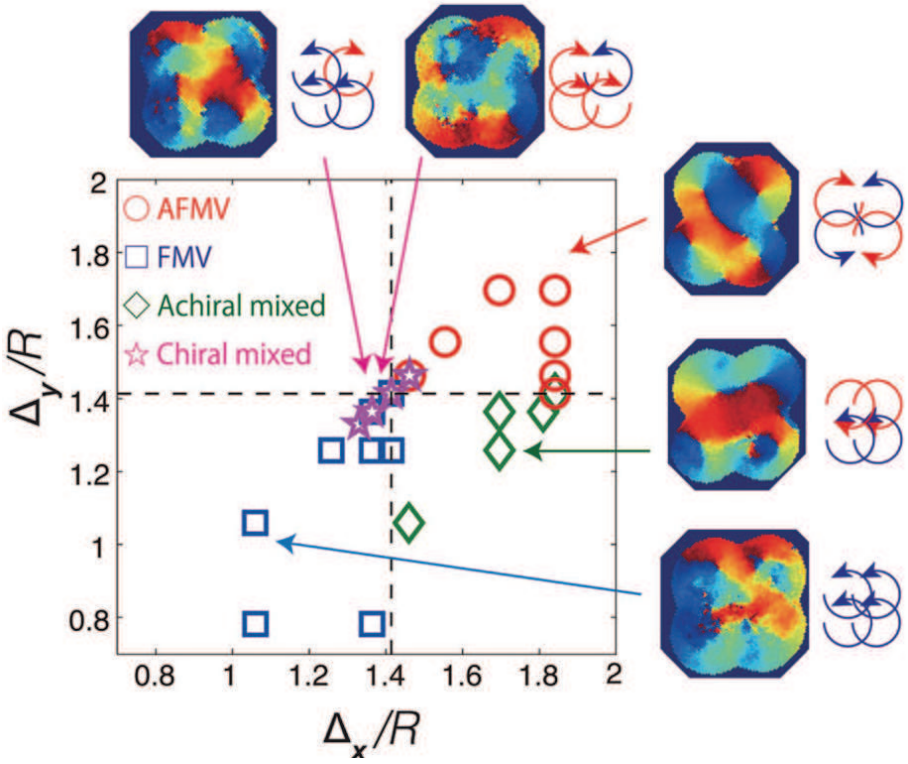

Figure 2.14: Phase diagram of pairing order in quadruplet circular microwells. The dashed lines denote $\Delta_{x,c}/R = \Delta_{y,c}/R = \sqrt{2}$. The FMV phase, the Achiral mixed phase, and the AFMV phase emerge on the basis of this criterion. Close to the transition point at which two dashed lines intersect, the Chiral mixed phase appears.

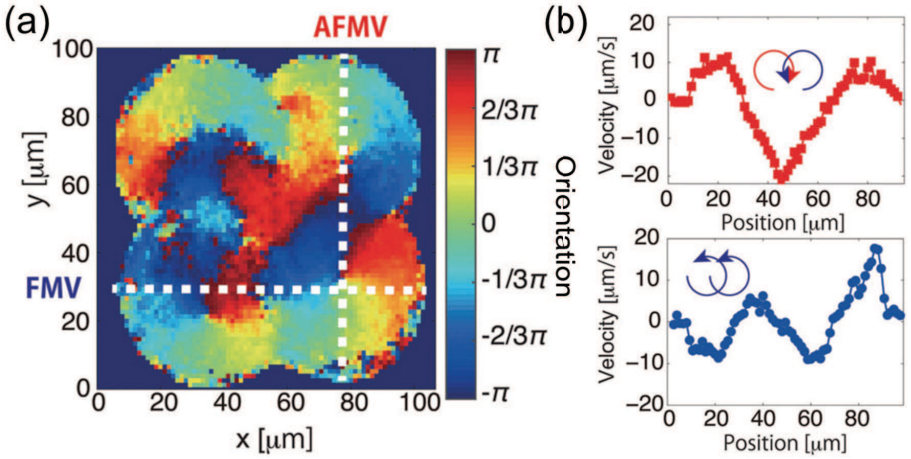

Figure 2.15: Velocity profile of a vortex pairing pattern. (a) Orientation map of velocity field measured in a quadruplet circular microwell of $R = 25\,\mu\text{m}$ and $\Delta_x/R = \Delta_y/R = 1.33$. (b) Profile of velocities extracted along the dotted diagonal lines in (a).

2.7 Summary of Chapter 2

We studied geometric features of interacting ordered vortices inherent in bacterial turbulence using the fabricated PDMS devices. A dense bacterial suspension confined in a doublet microwell defined by two overlapping circles with a radius R separated by a distance Δ exhibited two distinct patterns of vortex pairing: ferromagnetic vortices (FMV) for large overlap of circular compartments and antiferromagnetic vortices (AFMV) for small overlap. Importantly, switching of these patterns is found to be ruled by the dimensionless parameter $\Delta/R \sim 1.4$. Our theoretical model for orientational dynamics at a tip where bacterial vortices collide explained that the appearance of FMV and AFMV becomes equiprobable at the geometric boundary condition $\Delta/R = \sqrt{2}$, leading to the discovery of the geometric rule in pairing order transition. We further tested the applicability of the geometric rule to more complex boundary conditions like a quadruplet circular microwell. We found that a variety of pairing orders is switched on the basis of $\Delta/R = \sqrt{2}$. This investigation corroborated the presence of geometric rule in active turbulence.

Chapter 3

Chiral edge current and pairing order transition

3.1 Introduction

In general, active turbulence holds the symmetry in that the global vorticity should be always zero, implying the presence of robust anti-ferromagnetic vortices over length scales. Although engineering the dynamics of active turbulence under geometrical constraints has been extensively studied [68, 69, 76], much less is still known how we can control ordered vortices with a net circulation over the scales much larger than an intrinsic vortex. Elucidating this problem will provide not only a novel strategy to control active turbulence but also technology for engineering a self-sustained soft material that efficiently harvests energy from turbulent-like disordered motions.

To address the above problem, we explore the effects of the important yet overlooked nature, chirality, i.e., the mirror-symmetry breaking of individual units, which is ubiquitous in nature ranging from amino acid and cytoskeletons to organs and humans with dominant hand. Bacteria also have chirality in their swimming such that the flagella rotate in a counterclockwise (CCW) direction and the body rotates in a clockwise (CW) direction (when viewed from behind) (Fig. 3.1 (a)). This intrinsic chirality causes a bent (CW curved when viewed from above) trajec-

tory of swimming of bacteria above but near a solid surface due to hydrodynamic interactions (Fig. 3.1 (b)) [78, 79]. Recently, the so-called chiral active matter has also attracted many physicists because of various intriguing features. Liebchen and Levis have reported that the Vicsek model including chirality exhibits the formation of a large flocking in an unconfined system [80]. Besides, the presence of a boundary wall often selects unidirectionally biased motion of active chiral particles (Fig. 3.1 (c)) [81]. Due to similar mechanisms, populations of chiral active spinners and chiral self-propelled particles under spatial constraints have been found to form chiral edge currents [82–85] that are reminiscent of those in the quantum Hall effect (Fig. 3.1 (d) and (e)) [86]. As for bacterial turbulence, however, the mirror-symmetry is recovered at a collective level, and hence the role that bacterial chirality plays in bacterial turbulence remains unexplored. In Chapter 2, it has been shown that when two bacterial vortices interact with one another via the near-field orientational interaction, two types of pairing order, either the co-rotational vortices (ferromagnetic vortices, FMV) or anti-rotational ones (antiferromagnetic vortices, AFMV), arise in a geometry-dependent manner. As such, the ordered vortices are indeed sensitive to the geometry of the boundary. In other words, the appearance of robust FMV or AFMV implies the limitation in controlling the ordered vortices. However, if a chiral edge current exists robustly along the boundary, it is expected to rectify the transition point of the FMV-AFMV pairing order. In this chapter, we both theoretically and experimentally demonstrate how the FMV-AFMV pairing order transition can be controlled by chirality and offer a novel strategy to control active turbulence with chiral edge currents.

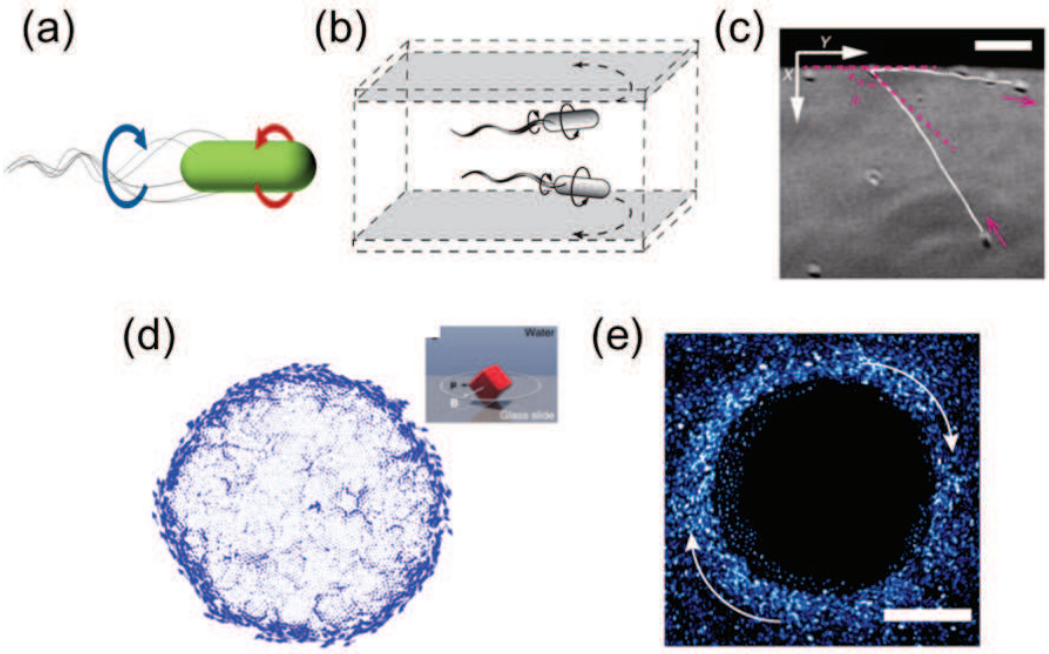

Figure 3.1: Bacterial chirality and chiral edge currents. (a) Schematic of bacterial chirality. (b) Chiral swimming of bacteria due to hydrodynamic interactions between swimming bacteria and a boundary surface. The image is adapted from Ref. [78]. (c) Turning of swimming direction at a colony edge due to chirality. Scale bar, 20 µm. The image is adapted from Ref. [81] (d) Chiral edge flows of a chiral fluid of spinning colloidal magnets. Blue arrows show velocity field. The image is adapted from Ref. [82]. (e) Image of cultured neural progenitor cells organizing a chiral edge flow. Scale bar, 200 µm. The image is adapted from Ref. [85].

3.2 Experimental setup

To give a slight bias with respect to chirality in the vertical top-bottom axis while keeping the lateral boundary achiral, we developed a new device that allows us to impose not only lateral geometrical boundaries but also top/bottom asymmetric interfaces with different properties on confined bacterial suspensions. Following the method shown in Appendix B, we confined a dense *E. coli* suspension in microwells with asymmetric interfaces (top: an oil/water interface, bottom: a water/PDMS one) (Fig. 3.2), which may be more natural rather than a perfect symmetric one in nature, e.g., biofilm formation [87] and bioremediation in an oil spill [88].

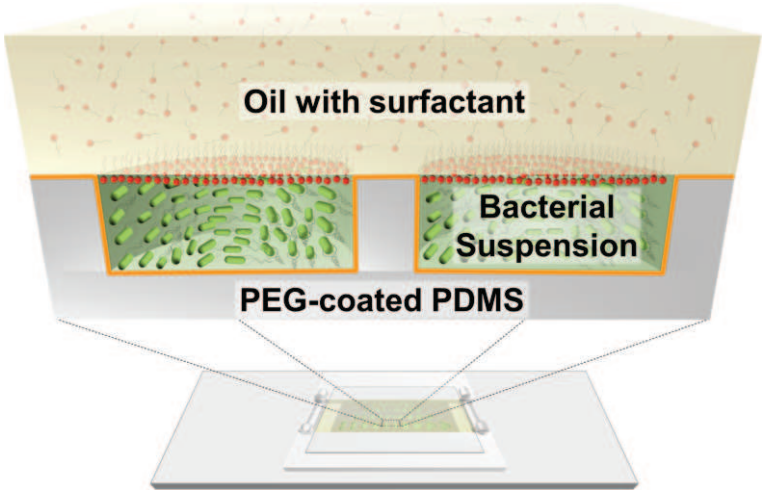

Figure 3.2: Schematic illustration of experimental setup. A dense bacterial suspension is confined in hydrophilic-treated PDMS microwells and sealed by a water (0.8 mPa s)/oil (32 mPa s) interface stabilized with a surfactant.

3.3 Chiral bacterial vortex

Once a dense bacterial suspension is enclosed into circular microwells with the asymmetric interfaces, the suspension starts to generate a stable single vortex in microwells whose size is comparable with an intrinsic vortex size in bacterial turbulence ($\sim 35\,\mu$m). Fig. 3.3 displays arrays of bacterial vortices confined in circular microwells which are overlapped with the orientation field of the velocity field $\boldsymbol{v}(\boldsymbol{r}_i)$ obtained by the particle image velocimetry (PIV). The directionality of the emergent vortices was surprisingly selective towards the CCW direction when viewed from above (later referred to as "top view") in spite of the absence of built-in chirality in the geometry of the lateral boundary, e.g., rachets [89, 90]. We then analyze the rotational selectivity of vortical motions of bacteria confined in microwells with the asymmetric interfaces and water-in-oil droplets squeezed between two glass slides (symmetric conditions) as a control experiment. These statistics of vorticity averaged over inside of a compartment and the observation time 10 s are shown for both cases (Figs. 3.4 (b) and (d)). The bacterial vortex that appears in the asymmetric system exhibits CCW in the probability of 95 % or

more ($N = 145$), named "chiral bacterial vortex", whereas the rotation of vortex in the symmetric system is equiprobable between CW and CCW, which is consistent with previous works. In addition, a reversal of the rotation in the chiral vortices was not observed within at least the observation time of 30 s, indicating that a chiral bacterial vortex is more stable than a bacterial vortex in droplets that shows oscillation depending on a condition (Figs. 3.4 (e) and (f)) [75]. Importantly, we find coherent flows only close to the lateral boundary (edge layer within 10 µm apart from the boundary) in larger microwells despite turbulent-like flows in the bulk, named chiral edge current (Fig. 3.5 (b)).

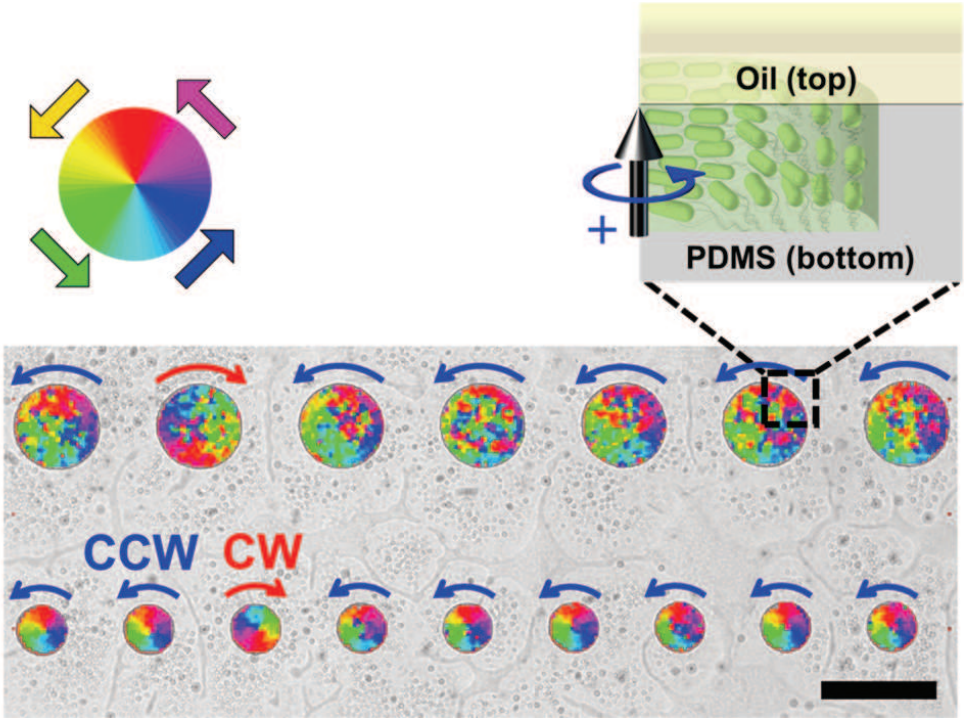

Figure 3.3: Chiral bacterial vortex. Arrays of velocity orientation maps measured in microwells with radii $R = 35$ µm (top row) and $R = 20$ µm (bottom row) and a height $h = 20$ µm. The bacterial density is 20%v/v. Scale bar, 100 µm. A schematic illustration of a cross-section of a bacterial vortex in a single microwell is depicted, and "+" defines the positive sign of CCW rotation. CCW and CW occurrences are displayed in blue and red arrows, respectively.

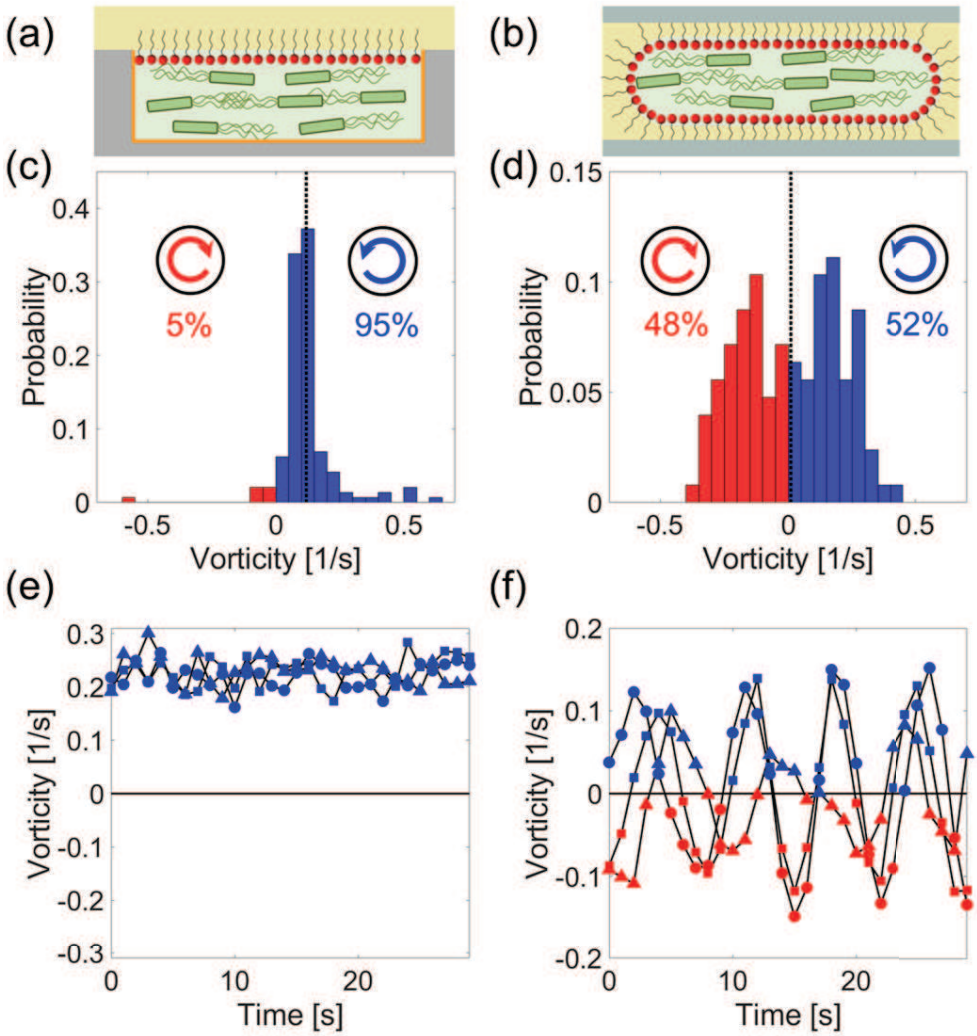

Figure 3.4: Symmetric interfaces vs Asymmetric interfaces. (a) Schematic of cross-section of a dense bacterial suspension confined in a microwell ($R = 20\,\mu\text{m}$) under asymmetric conditions with top (oil/water) interface and bottom (water/PDMS) interface. (b) Schematic of control experiment under the symmetric condition with the top (water/PDMS) and bottom (water/PDMS) interfaces. An emulsion droplet encapsulating a dense bacterial suspension is squeezed between two glass slides. (c) Distributions of vorticity averaged over 10 s and their respective average (vertical dashed line) measured in a microwell ($R = 20\,\mu\text{m}$) with asymmetric interfaces ($N = 145$, average vorticity 0.12 / sec). Proportions of CCW and CW occurrences are displayed in blue and red at the top of each plot. (d) The distributions of vorticity and their respective average (vertical dashed line) measured in an emulsion with $15\,\mu\text{m} \leq R \leq 35\,\mu\text{m}$ ($N = 126$, average vorticity 0.01 / sec). Under the symmetric condition, CW and CCW rotations are observed with the same frequency. (e) Persistent dynamics of vorticity of representative data. The vorticity of velocity field, $\boldsymbol{\Omega} = \boldsymbol{\nabla} \times \boldsymbol{v}$, is always positive without sign change, meaning that CCW rotation is stable over the range of our measurement (30 s). (f) Oscillatory dynamics of vorticity in some of the water-in-oil droplets. The time evolution exhibits a change of vorticity sign at a period of ~ 8 s, indicating that switching between CW and CCW rotations occurs.

3.4 Chiral edge current

We in turn investigated the dependence of the edge current on the compartment size. We define the unit tangential vector $\boldsymbol{t}(\theta_i)$ in the CCW direction along the circular boundary, and the azimuthal component of velocity is given by $v_\theta(\boldsymbol{r}_i) = \boldsymbol{v}(\boldsymbol{r}_i) \cdot \boldsymbol{t}_i$. The extent to which the edge current is aligned along the boundary wall is analyzed by $\langle v_\theta(\boldsymbol{r}_i)\rangle / \langle|\boldsymbol{v}|\rangle$ where $\langle\cdot\rangle$ denotes the average over all possible grids i. To characterize edge currents close to the boundary, the analysis region is divided into two regions of interest: an edge layer within 10 µm away from a boundary and a bulk around a center region excluding the edge layer (Fig. 3.5 (b)). The order parameter of an edge current is highly maintained even in very large microwells ($R \geq 100\,\mu\text{m}$) whose size is much larger than the intrinsic bacterial vortex in the bulk ($\approx 35\,\mu\text{m}$), whereas that in the bulk rapidly decays with the increase of radius R due to the development of active turbulence (Fig. 3.5 (c)). When a dense bacterial suspension is enclosed in circular microwells with symmetric conditions (water-PDMS interfaces for both top and bottom), on the other hand, the coherent flow along the boundary disappeared due to the nonstationary dynamics as the turbulent state develops in the large microwells (Fig. 3.6), implying that the edge current appears selectively under asymmetric conditions.

To further investigate the robustness of chiral edge currents to the boundary geometry, which is known to be a key feature in confined chiral many-body systems, we extended the circular microwell to the concentric microchannels fabricated by PDMS whose widths are set to $w = 50\,\mu\text{m}$ and $100\,\mu\text{m}$ to suppress turbulent-like flows (Fig. 3.7 (a)). The annular microchannels to confine a dense bacterial suspension with the asymmetric condition allow us to investigate the effect of curvatures from 0.2×10^{-3} µm^{-1} to 1.0×10^{-2} µm^{-1}. When viewed from the center of annuli and above, edge currents rotating in the CCW (CW) direction occurred at an outer (inner) edge (Fig. 3.7 (b)). As in the analysis of edge currents in circular microwells, the order parameter is plotted as a function of the curvature radius of annuli in Fig. 3.7 (c). We found the robust chiral edge currents almost irrespective of the curvature of boundaries and the width of channels.

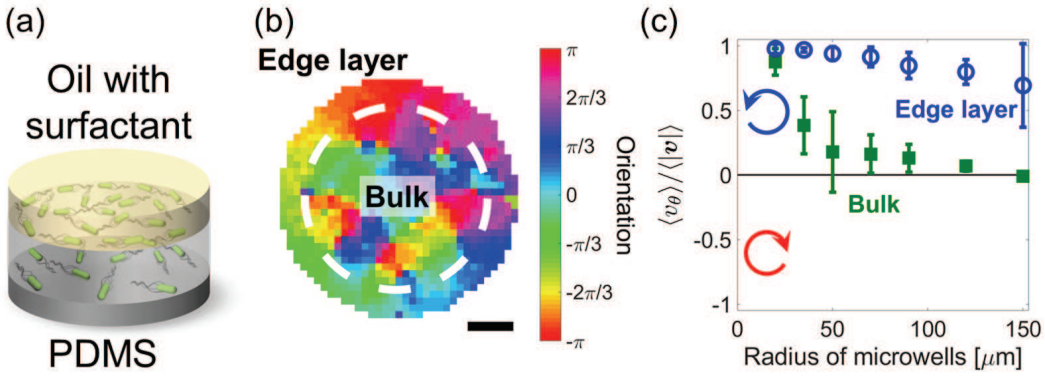

Figure 3.5: Chiral edge current in circular microwells. (a) Schematic illustration of a dense bacterial suspension confined in a microwell under asymmetric conditions (Oil/PDMS interface). (b) Color map of velocity orientation of collective motion in a circular microwell of $R = 50\,\mu\text{m}$. The edge layer, defined as the area within 10 µm from the boundary, is separated from the rest of a microwell (the bulk) by a broken white line. The height of the microwell is 20 µm. The bacterial density is 20%v/v. Scale bar, 20 µm. (c) Normalized azimuthal velocity in microwells with various sizes. The blue circles indicate the order parameter of edge currents, and the green squares indicate the motion in bulk. v_θ averaged over 10 s and normalized by the average magnitude of velocity is plotted with error bars representing standard deviation.

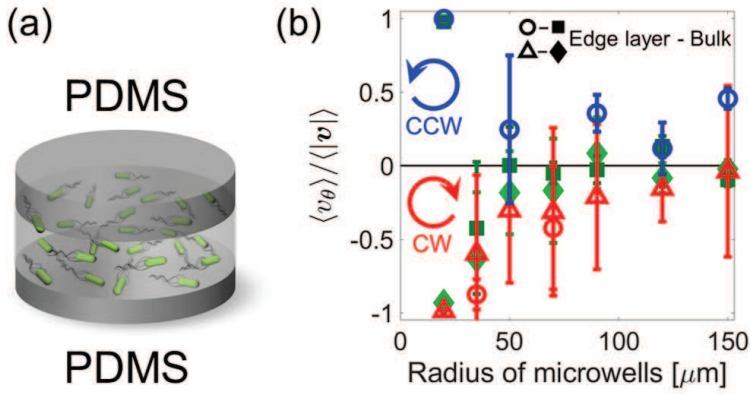

Figure 3.6: Edge current order in confined bacterial suspensions with the symmetric condition. (a) Schematic illustration of a dense bacterial suspension confined in a microwell under symmetric conditions (PDMS/PDMS interface). (b) The normalized azimuthal velocity in symmetric PDMS microwell, calculated within a bulk and a 10 µm edge layer from the lateral boundary. Normalized azimuthal velocity is plotted against radii of circular microwells. The blue circles (or red circles) indicate edge currents flowing in the CCW direction (or CW direction, respectively), and the green squares stand for vortical collective motions in bulk. Normalized azimuthal velocities averaged over 10 s are plotted with error bars representing standard deviations of their time series.

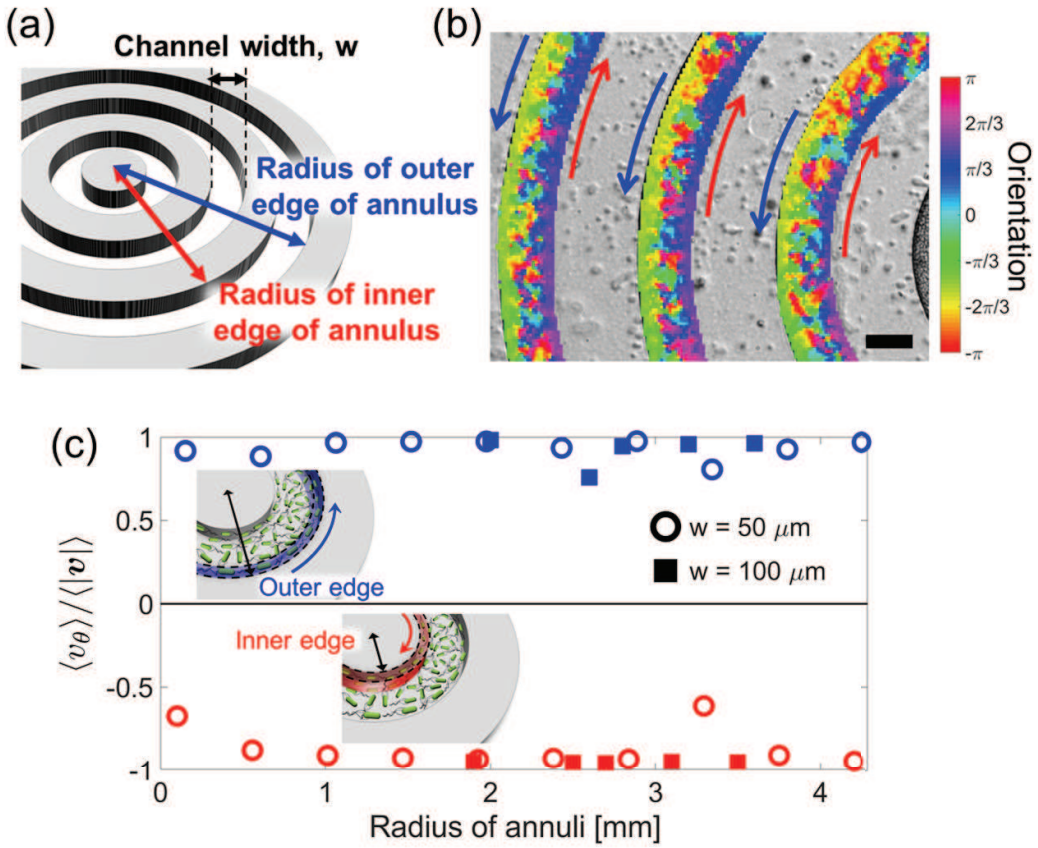

Figure 3.7: Chiral edge current in annular microchannels. (a) Schematic illustration of annular microchannels under asymmetric conditions. (b) Velocity orientation map of collective motion in annular microchannels. The height of annulus microchannels is $h = 20\,\mu\text{m}$. The bacterial density is 20%v/v. Scale bar, 50 µm. (c) Edge currents in annular channels with different curvatures. Normalized azimuthal velocities averaged over 10 s are plotted against curvature radii of annuli. The blue circles and squares (red circles and squares) indicate the extent of coherent circulating motions in the CCW direction (in the CW direction) within an edge layer in the channels with the width $w = 50\,\mu\text{m}$ and $w = 100\,\mu\text{m}$, respectively.

3.5 Origin of chiral edge current

To elucidate the underlying mechanism of the emergent chiral edge current, we scrutinized individual motions of bacteria inside a microwell, in particular near the top and bottom interfaces that induce chiral motions of bacteria due to the hydrodynamic interaction. In this section, we report three vital factors for the origin of chiral edge currents: interface-induced chiral motions and their bias near the

edge, an interplay between chiral collective motions at top and bottom interfaces, and a density heterogeneity in the height direction.

3.5.1 Individual bacterial motions in a dilute suspension inside a microwell

Let us first give the evidence for chiral motions of bacteria near the interfaces. By measuring individual motions of YFP bacteria swimming near an oil/water and a water/PDMS interfaces in a dilute suspension (0.01%v/v) with the confocal microscopy and analyzing the angular velocity for curved trajectories tracked by PTV analysis (see Appendix C for details), we confirmed that a swimming bacterium circles in a CW direction above the water/PDMS interface in an open boundary owing to the torque generated by the difference in viscous forces between the surface and bulk side, acting on both the cell body and the helical bundle of flagella. (Fig. 3.8 (a), (d), and (g)). Even in the microwells sealed by a surfactant-covered oil/water interface, a bacterium near the bottom water/PDMS interface swims in a CW direction (top view) (Fig. 3.8 (c), (f), and (i)), whereas a bacterium beneath the top oil/water interface swims in a CCW direction because of the high shear by the almost no-slip boundary condition, as in the case of the solid surface (Fig. 3.8 (b), (e), and (h)) [77, 92]. The measured typical magnitudes of angular velocities for all the cases were comparable (Table 3.1).

Intuitively, if bacteria have CCW chirality in their swimming at the top, the interaction with an edge is more likely to give rise to the stable CW rotational motion along the edge, reminiscent of the edge current of the quantum Hall effect. In our experiment, however, bacteria interacting with a lateral wall tend turn in a CCW direction owing to the torque of intrinsic chirality, which leads to the effective polar interaction between bacteria and the lateral wall (Fig. 3.9) [81]. Besides, the resulting CCW motion along the boundary wall appears to be persistent presumably due to the hydrodynamic trapping to the wall. In the top view, however, the biased directions at both top and bottom are opposite, and hence no net chirality of swimming bacteria should be observed. The question of why the net global CCW rotation takes place is raised next.

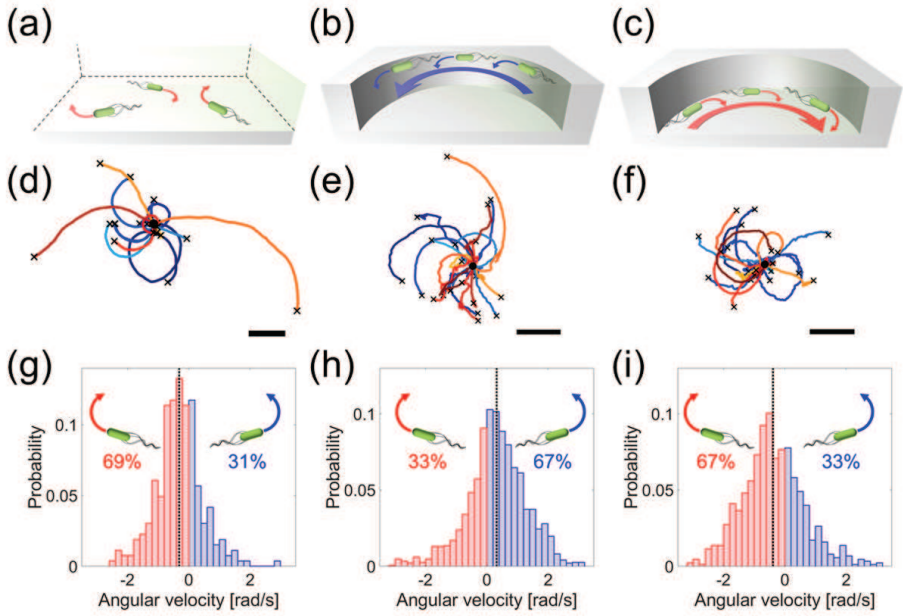

Figure 3.8: Intrinsic bacterial chiral swimming near interfaces (top view). (a-c) Schematic illustrations of (a) CW rotation of bacterial swimming on a solid PDMS interface with open lateral boundaries, (b) CCW rotation of bacterial swimming beneath the oil/water interface with lateral solid PDMS wall, and (c) CW rotation of bacterial swimming on the solid PDMS interface with lateral solid PDMS wall. (d-f) Representative trajectories of individual bacterial swimming in each of the conditions corresponding to (a-c), in dilute bacterial suspensions. The start points of each trajectory are fixed at the center of the plot, and their endpoints are displayed by a black cross. Colors code for different trajectories. Scale bar in (d) is 50 µm, and scale bars in (e) and (f) are both 20 µm. (g-i) Histogram of the mean angular velocities of the detected trajectories in each of the conditions corresponding to (a-c). Proportions of rotation directions are given in blue for CCW and red for CW.

Table 3.1: Average angular velocities and sample sizes measured under different confinement conditions, presented in Fig. 3.8.

	Solid interface	Top oil/water interface	Bottom water/PDMS interface
spatial constraint	Boundary-free	Circular microwell	Circular microwell
sample size, N	$N = 264$	$N = 1469$	$N = 876$
average angular velocity	$-0.312\,\mathrm{rad/s}$	$0.325\,\mathrm{rad/s}$	$-0.385\,\mathrm{rad/s}$

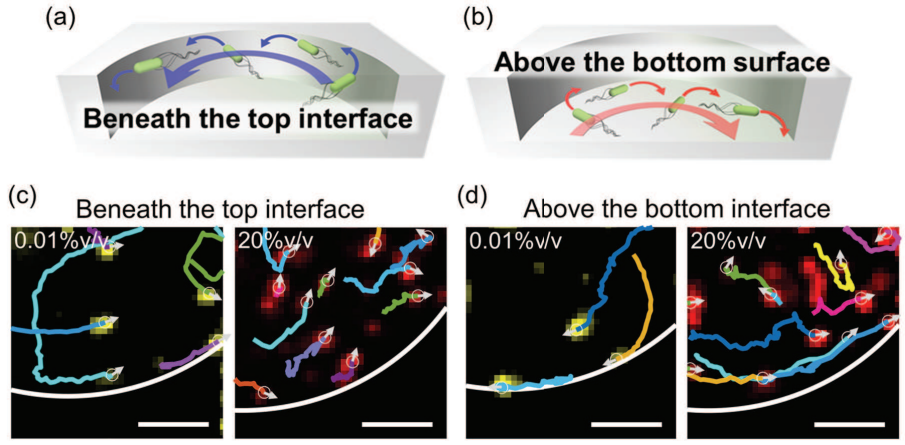

Figure 3.9: Chiral swimming of bacteria near the interfaces. (a) and (b) Schematic illustrations of chiral bacterial swimming (a) beneath the top oil/water interface and (b) above the bottom water/PDMS interface. Near the top interface, individual bacterial swimming is CCW-biased (blue arrow), while near the bottom interface it is CW-biased (red arrow). (c) Trajectories of chiral swimming near the wall of a single bacterium beneath the top interface in a dilute condition (0.01%v/v, left) and in a dense condition (20%v/v, right) (top view). The white arrow indicates the heading angle at the end of the track. (d) Trajectories of chiral swimming close to the wall of individual bacteria above the bottom interface in dilute (0.01%v/v, left) and dense (20%v/v, right) suspensions. The radius of microwells is $R = 35\,\mu\text{m}$. Scale bars, $10\,\mu\text{m}$.

3.5.2 Individual bacterial motions and fluid flows in a dense suspension inside a microwell

Before examining the origin of chirality selection, we need to verify the evidence of chiral edge currents that emerge independently of radius of microwells. To do so, we scrutinized individual bacterial motions, collective velocities, and fluid flows in a dense bacterial suspension (20%v/v) undergoing collective motions in circular microwells with $35\,\mu\text{m}$ and $50\,\mu\text{m}$ in radius under the asymmetric condition. For the sake of measuring individual motions of single bacteria in a dense bacterial suspension, we labeled a small fraction (0.7%v/v) of swimming bacteria with red fluorescent proteins (dTomato proteins). For the measurement of fluid flows, $0.5\,\mu\text{m}$ polystyrene tracer particles with red fluorescence (Molecular probes) are dispersed at a low density of 0.026%v/v, where individual particles could be tracked inside the bacterial suspension. In each edge layer and bulk, the trajec-

tories of labeled bacteria and tracer particles at different planes were acquired with confocal microscopy and PTV analysis. Figs. 3.10 (a) and (b) display the histogram of the azimuthal velocity averaged over the tracked time for each trajectory. Bacterial motions are biased towards a CCW direction in the edge layers in microwells of both $R = 35\,\mu\text{m}$ and $R = 50\,\mu\text{m}$, while those in the bulk in microwells of $R = 50\,\mu\text{m}$ have no bias, indicating the presence of the chiral edge current only near the boundary wall. Moreover, we checked the bias of flows of surrounding fluid at the top interface and the middle plane (Figs. 3.10 (c) and (d)). Although the magnitude of the velocity of tracer particles is slightly smaller than that of swimming bacteria, its bias towards a CCW direction appears to be clearer than that of single bacteria. The azimuthal velocity distribution of collective velocities obtained from PIV analysis is also analyzed in Fig. 3.10 (e), which is consistent with the results of single bacteria and tracer particles. These results would suggest that the thorough investigation of individual bacteria in a microwell of $R = 35\,\mu\text{m}$ is sufficient to clarify the underlying mechanism of the emergent chiral edge currents. Then, how is the chiral edge current formed in a dense bacterial suspension, though top and bottom interfaces induce opposite chiral motions?

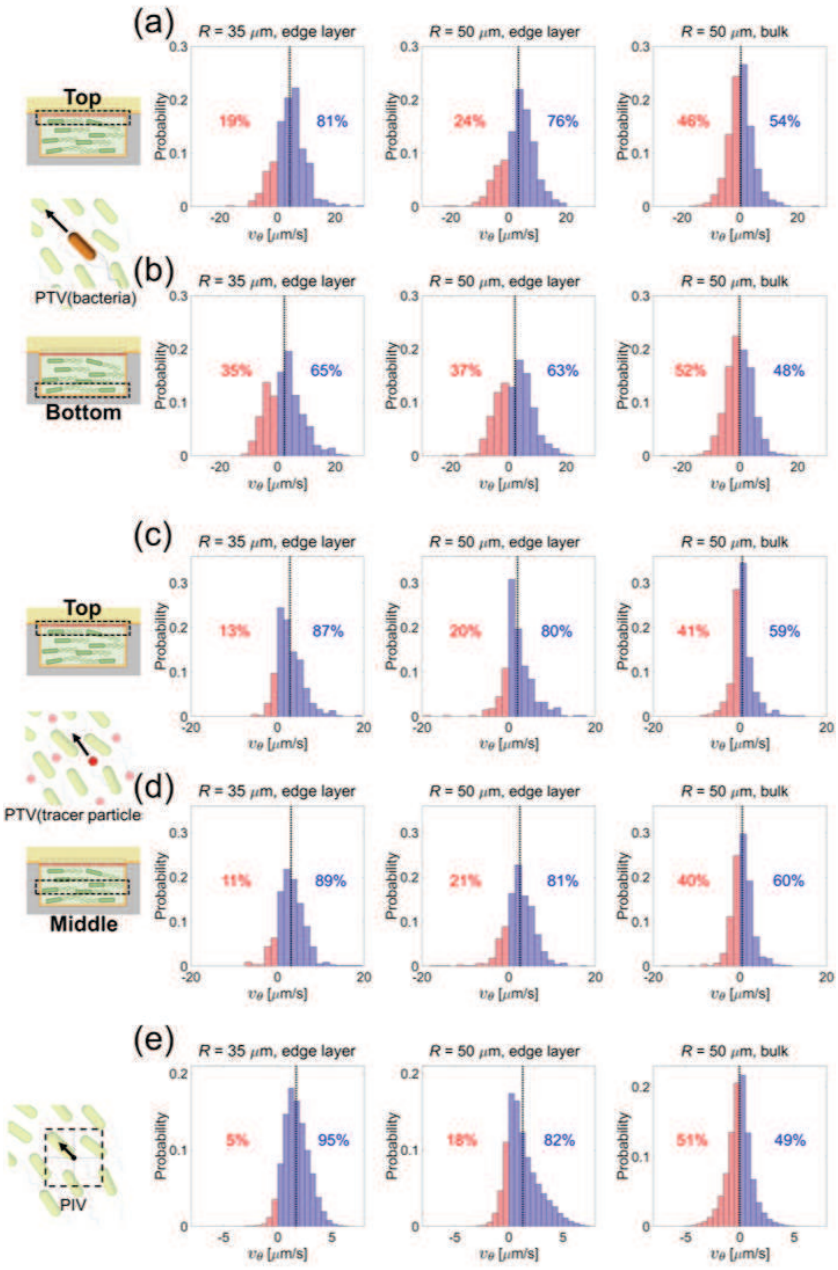

Figure 3.10: Histograms of azimuthal velocities of tracked bacteria, tracer particles, and velocity fields in the dense bacterial suspension (20%v/v). (a) and (b) Individual bacteria swimming near (a) the top oil/water interface and (b) the bottom water/PDMS interface. (c) and (d) Fluid flows measured by tracer particles near (c) the top oil/water interface and (d) the middle of PDMS microwell. (e) PIV velocity field of collective bacterial motion observed under bright field. The blue bars indicate the probability of CCW rotation, while the red bars indicate CW rotation. Collective motions in microwells of two different sizes ($R = 35\,\mu\text{m}$ and $R = 50\,\mu\text{m}$) are analyzed. The edge layer is defined as a region within $10\,\mu\text{m}$ from the lateral boundary, and the bulk is a region more than $10\,\mu\text{m}$ away from the lateral wall.

3.5.3 Interplay between chiral collective motions at top and bottom

In order to address this question, we assess the interplay between collective motions at both top and bottom interfaces by changing the height h of microwells from 20 µm to 50 µm. The collective motions near the two interfaces are examined by the orientation map of the velocity field for each microwell with different heights in Fig. 3.11. In a shallow microwell of $h = 20$ µm, the coherent rotation between top and bottom could be generated (Fig. 3.11, left). This is because collective motions are fully correlated throughout the microwell whose height is comparable with the orientation correlation length in bacterial turbulence (~ 18 µm). With increasing the height, on the other hand, collective motion at the bottom became disordered in a microwell of $h = 32$ µm (Fig. 3.11, middle) and eventually changed to chiral collective motion towards a CW direction in a deep microwell of $h = 49$ µm (top view), resulting in the counter-rotating collective state (Fig. 3.11, right). This may be because the height is much longer than the correlation length and in turn, chirality-induced collective motions independently occur at both interfaces. The fact that we observe the robust CCW chiral edge currents implies that there is a perturbation biased towards CCW chiral collective motions induced at the top.

To quantify the extent to which swimming bacteria within the edge layer of 10 µm are biased towards the CCW direction depending on microwells with different heights, using labeled bacteria with a small fraction (0.7%v/v), we analyzed the distribution of mean azimuthal velocity (Fig. 6.16 in Appendix D) and its proportion of CCW rotation to total tracked trajectories (Fig. 3.12), as in the analysis in Fig. 3.10. At $h = 20$ µm, the tracked bacteria within an edge layer exhibit a predominantly CCW rotation near both the top and bottom interfaces, although that at the top was more biased towards the CCW direction (Fig. 3.12). When the height of the microwells exceeds the correlation length, the bias towards the CCW direction disappeared above the bottom interface at $h = 32$ µm and then changed to the CW rotation at $h = 49$ µm, while the bias of CCW rotation was maintained only beneath the top interface (≈80% fraction) at any height. Note that the average speeds $\langle |v| \rangle$ near both interfaces were comparable (e.g., top: 10.9 µm/s and

bottom: 11.0 µm/s at $h = 49\,\mu\text{m}$). These results suggest that collective motions at the top and bottom where opposite chiral motions are induced compete with each other, and in turn, chiral collective motion at the top becomes predominant. Then, what is the origin of the preponderance at the top interface?

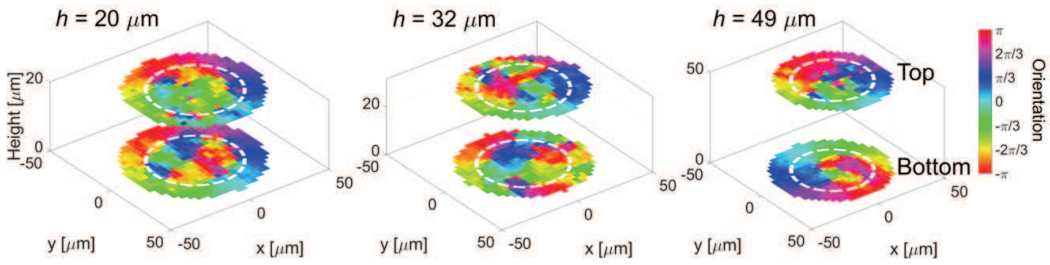

Figure 3.11: Color map of velocity orientation of collective motion at top and bottom interfaces in microwells of different heights h. The bacterial density is 20%v/v. (left) $h = 20\,\mu\text{m}$, (middle) $h = 32\,\mu\text{m}$, (right) $h = 49\,\mu\text{m}$. White dashed lines indicate the edge layer.

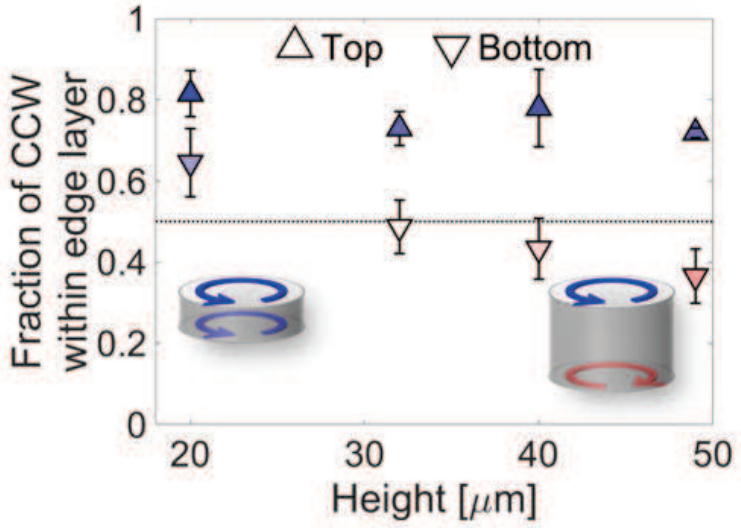

Figure 3.12: Fraction of CCW rotation of individual bacteria within the edge layer in microwells of different heights. Triangle: top interface, inverted triangle: bottom interface. CCW and CW rotations are displayed by blue and red symbols, respectively.

3.5.4 Density distribution inside microwells

The question above motivated us to measure the density distribution in the height direction with confocal microscopy. Due to the problem in the measurement resolution in the height direction, we focused only on the top and the bottom plane manually and counted labeled bacteria in a dense bacterial suspension by means of trackmate of an ImageJ plugin. We then analyzed the ratio of the number of bacteria at the top to that at the bottom for each microwell with different heights. In this measurement, we found that the bacterial density near the top interface is 1.2-1.6 times higher (about 2-4%v/v increase) than that near the bottom, almost regardless of the height of microwells. This non-equivalence reflects the dominant role of the top interface in the chirality selection and determines the global rotational direction of collective swimming that results from the competition between the opposing chiral collective motions.

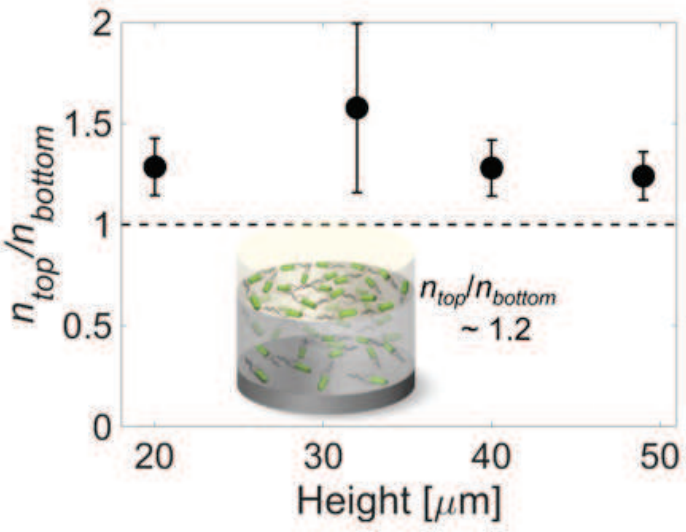

Figure 3.13: The relative number density of bacteria (the ratio of the density at the top to that at the bottom) in microwells of different heights.

3.5.5 Effect of bacterial density on chiral edge current

To gain further insight into the onset of the chiral edge current by collective effects, we examined the effect of bacterial density in the shallow microwell of $h = 20\,\mu\mathrm{m}$. In the same way as the analysis above, we recorded the trajectories of bacteria with fluorescent proteins and analyzed the distribution of azimuthal velocity within an edge layer and its fraction of CCW rotation at various bacterial densities from 0.01%v/v to 20%v/v (Fig. 3.14 and Fig. 6.18 in Appendix D). In a dilute suspension with 0.01%v/v, bacteria often swim in contact with the boundary wall in a CCW direction beneath the top interface but in the opposite CW direction above the bottom interface, suggesting that motions of bacteria swimming at the top and bottom were not correlated at a low density, as expected. When the density increases to 11%v/v, the CCW rotation within the edge layer becomes slightly dominant at both interfaces. As the bacteria are more highly concentrated, the bacterial motions become more correlated within the edge layer between top and bottom via the interactions, so that more obvious coherent rotations towards the CCW direction appear (Fig. 3.14). The global rotation of CW or CCW is chosen out of the competition between collective motions at top and bottom interfaces, resulting in symmetry breaking. Therefore, the overall direction can be controlled by a small perturbation. That is why no global collective motion arises despite the preponderance at the top in deeper microwells where the interplay is weak between two interfaces. Once the height of microwells becomes small, i.e., the interplay is increased, a slight difference in the density leads to aligned edge currents with CCW handedness (Fig. 3.15).

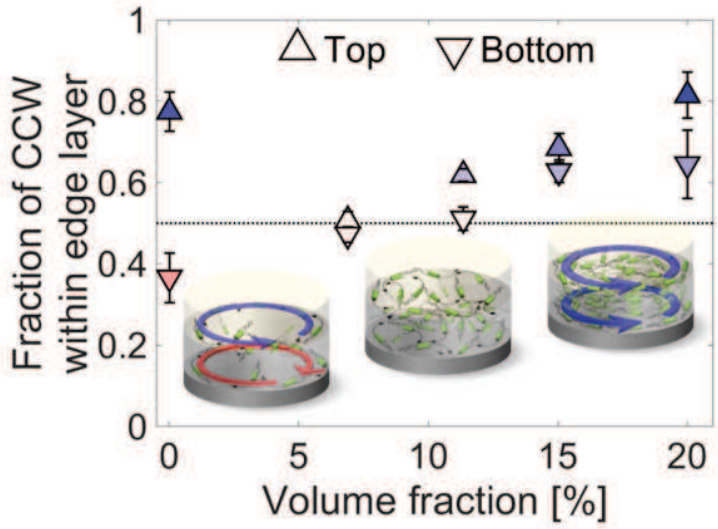

Figure 3.14: Fraction of CCW rotation of individual bacteria within the edge layer at different bacterial densities. The height is $h = 20\,\mu\text{m}$.

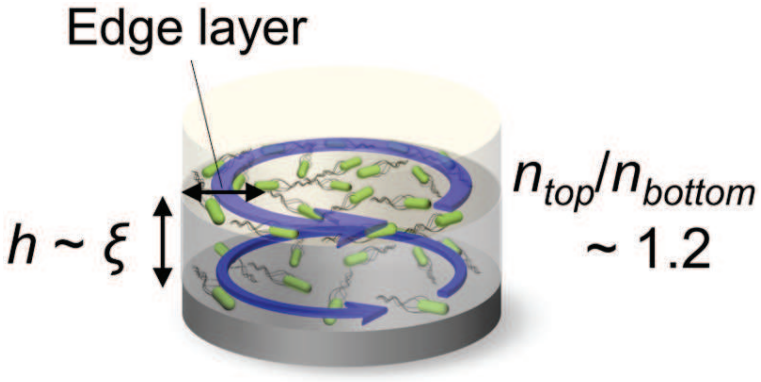

Figure 3.15: Schematic model for the emergent chiral edge current. The key is chirality-induced CCW motions at the edge, coupling between top and bottom within the correlation length ($\xi \sim 18\,\mu\text{m}$), and the top preponderance in terms of the density.

3.5.6 Effect of physical properties of interfaces on chirality selection

The effect of interface properties on the chirality selection is worthy of investigation to explore other possibilities for the origin of symmetry breaking. We first removed the surfactant (SPAN80) that can alter the behaviors of bacteria near the interface and slip conditions of the fluid flow. Before assessing collective motions under that condition, we checked trajectories of individual motions of bacteria swimming beneath the water/mineral oil interface without the surfactant. We observed curved trajectories with a large curvature but the same CCW bias as the case of the water/mineral oil interface with the surfactant, which may stem from a high shear condition of a flow at the interface due to the large difference in their viscosities (water: 0.8 mPa·s, mineral oil: 32 mPa·s). In the same way as experiments with the surfactant, we then examined collective motions near the top and bottom interfaces, the density difference between top and bottom, and mean swimming speed at both interfaces. Even in the absence of the surfactant, a chiral edge current with CCW handedness was observed in a shallow microwell, and the counter-rotating state of CCW at the top and CW at the bottom was observed when the height of microwells is increased (Fig. 3.16). Although the swimming speeds at both interfaces were comparable, the density at the top was 1.3 - 1.4 times higher than that at the bottom. To further investigate the effect of viscosity, we changed the oil viscosity by replacing mineral oil (32 mPa·s) with hexadecane (2.7 mPa·s), but the results were still the same as those of mineral oil (Fig. 3.17). In short, we do not find any significant difference in the resulting chiral edge currents at any conditions: mineral oil with surfactant, mineral oil without surfactant, and hexadecane without surfactant (Table 3.2) (see Appendix D for details). This implies that the emergent chiral edge currents originate from the density difference between top and bottom rather than the hydrodynamic asymmetric condition of shear flows induced by bacteria inside a microwell. The mechanism of the appearance of density heterogeneity in the height direction remains an open question, which may stem from a difference in bacterial motility in response to a difference in oxygen supply or some complex interactions between bacteria and an oil/water

interface [93, 96]. (Note that the gravity effect is irrelevant to the density heterogeneity because the density at the top is measured after inverting a device and hence both interfaces are set downward with respect to the direction of gravity during the measurement.)

Interestingly, the net chirality of the bacterial vortex was reversed in the CW direction in a shallow microwell with a top water/air interface, because bacterial swimming beneath a water/air interface in a dilute suspension (0.01%v/v) did not show obvious bias towards either the CW or the CCW direction possibly due to a slip boundary condition, meaning that only the bottom interface induce chiral collective motion (Fig. 6.20 in Appendix D). Although the density at the top is still slightly (∼1.1 times) higher than that at the bottom and the collective motion at the top appears to be biased towards the CCW direction in a deep microwell (Table 3.2 and Fig. 6.21 in Appendix D), the collective motion with no obvious chirality bias at the top interface is considered to be aligned with the CW chiral collective motion at the bottom in a shallow microwell, leading to the CW coherent rotation.

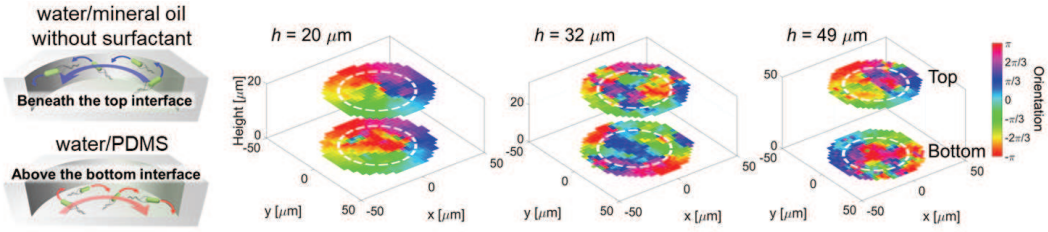

Figure 3.16: Color map of the orientation of collective velocities at top (water/mineral oil without surfactant) and bottom (water/PDMS) interfaces in microwells of different heights h. The bacterial density is 20%v/v. (left) $h = 20\,\mu\text{m}$, (middle) $h = 32\,\mu\text{m}$, (right) $h = 49\,\mu\text{m}$. White dashed lines indicate the edge layer.

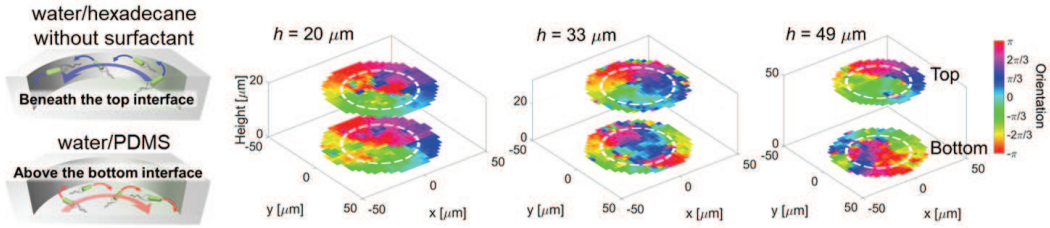

Figure 3.17: Color map of the orientation of collective velocities at top (water/hexadecane without surfactant) and bottom (water/PDMS) interfaces in microwells of different heights h. The bacterial density is 20%v/v. (left) $h = 20\,\mu\text{m}$, (middle) $h = 33\,\mu\text{m}$, (right) $h = 49\,\mu\text{m}$. White dashed lines indicate the edge layer.

Table 3.2: Properties of chiral swimming in microwells with various asymmetric interfaces. In *Chiral swimming*, biases of directions of chiral swimming in dilute suspensions (0.01%v/v) is presented at both top and bottom interfaces. In *Swimming velocity* $\langle|v|\rangle$, mean swimming speed of bacteria in microwells of $h = 49\,\mu\text{m}$ and $R = 35\,\mu\text{m}$ is measured. The bacterial density is 20%v/v. In *Relative density at the top*, the ratio of bacterial density at the top to that at the bottom is shown (top values for $h = 49\,\mu\text{m}$ and bottom values for $h = 20\,\mu\text{m}$). The bacterial density is 20%v/v. *Selected chirality* denotes the rotational direction of emergent chiral edge currents in microwells of $h = 20\,\mu\text{m}$ and $R = 35\,\mu\text{m}$. The bacterial density is 20%v/v.

Material of the top interface	Chiral swimming	Swimming velocity $\langle\|v\|\rangle$	Relative density at the top	Selected chirality
Mineral oil with surfactant (32 mPa s)	Top: CCW Bottom: CW	Top: 10.9 μm/s Bottom: 11.0 μm/s	1.24 ± 0.12 (1.29 ±0.14)	CCW
Mineral oil without surfactant (32 mPa s)	Top: CCW Bottom: CW	Top: 10.2 μm/s Bottom: 11.0 μm/s	1.30 ± 0.08 (1.37 ±0.09)	CCW
Hexadecane without surfactant (2.7 mPa s)	Top: CCW Bottom: CW	Top: 13.2 μm/s Bottom: 15.1 μm/s	1.45 ± 0.40 (1.49 ±0.33)	CCW
Air	Top: Equal mix of CCW and CW Bottom: CW	Top: 8.7 μm/s Bottom: 8.9 μm/s	1.11 ± 0.19 (1.11 ±0.07)	CW

3.5.7 Numerical simulation of chirality selection

The preponderance of collective motion at the top in terms of the bacterial density would be sufficient to account for the reason why the collective motion at the bottom follows that at the top in the competition between two interfaces. To support this, we simulated an agent-based Vicsek model in which the collective motions with different densities between the two and bottom interfaces couple through polar alignment of chiral self-propelled particles. Note that simulations here were conducted by Prof. Yutaka Sumino. We assume that self-propelled particles move at a constant velocity v_0 at the top and bottom interfaces, while ferromagnetically interacting with surrounding particles and being confined into a

circular boundary of radius R (Fig. 3.18). We define two planes (corresponding to top and bottom interfaces) that have the constant numbers of particles, N_t on the top and N_b on the bottom, and the particles do not move across. The self-propelled particles also have a constant angular velocity, i.e., chirality, with CCW handedness at the top interface and CW at the bottom. In addition, the motion of the particles is considered to be biased towards the CCW direction in colliding a boundary wall at the top (CW direction at the bottom) due to the intrinsic chirality (Fig. 3.18). As for orientational interactions, the particles in the same plane align their heading angles of particles within the effective range of ε (Fig. 3.18, *at the same interface*). Moreover, the polar alignment is also applied between the particles on the top and bottom planes within an effective range projected to the opposite interface, ε_{tb} (Fig. 3.18, *between two interfaces*). The effective range of polar alignment ε is assumed to be longer than (or comparable to) that across two interfaces ε_{tb}, and the numerical simulation was performed by setting $\varepsilon = 1$ (for the normalization in length scale) and $\varepsilon_{tb} \leq 1$. Increasing ε_{tb} leads to the aligned orientations of particles over the two interfaces. Because changing ε_{tb} corresponds to controlling the strength of correlation between collective motions at the top and the bottom interfaces, it corresponds to the experimental condition of varying the height of microwells.

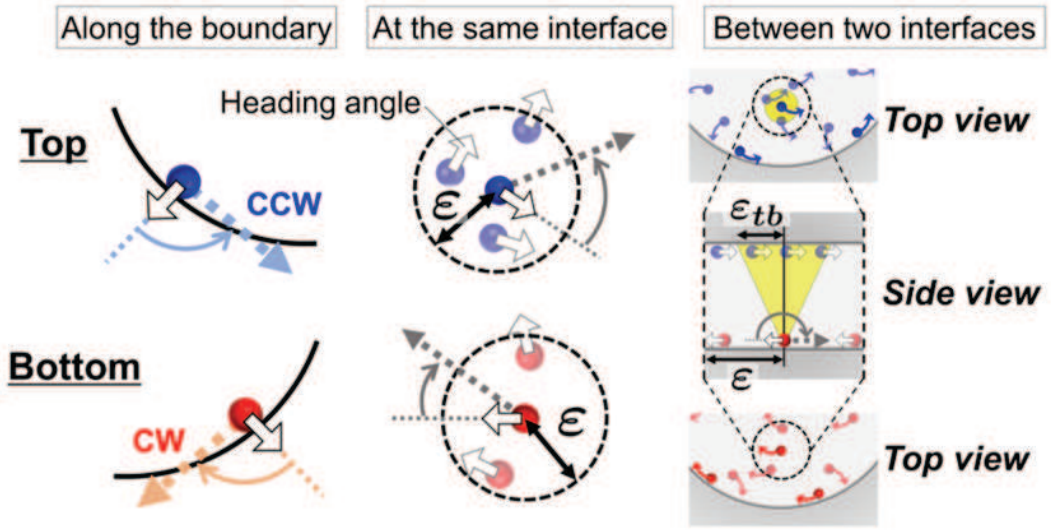

Figure 3.18: Schematics of the simulation setup. Two different planes (top and bottom) particles belong to are defined. Self-propelled particles ferromagnetically interact with a boundary wall, neighboring particles at the same plane, and particles belonging to the different planes. For the alignment with a wall, particles are biased towards the CCW (CW) direction at the top (bottom) due to the intrinsic chirality. For the polar alignment in the same plane, particles are aligned within the effective radius ε ($\varepsilon = 1$). For the coupling with particles at the other plane, the polar alignment works when the particles at the different plane are within the effective interaction range projected to the facing plane, $\varepsilon_{tb} \leq 1$. The colored bent arrows represent the intrinsic chiral motion.

Let us here describe the details of the numerical calculation. We define the polar coordinate (r, φ) and set its origin at the center of the circle. The position and the orientation of self-propelled particle m is defined as $\boldsymbol{r}_m^z(t) = (x_m^z(t), y_m^z(t)) = r_m^z(\cos\varphi_m^z, \sin\varphi_m^z)$ and $\boldsymbol{d}(\theta_m^z) = (\cos\theta_m^z, \sin\theta_m^z)$, respectively. The superscript z indicates which plane the particle belongs to, the top (i.e., $\boldsymbol{r}_m^t(t)$) or bottom (i.e., $\boldsymbol{r}_m^b(t)$). The position of the particle on the top interface is evolved as follows:

$$\dot{\boldsymbol{r}}_m^t = \boldsymbol{v}(\theta_m^t(t)) + \frac{2\kappa}{l^2} \sum_{r_{mn}^t < \varepsilon} (\boldsymbol{r}_m^t - \boldsymbol{r}_n^t) \exp\left[-\left(\frac{r_{mn}^t}{l} \right)^2 \right] - \kappa_b \frac{\boldsymbol{r}_m^t}{r_m^t} \Theta(r_m^t - R), \quad (3.1)$$

and the position of the particle at the bottom interface is given by

$$\dot{\boldsymbol{r}}_m^b = \boldsymbol{v}(\theta_m^b(t)) + \frac{2\kappa}{l^2} \sum_{r_{mn}^b < \varepsilon} (\boldsymbol{r}_m^b - \boldsymbol{r}_n^b) \exp\left[-\left(\frac{r_{mn}^b}{l} \right)^2 \right] - \kappa_b \frac{\boldsymbol{r}_m^b}{r_m^b} \Theta(r_m^b - R), \quad (3.2)$$

where the speed of the particles is set to $v_0 = 1$, r^t_{mn} (or r^b_{mn}) represents the distance between m-th and n-th particles at the top interface (or the bottom interface), and ε is the effective radius of polar interaction ($\varepsilon = 1$ in numerical simulations). Due to the presence of the excluded volume effect between bacteria, the soft repulsive force with the coefficient κ and the length scale of soft repulsive interaction l is incorporated in our model. The particles are constrained by the soft repulsion with the coefficient κ_b from the lateral wall. $\Theta(x)$ denotes Heaviside step function defined as

$$\Theta(x) = \begin{cases} 1, & x > 0 \\ 0, & x \leq 0 \end{cases} \tag{3.3}$$

According to the experiment, bacteria have chirality in their swimming with CW (CCW) handedness above (beneath) the interface with no-slip condition from the top view. Thus, we set the constant angular velocity in bulk as ω^t_0 on the top interface and $-\omega^b_0$ on the bottom, respectively. As discussed above, we introduce the coupling among particles belonging to two different planes. In doing so, we set the distance between two particles in different planes, defined as $r^{tb}_{mn} = r^t_m - r^b_n$, and polar orientation interaction works between particles when the distances on the projected plane are within ε_{tb}. In addition, the nematic interaction with a boundary wall is imposed on the particles in contact with it. Since a chiral edge current is attributed to a re-orientation by chiral swimming near the lateral boundary, we incorporate the weak unidirectional orientation at the lateral boundary (CCW rotation at the top interface and CW rotation at the bottom interface, from the top view). Taken together, the orientational dynamics of the particle at the top plane is governed by the following equation:

$$\begin{aligned} \dot{\theta}^t_m = \omega^t_0 - \bar{\gamma}_p \Bigg[\sum_{r^t_{mn} < \varepsilon} \sin(\theta^t_m - \theta^t_n) - \sum_{r^{tb}_{mn} < \varepsilon_{tb}} \sin(\theta^b_n - \theta^t_m) \Bigg] \\ - \left[\gamma^t_e \sin\left(\theta^t_m - \varphi - \frac{\pi}{2}\right) - \gamma_w \sin 2\left(\theta^t_m - \varphi - \frac{\pi}{2}\right) \right] \Theta(r^t_m - R) + \eta^t_m, \end{aligned} \tag{3.4}$$

where $\bar{\gamma}_p$, γ^z_e, and γ_w denote the coefficients of polar alignment of the adjacent particles, polar alignment with a wall by an edge current on the z plane, and nematic alignment along the boundary wall, respectively. $\eta(t)^z_m$ is angular fluctu-

ation that satisfies $\langle \eta_m^z \rangle = 0$ and $\langle \eta_m^z(t)\eta_n^{z'}(t')\rangle = 2D\delta_{zz'}\delta_{mn}\delta(t-t')$. Besides, the orientational dynamics of the particle at the bottom plane is given by

$$\begin{aligned}\dot{\theta}_m^b = &-\omega_0^b - \bar{\gamma}_p\Bigg[\sum_{r_{mn}^b<\varepsilon}\sin(\theta_m^b-\theta_n^b) - \sum_{r_{mn}^{tb}<\varepsilon_{tb}}\sin(\theta_n^t-\theta_m^b)\Bigg] \\ &- \left[\gamma_e^b \sin\left(\theta_m^b-\varphi-\frac{\pi}{2}\right) - \gamma_w \sin 2\left(\theta_m^b-\varphi-\frac{\pi}{2}\right)\right]\Theta(r_m^b-R) + \eta_m^b.\end{aligned} \tag{3.5}$$

We set to $\bar{\gamma}_p = 0.5\,\mathrm{s}^{-1}$, $D = 0.1\,\mathrm{s}^{-1}$, and $\omega_0 = 0.3\,\mathrm{s}^{-1}$, comparable to the experimental value. We nondimensionalize the length scale with the length of the bacteria $L = 3\,\mu\mathrm{m}$ and the time scale with the speed of particles $v_0 = 12\,\mu\mathrm{m/s}$ as by setting $\tau = L/v_0 \sim 0.2\,\mathrm{s}$ as the unit for the time. The radius of a circular boundary is set to $36\,\mu\mathrm{m}$. In the dimensionless form in Eqs. (3.1)-(3.5), the parameters are $\bar{\gamma}_p = 0.1$, $D = 0.02$, and $R = 12$. Other parameters are set as follows: $\kappa = 3$, $\ell = 0.3$, $\kappa_b = 10$, $\gamma_w = 1$, $\gamma_e^t = \gamma_e^b = 1$, and $\omega_0^t = \omega_0^b = 0.06$. Eqs. (3.1)-(3.2) and Eqs. (3.4)-(3.5) were integrated using the Heun's method with a time step width, $\delta t = 0.01$, which was conducted up to $T = 2500$. The data were taken from $T = 1$ to 2500 with the sampling rate, $\delta t = 1$.

We performed the numerical calculations by setting a density ratio $N_t/N_b = 1.22$ ($N_t = 5500$ and $N_b = 4500$), which refers to the experimental values at the oil/water interface. Fig. 3.19 shows the orientation fields at the top plane and the bottom one for each condition of the coupling strength, which is obtained from the direction defined by the time difference of the position. They are averaged over $T = 2401$ to 2500 with the mesh size δx=1. At a small ε_{tb} ($\varepsilon_{tb} = 0.01$), the interplay between particles at the top and bottom planes is weak, resulting in chiral collective motions independently rotating in different directions. As ε_{tb} increases to ($\varepsilon_{tb} = 0.25$), the particles at the bulk of the bottom plane follow the chiral collective motion at the top plane and turn into the CCW rotation, but chiral rotation in the CW direction near the boundary still remains. At a sufficiently large ε_{tb} ($\varepsilon_{tb} = 0.5$), the strong correlation allows the populations over two planes to stably rotate in the CCW direction, so that the collective motions at the bottom undergoing a CW rotation completely follow those at the top (Fig. 3.20). We plotted the fraction of particles rotating in the CCW direction within

an edge layer ($11 \leq R \leq 12$), which is calculated by the total number of CCW particles in the edge layer divided by the total number of particles in the layer, as a function of ε_{tb} (Fig. 3.20). We found that only the particles at the bottom transit from the CW to the CCW rotation, consistent with our experimental results.

Moreover, the numerical simulation can also account for the chirality reversal by decreasing chiral bias at the top air/water interface, implying that not only the density heterogeneity but also chirality bias at the single-cell level near interfaces is important for the symmetry breaking of the global rotation (see Appendix D for details).

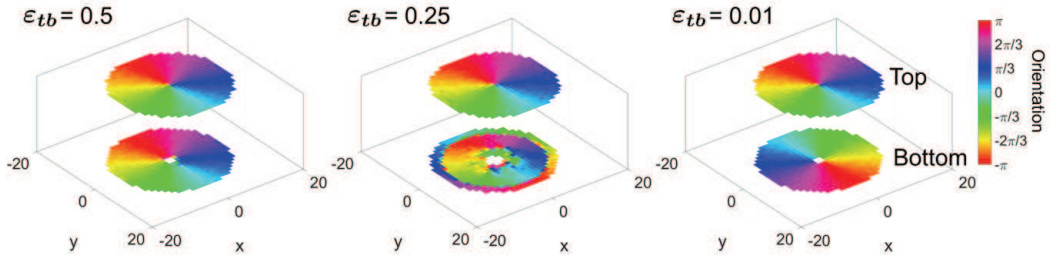

Figure 3.19: Numerical simulation of chirality selection in the coupled collective motion of chiral self-propelled particles at various ε_{tb}.

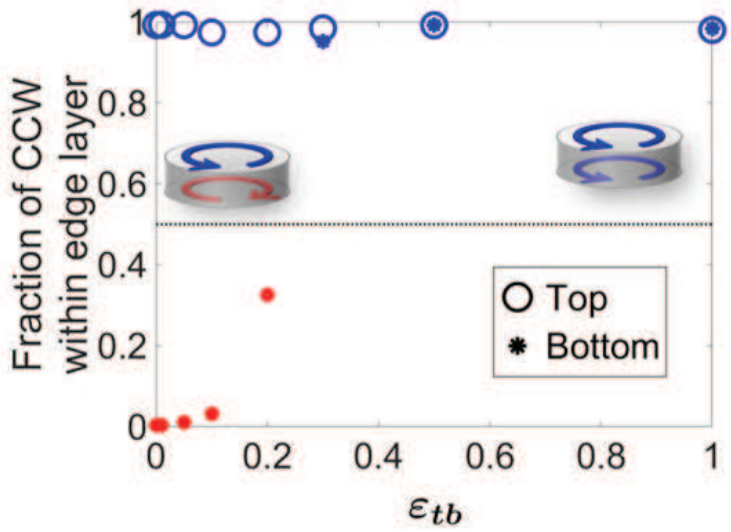

Figure 3.20: Fraction of CCW rotation of individual particles within the edge layer in a circular boundary at various ε_{tb}. Circle: top interface, aster: bottom interface. CCW and CW rotations are displayed in blue and red symbols, respectively.

3.6 Fast material transport in chiral bacterial vortices

Thanks to the properties of chiral vortices or edge currents, it is possible to extract the unidirectional rotation of achiral objects. As reported in Refs. [89–91], collective motions of suspended self-propelled particles are capable of enhancing transport properties in active fluids under built-in geometrical boundaries to direct the motion of objects larger than the suspended particles, e.g., gear-shape or ratchet-shape. To further illustrate the transport properties of chiral bacterial vortices found above, we confined a rigid rod with 20 µm in length and 4 µm in thickness that is made of SU-8 photoresist into a circular microwell with 20 µm in radius, which is much longer than the bacterial body with 3.5 µm in length and 0.8 µm in thickness (Fig. 3.21 (a)). Note that the SU-8 rod was provided by Prof. Yamanishi Yoko and Dr. Tasuku Sato. The polarity of the confined rod is defined and the time series of its rotation is analyzed in Fig. 3.21 (b). The rod persistently rotates in the CCW direction over multiple rounds at 0.5 rad/s, which is 6 times faster than the rotation of ratchet-shaped gears in a bacterial suspension previously reported [89]. Even in the absence of the lateral confinement and the asymmetric condition, as expected, a rod can be rotated by the disordered vortices in active turbulence in a quasi-two-dimensional chamber. However, due to the nature of transient and intermingled vortices, the rotational direction of the rod stochastically changes between CW and CCW, though the magnitude of the angular velocity remains constant ($\simeq 0.7$ rad/s) (Fig. 3.21 (c) and (d)). Consequently, chiral bacterial vortices or edge currents offer simple and fast material transport without built-in chirality [91, 95].

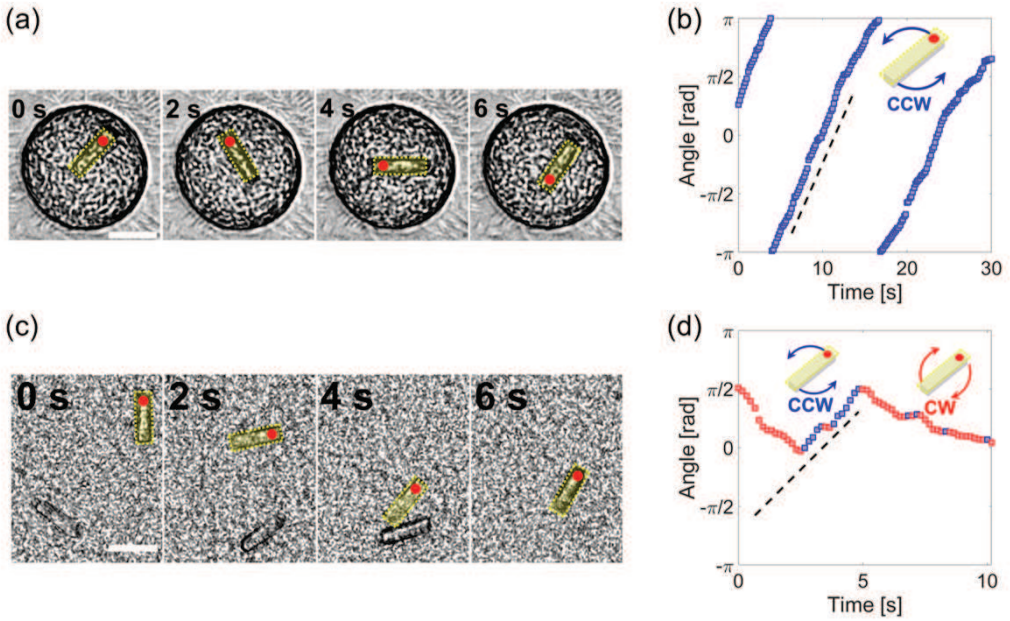

Figure 3.21: (a) Snapshots of movement of a rigid (SU-8) rod in chiral bacterial vortex over 6 s. The red point indicates the head-end of the rod. Scale bar, 20 µm. (b) Corresponding orientation angle increases linearly with time, which displays a constant CCW angular velocity. The dashed line has a slope of 0.51 rad/s. (c) Snapshots of bright field images over 6 s of the random rotation and translation of a rigid rod in a dense bacterial suspension under quasi-two-dimensional confinement. The rod of interest is colored yellow in the image, and its head is arbitrarily defined by a red dot. Scale bar, 20 µm. (d) Time evolution of the orientation angle of the marked rod. The blue color represents the CCW rotation and the red color, the CW rotation. Both rotation directions have comparable angular velocities. The black dashed line has a slope of 0.67 rad/s. Scale bar, 20 µm.

3.7 Edge-current-induced pairing order transition of chiral vortices

It has been shown that chiral vortices with an edge current result from the interplay of opposing collective motions induced at top and bottom interfaces. Next, it is imperative to unveil whether the robust nature of chiral vortices or chiral edge currents, found to be independent of the curvature of the boundary, controls the self-organization of bacterial vortices. Furthermore, it is still poorly understood what physical factor for edge current plays a crucial role in controlling interacting ordered vortices inherent in active turbulence. To this end, we address these

questions by examining the ordered patterns of chiral vortices that are constrained by a doublet boundary of overlapping circular microwells with a radius R and an inter-center distance Δ. As previously discussed in Chapter 2, in the absence of an edge current (under the top/bottom symmetric condition), there is the geometric rule that the transition from FMV to AFMV occurs at $\Delta_c/R = 2\cos 45° = \sqrt{2}$ such that their probabilities are equiprobable. On the other hand, in the presence of an edge current (under the asymmetric condition), the configuration flowing along the wall, FMV, is expected to be induced rather than AFMV (Fig. 3.22). In this section, we both theoretically and experimentally demonstrate the FMV-AFMV pairing order transition controlled by chirality, measure the strength of the chiral edge current, and evaluate its effectiveness in controlling active turbulence.

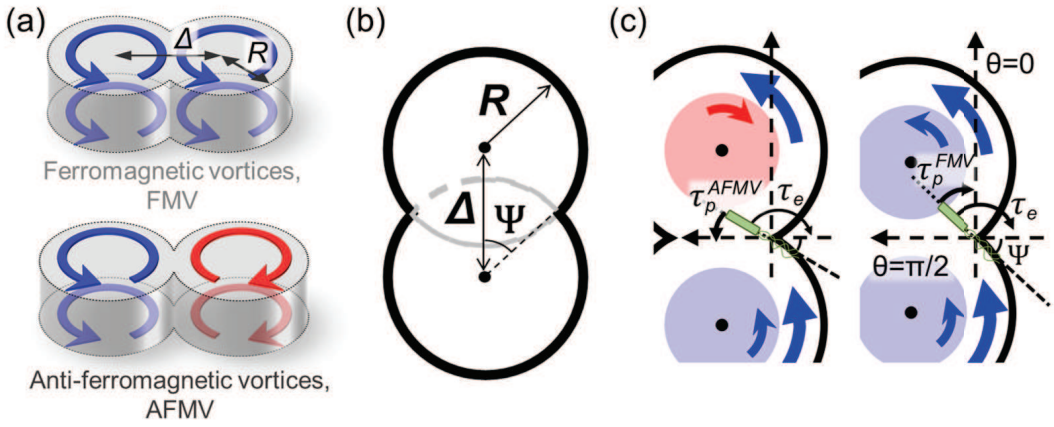

Figure 3.22: (a) Pairing order: ferromagnetic vortices (FMV) and anti-ferromagnetic vortices (AFMV). (b) Geometry of the doublet circular boundary. (c) Schematics of chiral edge current effects. For both patterns, chiral edge currents align particles along the boudnary wall. τ_p denotes a torque exerted by polar interactions in the case of FMV or AFMV, and τ_e is an extected alignment by an edge current effect.

3.7.1 Theoretical analysis for chirality-induced pairing order

To predict how a chiral edge current affects the previously established geometric rule, we constructed a theoretical model based on the Vicsek model including the effect of a chiral edge current, in the same way as the agent-based model above.

Note that we here consider the interacting chiral vortices where the collective motions at the top and bottom interfaces are fully correlated, which corresponds to the condition of $\varepsilon_{tb} \simeq \varepsilon$ in the agent-based model proposed in the previous section. The equation of the orientational dynamics is given by

$$\dot{\theta}_m = -\bar{\gamma}_p \sum_{r_{mn}<\varepsilon} \sin(\theta_m - \theta_n) - \bar{\gamma}_e \sum_{r_{mn}<\varepsilon} \sin(\theta_m - \theta_w) + \eta_m(t), \tag{3.6}$$

where the strength of an edge current γ_e is defined as $\gamma_e = \sum_{r_{mn}<\varepsilon} \bar{\gamma}_e$. θ_n in the first term is set to $\theta_n = \theta_w$ or $\theta_n = \theta_w + \pi$, which follows the chiral edge current or moves against it. Since the asymmetric interfaces continuously offer the bias of chiral bacterial swimming towards the CCW direction, we assume that such chirality effect is present regardless of whether the vortex pairing is FMV or AFMV. At a tip with an angle 2Ψ where two circles intersect, two tangential angles in the CCW direction are defined as $\frac{\pi}{2} - \Psi$ for a left circle and $-\frac{\pi}{2} + \Psi$ for a right circle. The re-orientation resulting from a CCW edge current at the tip is described by $\bar{\gamma}_e \sum_{r_{mn}<\varepsilon} \sin(\theta_m - \theta_w) = \frac{\gamma_e}{2}(\sin(\theta_m - \frac{\pi}{2} + \Psi) + \sin(\theta_m + \frac{\pi}{2} - \Psi))$. This reads

$$\dot{\theta}_m = -\bar{\gamma}_p \sum_{r_{mn}<\varepsilon} \sin(\theta_m - \theta_n) - \gamma_e \sin\theta_m \sin\Psi + \eta_m(t). \tag{3.7}$$

In the same way as Ref. [76], by considering collisions at the tip between bacteria coming from different parts of the circle, which are constrained by the its geometry, the Fokker-Planck equations for both AFMV and FMV patterns with the chiral edge current can be written as follows: for the AFMV pattern with the edge current,

$$\frac{\partial P_{AFMV}}{\partial t} = D\frac{\partial^2 P_{AFMV}}{\partial \theta^2} - \frac{\partial}{\partial \theta}\Big(\big[\gamma_p \cos\theta \cos\Psi - \gamma_e \sin\theta \sin\Psi\big] P_{AFMV} \Big), \tag{3.8}$$

and for the FMV pattern with the edge current,

$$\frac{\partial P_{FMV}}{\partial t} = D\frac{\partial^2 P_{FMV}}{\partial \theta^2} + \frac{\partial}{\partial \theta}\Big(\big[\gamma_p \sin\theta \sin\Psi + \gamma_e \sin\theta \sin\Psi\big] P_{FMV} \Big), \tag{3.9}$$

where the strength of polar alignment is rewritten as $\gamma_p = \sum_{r_{mn}<\varepsilon} \bar{\gamma}_p$. In the steady state ($\partial tP = 0$), the probabilities of realizing the FMV and AFMV patterns can be solved as follows:

$$P_{AFMV}(\theta;\Psi) = A(\Psi)\exp\left[\frac{\gamma_p \sin\theta\cos\Psi + \gamma_e\cos\theta\sin\Psi}{D}\right], \tag{3.10}$$

and

$$P_{FMV}(\theta;\Psi) = B(\Psi)\exp\left[\frac{(\gamma_p+\gamma_e)\cos\theta\sin\Psi}{D}\right] \tag{3.11}$$

where $A(\Psi)$ and $B(\Psi)$ are normalization factors dependent on Ψ. Given that $\theta = 0$ means particles' orientation along the wall and hence corresponds to an FMV pattern ($P_{AFMV}(\theta = 0;\Psi)$), while $\theta = \pi/2$ is assigned to an AFMV pattern $P_{AFMV}(\theta = \pi/2;\Psi)$, one can rewrite

$$P_{AFMV}(\theta = \pi/2;\Psi) = A(\Psi)\exp\left[\frac{\gamma_p\cos\Psi}{D}\right], \tag{3.12}$$

and

$$P_{FMV}(\theta = 0;\Psi) = B(\Psi)\exp\left[\frac{(\gamma_p+\gamma_e)\sin\Psi}{D}\right]. \tag{3.13}$$

Then, the transition point can be obtained at $P_{FMV}(\theta = 0;\Psi) = P_{AFMV}(\theta = \pi/2;\Psi)$. This readily reads

$$\log\left[\frac{A(\Psi)}{B(\Psi)}\right] + \frac{\gamma_p}{D}\cos\Psi = \frac{(\gamma_p+\gamma_e)}{D}\sin\Psi. \tag{3.14}$$

From the condition of Ψ satisfying Eq. (3.14), the transition point between FMV and AFMV patterns can be obtained.

Meanwhile, the relation equivalent to Eq. (3.14) can be also derived by the argument of potentials obtained from the above mean-field model that allows us to more simply discuss the transition between FMV and AFMV. The effective torque for re-orientation is written as the form: $\tau = -\partial U/\partial\theta$ (Fig. 3.22 (c)). As such, geometry-dependent potentials for re-orientation by an edge current and polar alignments of FMV and AFMV configurations can be described by $U_e = -\gamma_e\cos\theta\sin\Psi$ with edge current's coefficient γ_e, $U_p^{FMV} = -\gamma_p\sin\Psi$ at $\theta = 0$,

and $U_p^{AFMV} = -\gamma_p \cos\Psi$ at $\theta = \pi/2$ with the strength of the polar alignment $\gamma_p > 0$, respectively. The respective summations of the potentials coincide at the transition point, i.e., $(U_p^{FMV} + U_e)|_{\theta=0} = (U_p^{AFMV} + U_e)|_{\theta=\frac{\pi}{2}}$, yielding

$$(\gamma_p + \gamma_e) \sin\Psi_c = \gamma_p \cos\Psi_c, \tag{3.15}$$

where $\gamma_p + \gamma_e$ determines the enhancement of FMV pairing by the chiral edge current. Using the relationship of the definition of the geometrical boundary, $\Delta_c/R = 2\cos\Psi_c$, and expanding Eq. (3.15) around $\Delta_c/R = \sqrt{2}$, the transition point can be rewritten as

$$\frac{\Delta_c}{R} = \frac{2}{\sqrt{1 + \left(\frac{\gamma_p}{\gamma_p+\gamma_e}\right)^2}} \simeq \sqrt{2}\Big(1 + \frac{\gamma_e}{2\gamma_p}\Big). \tag{3.16}$$

The obtained geometric relation Eq. (3.16) can be readily reduced to the original expression of $\Delta_c/R = \sqrt{2}$ when there is no chiral edge current. This result suggests that an FMV pattern is stabilized even in the regime of $\Delta/R \geq \sqrt{2}$ and the relative strength of the edge current to the polar interaction γ_e/γ_p determines the shift of the transition point. The full description for the transition point of Eq. (3.16) is shown as the phase diagram in Fig. 3.23. The phase boundary shows a linear increase around $\Delta_c/R = \sqrt{2}$ and then approaches asymptotically to the limit value of $\Delta_c/R = 2$.

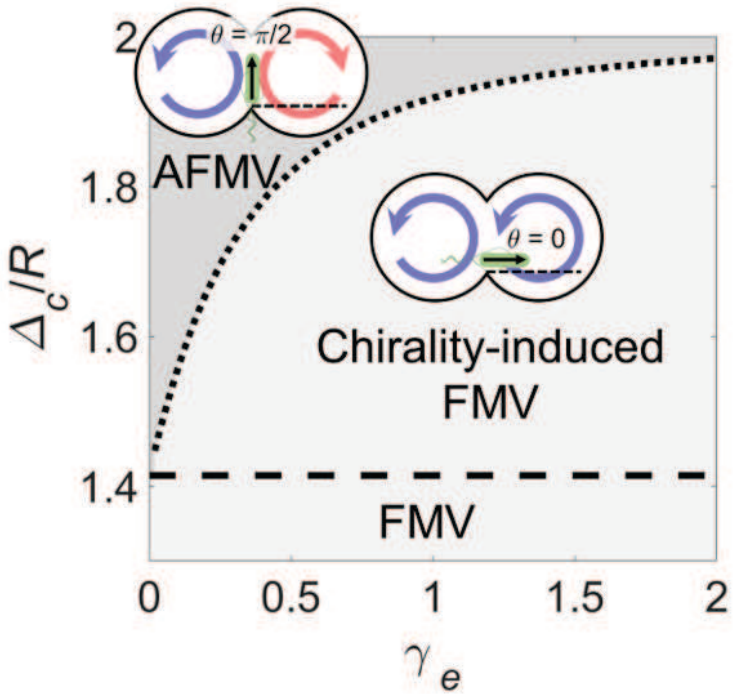

Figure 3.23: Phase diagram of pairing order depending on the geometric parameter Δ/R and the coefficient of chiral edge current γ_e. The coefficient of polar alignment γ_p is set to $0.42\,\mathrm{s}^{-1}$ obtained from the independent experiment (we will detail later). The dotted line indicates the transition point increased by chirality, and the horizontal broken line represents the original transition point $\Delta/R = \sqrt{2}$ without a chiral edge current.

3.7.2 Edge-current-induced co-rotational order

In order to verify the occurrence of chirality-induced vortex pairing, we investigated the emergent patterns in doublet circular microwells with $R = 19\,\mu\mathrm{m}$ and $h = 20\,\mu\mathrm{m}$ within the range of $0 \leq \Delta < 2R = 38\,\mu\mathrm{m}$. Fig. 3.24 (a) and (b) exhibit arrays of the instantaneous vorticity $\Omega(\boldsymbol{r}_i) = \nabla \times \boldsymbol{v}(\boldsymbol{r}_i)$ and velocity field in the steady state under both the symmetric and asymmetric conditions. The pairing order can be characterized by the absolute value of the spatial average of vorticity inside the microwell, $|\langle\Omega\rangle|$, which represents 0 for AFMV (achiral pattern) and a finite value ($\gtrsim 0.1$) for FMV (chiral pattern) which roughly corresponds to the mean vorticity of a single vortex. Under the asymmetric condition, the transition to 0 was found to be at $\Delta_c/R \simeq 1.8$ to 1.9, whereas it occurred at $\Delta_c/R \simeq 1.4$ under symmetric conditions, suggesting that FMV pairing is favored in the presence of

edge currents. Conversely, AFMV pairing can still occur despite the presence of edge currents robust to the boundary shape.

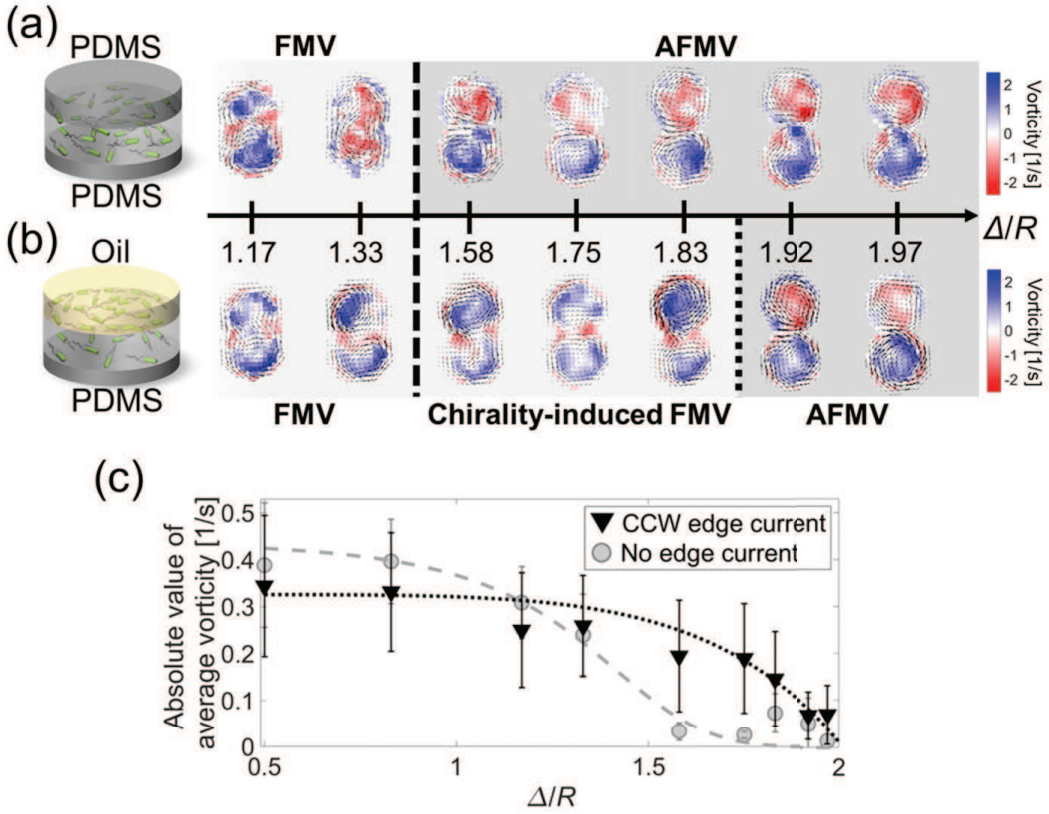

Figure 3.24: Arrays of vorticity map of collective motions in the steady state under different conditions of interfaces. The top and bottom arrays show representative data at various Δ with $R = 19\,\mu\text{m}$ and $h = 20\,\mu\text{m}$ under the top/bottom symmetric interfaces (a) and the asymmetric interfaces (b), respectively. The density of bacteria is 20%v/v. (c) Absolute value of the average vorticity of interacting bacterial vortices at various Δ/R, with a CCW edge current (inverted black triangles) and without edge current (grey circles). Error bars denote standard deviation. A sigmoidal line is fitted to the experimental data for clarity of the transition behavior.

To quantitively compare our theoretical model and experimental results, we furthermore estimated the physical parameters: γ_p and γ_e, from the probability distribution of the bacterial orientation at a tip. To do so, we firstly estimated the intrinsic angular fluctuation D by tracking trajectories of single swimming bacteria apart from interfaces and lateral walls in a dilute bacterial suspension (0.01%v/v, Fig. 3.25 (a)). We consider single bacteria as self-propelled point particles, with

a position $\boldsymbol{r}(t) = (\boldsymbol{x}(t), \boldsymbol{y}(t))$ and an orientation (defined as the unit vector along the long-axis) $\boldsymbol{d}(t) = \boldsymbol{d}(\theta(t)) = (\cos\theta(t), \sin\theta(t))$ for two-dimensional coordinates. (Note that the orientation is calculated from the direction of the instantaneous velocity because the swimming direction nearly coincides with the heading angle of bacteria and should be more important for the polar interaction.) The mean-square angular displacement (MSAD) is analyzed as $\langle \left[\boldsymbol{d}(\theta(t+\delta t)) - \boldsymbol{d}(\theta(t))\right]^2 \rangle_t$ where $\langle\cdot\rangle$ denotes an ensemble average. This should be fitted to the function, $2(1-\exp[-D\delta t])$ with a time sampling δt and the angular diffusion coefficient D that is the angular fluctuation at single cell level [94], yielding $D = 0.12\,\mathrm{s}^{-1}$ (Fig. 3.25 (b)).

With the rotational diffusion coefficient obtained from the independent experiment, we next examined the probability distribution functions of Eq. (3.10) and Eq. (3.11) to estimate γ_p and γ_e. In a dense bacterial suspension undergoing an AFMV pattern, swimming bacteria at a tip should have a heading angle close to $\theta \approx \pi/2$. Therefore, the probability distribution function of $P_{AFMV}(\theta;\Psi)$ in Eq. (3.10) can be rewritten as a Gaussian distribution function in the following:

$$P_{AFMV}(\theta;\Psi) \approx A(\Psi)\exp\left[\frac{\gamma_p\cos\Psi}{2D}\left(2+\left(\frac{\gamma_e}{\gamma_p}\tan\Psi\right)^2\right)\right]\exp\left[-\frac{\gamma_p\cos\Psi}{2D}\left(\theta-\frac{\pi}{2}-\frac{\gamma_e}{\gamma_p}\tan\Psi\right)^2\right] \tag{3.17}$$

with the approximations $\sin\theta \approx 1-\frac{1}{2}\left(\theta-\frac{\pi}{2}\right)^2$ and $\cos\theta \approx \theta-\frac{\pi}{2}$ around at $\theta \approx \pi/2$. In the same way, as for a dense bacteria suspension undergoing an FMV pattern in which bacteria tend to head $\theta \approx 0$, we obtain an approximation form of P_{FMV},

$$P_{FMV}(\theta;\Psi) \approx B(\Psi)\exp\left[\frac{(\gamma_p+\gamma_e)\sin\Psi}{D}\right]\exp\left[-\frac{(\gamma_p+\gamma_e)\sin\Psi}{2D}\theta^2\right] \tag{3.18}$$

by using the approximations $\cos\theta \approx 1-\frac{1}{2}\theta^2$. With these Gaussian distribution functions of bacterial orientation at the tip with respect to AFMV and FMV, we can express the variance of θ as $\sigma^2_{AFMV} = \frac{D}{\gamma_p\cos\Psi}$ for the AFMV pattern and $\sigma^2_{FMV} = \frac{D}{(\gamma_p+\gamma_e)\sin\Psi}$ for the FMV pattern. From these expressions, the coefficients of polar alignment γ_p and the alignment by the edge current γ_e can be estimated by measuring the variances of θ in two types of pairing order with the angular

fluctuation $D = 0.12\,\mathrm{s}^{-1}$. To measure the variance of the distributions of the bacterial angle θ at a tip, we tracked labeled (dTomato) bacteria in dense bacterial suspensions with a high density of 20%v/v which are confined in doublet circular microwells with $\sin\Psi = 0.61$ (i.e., $\Delta/R = 1.58$) and $\cos\Psi = 0.96$ (i.e., $\Delta/R = 1.92$) that induces FMV and AFMV patterns, respectively (Fig. 3.26). The distributions in Fig. 3.26 show the variances in θ of $\sigma^2_{AFMV} = 0.30$ for the AFMV pattern and $\sigma^2_{FMV} = 0.21$ for the FMV pattern. Accordingly, we can obtain the estimated parameters $\gamma_e = 0.51\,\mathrm{s}^{-1}$ and $\gamma_p = 0.42\,\mathrm{s}^{-1}$. Substituting the estimated parameters into the geometric rule (3.16) gives a transition point $\Delta_c/R = 1.83$, which is in good accordance with the experimental result. This implies that chiral edge current can suppress orientation fluctuations to the same extent as polar orientation interaction and in turn lead to the dominant FMV ordering with a net circulation in larger scales. Furthermore, the evaluation of the strength with which the edge current controls the active turbulence is important to understand the effect of chirality on collective motion.

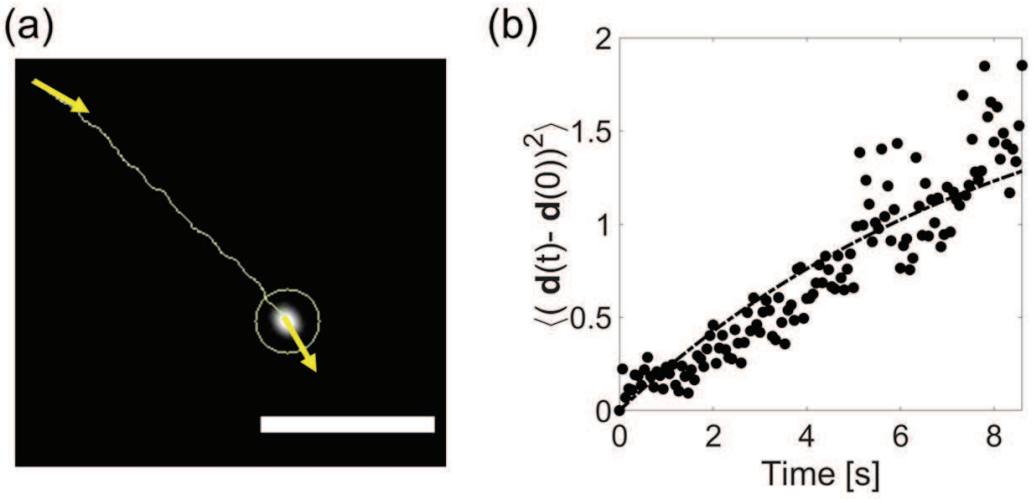

Figure 3.25: Measurement of rotational fluctuations of single bacterial swimming in bulk at a low density of 0.01%v/v. (a) The typical trajectory of swimming individual bacteria in bulk. Scale bar, 20 µm. (b) Mean square angular displacement (MSAD) of the heading angles of individual bacteria. The slope of this MSAD curve is fitted with $2(1-\exp[-D\delta t])$, where D reflects the orientation fluctuations of smoothly swimming bacteria [94].

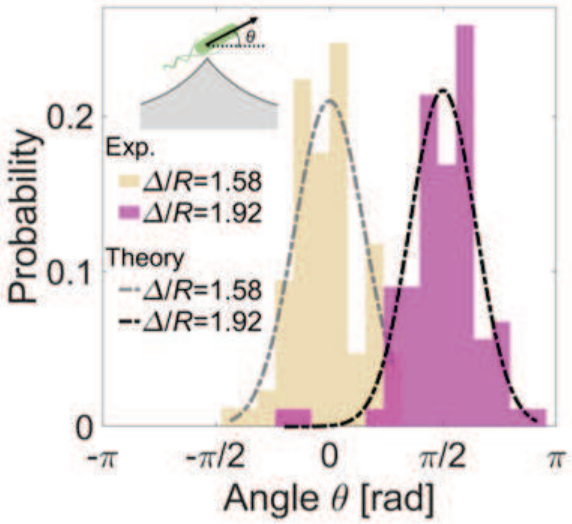

Figure 3.26: Orientation distribution of bacteria at a high density of 20%v/v. In microwells of $\Delta/R = 1.58$ (yellow) and $\Delta/R = 1.92$ (purple), by labeling single bacteria with fluorescent dTomato proteins, we tracked those swimming trajectories in the vicinity of the tip, and the distribution of its heading angle (velocity direction) was analyzed. For $\Delta/R = 1.58$ (yellow), the bacterial population exhibited an FMV pairing, while for $\Delta/R = 1.92$ (purple) it showed an AFMV pairing. The black and gray dotted curves are fitting curves by a Gaussian distribution function of Eq. (3.17) and Eq. (3.18). From the variance of these probability distributions, we can estimate the coefficients of the polar alignment γ_p and the alignment by the chiral edge current γ_e.

3.8 Summary of Chapter 3

To sum up, we investigated the effect of chirality on the self-organization of bacterial suspensions by imposing asymmetric (top: oil/water, bottom: water/PDMS) interfaces. As a result of the experiment, confined bacterial suspensions exhibited a chiral vortex and a chiral edge current near a lateral wall. The investigation of a density distribution and an interplay between opposing chiral collective motions at the top and the bottom revealed that the chiral edge current is attributed to three essential factors: (i) the motions selected only near the boundary by chirality, (ii) the full correlation inside a microwell such that its height is comparable to the orientational correlation length in active turbulence, and (iii) the preponderance of top-induced chiral collective motions in terms of the density distribution in the

top-bottom direction. The chiral edge current occurs almost independently of the boundary geometry, whereas bacterial turbulence has intrinsically interacting vortices like ferromagnetic vortices and anti-ferromagnetic ones, which are ruled by the ratio of the distance between vortices to the radius of vortices, $\Delta/R = \sqrt{2}$. Despite such apparent geometry dependence of ordered vortices, chiral edge currents suppress the occurrence of anti-rotational pairing order, allowing us to control active turbulence and produce a larger scale flow with a net circulation. Furthermore, our theoretical model based on confined self-propelled particles including an edge current successfully explains the enhancement of co-rotational pairing order, leading to the extended geometric rule where its shift is described by the ratio of an edge current to a local polar alignment. These results would offer a new route not only to the strategy to control active turbulence but also to the engineering of self-organized chiral micromachines with high energy efficiency, which is reminiscent of the spintronic device.

Before closing Chapter 3, let us discuss an outlook for this research field. Chiral active matter is indeed in the emerging field of active matter physics. Chiral active fluids composed of active spinners exhibit some intriguing features, e.g., a dissipationless viscosity (odd viscosity) [82, 97] and a chiral edge current that can be described as a topologically protected edge mode [83], which is analogous to topological insulators. Bridging between active matter and classical condensed matter in the topological view would be one of the challenges [98, 99], which is also for chiral bacterial suspensions we found. In addition, the chiral edge currents have been recently observed in various biological systems such as the neural progenitor cells and fibrosarcoma cells [85, 100]. Furthermore, the intrinsic chirality and its interaction with the boundary would be relevant to the chiral alignment patterns depending on cell species [101] and even the left-right asymmetry of organs in our body [102]. Remarkably, cancer cells confined in a micropatterned surface exhibit a chiral alignment pattern different from the normal counterpart. Therefore, elucidating not only the physical but also the biological or physiological significance of the emergent chiral collective behaviors would be an important future task in this field.

Chapter 4

Geometric control of a confined active cytoskeleton system

It has been found that there exists the geometric rule governing the vortex pairing order in a dense bacterial suspension (with or without chirality effect) which is in general classified into self-propelled particles with the polarity both in the movement and in the interaction with surrounding particles. It is imperative to investigate a geometric rule in another type of active matter to explore the geometric universality behind various active matter systems. According to our theoretical model for the pairing order based on geometrically constrained collisions, suppose that the confined self-propelled particles in an overlapping circular boundary have not polar orientational interactions but nematic interactions, both the co-rotational pairing (FMV) and the anti-rotational pairing (AFMV) are expected to give the same effective potential for the re-orientation, $U(\theta;\Psi) = \frac{1}{2}\cos 2\theta \cos 2\Psi$. This means that nematic interactions have no preference between FMV and AFMV. Hence, the next question is what geometric rule exists in self-propelled rods with nematic interactions. In this chapter, we report on collective motions of gliding microtubules (MTs) driven by kinesin motors confined in our designed boundaries. All of the experiments in this chapter were performed by one of the collaborators, Shunya Araki, and experimental materials were provided by Prof. Akira Kakugo and Dr. Arif Md. Rashedul Kabir. The numerical simulation and the theoretical

work were done by Kazusa Beppu.

4.1 Experimental setup

In the same way as the previously shown microfabricated system, we enclosed MTs driven by kinesin molecular motors in microwells with a predesigned boundary shape to seek a geometric rule. We used a recombinant kinesin composed of the first 573 amino acid residues of human kinesin-1 [103]. To visualize MTs, they were labeled by Rhodamine by polymerizing a mixture of rhodamine-labeled tubulin (RT) and non-labeled tubulin (WT) for 30 min at 37 °C and a molar ratio of (RT: WT) of 4:1. We fabricated the flow cell consisting of polydimethylsiloxane (PDMS) microwells, a glass slide, and a double-sided tape in the same way as our previous research in Chapter 3. Kinesin proteins were adsorbed on the PDMS surface, and then we waited for the deposition of MTs at various densities after injecting them into the chamber. MTs attached to the kinesin motors at the surface spontaneously move while consuming ATP. The mean length of the MT was 18.9±14.3 µm, and its density was tuned from 0.022 to 1.54 filaments/µm^2. The density 0.88 filaments/µm^2 is used, unless otherwise specified. MTs interact with surrounding ones through near-field interactions such as depletion force of 0.3% methylcellulose in the solution and steric interactions due to the rod shape of MTs [104]. The gliding speed of the MTs was 0.24±0.04 µm s^{-1} in 0.3% methylcellulose solution.

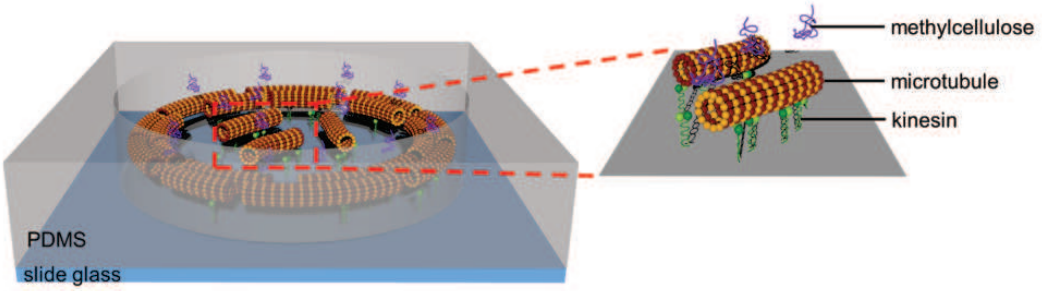

Figure 4.1: Schematic illustration of the experimental setup. Kinesin molecular motors were attached to the bottom PDMS substrate. MTs are driven by the force exerted by the kinesin motor proteins.

4.2 Unconfined motile microtubules

As introduced in Chapter 1, the collection of gliding MTs is known to give rise to long-range nematic order in an open boundary. We firstly checked such transition behavior from disordered motions to long-range nematic order depending on the density of MTs. To calculate the local orientation $\theta(r)$ of MTs, we used OrientationJ of an ImageJ plugin that detects the direction of the largest eigenvector of the structure tensor of the image. Fig. 4.2 (a) displays fluorescent images and orientation fields obtained with the tensor method for each image. The nematic order parameter S is defined as $|\langle e^{2i\theta(\boldsymbol{r})}\rangle|$ where $\langle\cdot\rangle$ denotes the ensemble average over the region of interest. Above a microtubule density $\rho = 0.22$ filaments/μm^2, the MTs' orientation was nematically ordered over a long-range (Fig. 4.2 (b)). We hereafter focus on the regime from $\rho = 0.22$ filaments/μm^2 to $\rho = 1.54$ filaments/μm^2 at which collective motions can be observed.

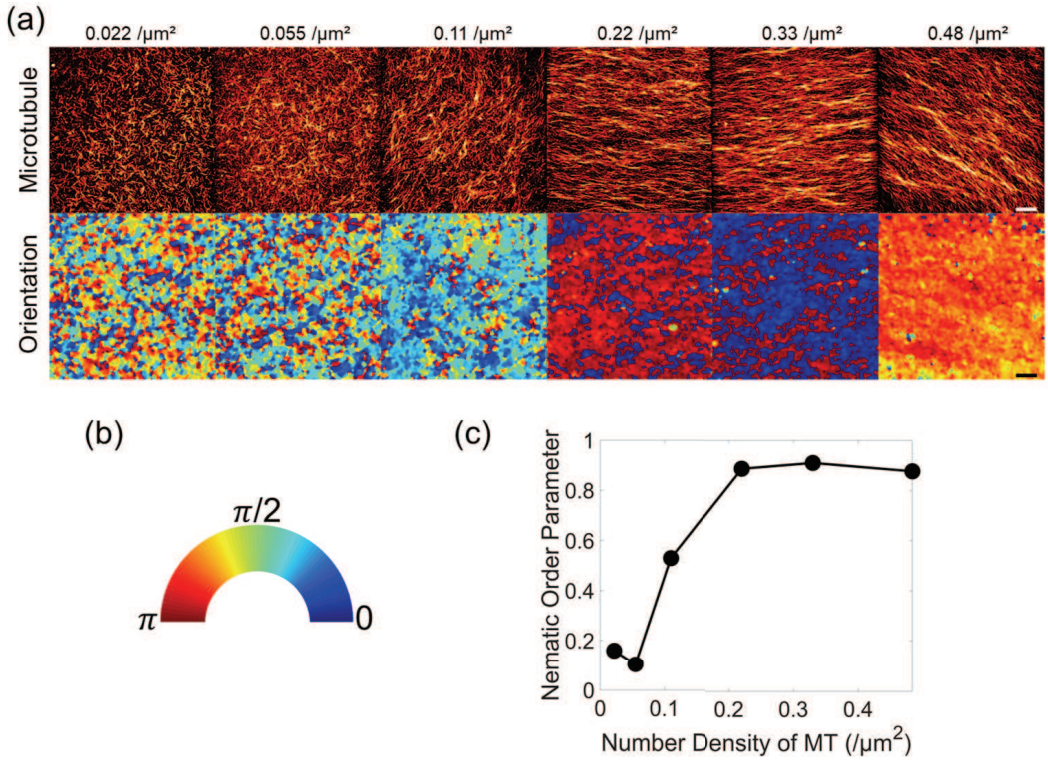

Figure 4.2: The density-dependent transition from disordered motions to collective motions in the collection of unconfined gliding MTs. (a) Top: fluorescent images of motile MTs. Bottom: orientation field of aligned microtubules calculated from corresponding fluorescent images. Scale bar, 50 μm. (b) Color code for orientation. (c) Nematic order parameters at various microtubule densities.

4.3 Emergent patterns in confined motile microtubules

To test the effect of the simplest geometrical constraint, that is, circular confinement on the active cytoskeletons composed of kinesins and MTs, we confined them in a circular microwell with a radius of $R = 82\,\mu\text{m}$ and height of $h = 25\,\mu\text{m}$. As expected, motile MTs collide with the wall in a nematic-alignment manner, resulting in the accumulation of MTs near the boundary (Fig. 4.3 (a)). For the first 10 min, the MTs moved collectively in the microwell while interacting with others, but after 30 min, most of them started to move along the wall due to nematic

collisions. The motile MTs were localized close to the boundary wall after 60 min, and in turn, the assembly formed a bundled structure. This suggests that the confinement is effective for steering the collective motion of motile MTs based on designed boundaries.

We designed doublet and triplet circular microwells to investigate the effect of collective collision of gliding MTs on pattern formations in a geometry-dependent manner. Because the angle of the collision among MTs plays an important role in their orientational interaction and even in the resulting macroscopic order, the overlapping circular boundaries should be the best geometry for guiding the geometry-dependent collision of MTs oriented along the boundary [76, 105]. We examined the emergent patterns of dense self-propelled MTs by varying the distance between circles Δ from 41 µm to 161 µm while keeping the same radius $R =$ 82 µm. In the doublet microwell with a large overlap of two circles ($\Delta = 96$ µm, $\Delta/R = 1.17$), a protruding bundle extending from the tip in the lateral direction was formed (Fig. 4.3 (b), top and Fig. 4.4 (a) and (b), left). On the other hand, as the overlapping circles are largely separated ($\Delta = 157$ µm, $\Delta/R = 1.92$), the protruding bundles from both two tip regions were combined into a bridge pattern (Fig. 4.3 (b), bottom and Fig. 4.4 (a) and (b), right). Remarkably, the protruding bundles tend to be unidirectionally tilted, and MTs gliding therein move in a counterclockwise (CCW) direction. Its statistics of the emergent chiral protruding structures was the sample number n=5 for CCW, n=1 for CW, and n=7 for achiral one. Such weak bias of the movement of MTs in the CCW direction can be characterized by the average angular velocity, which was $\omega = +1.1\times10^{-3}$ s^{-1}. This implies that the slight chirality at the microscopic scale could be amplified by collective interactions, leading to the formation of the tilted protruding bundles at the macroscopic scale.

The understanding of interactions between the bundles protruding from the tip in the bulk is also important for the controlling of MT's assemblies. In particular, emergent behaviors in triplet circular boundaries are nontrivial because the three tip-to-centroid axes cross at $2\pi/3$, which is not the most stable in terms of nematic alignments. Therefore, we investigated pattern formations in a triplet circular

microwell, as well as in the doublet boundaries. When three circles are largely overlapped ($\Delta = 96\,\mu m$ and $\Delta/R = 1.17$), a protruding bundle pattern emerged from the three tips, which is similar to that in the doublet circular boundary (Fig. 4.3 (c), top and Fig. 4.4 (c), left). In the triplet boundary with a small overlap of circles ($\Delta = 157\,\mu m$ and $\Delta/R = 1.92$), the MTs' bundled patterns from three tip regions formed a bridge pattern where two of them or all of the three ones were oriented towards each other (Fig. 4.3 (c), bottom and Fig. 4.4 (c), right). This result suggests that the collection of motile MTs confined even in the complex geometrical boundaries can be simply controlled by the geometric parameter Δ/R.

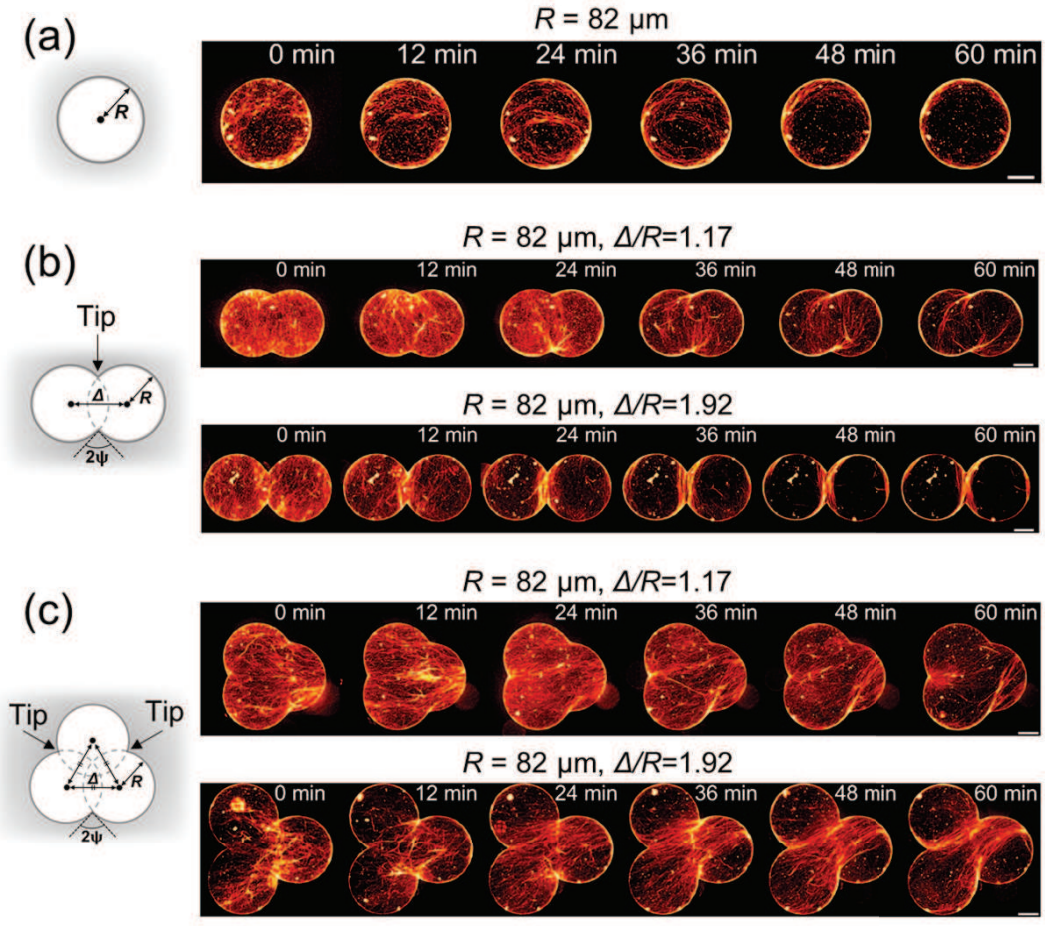

Figure 4.3: Time series of collective motion in MTs driven by kinesin confined in a circular microwell (a), doublet circular microwells (b), and triplet circular microwells, whose $R = 82\,\mu m$. Regardless of boundary shapes, the collective motion reaches a steady pattern in 60 min. Scale bars, $50\,\mu m$.

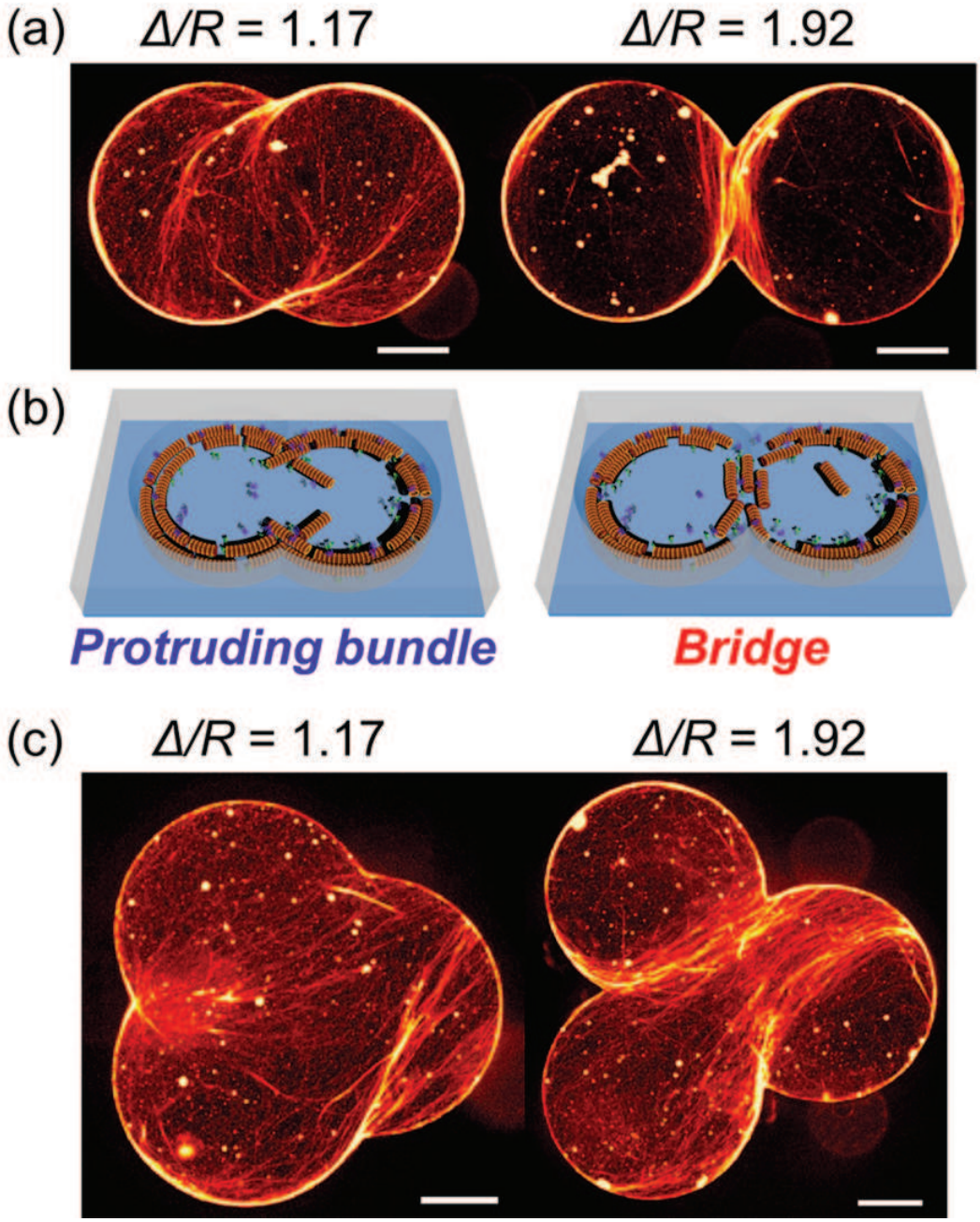

Figure 4.4: Tow distinct bundled patterns. (a) Assembled patterns of MTs confined in the doublet circular microwells in the steady state (60 min). (Left) $\Delta = 96\,\mu m$ and $\Delta/R = 1.17$, (right) $\Delta = 157\,\mu m$ and $\Delta/R = 1.92$. As shown in schematic illustrations in (b), the protruding bundle pattern of MTs can be observed at $\Delta/R = 1.17$ (a, left), while the bridge pattern of MT bundles can be formed at $\Delta/R = 1.92$ (a, right). (c) Assembled patterns of MTs confined in the triplet circular microwells in the steady state (60 min). (Left) $\Delta = 96\,\mu m$ and$\Delta/R = 1.17$ and (right) $\Delta = 157\,\mu m$ and $\Delta/R = 1.92$. Similar protruding bundle pattern is formed at $\Delta/R = 1.17$, while the bundled structures form bridges among the three tips at $\Delta/R = 1.92$. The scale bars in (a) and (c) are $50\,\mu m$.

We then investigated the transition from the protruding bundle pattern to the bridge pattern by varying Δ/R from 0.5 to 1.97 while fixing $R = 82\,\mu\text{m}$. In the doublet microwells, the protruding bundle pattern was observed below $\Delta/R = 1.33$, whereas the bridge patterns were formed above $\Delta/R = 1.33$ (Fig. 4.5 (a)). Similar transition behavior was found in the triplet microwells (Fig. 4.5 (c)). To quantify the alignment of MTs and its ordered structure, we analyzed the orientation field of MTs $\theta(\boldsymbol{r})$ at position $\boldsymbol{r}$ in doublet and triplet circular boundaries (Fig. 4.5 (b) and (d)). The transition of two patterns can be characterized using the order parameter for the bridge formation, Φ, defined as $\Phi = \langle \cos 2(\theta(\boldsymbol{r}) - \theta_{bdg}) \rangle_{ROI}$, where θ_{bdg} is the angle of the axis from the centroid of the microwell to the tip, and $\langle \cdot \rangle_{ROI}$ denotes the ensemble average over two semicircle areas with a radius $R/6$ where the center is set to the tip (Fig. 4.6 (a) and (b)). The order parameter monotonically increased with increasing the value of Δ/R, regardless of microwell sizes ranging from $R = 46, 82, 91,$ to $100\,\mu\text{m}$. This geometry-induced transition is almost the same as the case of triplet circular microwells.

To clarify whether only the parameter Δ/R is a crucial factor for the transition of patterns, we tested the dependence of the pattern formations on MT's number density, which is an important parameter for ordering of self-propelled MTs and considered to contribute to a change of the strength of local orientational interactions. We changed the density values from 0.22 filaments/μm^2 (Figs. 4.6 (a) and (b), deep green) to 1.54 filaments/μm^2 (Figs. 4.6 (a) and (b), purple). Setting the threshold of order parameter to $\Phi_c = 0$, which corresponds to an isotropic orientation, allows us to distinguish between protruding bundle and bridge patterns at various conditions: microwell sizes ($R = 46, 82, 91, 100\,\mu\text{m}$) and different MT densities (0.22, 0.88, 1.54 filaments/μm^2). For the doublet circular microwell, the order parameter exceeds $\Phi = 0$ around $\Delta/R = 1.3 - 1.4$ (Fig. 4.6 (a) and (c)), indicating that the transition from the protruding bundle pattern to the bridge pattern can be ruled by a common geometric condition $\Delta/R \sim 1.4$, independently of MT densities and confinement sizes. Furthermore, the assembly of motile MTs confined in the triplet circular boundary showed the order parameter changes across $\Phi \approx 0$ close to $\Delta/R = 1.5 - 1.6$ (Fig. 4.6 (b) and (d)). This slight

shift of the transition point reflects the appearance of bridge structures that are connected in a three-way branching pattern, which reduces the order parameter value because of the aligned configuration deviated from the defined bridge axes.

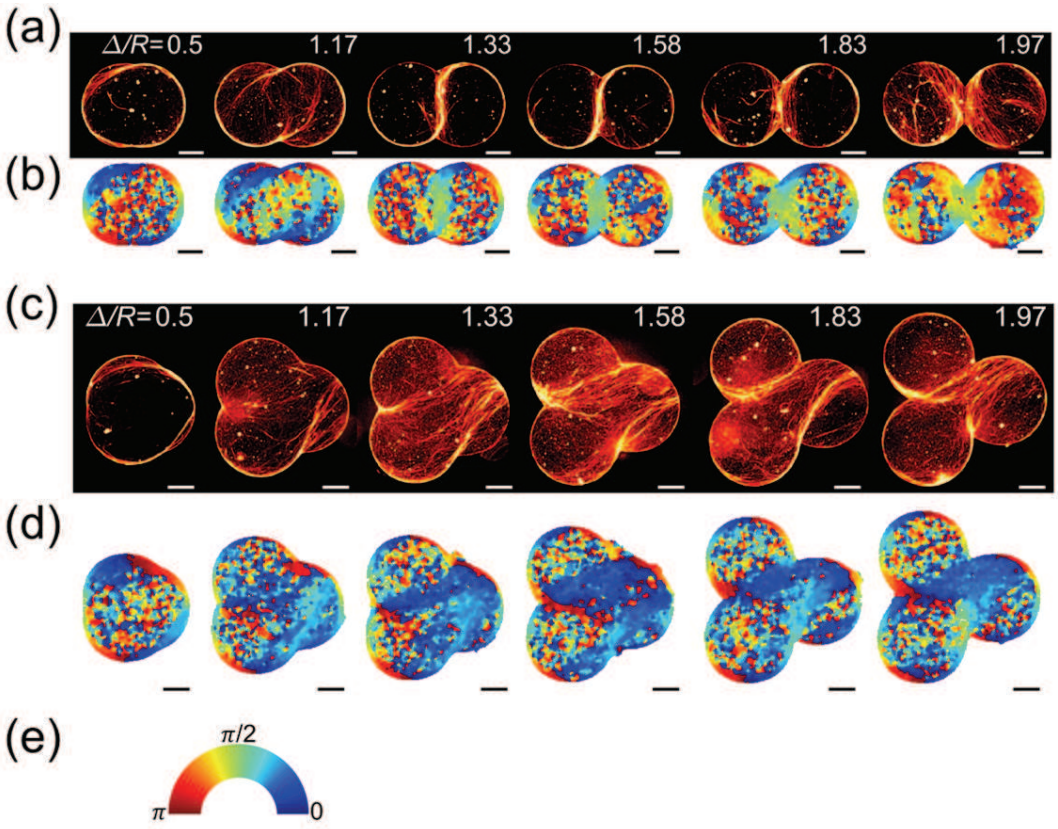

Figure 4.5: Geometric dependence of the protruding bundle and bridge patterns. (a) Assembled patterns of self-propelled MTs at the doublet circular boundary. The inter-center distance Δ between two circles is varied while the radius of the unit circle, $R = 82\,\mu\text{m}$, is kept constant. (b) Orientation field $\theta(\boldsymbol{r})$ of MTs at the doublet circle boundary. (c) Collective motion of MTs confined to the triplet circle boundary. As in the case of (a), the distance Δ is varied while keeping $R = 82\,\mu\text{m}$. (d) Orientation field $\theta(\boldsymbol{r})$ of MTs at the triplet circle boundary. (e) Color code for orientation. Scale bars, 50 µm.

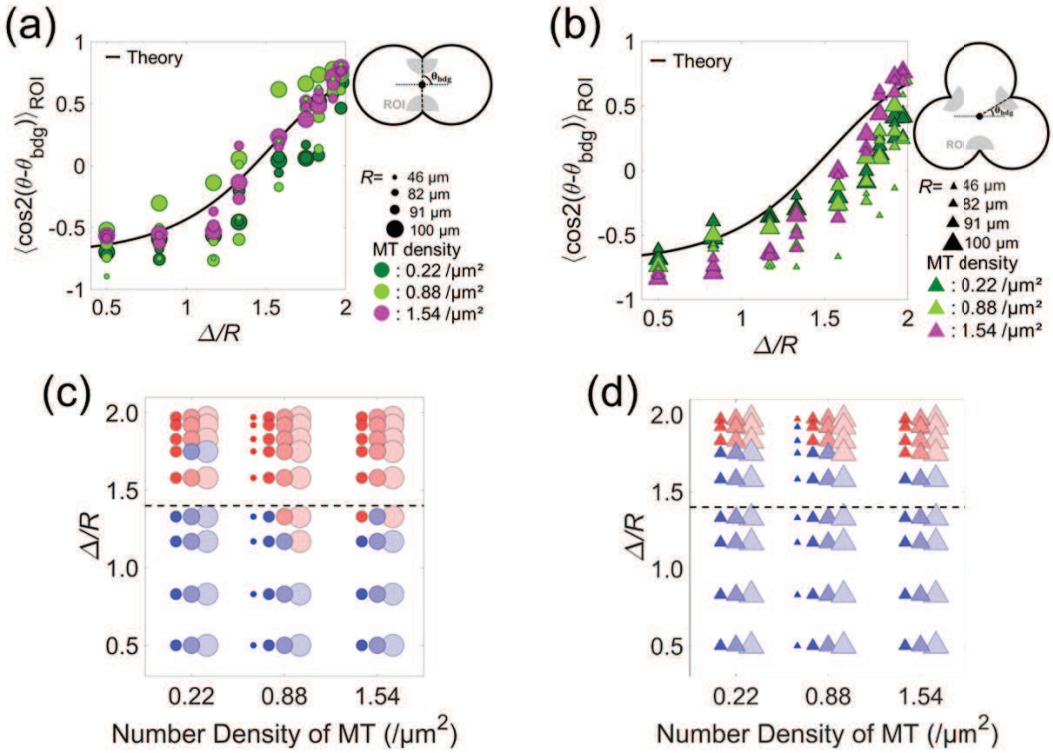

Figure 4.6: The transition between two assembled patterns of MTs. (a) The order parameter of the MT's orientation in the doublet circular boundary at various values of Δ/R. (b) The order parameter of the MT's orientation in the triplet circular boundary at various values of Δ/R. The black solid lines in (a) and (b) are obtained from Eq. (4.7) with the fitting parameter $\gamma = 1.9\times10^{-2}$ s^{-1}. Inset figures in (a) and (b) represent *ROI* for the order parameter calculation. (c) and (d) Phase diagrams of protruding bundle and bridge patterns in doublet (left panel, circle) and triplet circular boundaries (right panel, triangle). The various radii of $R = 46, 82, 91$, and $100\,\mu$m were used for each geometrical boundary, and the densities of MTs used here is 0.22, 0.88, and 1.54 filaments/μm^2. The bridge pattern is displayed in red and the protruding bundle pattern in blue, which is defined by the sign of the order parameter (positive for red and negative for blue). The broken line in (c) and (d) denotes $\Delta_c/R = \sqrt{2}$.

4.4 Theory for self-propelled rods

To elucidate why the pattern formation of self-propelled MTs is dominated by the single geometric parameter Δ/R, we constructed a theoretical model by modeling the motile MTs as self-propelled rods that have not polar but nematic interactions in their alignment among neighboring particles [2, 10, 13, 106].

4.4.1 Numerical simulation

To test whether the numerical model can reproduce the pattern formation of MTs, we implemented the numerical simulation by referring to our previous study [105]. The model is almost the same as the previously established model except for the symmetry of orientational interactions, but let us briefly explain it below. Since we consider the self-propelled rods confined in a doublet (or triplet) circular boundary, we define the polar coordinate (r, φ) in a two-dimensional plane and its origin is set at the center of either of the two (or three) circles the rod belongs to. The position of the rod m at time t and the velocity are defined by $\boldsymbol{r}_m(t)$ and $\boldsymbol{v}_m(t) = v_0\boldsymbol{d}(\theta_m)$ with the unit vector of $\boldsymbol{d}(\theta_m)$=$(\cos\theta_m(t), \sin\theta_m(t))$, respectively. The rod moves at a constant speed v_0 under a geometric constraint defined by Δ and R. Given that the re-orientation is determined by the interaction potential $U(\boldsymbol{r}_m, \theta_m)$, the dynamics of the position of self-propelled rods can be described by

$$\dot{\boldsymbol{r}}_m = \boldsymbol{v}(\theta_m(t)) + \frac{2\kappa}{l^2}\sum_{r_{mn}<\varepsilon}(\boldsymbol{r}_m - \boldsymbol{r}_n)\exp\left[-\left(\frac{r_{mn}}{l}\right)^2\right] - \kappa_b\frac{\boldsymbol{r}_m}{r_m}\Theta(r_m - R), \quad (4.1)$$

where $r_{mn} = |\boldsymbol{r}_m - \boldsymbol{r}_n|$ denotes the distance between two rods m and n, and the interaction works when the particles are within the effective radius of nematic alignment ε. To avoid overlap of rods at the lateral wall, we incorporated soft repulsive force with the coefficient κ into the Vicsek nematic model. l sets the length scale of soft repulsive interaction. κ_b is the coefficient of the repulsive force to confine the rod in the doublet or triplet circular boundary, and $\Theta(x)$ represents Heaviside step function defined as

$$\Theta(x) = \begin{cases} 1 \text{ for } & x > 0 \\ 0 \text{ for } & x \leq 0. \end{cases} \quad (4.2)$$

The orientation of self-propelled rods can be changed through nematic interactions with the effective range of $r_{mn} < \varepsilon$ and random noise. Additionally, we considered an intrinsic angular velocity ω of self-propelled rods to reproduce a chiral protruding bundle pattern, as observed in the experiment. Moreover, the

nematic interaction with a boundary wall is considered to impose a re-orientation on the particle in contact with the boundary. From the experimental observation that MTs move almost perfectly parallel to the wall, we simply set the strong nematic alignment such that the rod immediately aligns in the tangential direction of the boundary in colliding it, which guarantees a collision at a designed angle of a tip. Taking together, the orientational dynamics of the self-propelled rod is governed by

$$\dot{\theta}_m = \omega - \bar{\gamma} \sum_{r_{mn}<\varepsilon} \sin 2(\theta_m - \theta_n) + \eta_m, \tag{4.3}$$

where $\bar{\gamma}$ is the coefficient of nematic alignment of nearby rods, and $\eta(t)_m$ is angular fluctuation such that $\langle \eta_m \rangle = 0$ and $\langle \eta_m(t)\eta_n(t') \rangle = 2D\delta_{mn}\delta(t-t')$ with the angular diffusion coefficient D.

The simulations were implemented using the following parameters: $v_0 = 0.3\,\mu\text{m/s}$, $\bar{\gamma} = 0.05/\text{s}$, $D = 0.002/\text{s}$, $\omega = 0.002/\text{s}$, $\varepsilon = 0.3\,\mu\text{m}$, $\kappa = 0.2\,\mu\text{m}^2/\text{s}$, $l = 0.1\,\mu\text{m}$, $\kappa_b = 10\,\mu\text{m/s}$, $R = 40\,\mu\text{m}$. We integrated the equations above using the Euler method and a time width $\delta t = 0.01$, which was conducted up to $T = 800$. We set the number density of rods to 1.54 rods/μm^2 which is the same as the experimental highest value for observing collective motions. The snapshots of self-propelled rod vectors confined in the doublet and triplet circular boundaries at the endpoint ($T = 800$) are shown in Fig. 4.7. For the sake of quantitative comparison with the experimental results, we analyzed coarse-grained orientation fields with the mesh size $\Delta x = 1.6\,\mu\text{m}$. In the same way as the calculation of the order parameter in the experiment, we calculated the order parameter in the semicircular areas with radius $R/6$ by averaging from $T = 701$ to 800 with the sampling rate $\Delta t = 1$ (Fig. 4.8). The transition from protruding bundle pattern to bridge pattern took place around $\Delta/R = 1.4$ for both doublet and triplet circular boundaries, which is in accordance with the experimental result.

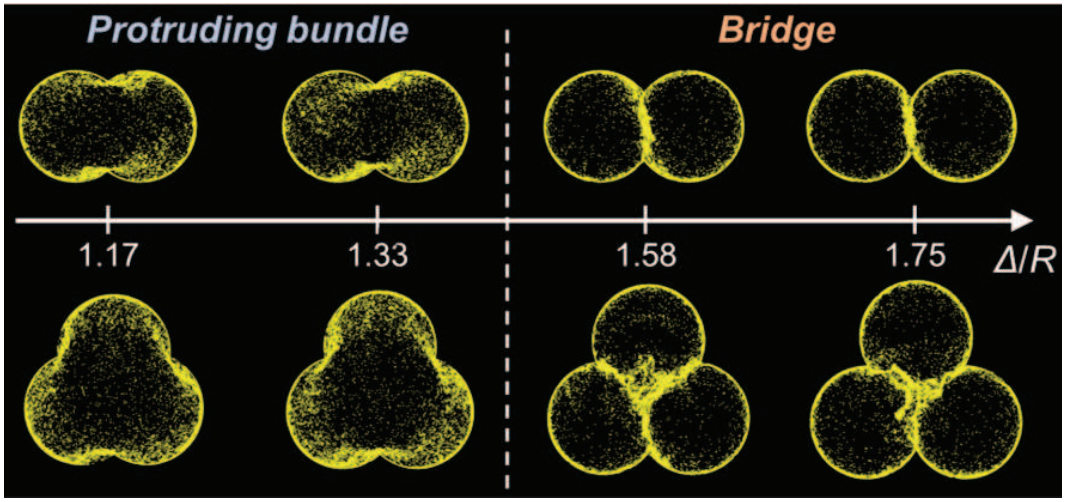

Figure 4.7: Numerical simulation of confined self-propelled rods, based on an agent-based model, with the boundary of either the doublet or triplet overlapping circles. The density of the particles is set to 1.54 particles/μm^2, and the other parameters are $R = 40\,\mu m$, $\gamma = 5.0\times10^{-2}$ s^{-1}, $\omega = 2.0\times10^{-3}$ s^{-1} and $D = 2.0\times10^{-3}$ s^{-1}.

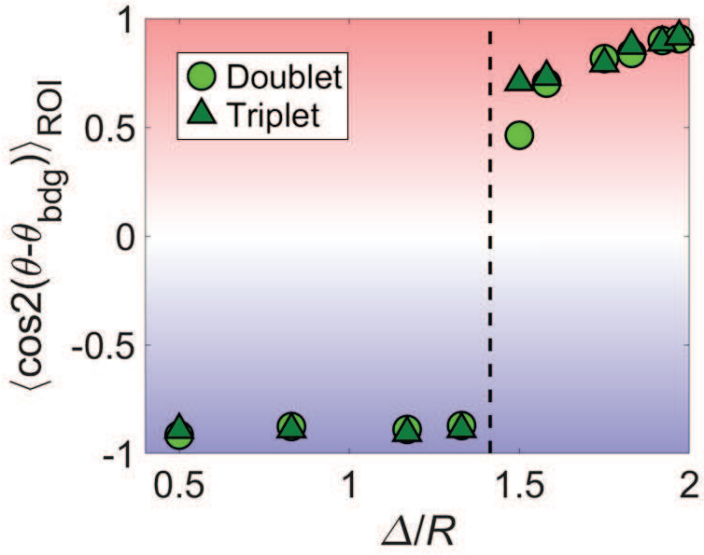

Figure 4.8: The order parameter of collective motion of confined self-propelled rods in doublet and triplet circular boundaries. The transition from protruding bundle pattern to bridge pattern occurs around $\Delta/R = 1.4$ for both doublet and triplet circular boundaries.

4.4.2 Theoretical analysis

In order to analytically obtain the transition point of two distinct patterns, we built a mean-field model for the orientational dynamics at a tip in the same way as our works reported in the previous chapters. Firstly, we neglect the dynamics of the rod's position and only consider the re-orientation determined by the interaction potential $U(\boldsymbol{r}_m, \theta_m)$ because we focus on how nematically preferred alignment configurations emerge on the basis of tip geometry in the steady state. The simplified orientational dynamics is described by

$$\dot{\theta}_m(t) = -\bar{\gamma}\frac{\partial U}{\partial \theta} + \eta_m(t), \tag{4.4}$$

where the nematic potential $U(\boldsymbol{r}_m, \theta_m)$ is given by

$$U(\boldsymbol{r}_m, \theta_m) = -\sum_{|\boldsymbol{r}_{mn}|<\epsilon} \cos 2(\theta_m - \theta_n). \tag{4.5}$$

The moving direction of rods around the tip is constrained in the tangential directions of the boundary wall, so that the self-propelled rods could have four possible directions $\pi/2 \pm \Psi$ and $-\pi/2 \pm \Psi$ before interactions. (Note that unlike FMV and AFMV pairing in ordered bacterial vortices, the symmetry of nematic interactions allows the coexistence of four different moving directions, leading to only one effective potential that can describe two distinct patterns.) By substituting these orientation angles into Eq. (4.5), we applied the mean-field approximation, yielding the effective potential $U(\theta; \Psi) = \frac{1}{2}\cos 2\theta \cos 2\Psi$. The resulting potential landscape illustrates that at a large Ψ the protruding bundle pattern is more preferred because the potential takes local minima at two angles, $\theta = 0$ and π, whereas at a small Ψ, the bridge pattern is more stable because the local minimum of the potential is shifted to $\theta = \pi/2$. The effective potential demonstrates that there is no preferential direction at $\Psi_c = \pi/4$, bringing the transition point between the protruding bundle and bridge patterns,

$$\frac{\Delta_c}{R} = 2\cos\Psi_c = \sqrt{2}, \tag{4.6}$$

which agrees with the experimental findings $\Delta_c/R \approx 1.3$-1.4. For a quantitative comparison with the experimental results, we analyzed the probability distribution function of the MT's orientation at the tip. In the same way as our previous work, we can obtain it from the Fokker-Planck equation as follows:

$$P(\theta;\Psi) = \frac{\exp\left(-\frac{\gamma}{2D}\cos 2\theta \cos 2\Psi\right)}{2\pi I_0\left(\frac{\gamma}{2D}\cos 2\Psi\right)}, \tag{4.7}$$

where $\bar{\gamma}$ is rewritten as $\gamma = \sum_{|\boldsymbol{r}_{mn}|<\epsilon} \bar{\gamma}$, and $I_0(\cdot)$ is the modified Bessel function of the first kind. The density distribution of MTs around the tip was measured by the fluorescent intensity distribution within a region of interest (a circular area of a radius $R/6$ around a tip), which corresponds to the theoretically predicted distribution of the orientation angle at each geometric condition (from $\Delta/R = 0.50$ to 1.97). Here, the strength of nematic interactions can be estimated to $\gamma = 1.9\times10^{-2}$ s^{-1} by fitting the expected value of $\cos(\theta - \theta_{bdg})$, calculated from the theory (Eq. (4.7)), to the geometry-dependent order parameter of the bridge pattern in the experiment (Fig. 4.6). Note that the angular fluctuation $D = 5.2\times10^{-3}$ s^{-1} was measured from mean square angular displacement in the independent experiment (Fig. 4.10). This good agreement implies that the global aligned structures of the confined self-propelled MTs can be controlled by local nematic alignments based on the geometrical boundary.

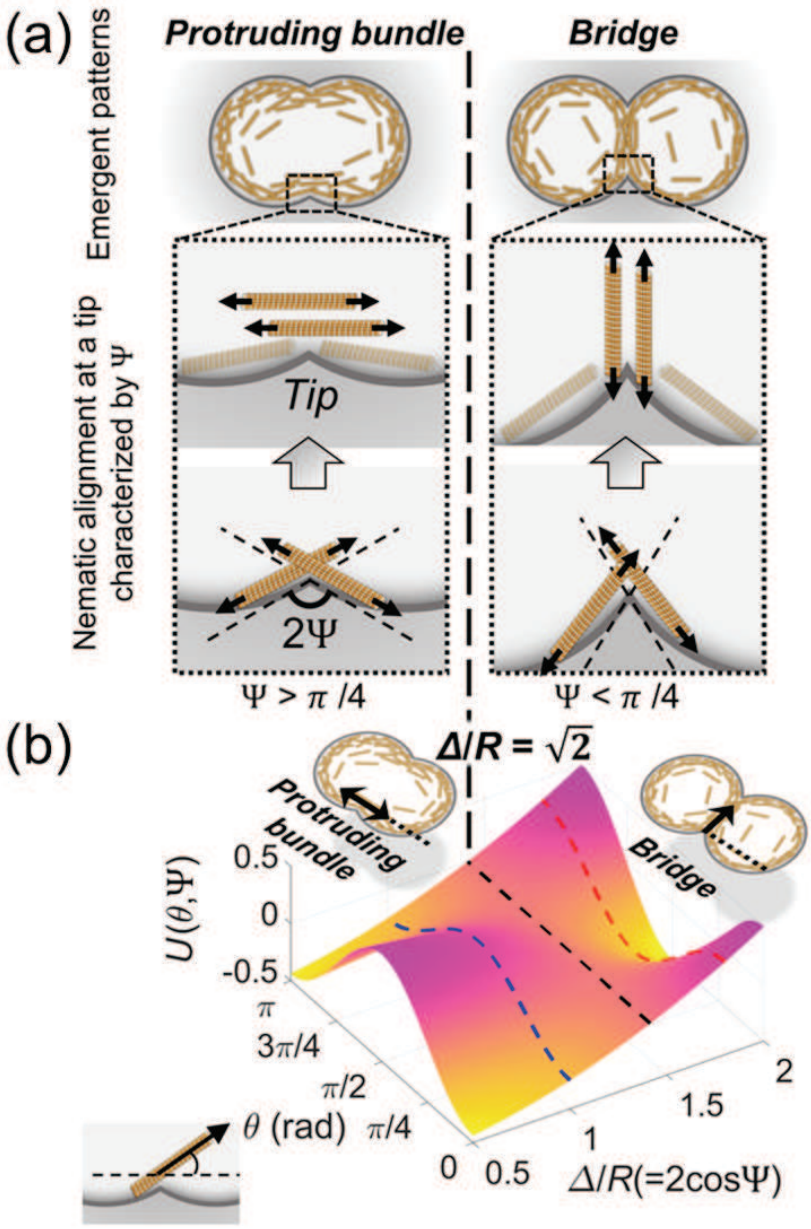

Figure 4.9: (a) Orientation interactions of MTs at a tip and their geometric dependence in the formation of (left) protruding bundle pattern and (right) bridge pattern. The transition of two patterns occurs at the angle of the tip at which 2Ψ is equal to $\pi/2$. (b) The potential landscape of the orientation interactions depending on the geometry. The potential of the nematic orientation interactions between the rods was calculated for each geometrical parameter Δ/R and an orientation angle θ. A higher potential (red) indicates a lower probability of the rod heading the corresponding orientation angle for a given geometric parameter. A lower potential (yellow) indicates a higher probability of the rod heading the corresponding orientation angle.

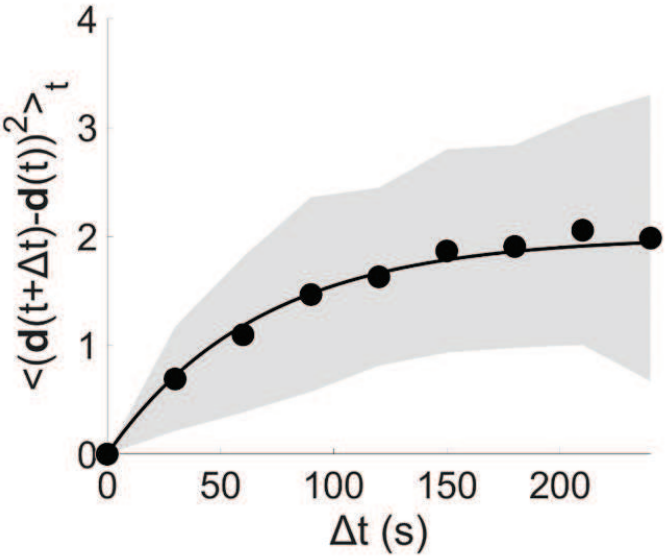

Figure 4.10: The mean square angular displacement (MSAD) of the orientation angle of motile MTs. The MSAD curve is fitted with $2(1-\exp[-D\Delta t])$, where D corresponds to the orientation fluctuation.

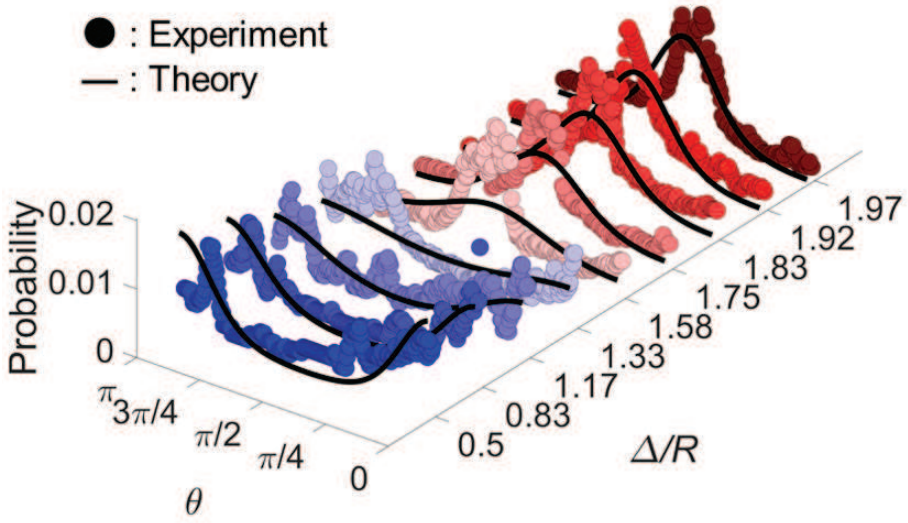

Figure 4.11: Comparison of the theoretical calculation and the experimental result for the geometrical dependence of the rod orientation angle. The number density of oriented MTs is acquired based on their fluorescence intensity around the tip.

It is worth discussing the effect of chirality on the transition point from the protruding bundle pattern to the bridge pattern. The existence of chirality in

motile MTs has been reported in Refs. [23, 107, 108], which is considered to contribute to the formation of the chiral protrusion pattern in either direction. We here considered the orientational dynamics including the intrinsic chirality, that is, the constant angular velocity ω:

$$\dot{\theta}_m = -\bar{\gamma}\frac{\partial U}{\partial \theta} + \omega + \eta_m(t). \tag{4.8}$$

We applied the same procedure as the previous mean-field approach to Eq. (4.8). Taking the alignment at a tip into account, the orientational dynamics is rewritten by

$$\dot{\theta}_m = -\gamma \sin 2\theta_m \cos 2\Psi + \omega + \eta_m(t), \tag{4.9}$$

and the Fokker-Planck equation is given by the following equation:

$$\frac{\partial P}{\partial t} = D\frac{\partial^2 P}{\partial \theta^2} + \gamma\frac{\partial}{\partial \theta}\left[\left(\sin 2\theta \cos 2\Psi - \frac{\omega}{\gamma}\right)P\right]. \tag{4.10}$$

By solving Eq. (4.10) under the steady state condition ($\frac{\partial P}{\partial t} = 0$), we obtain the probability distribution of rod's orientation, $P(\theta;\Psi)$, as follows:

$$P(\theta;\Psi) = \frac{\exp\left(-\frac{\gamma}{2D}\left[\cos 2\theta \cos 2\Psi - \frac{2\omega}{\gamma}\theta\right]\right)}{2\pi I_0(\frac{\gamma}{2D}\cos 2\Psi)}. \tag{4.11}$$

From the above description, we obtain an effective potential including chirality, $U(\theta,\Psi) = \frac{1}{2}\cos 2\theta \cos 2\Psi - \frac{\omega}{\gamma}\theta$. The transition point can be derived from $U(\theta = 0, \Psi_c) = U(\theta = \pi/2, \Psi_c)$, yielding

$$\begin{aligned} \cos 2\Psi_c &= -\cos 2\Psi_c - \frac{\pi\omega}{\gamma}, \\ 2\cos^2 \Psi_c &= 1 - \frac{\pi\omega}{2\gamma}, \\ \Delta_c/R &= \sqrt{2(1 - \frac{\pi\omega}{2\gamma})}. \end{aligned} \tag{4.12}$$

The obtained transition point is drawn in Fig. 4.12, which indicates that the bridge formation can be enhanced by chiral motions of MTs, as compared to the

case in the absence of chirality. The experimental value of the angular velocity was $\omega = +1.1\times10^{-3}$ s^{-1}, obtained from the measurement of the mean angular velocity of labeled MTs in unconfined dense MTs, but the resulting shift of the transition point ω/γ is approximately 0.1, which has only a negligible effect on the pattern transition of self-propelled microtubules. Thus, the geometric rule of two patterns $\Delta_c/R \approx 1.4$ still holds in the presence of slight chirality.

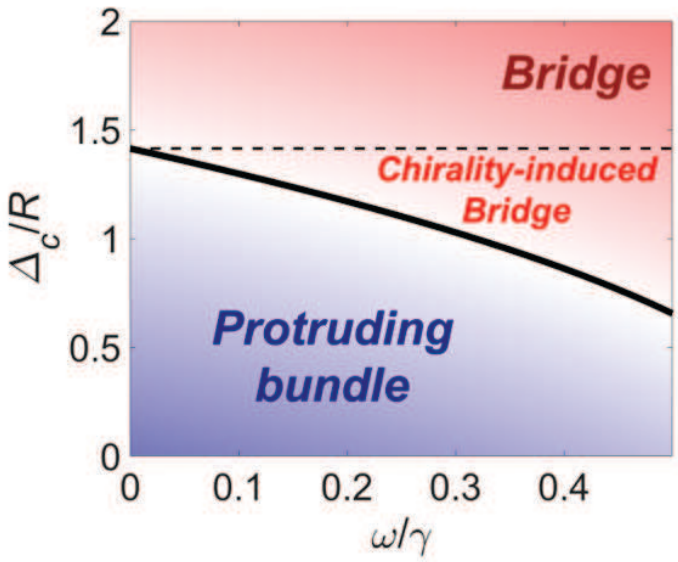

Figure 4.12: Phase diagram of protruding bundle and bridge patterns under the effect of chiral motion. The phase boundary is plotted with $\Delta_c/R = \sqrt{2(1-\frac{\pi\omega}{2\gamma})}$ as a function of angular speed of the chiral self-propelled rod. The strong chirality can shift the transition point.

4.5 Compartmentalization in channels by bundled patterns

Our findings demonstrate that the collective motions of confined motile MTs can be controlled by tuning the collision angle by designed boundaries. Indeed, ordered cytoskeletal structures can be seen in compartments, ranging from the contractile FtsZ cytoskeleton involved in the division of rod-shaped bacteria [111] to the cell plate during plant cell division [109]. To investigate the link between our findings and biological systems, we performed the experiment using microchannels with tiny tip-like obstacles attached to the wall. The microchannel has a width of 60 µm, triangle-shaped obstacles of 20 µm placed at regular intervals of 200 µm with the apex angle of this obstacle 2Ψ ranging from 0.11π to π (corresponding to $\Delta/R = 0$ to 1.97). As a result, a bridge pattern was formed in the regime of $0.18\pi < 2\Psi < 0.42\pi$, whereas a protruding bundle pattern extending in the transverse direction was observed under $0.54\pi < 2\Psi < \pi$. At collision angles of $2\Psi < 0.5\pi$, the formed bridge structures compartmentalize the microchannels, which creates the cytoskeletal structures like living cells. On the other hand, at collision angles of $2\Psi > 0.5\pi$, protruding bundles are aligned parallel to the long axis of microchannels. Hence, the collision angle constrained by the local geometrical structure like a tip can determine the transition from the laterally aligned bundled structure to the bridge one partitioning the compartments.

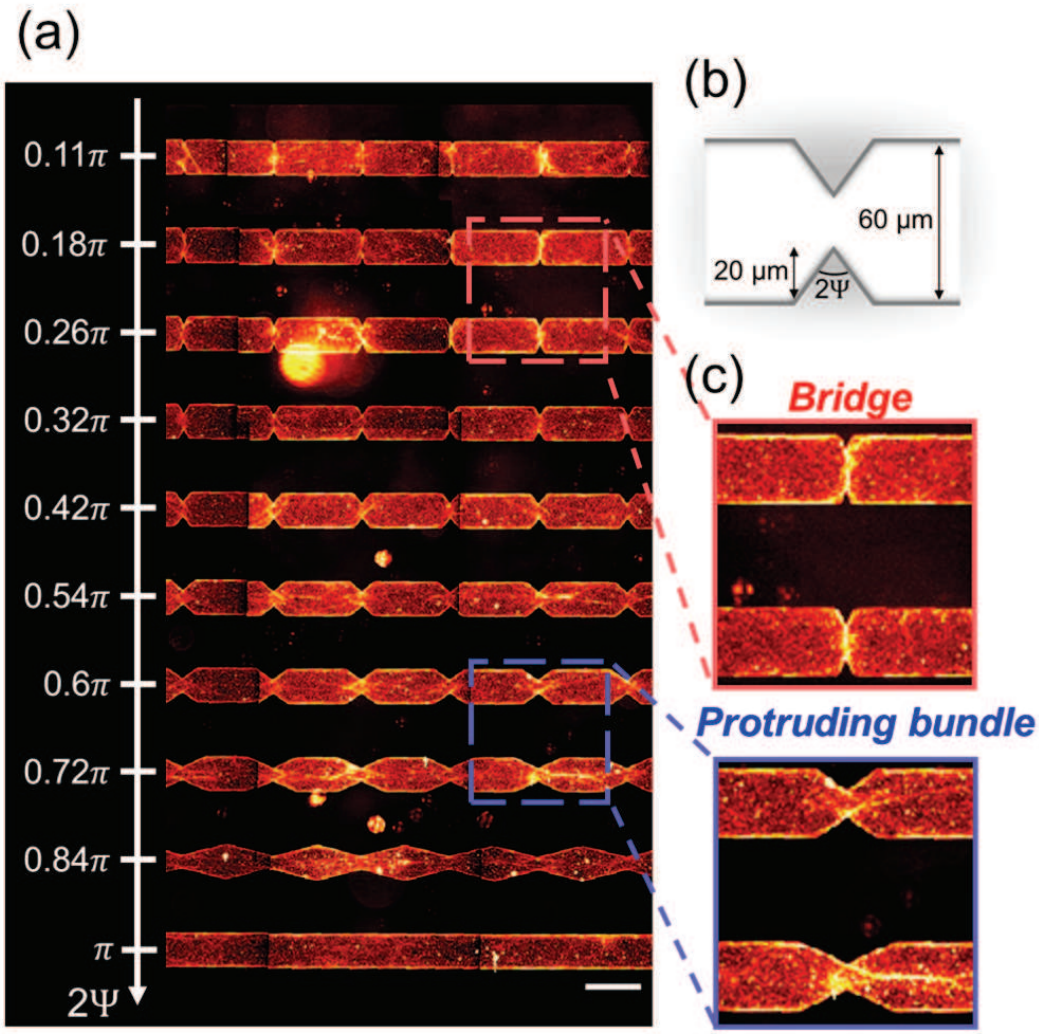

Figure 4.13: Partitioning of microcompartments by geometrically controlled MT bundles. (a) The protruding bundle pattern and the bridge pattern in designed microchannels with tips. The scale bar, 100 μm. (b) The geometry of designed microchannels. (c) Zoom of the protruding bundle and bridge patterns. The bridge patterns appear up to $2\Psi = 0.26\pi$, and the protruding bundle patterns appear along the channel from $2\Psi = 0.54\pi$ to 0.84π.

4.6 Summary of Chapter 4

We studied a geometric control of the pattern formations of self-propelled MTs using the doublet and triplet circular PDMS microwells defined by a radius of circle R and a distance between circles Δ. We found two distinct aligned bundle patterns in a geometry-dependent manner: a protruding bundle pattern and a bridge pattern. Importantly, they can be controlled by a single geometric parameter Δ/R, and we discovered that the transition between two patterns occurs around $\Delta_c/R = 1.4$. Furthermore, our mean-field theory based on the self-propelled rod model accounted for the transition point $\Delta_c/R = \sqrt{2}$, that is, a dimensionless geometric rule that would allow for the size-independent control of collective behaviors. As predicted in our theoretical model including intrinsic chirality, the chirality of motile MTs may induce the protruding bundle tilted towards the other tip, which may facilitate the formation of a bridge pattern. The experimental verification remains a challenge, which could be verified by means of microtubules (GMPCPP-MTs) that are known to reflect strong chirality in their motion [23,107,108]. Our findings would provide a blueprint for the programmable collection of a broad class of active matter, from cytoskeletons [2,110] to nanoparticles with chirality [97, 112, 113].

Chapter 5

Future perspective: frustrated vortices

One of the important residual issues is to clarify the effect of geometrical frustration on the collective motions in active matter systems. As reported in the previous chapters, the ordered vortices of swimming bacteria confined in the doublet (or quadruplet) circular boundary can be governed by the geometric rules: $\Delta/R = \sqrt{2}$ without chirality effect and $\Delta/R = \sqrt{2}(1+\gamma_e/(2\gamma_p))$ with chirality effect. However, if three bacterial vortices anti-ferromagnetically interact, frustration should be generated. Intriguingly, it has been reported that a dense bacterial suspension confined in a triangular lattice exhibits a highly ordered ferromagnetic state (Fig. 5.2 (a)) [68]. As for the active nematics, the dynamic change of collective flows in the rotational direction has been found in the mixture of microtubules and motor proteins confined in a triplet annular pattern due to the accumulation of the frustration (Fig. 5.2 (b)) [112]. Furthermore, the recent theoretical works have reported that polar active matter shows topologically protected sound modes in the presence of periodic structures with kagome lattice geometry (Fig. 5.2 (c)) [98] and that the symmetry breaking of turbulent vortices in active turbulence occurs to avoid the frustration (Fig. 5.2 (d)) [71]. Although geometric frustrations play an important role in macroscopic collective motions, geometric rules hidden in frustrated active matter systems remain uncharted. In this chapter, we introduce

the preliminary experimental results and the numerical work.

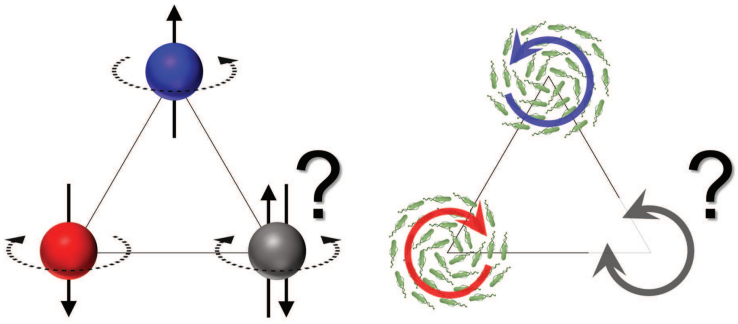

Figure 5.1: Correspondence of spins and bacterial vortices and frustration.

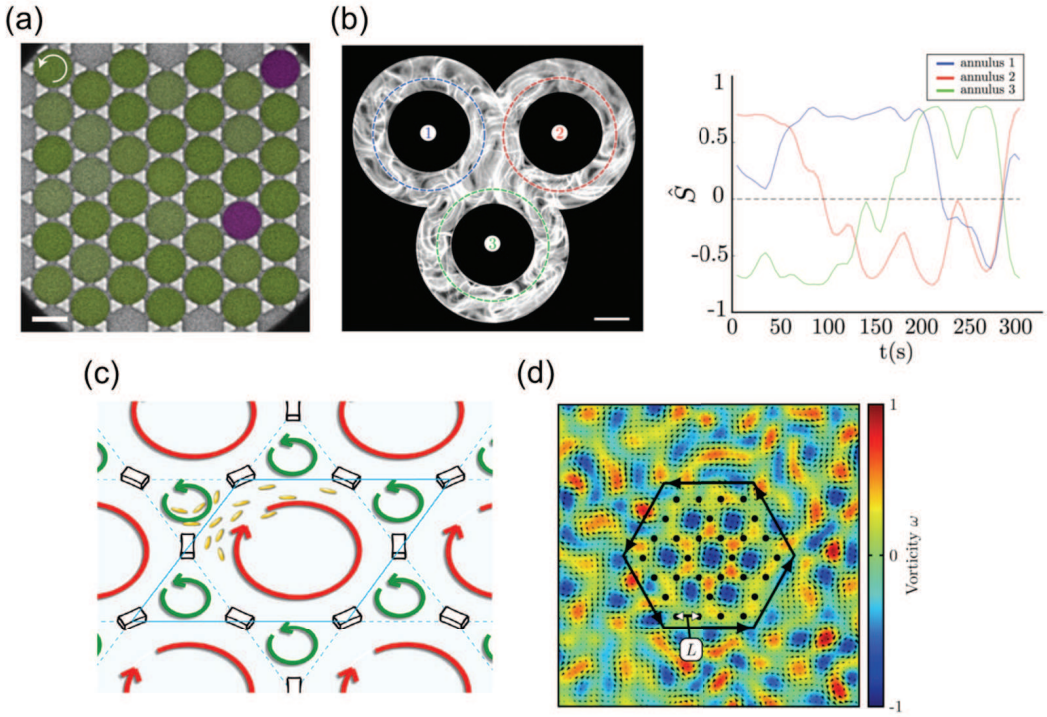

Figure 5.2: Frustration and active matter systems. (a) Ferromagnetic order of a dense *B. subtilis* suspension confined in a triangular lattice. The image is adapted from Ref. [68]. (b) A mixture of microtubules and kinesin motors confined in a triplet annular channel (left) and flow order parameter $\hat{S}$ against time for each annulus (right). $\hat{S} = 1$ (or $\hat{S} = -1$) denotes an ideal CW (or CCW) transport current. Images are adapted from Ref. [112]. (c) Toner-Tu fluids under periodic structures with kagome lattice geometry. The image is adapted from Ref. [98]. (d) Active turbulence under circular pillars' spacing of kagome lattice, simulated based on the TTSH equation. The image is adapted from Ref. [71].

5.1 Vortex pairing order in triplet circular microwells

To investigate emergent patterns in a triplet boundary comprising three overlapping circles, we confined a dense bacterial suspension in triplet circular microwells, defined by a radius of circles and a distance between circles (Fig. 5.3), with the symmetric (PDMS/PDMS) interfaces. Fig. 5.4 (a) represents the arrays of vorticity and velocity analyzed inside a microwell. For the symmetric condition, i.e., in the absence of a chiral edge current, FMV and the coexistence of FNV and AFMV, named frustrated AFMV, were observed in a geometry-dependent manner. Moreover, the FMV pairing was more favored than that in the doublet (or quadruplet) circular microwells, which is consistent with the previous work [68]. To quantify the pairing order transition, we defined an order parameter of coherent flows along the boundary as an average of a velocity component tangential to the boundary normalized by the magnitude of the velocity. Fig. 5.4 (c) shows representatives of FMV and frustrated AFMV mapped by the local normalized velocity tangential to the triplet boundary. The order parameter averaged over the space and the observation time (10 s) is plotted as a function of the geometric parameter Δ/R in Fig. 5.4 (d). The co-rotational order was highly maintained until $\Delta/R = 1.58$, while it sharply changed to the frustrated AFMV around $\Delta/R = 1.7$.

As shown in the previous chapter, the chiral edge current is also able to enhance FMV patterns. To assess the vortex pairing in the presence of both edge currents and geometric frustration, we confined the dense bacterial suspension in a triplet microwell with the asymmetric (oil/PDMS) interfaces (Fig. 5.4 (b)). The transition to the frustrated AFMV was found around $\Delta/R = 1.9$, implying that the cooperation of the geometric frustration and the chiral edge current makes FMV pairing more stable. The geometric rule including the geometric frustration and the chirality effect remains an open question, but the understanding of geometric features of chiral polar fluids would give a new insight into controlling various collective ordering.

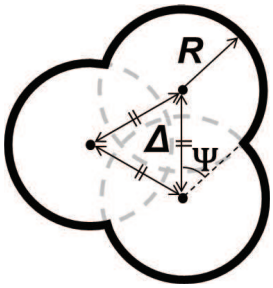

Figure 5.3: Geometry of a triplet circular boundary.

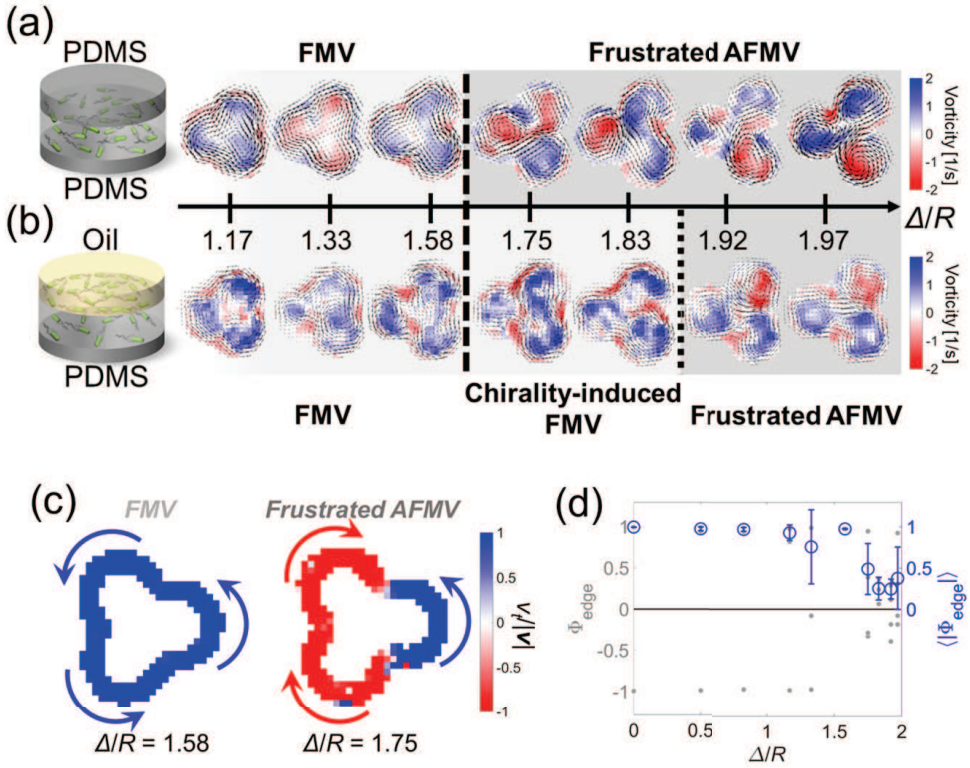

Figure 5.4: The transition from FMV to frustrated AFMV under different conditions of interfaces. (a) and (b) show representative data of vorticity maps at various Δ with $R = 19\,\mu\text{m}$ and $h = 20\,\mu\text{m}$ under the top/bottom symmetric interfaces and the asymmetric interfaces, respectively. The density of bacteria is 20%v/v. (c) Representative data mapping velocity components tangential to the boundary wall normalized by the magnitude of velocity within an edge layer $10\,\mu\text{m}$ for $\Delta/R = 1.58$ and $\Delta/R = 1.75$. (d) Geometry dependence of order parameter defined as the spatiotemporal average of normalized tangential velocity in (c). The left axis includes the information on the rotational direction of flows near the boundary. The right axis denotes its absolute value. Data acquired under top/bottom symmetric conditions are used in (c) and (d).

5.2 Simulation based on a simple Toner-Tu model

We sought the reason why the transition from FMV to frustrated AFMV occurs not at $\Delta/R = 1.4$ but $\Delta/R = 1.7$. Because our mean-field model based on the Vicsek model alone cannot account for the transition point $\Delta_c/R \sim 1.7$, we considered the effect of not only polar interactions at a tip but also behavior in the bulk. We here simulated the simplified Toner-Tu model that corresponds to the continuum theory of the Vicsek model in the following [21, 71, 98]:

$$(\partial_t + \lambda_0 \boldsymbol{v} \cdot \nabla)\boldsymbol{v} = \alpha \boldsymbol{v} - \beta |\boldsymbol{v}|^2 \boldsymbol{v} - \nabla(P - \lambda_1 |\boldsymbol{v}|^2) + D_T \nabla^2 \boldsymbol{v} - \gamma_v M(\boldsymbol{r})\boldsymbol{v}, \quad (5.1)$$

where $M(\boldsymbol{r})$ denotes a mask to impose a boundary condition on the Toner-Tu fluid such that an inside of boundary is assigned as 0, and hence the term $-M(\boldsymbol{r})\boldsymbol{v}$ with the coefficient γ_v damps the velocity field outside the confinement. In this model, we postulate uniform density and incompressibility due to sufficiently high density of bacteria. Therefore, the equation of the density field and some terms including divergence of velocity in Eq. (1.24) are neglected. Note that since the higher-order term $D_2(\boldsymbol{v} \cdot \nabla)^2 \boldsymbol{v}$ in Eq. (1.24) did not significantly change results in our simulation, we neglect it for simplicity.

5.2.1 Numerical method

To simulate the above model, we used a pseudo-spectral algorithm and a vorticity method, employed in Refs. [39, 71]. The system size and the number of meshes are set to $L = 64$ and $N = 128$, respectively. Simulations were performed with the following parameter set: $\lambda_0 = 1, \alpha = 0.2, \beta = 0.3, D_T = 0.35$, and $\gamma_v = 40$. Time steps were $\delta t = 0.005$, and the total number of time steps was $T = 30000$, at which the system is almost regarded as the steady state. Snapshots in Fig. 5.5 were acquired from data at the endpoint of simulations. The integration was conducted with the second-order Runge-Kutta methods. Simulations were initiated with randomly chosen flow fields. Masks were set by a step function that is 0 for the inside of a boundary and 1 for its outside.

5.2.2 Geometry dependence of confined Toner-Tu fluids

We first tested whether this model reproduces the experimental result regarding the pairing order transition in doublet circular boundaries. The Toner-Tu fluids confined in doublet circular boundaries exhibited the paring order transition similar to the experiment (Fig. 5.5 (a)). The AFMV pairing appeared above $\Delta/R = 1.4$, which is consistent with the experiment and our mean-field model of the Vicsek model. Even though flow configurations in a doublet circular boundary with larger than $\Delta/R = 1.4$ are initially biased to the FMV paring, the pattern changes to the AFMV pairing owing to its instability (Fig. 5.6 (a)). We then imposed triplet circular confinements on the Toner-Tu fluids. As a result, a frustrated AFMV was observed at $\Delta/R = 1.8 \sim 1.9$, larger than that of doublet circular boundaries, while below it, a single large vortex emerged around the center of triplet circles (Fig. 5.5 (b)). This is also similar to the experiment, although the transition point seems to be slightly different. Interestingly, at a small Δ/R, e.g., $\Delta/R = 1.75$, vortices initially positioned at each circle changed to a single vortex and were eventually centered, whereas at $\Delta/R = 1.92$, vortices positioned at each circle were static (Fig. 5.6 (b)).

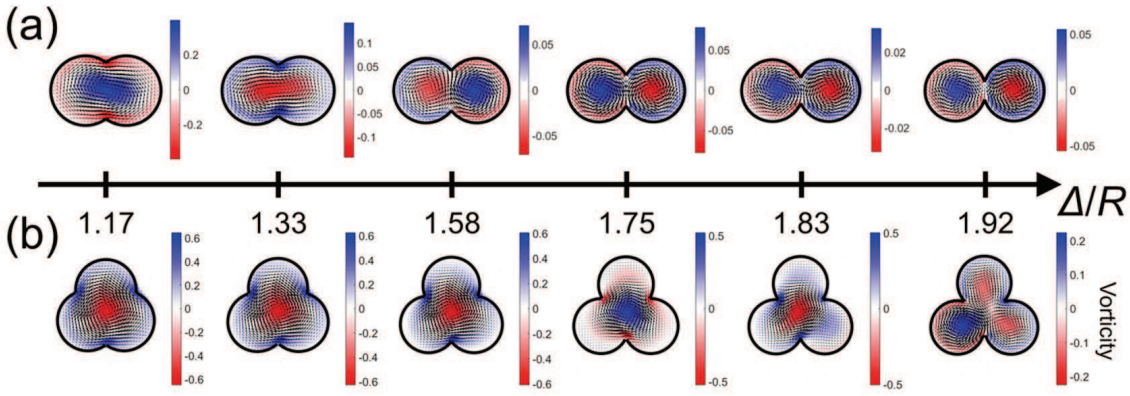

Figure 5.5: Geometry dependence of Toner-Tu fluids confined in doublet (a) and triplet (b) circular boundaries. Vorticity maps with velocity fields are displayed against various Δ/R.

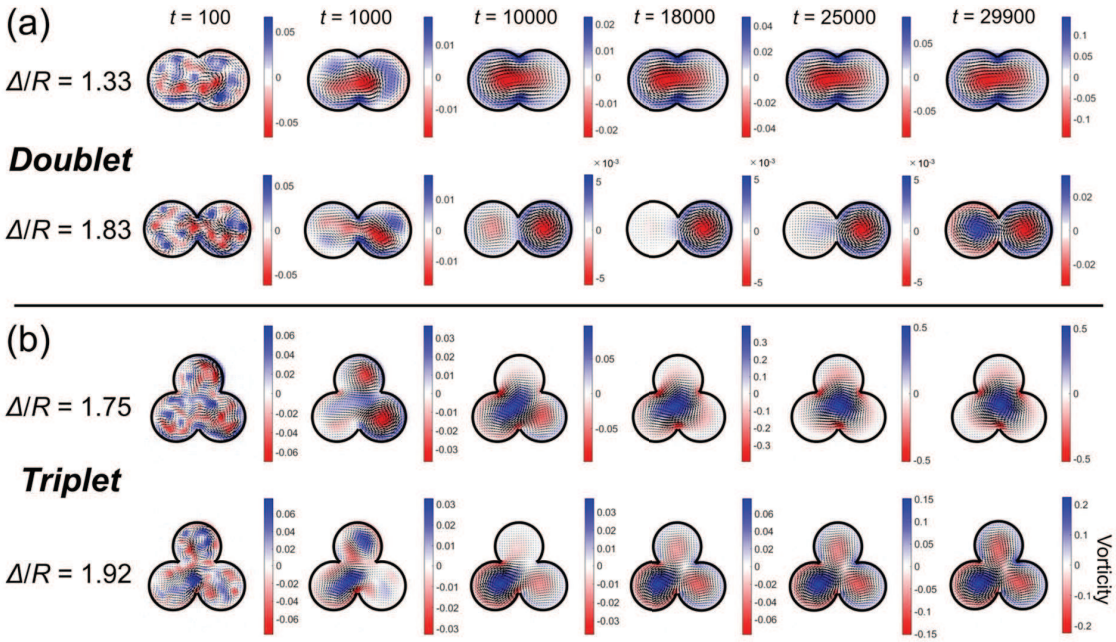

Figure 5.6: Dynamics of confined Toner-Tu fluids. Arrays show time series of vorticity maps with velocity field of representative data for both doublet (a) and triplet (b) circular boundaries.

From this observation, we speculate the transition mechanism on the basis of the triplet geometry. The key notion is vortex positioning at either a bulk region (around the center) or each circle of triplet, which could be determined by the penalty of flow distortions, exerted by the viscosity term $D_T\nabla^2\boldsymbol{v}$. When Δ/R is small, a single vortex is likely to emerge such that the penalty is minimized since the bulk area with a radius R_c is larger than each circle with a radius R. On the other hand, when R_c goes below R (at a large Δ/R), three vortices are likely to be stabilized at each circle rather than the bulk region. This transition could occur at $R_c = R$ where R_c can be written as $R_c = R(\sin(\frac{\pi}{6}) + \sin\Psi)$. This reads

$$\begin{aligned} \sin(\frac{\pi}{6}) + \sin\Psi_c &= 1, \\ \Psi_c &= \frac{\pi}{6}, \\ \Delta_c/R = 2\cos(\frac{\pi}{6}) &= \sqrt{3}, \end{aligned} \tag{5.2}$$

yielding the geometric rule in three interacting vortices (Fig. 5.7). These results

suggest that the concept of vortex positioning may open a new route to understand the underlying mechanism of multiple active vortices including frustrated vortices and give an insight into more general geometric rules in active turbulence.

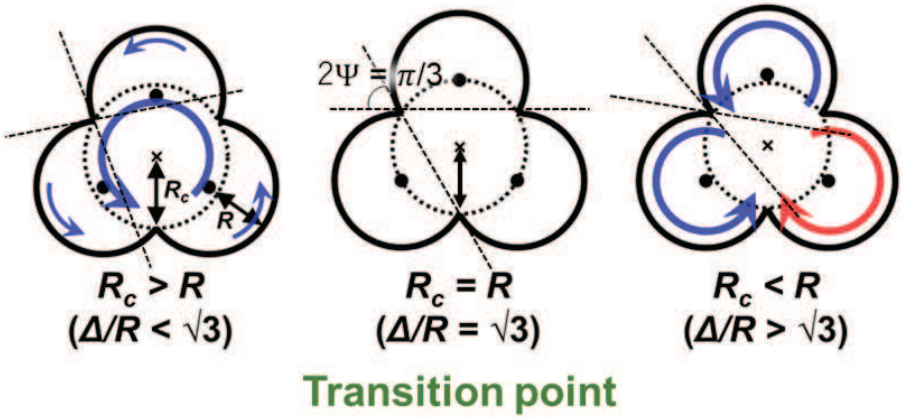

Figure 5.7: Speculation for pairing order transition in a triplet circular boundary. To characterize area of bulk, R_c is defined as a distance between a centroid of triplet circles and a tip: $R_c = R(\sin(\frac{\pi}{6}) + \sin\Psi)$. For $R_c > R$, a vortex is likely to form at the center region rather than at each circle, while for $R_c > R$, three vortices are likely to emerge at each circle due to the narrow space in the bulk. In this sense, at $R_c = R$, i.e., $\Delta/R = \sqrt{3}$, emergent vortices no longer have any preference between each circle and the center area, which could lead to the transition point.

Chapter 6

Conclusion and outlook

In conclusion, geometrically controlling active matter systems have unveiled geometric features of constituent ordered vortices hidden in the chaotic behavior of active turbulence. By simply focusing on two physical quantities of ordered vortices: a radius of vortex R and a distance between vortices Δ, and designing a boundary with our microfabrication technology, we found that two distinct patterns of vortex pairing, ferromagnetic vortices (FMV) and anti-ferromagnetic ones (AFMV), arise in doublet circular microwells in a geometry dependent manner. The transition from FMV to AFMV occurred around $\Delta/R = 1.4$. Applying the mean-field approximation to the Vicsek model of self-propelled particles with polar interactions, the polar alignment at a tip where two vortices collide was found to prefer either FMV or AFMV depending on geometry. This can be understood by the argument of the potentials obtained for each pairing. Given that a state with lower potential is realized, the minimum value between them switches at $\Delta/R = \sqrt{2}$ where the probabilities of FMV and AFMV coincide (Fig. 6.1 (a)). This perfect agreement between the experiment and the theoretical model highlights the presence of geometric rule in ordered vortices inherent in active turbulence.

We further investigated the role of chirality in active turbulence, which has been overlooked. We newly developed a well-controlled experimental system where the intrinsic chirality of bacterial swimming is simply induced by the presence of

asymmetric interfaces. In this system, we discovered a chiral bacterial vortex and a chiral edge current. The found chiral edge current stabilized FMV pairing order, leading to the shift of the transition point. The mean-field model including alignment by a chiral edge current gives effective potentials for both FMV and AFMV. The resulting potential landscape indicates the transition point $\Delta/R = 1.8 \sim 1.9$, consistent with the experiment, indicating the extended geometric rule in chiral vortices (Fig. 6.1 (b)).

We finally explored a geometric rule in active cytoskeletons that interact with the others in a nematic-alignment manner. In this system, assembly of gliding microtubules confined in microwells characterized by Δ/R formed two distinct bundled structures: a (laterally extending) protruding bundle pattern and a bridge pattern. Remarkably, these patterns were also found to be ruled by $\Delta/R = \sqrt{2}$, which can be analytically obtained by the mean-field SPR model (Fig. 6.1 (c)). Despite the different symmetry of interactions from bacteria, the common geometric rule was found, which may provide an insight into the understanding of geometric universality across a broad class of active matter systems.

Classification of phase transitions in collective behaviors is one of the important challenges in active matter physics. Fig. 6.1 reports that pairing or alignment order can be governed by the common rule despite different symmetries of individuals, but transition behaviors between them are expected to be different. For polar interactions, only either of two states is allowed even at the transition point, whereas for nematic interactions, resulting aligned configurations have no preference in any directions at the transition point. This may imply the presence of different mechanisms such as first-order and second-order phase transitions. The experimental demonstration could be future work.

One of the critical issues in active matter physics is that too many parameters prevent us from quantitatively evaluating phenomena and building a unified theory. Thus, our geometric approach is an elaborate tool to derive a macroscopic parameter (e.g., the relaxation of re-orientation) from a probability distribution in an equilibrium state and a microscopic fluctuation, akin to the fluctuation-dissipation theorem. Moreover, the discovery of geometric universality might help

us to seek unified descriptions like free energy independent of details of systems. Indeed, the transition of type I and type II of a superconductor is determined by the dimensionless ratio of the penetration depth λ and the coherence length ξ that correspond to characteristic length scales in vortex lattice induced by a magnetic field, $\lambda/\xi = 1/\sqrt{2}$, which can be derived from the Ginzburg-Landau free energy. In analogy to it, the ratio of two length scales in ordered vortices, Δ/R, may hint at universality, which could be an important challenge ranging from biological physics to classical condensed matter physics.

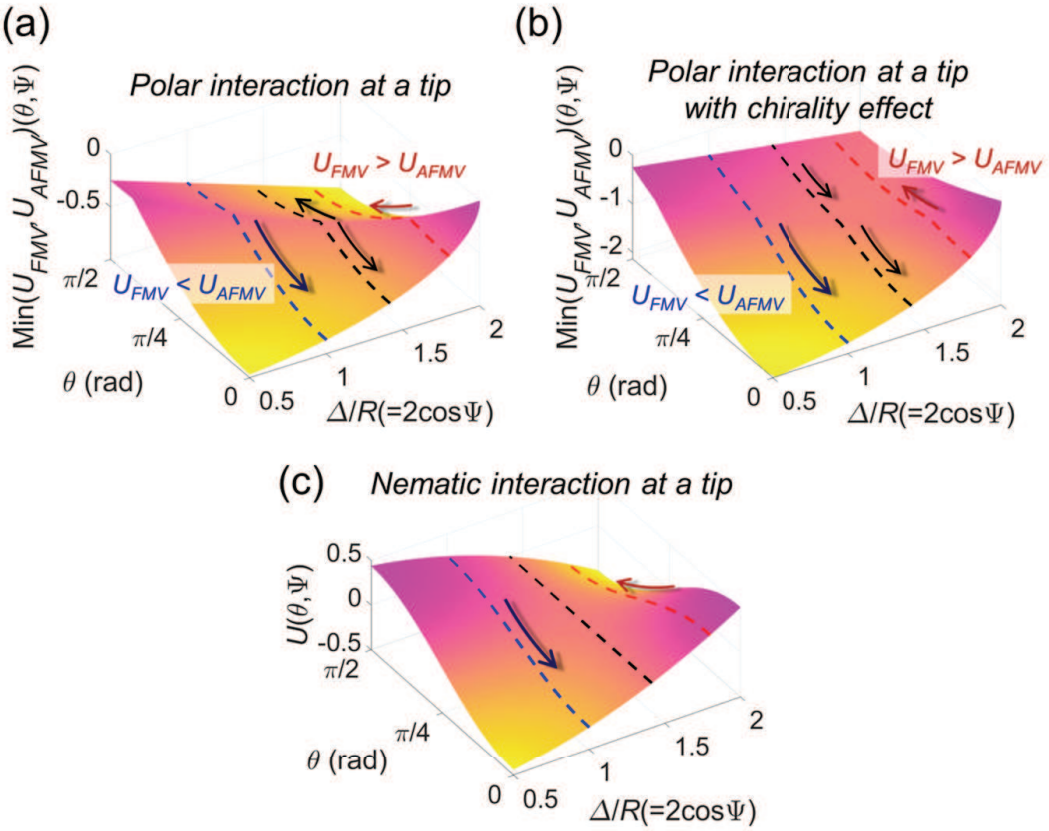

Figure 6.1: Geometric potential landscapes that govern active ordering. (a) Potential landscape obtained by taking a minimum value of either FMV or AFMV pairing potential. (b) Potential landscape including the effect of chiral edge currents. (c) The landscape of the effective nematic potential at a tip.

Appendix A

Preparation of bacterial suspensions

RP4979 strain

In our research, we use an RP4979 strain of *E. coli* which is a mutant showing smooth swimming without tumbling. Wild-type *E. coli* bacteria are able to perform chemotaxis, which is the movement in response to a chemical stimulus, by sensing attractant with chemotactic receptors on a cell membrane. In response to a decrease of attractant concentration, the chemoreceptors promote phosphorylation of the binding histidine protein kinase, CheA, and the phosphorylated CheA (CheA-P) phosphorylates its cognate response regulator, CheY. Once the phosphorylated CheY (CheY-P) diffuses inside the cell and binds to the flagellar motor, a switch in the rotational direction from CCW to CW is promoted, which causes a tumbling. As the chemoreceptor senses an attractant, CheA is deactivated and CheY-P decreases. Accordingly, the flagellar rotation in the CCW direction causes the bacteria to swim in a straight line. This is how *E. coli* bacteria perform chemotaxis, that is, a swimming behavior while stochastically changing its direction depending on attractant concentration in the surrounding environment (Fig. 6.2) [114]. Since the *E. coli* RP4979 strain, on the other hand, is a mutant lacking CheY, the tumbling does not occur, resulting in the smooth swimming without any stochastic changes in the direction.

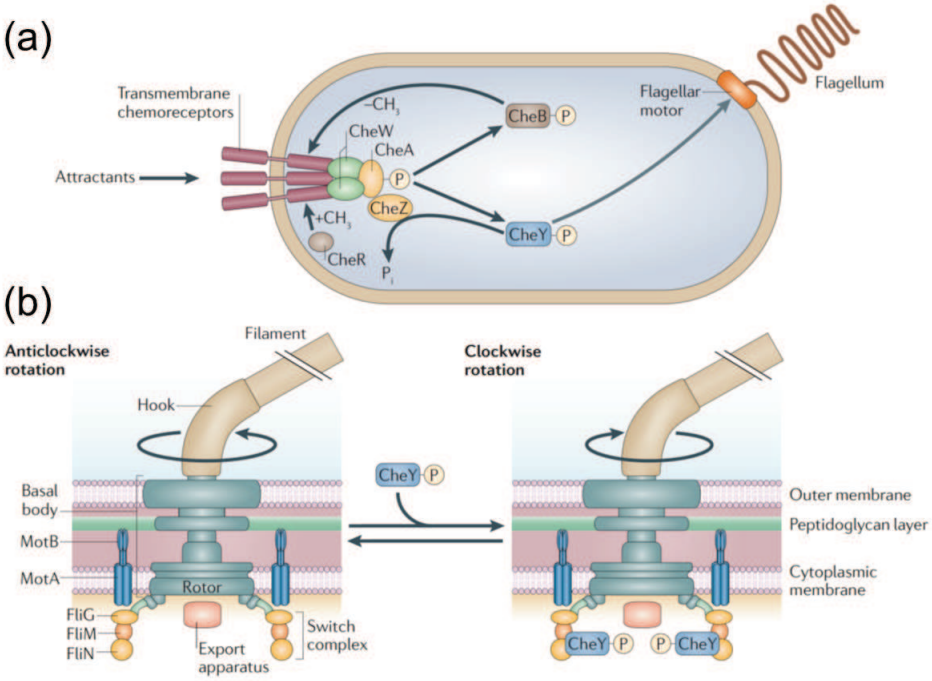

Figure 6.2: Chemotaxis pathway of *E. coli*. (a) Schematic illustration of the response transmission from a chemoreceptor to a flagellar motor. (b) Schematic illustration of the process of a switch in the rotational direction of the flagellar motor by the phosphorylated CheY (CheY-P). The image is adapted from Ref. [114]

Culture of *E. coli*

Here, we explain methods of culturing *E. coli* bacterial suspensions and making dense one. The *E. coli* RP4979 strain we use is genetically transformed by Plasmid DNA with antibiotic resistance gene and hence resistant to chloramphenicol (NACALAI TESQUE, INC., $C_{11}H_{12}Cl_2N_2O_5$) which is a protein synthesis inhibitor (antibiotic drug). Therefore, adding it into the culture medium or its agar plate can prevent contaminations of other unwanted bacteria. To measure the bacterial density, we use a strain that expresses yellow fluorescent proteins (YFP, excitation wavelength: 514 nm, fluorescent wavelength: 527 nm). To track individual motions of bacteria in a dense bacterial suspension, a strain that expresses red fluorescent proteins (dTomato, excitation wavelength: 554 nm, fluorescent wavelength: 581 nm) is also used. The bacterial colonies forming spores are stored on an agar plate of Luria-Bertani (LB) medium in a refrigerator at 4 °C.

Overnight culture

Overnight culture is made as follows. A single colony picked up from the stored agar plate with a sterilized micropipette is inoculated into an LB medium of 1 mL poured into a culture tube, and then the inoculated culture tube is shaken at 150 rpm overnight (12 hours) with a shaker (AS ONE, NEO SHAKER, NS LR) in an incubator (SANYO MIR-153) at 37 °C. The making of overnight culture is the first phase to activate bacteria in the spore state.

TB medium

In the second phase, we use a Terrific Broth (TB) medium that can cultivate *E. coli* activated above and enhance bacterial motility by having their flagella grown. We add the overnight culture of 100 µL into a TB medium of 20 mL in an Erlenmeyer flask (200 mL). We further prepare such bacterial suspensions of 50 mL with the same ratio and shake them at 150 rpm for 6 hours with a shaker (AS ONE, NEO SHAKER, NS LR) in an incubator (SANYO MIR-153) at 30 °C.

Measurement of optical density

To check the bacterial density in the incubated suspension, we measure OD (optical density) 600 using a microphotometer (Eppendorf Biophotometer). OD 600 indicates an optical density of a sample which is measured from the difference in the amount of light transmission (wavelength, 600 nm) for each target sample and its blank counterpart. In order to make a dense bacterial suspension with a volume fraction of more than 20 % at which collective motions can be observed, we set the above incubation time (6 h) that results in $0.4 \sim 0.5$ in OD.

Dense bacterial suspension

To make a dense bacterial suspension, we transfer the culture with about 0.4 into a conical tube (50 mL) and centrifuge it at 3000 rpm for 10 minutes. After that, removing a supernatant solution and leaving it to stand for 5 minutes while turning it upside down, we can finally get the approximately 2000 times concentrated bacterial suspension of $\sim 20\,\mu$L with a volume fraction of $\sim 20\%$. The flowchart recapitulating the process of how to make a dense bacterial suspension is shown in Fig. 6.3.

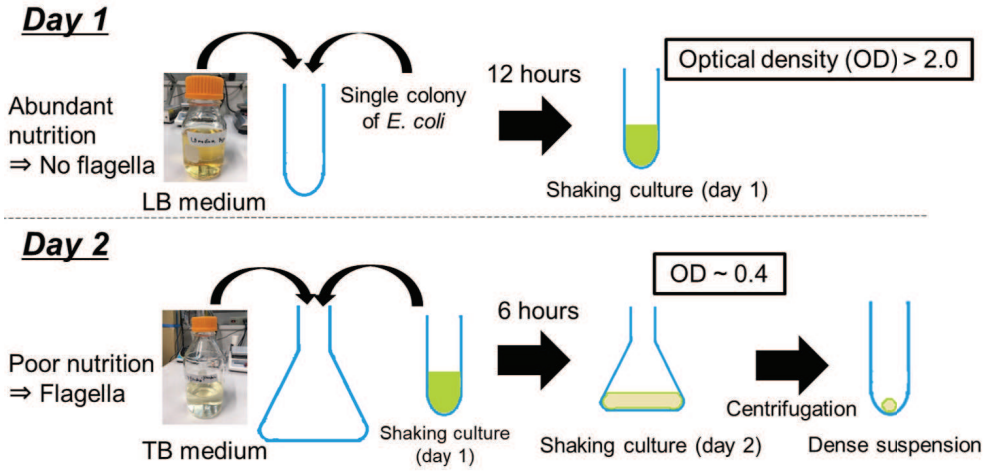

Figure 6.3: Flowchart of the making of a dense *E. coli* suspension.

Control of bacterial length

To test the effect of length of bacteria on collective motions, we control the body length of *E. coli* RP4979 strain ($3.5 \pm 0.6\,\mu m$) with cephalexin(SIGMA-ALDRICH, $C_{16}H_{17}N_3O_4S \cdot xH_2O$) which is a drug to inhibit not elongation but division of cells [115]. By adding cephalexin into a bacterial suspension in the middle of cultures, *E. coli* is elongated while repeating the cell division process without division. In this research, we tune the length to $\sim 8\,\mu m$ by adding it at the ratio, TB medium : cephalexin = 20 mL : 20 µL, 1 hour before the end of incubation (final concentration, 40 mg/mL).

Bacterial motility

Let us mention a typical velocity of free-swimming bacteria. As shown in Fig. 6.4, we record individual motions of bacteria by confining a bacterial suspension with 0.43 in OD 600 into a huge chamber with $\sim 20\,\mu m$ in height by means of particle tracking velocimetry (we will detail later). The typical swimming speed v averaged for tracked bacteria and its standard deviation were $v = 17.95 \pm 0.52\,\mu m\,s^{-1}$.

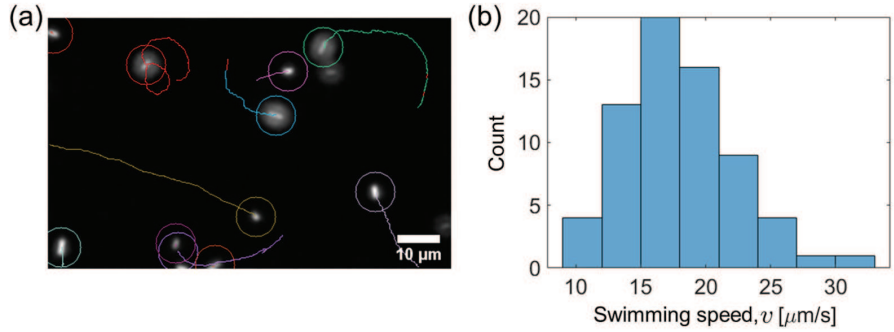

Figure 6.4: Tracking of *E. coli*. (a) Fluorescent image with recorded trajectories of *E. coli* (53 µm × 94 µm). (b) Histogram of swimming velocities averaged over tracked time.

Appendix B

Experimental setup

Microfluidic device

We fabricate a microfluidic device using polydimethylsiloxane(PDMS) and a patterned mold developed through conventional photo-lithography that allows us to impose designed geometric boundaries on a bacterial suspension. Here, let us explain details of the microfabrication of designed PDMS microwells. The advantage of using PDMS microwells is not only the precise boundary design but also the gas permeability that allows for long-time observations and the light transparency for the observation. There are the following three processes for how to make a PDMS device.

Process 1 Developing a designed pattern on a mold

Process 2 Transfering the designed pattern from the mold to PDMS

Process 3 Surface treatment of PDMS microwells

Process 1: Developing a designed pattern on a mold

◯ Spin coating of SU-8

After heating a silicon wafer (MATSUZAKI SEISAKUSHO CO., LTD., SILICONE WAFERS, diameter : 50 ± 0.5 mm, thickness : $300 \pm 25\,\mu m$) on a hot plate at 200°C to remove surface moisture, 2 mL of epoxy-based photoresist, SU-8 3025 (Microchem), is dropped on it and uniformly coated by a spin coater (MIKASA, Opticoat Spin Coater). The thickness that corresponds to the height of microwells is controlled by the rotation speed (rpm: rotation per minute). In many cases, it

is set to 3500 rpm to make the SU-8 pattern with 20 µm in height. After coating of SU-8, it is heated on a hot plate at 95°C for 5 minutes (Fig. 6.5 Step1,2).

◯ UV exposure

A photomask with designed patterns (MITANI MICRONICS CO., LTD., chrome mask) (Fig. 6.6 (a)) is placed on the wafer coated by SU-8, and then it is exposed by ultraviolet rays with a mercury lamp (Olympus, U-ULS100HG) for 20 s (Fig. 6.5 Step 3). The exposed UV light penetrates only at the part of holes of the photomask, thus resulting in the curing of SU-8 patterns exposed by UV light by cross-linking reaction. After that, removing the attached photomask, for the post-baking, the wafer is heated on a hot plate at 95°C for 5 minutes (Fig. 6.5 Step 4).

◯ Developing SU-8

The wafer is immersed in SU-8 developer and shaken for 12 minutes, and the SU-8 part that is not curing is removed. After that, the wafer is washed in ethanol (99.5 %) and ultrapure water (MilliQ water), and then it is heated on a hot plate at 200°C for 15 minutes. Finally, the wafer is heated in an oven (YAMATO, constant temperature oven DKN402) at 95 °C for an hour (Fig. 6.5 Step 5）.

Process 2: Transferring the designed pattern from the mold to PDMS

◯ Curing of PDMS elastomer

PDMS elastomer (Dow Corning, 98-0898, Sylgard, 184 SILICON ELASTOMER BASE) and curing agent (Dow Corning, 98-0898, Sylgard, 184 SILICON ELASTOMER CURING AGENT) are mixed at a 90-to-10 mass ratio and then poured onto the mold made in the process 1. After leaving it in the refrigerator at 4 °C for 30 minutes and degassing in a desiccator with a vacuum pump for 15 minutes, it is cured in an oven at 75 °C for 1 hour (Fig. 6.5 Step 6).

◯ Peeling off PDMS elastomer

By peeling off the cured PDMS elastomer from the mold, the PDMS microwells with a variety of designed patterns are fabricated (Fig. 6.5 Step 7, Fig. 6.6 (b)).

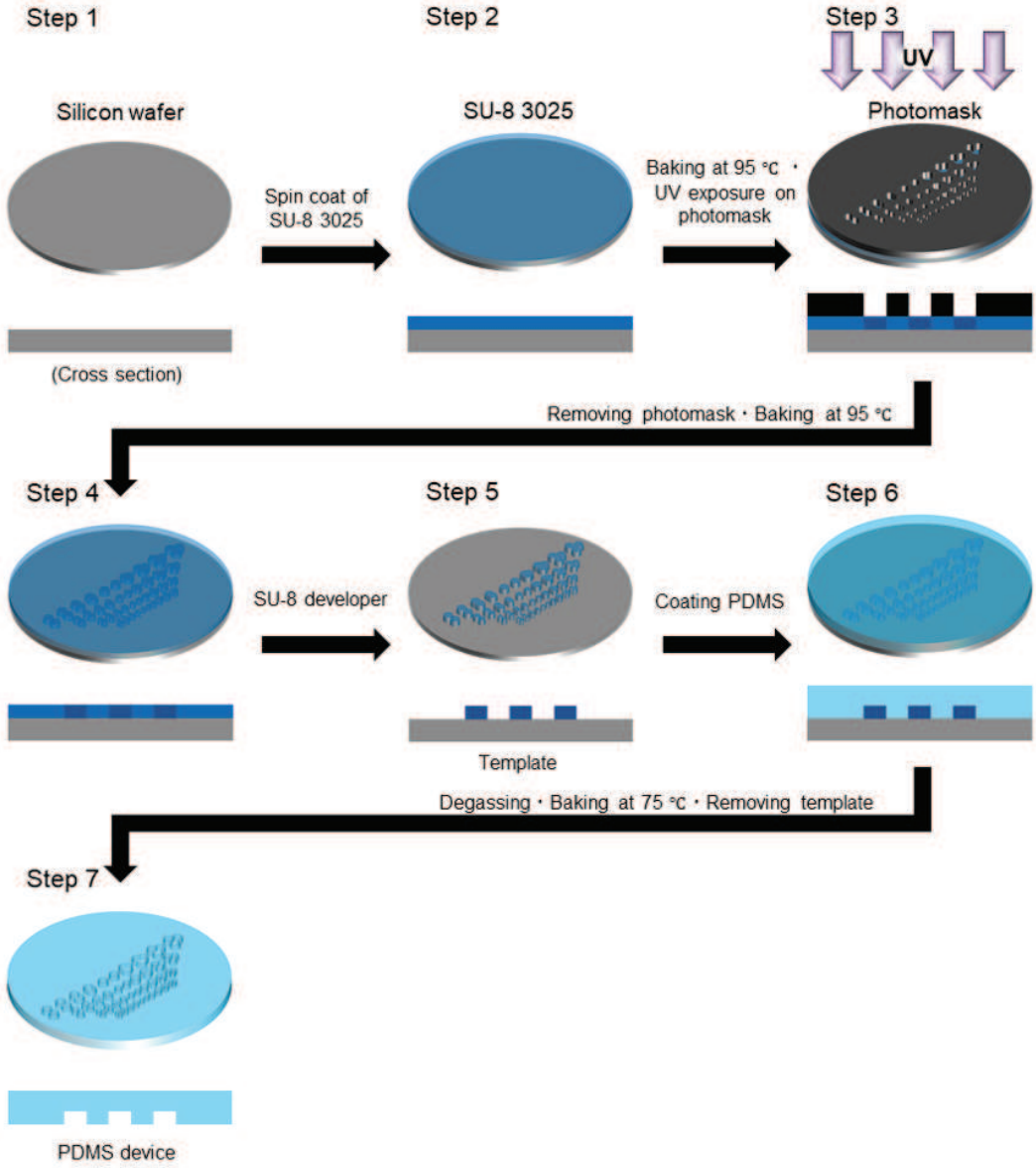

Figure 6.5: The process of making a mold and PDMS device.
Step 1: Removing surface moisture on a silicon wafer at 200 °C for 5 minutes.
Step 2: Spin coating of SU-8.
Step 3: After soft bake at 90°C for 5 minutes, UV exposure to covered photomask from above.
Step 4: Post bake at 90°C for 5 minutes.
Step 5: SU-8 developing and hard bake (Complete mold).
Step 6: Coating PDMS elastomer on the mold
Step 7: After degassing and then heating at 75°C for an hour, peeling off the PDMS part from the mold.

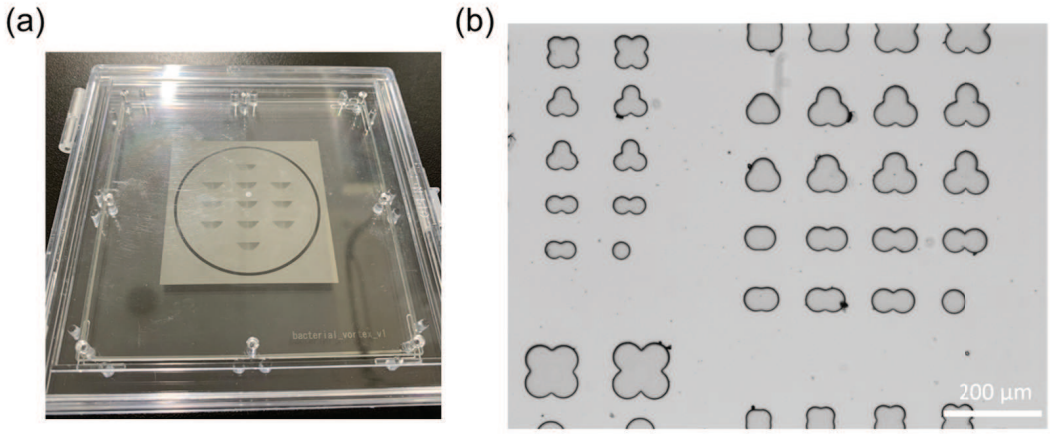

Figure 6.6: Images of photomask (chrommask) (a) and PDMS microwells (b).

◯ Making PDMS sheet and flow cell

In Chapter 3 based on the work [105], we employ a device of PDMS microwells with top/bottom asymmetric interfaces [116]. Let us here explain the details of how to fabricate a flow cell. Firstly, a thin PDMS film, which is made in the almost same way as the making of PDMS microwells above, is required for the flow cell. The degassed mixture (~ 2 mL) of PDMS and the curing agent was spin-coated at 1000 rpm for 30 seconds to reach a thickness of 100 µm on the mold. After curing at 75°C for an hour, the PDMS film is cut around a single array of microwells and peeled off. Its unpatterned flat surface is stuck on a glass slide that has been exposed to air plasma for 20 s beforehand (corona discharge gun, Shinko-Denso). Before covering with a coverslip (Matsunami, C218181, 0.1 mm) and making a flow cell, the PDMS microwells are treated with PEG-PLL (see Process 3 for the details). Finally, The flow cell is completed by sticking a cover glass slide (Matsunami, S1127, 1.0 mm) and a coverslip (Matsunami, C218181, 0.1 mm) with a double-sided adhesive tape (NICHI-BAN, NW-10, 100 µm) placed above the unpatterned areas of the PDMS sheet (Fig. 6.7).

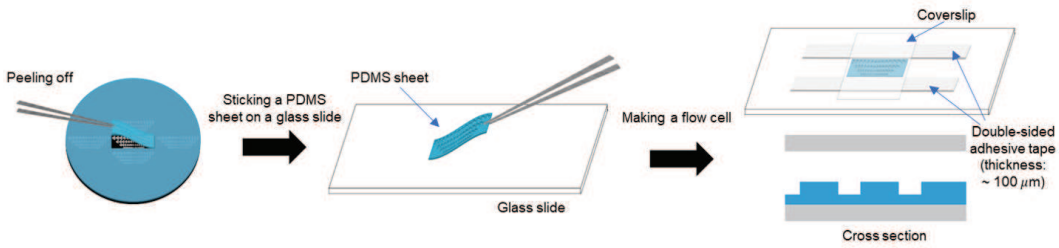

Figure 6.7: Schematic illustration of the process of making a flow cell.

Process 3: Surface treatment of PDMS microwells

We use three different ways for surface treatment of PDMS microwells according to the purpose.

◯ MPC polymer coat

MPC polymer is charged lipids that can prevent living cells and proteins from adsorbing on the substrate. It is used for observations of bacterial turbulence in a thin chamber without microwells and for the work in [76]. The process of the coating material and way to coat is as follows.

1. Dissolving Lipidure-CM5206 (NOF CORPORATION) with ethanol at 0.5 wt%.

2. Dropping 5 µL of the MPC coating material on a glass slide (MATSUNAMI, 24 × 60 mm MICRO COVER GLASS) and evenly spreading to a spot with 24 mm × 24 mm using an edge of another coverslip.

3. Dropping 5 ∼ 10 µL of the MPC coating material on PDMS microwells such that the drop covers the whole pattern.

4. Drying them in an oven at 50 °C for 1 hour.

◯ Triton coat

Although MPC polymer coating prevents the adsorption of proteins on a substrate, it makes it difficult to confine a bacterial suspension in a microwell, because it makes the surface hydrophobic. Thus, we also use a nonionic surfactant, Triton X-100. It is used for top/bottom symmetric confinement of bacterial suspensions in the work in [105]. The process of the way to coat is as follows.

1. Diluting Triton X-100 (SIGMA-ALDRICH, 4-(1,1,3,3-tetramethylbutyl)-phenyl-polyethylene glycol) with MilliQ water and getting 10 % Triton solution.

2. Immersing a PDMS device and a PDMS-coated glass slide (MATSUNAMI, 76 × 26 mm MICRO SLIDE GLASS) in the Triton solution (10 %) and leaving it in the refrigerator at 4 °C for more than 3 hours.

3. Washing the immersed devices with MilliQ water.

4. Drying them in an oven at 50 °C for 1 hour.

◯ PEG-PLL coat

The third method of surface treatment is PEG-PLL coating, which is able to make the surface more hydrophilic and avoid unspecific adhesion of bacteria. It is used for top/bottom asymmetric confinement of bacterial suspensions in the work in [105]. The process of the way to coat is as follows.

1. Dissolving a powdery PEG-PLL(COSMO BIO CO., LTD., Poly-L-Lysine polyethylene glycol Conjugate) with a buffer solution HEPES (100 mM) and diluting it 10 times with MilliQ water.

2. Exposing a PDMS device to air plasma (1 min for vacuation and 1 min at "High" for plasma, Plasma cleaner, Harrick Plasma).

3. Immediately after exposure to air plasma, covering the pattern of microwells with 12 µL of a solution of PEG-PLL and leaving it at rest for 30 minutes.

4. Washing away an ungrafted PEG-PLL solution with MilliQ water and removing remaining water with an air duster.

Encapsulation of bacterial suspensions

Top/bottom symmetric confinement

As for the top/bottom symmetric confinement, a bacterial suspension is confined in a microwell by dropping 1 µL of the suspension on a PDMS-coated glass slide, covering a PDMS device on it, and pressing from above by digital pressure. The surface of devices is treated by either MPC polymer or Triton X-100 (10 %) (Fig. 2.2). Note that although there are two different ways of surface treatment (the MPC-polymer-coated glass slide and PDMS device were used for the work in Chapter 2 [76], and the PDMS-coated glass and PDMS device treated by Triton X were used for the work in Chapter 3 [105]), their experimental results were consistent for both cases.

Top/bottom asymmetric confinement

To construct the microwell with top/bottom asymmetric interfaces, we fabricate the flow cell as shown before (Fig. 6.8, Step 1) and fill it with $\sim$ 20 µL of a bacterial suspension in the following process. The surface treatment of PEG-PLL coating enables the suspension to reach the inside of the microwell (Fig. 6.8, Step 2). After the flow cell is filled, $\sim$ 20 µL of oil (light mineral oil, Sigma Aldrich) containing surfactant (SPAN80, Nacalai) at 2.0wt% is flushed from the same side, and simultaneously, the excess bacterial suspension out of the microwells is flushed out while being absorbed with a filter paper from the other side of the flow cell, so that microwells are sealed by an oil/water interface (Fig. 6.8, Step 3). To avoid unwanted flow in the flow cell, both edges of the flow cell are sealed with epoxy glue (Huntsman, Ltd.). The sample of a confined bacterial suspension is then ready for the observation with a microscopy (Fig. 6.8, Step 4, and Fig. 3.2).

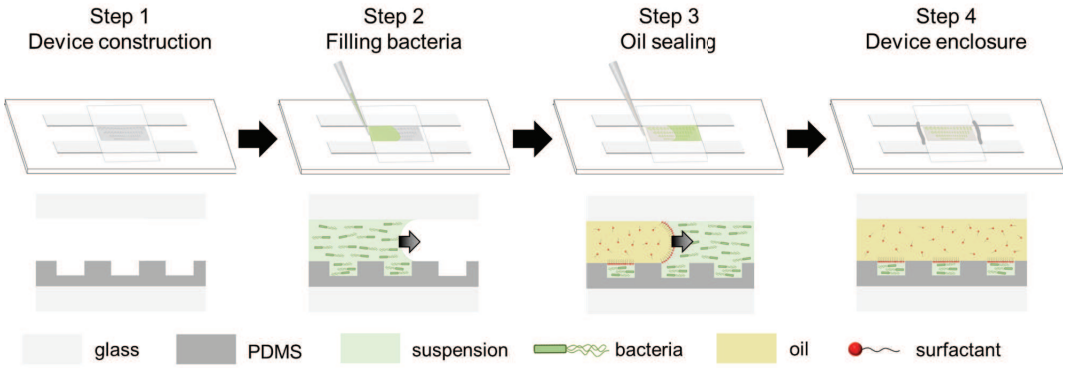

Figure 6.8: Schematic illustration of the filling process. Step 1: device construction. A thin PDMS sheet with designed microwells is transferred between the two glass slides and coated with PEG-PLL to prevent unspecific adhesion of bacteria. Step 2: A bacterial suspension is injected from an edge of the flow cell. Step 3: An excess bacterial suspension is flushed out by oil with (or without) surfactant. Step 4: Both edges of the flow cell are sealed by epoxy glue.

Appendix C

Measurement and analysis

Microscopy

The bright-field movie with a high image resolution for measuring collective velocities is acquired for 10 s $\sim$ 30 s using an inverted microscope (Olympus IX73) with a 20$\times$ objective lens and a high-speed CCD camera (DMK23G445, Imaging source) with a frame rate 30 fps, which is operated by NI LabVIEW 2013 software (Fig. 6.9).

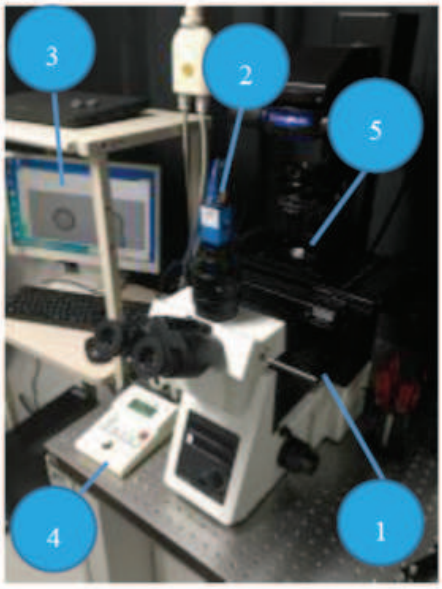

Figure 6.9: Setup of equipment. (1) Inverted microscope. (2) CCD camera. (3) PC. (4) Stage controller. (5) Sample.

For the measurement of a wider range of bright-field images, e.g., Fig. 3.3, we used the inverted fluorescent microscopy (IX73, Olympus).

For the sake of the measurement of the bacterial density, we measure the fluorescent intensity of *E. coli* bacteria that express yellow fluorescent proteins (YFP) using an inverted microscope (Olympus IX73) with a 20× objective lens (TU Plan ELWD 20 ×/0.40, Nikon) and CMOS camera (Neo5.5, Andor Technology). The fluorescence is excited by the light source, XLED(Lumen Dynamics), with GFP(470 nm) channel (Fig. 6.10), and its image is acquired by operating a software, MetaMorph(Molecular Devices).

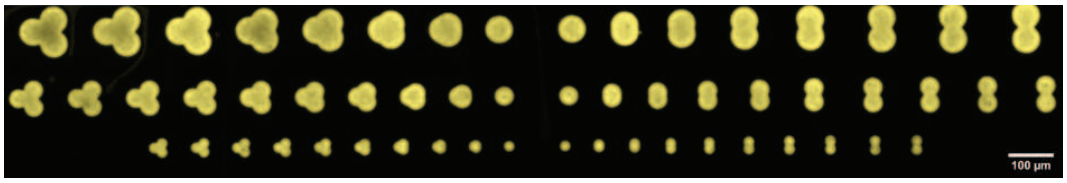

Figure 6.10: Fluorescent image of a dense bacterial suspension confined in microwells. The mean intensity measured for each microwell is used for the measurement of the volume fraction of bacteria.

To measure the density distribution of bacteria and motions of labeled bacteria or tracer particles, depending on the height level in microwells, recording of their trajectories was done with a confocal microscope (IX73 inverted microscope (Olympus), confocal scanning unit CSU-X1 (Yokogawa Electric Co. Ltd.), and iXon-Ultra EM-CCD camera (Andor Technologies)) under either green fluorescence channel (488 nm) or red fluorescence channel (561 nm). All the recordings were done at 33 frames per second (corresponding to the exposure time, 30 ms).

Particle Image Velocimetry (PIV) analysis

Due to the difficulty in measuring all of the bacterial motions in a dense bacterial suspension, we employ the Particle Image Velocimetry (PIV) analysis and visualize the collective dynamics of dense bacterial suspensions. PIV is a well-known analysis method to produce coarse-grained velocity fields as a matrix obtained by calculating a cross-correlation of interrogation areas in consecutive images at a given window, obtained by grid partitioning of the image, and time (Fig. 6.11).

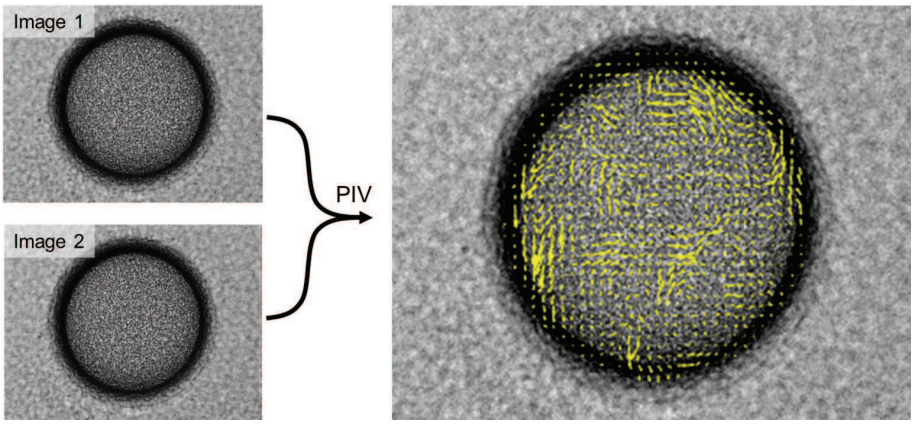

Figure 6.11: Schematics of PIV analysis method. The flow field is calculated from a cross-correlation of interrogation areas in consecutive images of an image taken at a certain time (image 1) and an image at the subsequent time step (image 2).

PIVlab

The velocity fields are obtained by PIV with the Wiener filter method using PIVlab based on MATLAB software (MathWorks). The parameters used in PIVlab are described later in the parameter list. The grid size is set to 16×16 pixels, corresponding to $2.98 \times 2.98\,\mu m^2$ in the actual scale. The outside region of the confinement boundary is basically out of analysis with a mask appropriately set manually.

Note that we also used an ImgaeJ plugin of PIV analysis for a wide range of images like Fig. 3.3.

Smoothing of velocity fields

The PIV analysis conducted in our research uses a pair of two consecutive images captured with a frame rate of 30 fps. For example, when we take 300 images for 10 s, a pair of images is taken as 1st and 2nd images, 3rd and 4th images,$\cdots$,299th and 300th images, and hence we can obtain 150 results of PIV. However, since the resulting velocity fields sometimes contain a large noise, we smooth the velocity fields by taking a time average of some consecutive images to reduce the influence of errors. We choose 1 s (15 PIV results) as the smoothing duration that corresponds to a typical lifetime of bacterial vortices in active turbulence so as to avoid a large error and not to neglect too much instantaneous dynamics of bacterial motions. Fig. 6.12 displays an example of the velocity field smoothed with 15 raw data of PIV analysis.

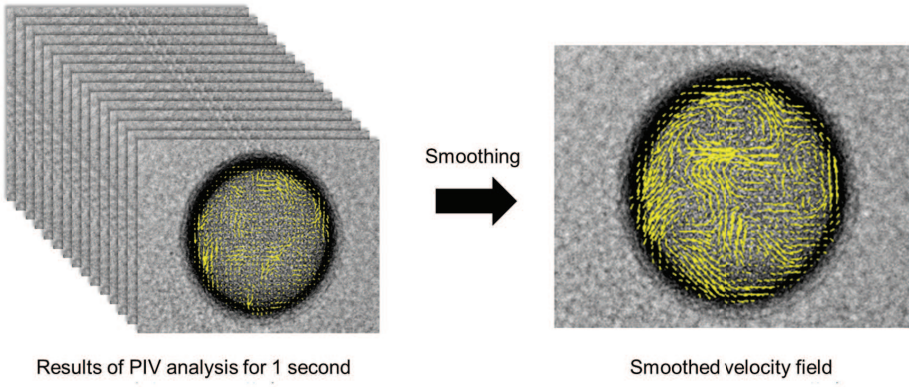

Figure 6.12: Schematic of smoothing of velocity fields. The velocity fields obtained from PIV analysis are averaged over 15 raw data taken for 1 s.

Parameter list of PIVlab

We used a script built based on a sample script in PIVlab, "PIVlab_commandline.m".

Parameter	Setting	Options
Int. area 1	64	window size of first pass
Step size 1	32	step of first pass
Subpix. finder	1	1 = 3point Gauss, 2 = 2D Gauss
Nr. of passes	2	1-4 nr. of passes
Int. area 2	32	second pass window size
Window deformation	*linear	'*spline' is more accurate, but slower
ROI	s{5,2}	same as in PIV settings
CLAHE	1	1 = enable CLAHE (contrast enhancement), 0 = disable
CLAHE size	20	CLAHE window size
Highpass	0	1 = enable highpass, 0 = disable
Highpass size	15	highpass size
Clipping	0	1 = enable clipping, 0 = disable
Wiener	0	1 = enable Wiener2 adaptive denaoise filter, 0 = disable
Wiener size	3	Wiener2 window size

Particle Tracking Velocimetry (PTV) analysis

In order to analyze not only coarse-grained collective velocities but also individual motions of labeled bacteria or tracer particles dispersed in a suspension, we perform the particle tracking velocimetry (PTV) using a plugin of Particle Tracker 2D/3D in the Fiji (ImageJ) software. Before performing it, the images are appropriately processed by enhancing the contrast, subtracting the background noise, and applying a Gaussian filter using the ImageJ software.

Measurement of bacterial concentration

The bacterial concentration is one of the most important physical parameters for collective behaviors as discussed in the Introduction. We investigate the effect of the density on collective motions by tuning it, but we use a dense bacterial suspension with a volume fraction $\sim 20\%$ for observing collective bacterial motions unless otherwise noted. To systematically measure the bacterial density, we use optical methods and quantify it with the resulting calibration curve in what follows.

Volume fraction

We measure the volume fraction of bacteria from the fluorescent intensity of bacteria expressing YFP. To do so, we assess the relationship between them by preparing *E. coli* suspensions with 1, 3/4, 1/2, and 1/4 times diluted densities and measuring their fluorescent intensity, whose volume fractions are already known using OD 600. We estimate 1.0 OD (a value of OD 600 is 1.0) as a density 8.0×10^8 cells/mL [117] and assume the volume of single *E. coli* bacterium to be 1 μm^3/cell $= 10^{-12}$ mL/cell. The mass change between before and after the centrifugation gives the estimation of the volume fraction.

Calibration between volume fraction and fluorescent intensity

Measuring the fluorescent intensity of each of confined bacterial suspensions with different dilution rates, we can obtain the calibration curve (Fig. 6.13), which represents a linear relation between them, allowing us to estimate a volume fraction from a fluorescent intensity of bacteria. The representatives of bright-field and

fluorescent images of confined bacterial suspensions with volume fractions $\phi = 0.055,\ 0.11,\ 0.16,$ and 0.24 are shown in Fig. 6.14.

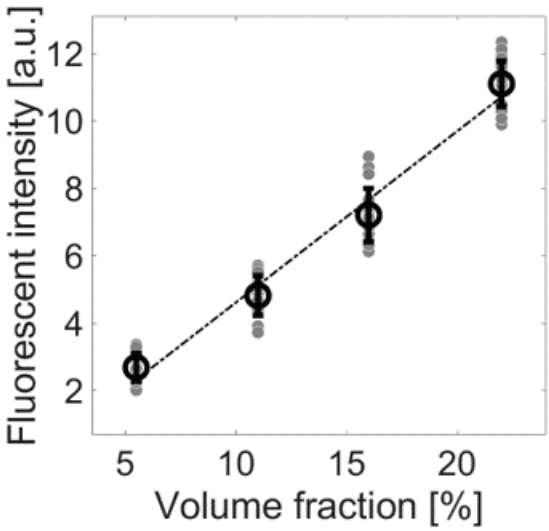

Figure 6.13: Calibration curve representing the relationship between the volume fraction of bacteria and the fluorescent intensity. The mean value and standard deviation of the fluorescent intensity measured for 20 microwells are plotted against each corresponding volume fraction, which are fitted by a curve with a function, $f = ax + b$ ($a = 0.509, b = -0.483$).

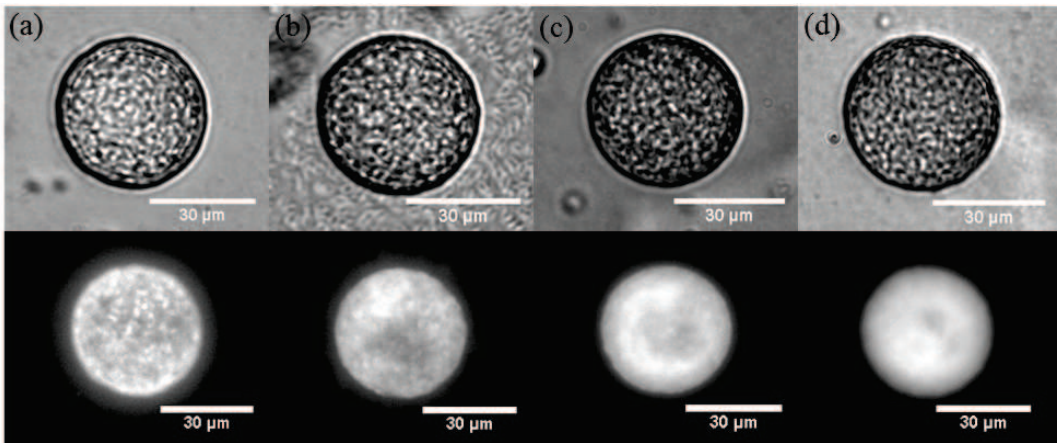

Figure 6.14: Representative bright-field (top) and fluorescent (bottom) images of confined bacterial suspensions at various volume fractions ϕ. (a) $\phi = 0.055$. (b) $\phi = 0.11$. (c) $\phi = 0.16$. (d) $\phi = 0.24$.

Appendix D

Density distribution in an xy plane and interface shape

In addition to the density distribution in the height direction discussed in the main text, the in-plane density distribution of bacteria and the flatness of the oil/water interface of the microwells were measured by confocal microscopy. We examined the density distributions of bacteria expressing YFP protein (YFP-bacteria of 20%v/v) in the radial direction. Fig. 6.15 (a) shows fluorescent images in xy-sectional and zx-sectional views. The radial distribution shows a slight increase, about 1%v/v, near the boundary at the middle plane ($z = 10\,\mu\text{m}$) (Fig. 6.15 (b)), which is probably due to the persistent motion of smooth-swimming bacteria within the edge layer 10 µm away from lateral boundary. To analyze the radial profile of top and bottom interfaces, we measured the fluorescent intensity of the red volume marker of Rhodamine-PEG5k (0.01%v/v), $f_{red}(x, y, z)$, for each of xy-sectional planes: top oil/water interface ($z = 20\,\mu\text{m}$, Fig. 6.15 (d) upper), middle plane ($z = 10\,\mu\text{m}$, Fig. 6.15 (d) middle), and bottom water/PDMS interface ($z = 0\,\mu\text{m}$, 6.15 (d) lower) of a microwell with 35 µm in radius. We set the polar coordinate $f(r, \theta, z)$ and analyzed the radial profile of red volume marker defined by $f_{red}(r, z) = \langle f_{red}(r, \theta, z)\rangle_\theta$ where $\langle\cdot\rangle_\theta$ denotes the average over angle. The normalized fluorescence intensity (NFI) of red volume marker is defined as $\frac{f_{red}(r,z)}{\int_0^R f_{red}(r,z)dr}$. As expected, NFI profiles both at the bottom interface and at the middle plane display nearly constant over all radial positions, meaning that the molecule of the volume marker uniformly distributes inside a microwell. By con-

trast, we found a subtle curved profile in the NFI at the section close to the top interface (Fig. 6.15 (d) upper), which indicates a meniscus at the point where the oil/water interface contacts the PDMS wall on the boundary, but the influence of the deformation on collective behaviors would be negligible because its size is submicron <1.0 µm in depth.

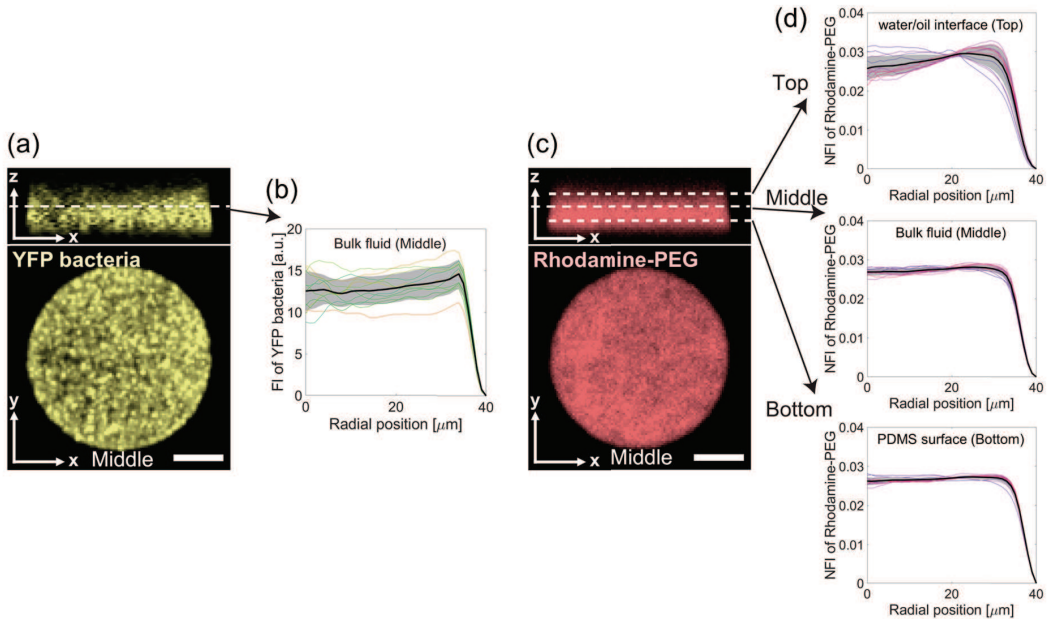

Figure 6.15: (a) Confocal microscopy images of bacteria expressing YFP (YFP-bacteria) encapsulated in a microwell of radius $R = 35\,\mu\text{m}$, at the (top) zx-section and the (bottom) xy-section. Scale bar, 20 µm. (b) The fluorescence intensity (FI) of YFP-bacteria is plotted in the xy-section at the median plane ($z = 10\,\mu\text{m}$). Each green line represents the profile of fluorescence intensity measured in each microwell. Bacterial density is slightly larger near the lateral boundary ($R = 35\,\mu\text{m}$). (c) Confocal microscopy images of Rhodamine-PEG volume marker encapsulated in a microwell with a radius of $R = 35\,\mu\text{m}$, taken in the (top) zx-section and (bottom) xy-section. Scale bar, 20 µm. The white dashed lines represent the xy-section layers at the top oil/water interface ($z = 20\,\mu\text{m}$), the median plane ($z = 10\,\mu\text{m}$), and the bottom water/PDMS interface ($z = 0\,\mu\text{m}$). (d) Radial distributions of Rhodamine-PEG fluorescence. The normalized fluorescent intensity (NFI) is plotted in the xy-sections at each of the top oil/water interface, median plane, and bottom water/PDMS interface. Each red line is an NFI curve measured from each microwell, and the black solid line is their mean value. The gray area represents their standard deviation. The NFIs of the volume marker at the top and bottom interfaces show their flatness. The NFI of the volume marker is constant over the radius of the microwell at the bottom and median planes. However, the slight deformation observed at the top interface near the lateral boundary of the microwell indicates the presence of a meniscus at the oil/water/PDMS contact line.

Interplay between chiral collective motions at top and bottom interfaces

Chiral swimming near top and bottom interfaces at various heights

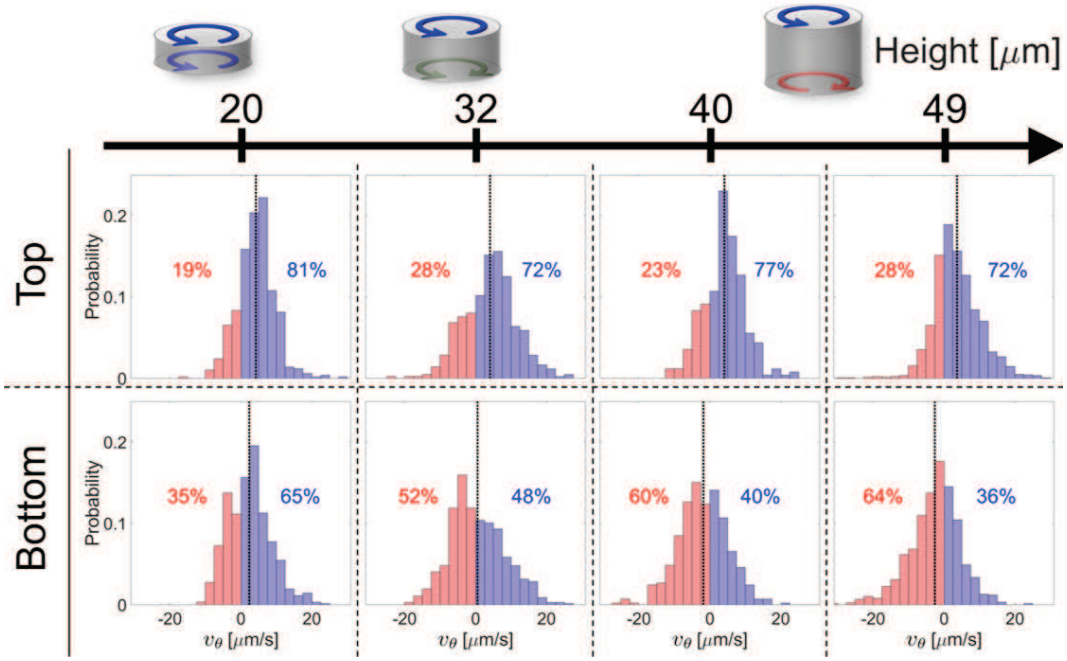

Figure 6.16: Histograms of azimuthal velocities of individual bacteria in the edge layer within 10 µm from the lateral boundary near the top oil/water interface and the bottom PDMS interface in circular microwells with different heights and the radius $R = 35$ µm. The blue bars correspond to the probability of CCW rotation while the red bars to CW rotation. The density is 20%v/v.

Table 6.1: Sample sizes N and average azimuthal velocities $\langle v_\theta \rangle$ of histograms presented in Fig. 6.16. The radius of the microwell is $R = 35\,\mu\text{m}$, and the density of bacteria is 20%v/v.

	$h = 20\,\mu\text{m}$	$h = 32\,\mu\text{m}$
TOP	$N = 491$, $\langle v_\theta \rangle = 4.24\,\mu\text{m/s}$	$N = 423$, $\langle v_\theta \rangle = 4.01\,\mu\text{m/s}$
BOTTOM	$N = 619$, $\langle v_\theta \rangle = 2.35\,\mu\text{m/s}$	$N = 665$, $\langle v_\theta \rangle = 0.57\,\mu\text{m/s}$
	$h = 40\,\mu\text{m}$	$h = 49\,\mu\text{m}$
TOP	$N = 252$, $\langle v_\theta \rangle = 4.12\,\mu\text{m/s}$	$N = 1347$, $\langle v_\theta \rangle = 3.73\,\mu\text{m/s}$
BOTTOM	$N = 412$, $\langle v_\theta \rangle = -1.82\,\mu\text{m/s}$	$N = 1157$, $\langle v_\theta \rangle = -2.60\,\mu\text{m/s}$

Chiral swimming near top and bottom interfaces at various densities

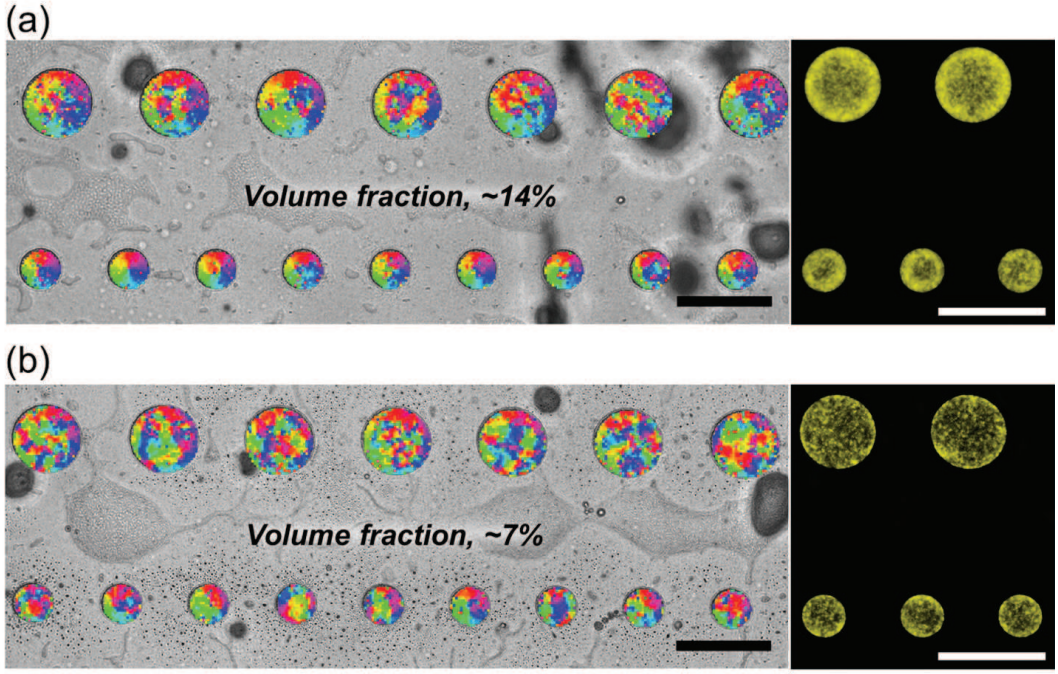

Figure 6.17: Color maps of the orientation of the velocity field (left) and fluorescent images (right) acquired for different bacterial densities: (a) 14%v/v and (b) 7%v/v. Scale bars, 100 µm.

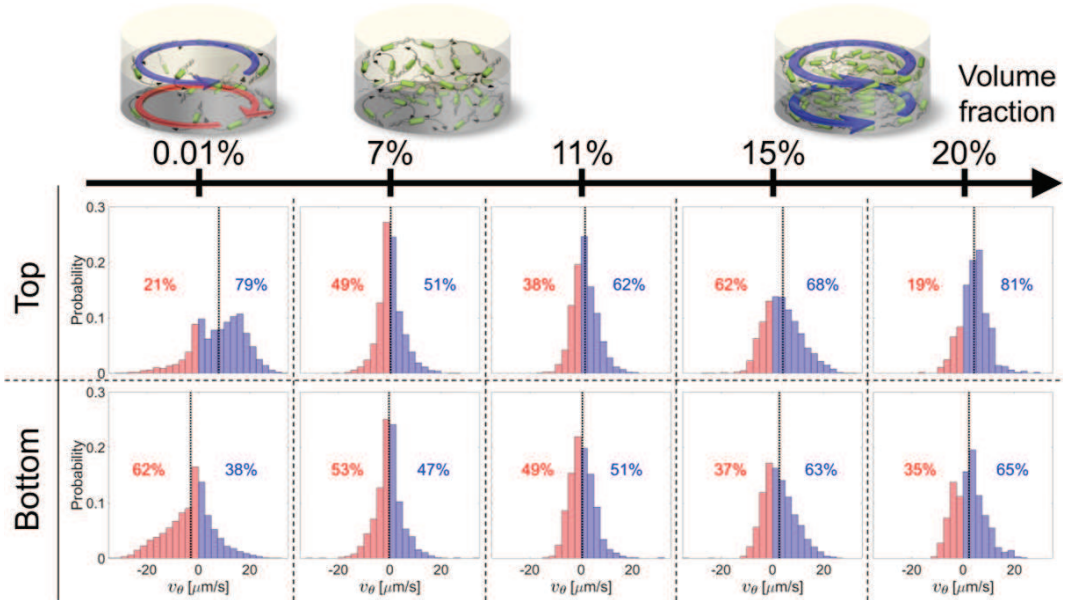

Figure 6.18: Histograms of azimuthal velocities at different bacterial densities. Individual bacteria swimming near the top oil/water interface and the bottom PDMS interface in microwells of the radius $R = 35\,\mu\text{m}$ and the height $h = 20\,\mu\text{m}$ are analyzed.

Table 6.2: Sample sizes N and average azimuthal velocities $\langle v_\theta \rangle$ of histograms presented in Fig. 6.18. The radius and the height of the microwell are $R = 35\,\mu\text{m}$ and $h = 20\,\mu\text{m}$, respectively.

	Density, 0.01%v/v	**Densiy, 7%v/v**
TOP	$N = 3433$, $\langle v_\theta \rangle = 8.02\,\mu\text{m/s}$	$N = 1979$, $\langle v_\theta \rangle = 0.42\,\mu\text{m/s}$
BOTTOM	$N = 4246$, $\langle v_\theta \rangle = -2.98\,\mu\text{m/s}$	$N = 2213$, $\langle v_\theta \rangle = -0.24\,\mu\text{m/s}$
	Density, 11%v/v	**Density, 15%v/v**
TOP	$N = 1286$, $\langle v_\theta \rangle = 1.58\,\mu\text{m/s}$	$N = 2063$, $\langle v_\theta \rangle = 4.07\,\mu\text{m/s}$
BOTTOM	$N = 1315$, $\langle v_\theta \rangle = 0.54\,\mu\text{m/s}$	$N = 1954$, $\langle v_\theta \rangle = 2.71\,\mu\text{m/s}$
	Density, 20%v/v	
TOP	$N = 491$, $\langle v_\theta \rangle = 4.24\,\mu\text{m/s}$	
BOTTOM	$N = 619$, $\langle v_\theta \rangle = 2.35\,\mu\text{m/s}$	

Effect of interface properties on chirality selection

Hexadecane interface without surfactant

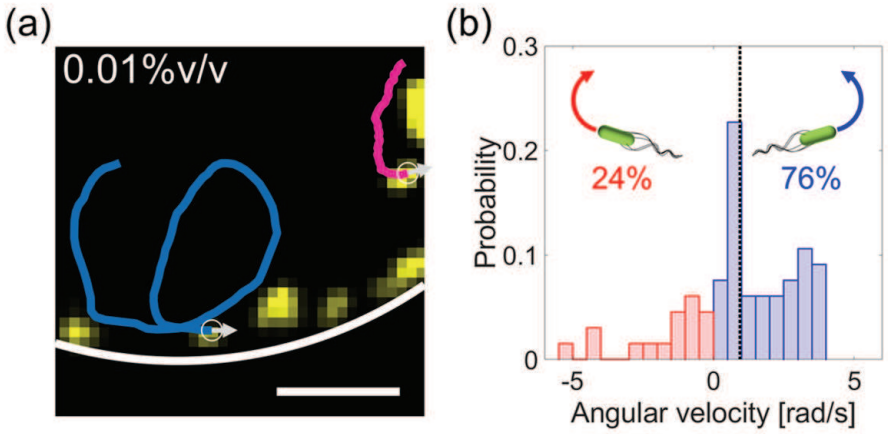

Figure 6.19: Individual motions of bacteria swimming beneath the top water/hexadecane interface without surfactant. (a) Representative trajectory of bacteria tracked near a wall in a microwell of $R = 35\,\mu m$. Scale bar, $10\,\mu m$. (b) Histogram of angular velocities of tracked bacteria. Swimming bacteria beneath the water/hexadecane interface still show the CCW bias in their curved trajectories.

Air/water clean interface

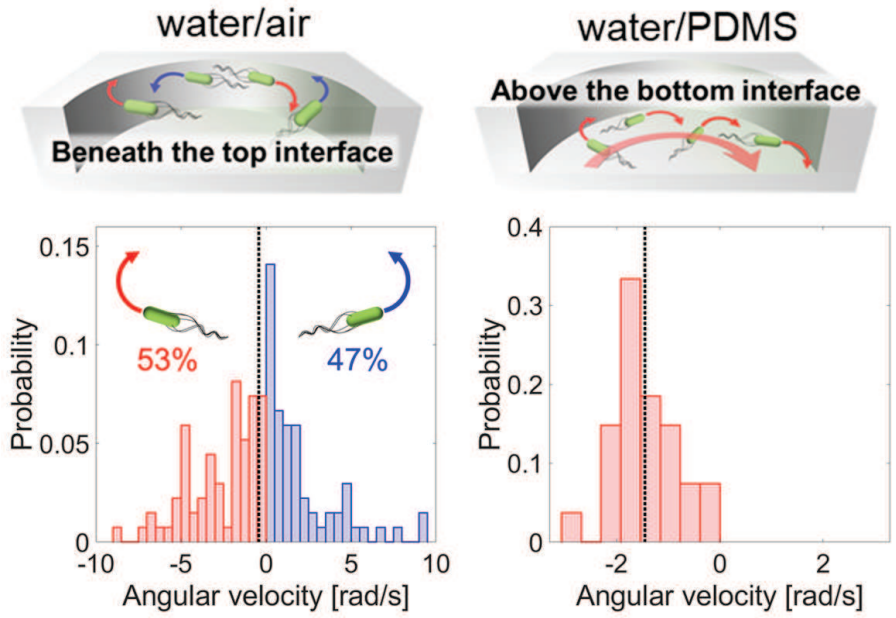

Figure 6.20: Histogram of angular velocities of swimming bacteria near the top water/air interface and the bottom water/PDMS interface. At the top, there is no obvious chirality bias, whereas at the bottom the bacterial swimming is strikingly biased towards the CW direction.

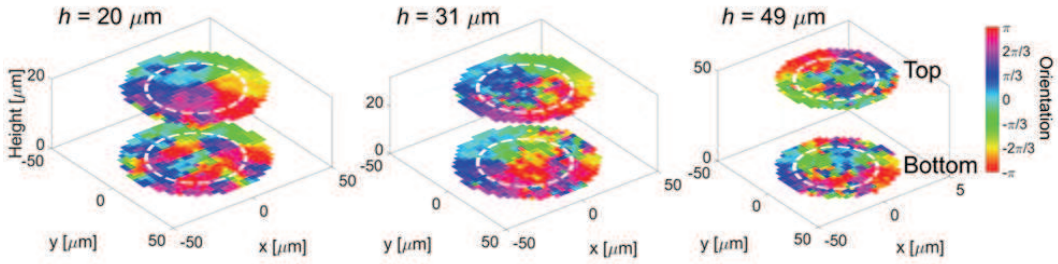

Figure 6.21: Color map of the orientation of collective velocities at top (water/air) and bottom (water/PDMS) interfaces in microwells of different heights h. The bacterial density is 20%v/v. (left) $h = 20\,\mu$m, (middle) $h = 31\,\mu$m, (right) $h = 49\,\mu$m. White dashed line indicates the edge layer.

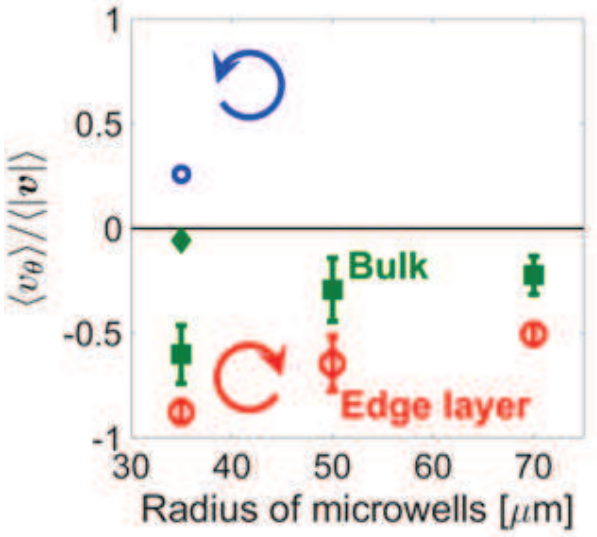

Figure 6.22: The normalized azimuthal velocity of collective motions in circular microwells of $h = 20\,\mu\text{m}$ with the water/air interface. The bacterial density is 20%v/v. The edge layer is defined as the region within $10\,\mu\text{m}$ apart from the boundary, and the rest is assigned to the bulk. Bacterial suspensions confined under the water/air interface exhibit edge currents with the CW handedness.

Numerical simulation corresponding to the experimental condition of the air/water clean interface

The numerical simulation further explains that the chiral collective motion with CW handedness at the bottom water/PDMS interface can dominate over the collective motion at the top interface which has no preferred handedness, even though the density of particles is slightly higher at the top ($N_t = 5300$ and $N_b = 4700$) (Fig. 6.23). In this simulation, we set $\gamma_e^t = 0$, $\gamma_e^b = 1$, $\omega_0^t = 0$, and $\omega_0^b = 0.06$ to imitate experimental conditions for an air/water interface. Fig. 6.23 shows velocity orientation fields at both top and bottom planes at different interaction radii projected to the opposite plane, ε_{tb}. At $\varepsilon_{tb} = 0$, the CCW rotation at the top occurs with a probability of 1/2 due to no chirality. As ε_{tb} increases to 0.5, the global chirality of collective motion is determined only by the chirality bias towards the CW direction at the bottom. Our experimental findings and numerical simulation suggest that the extent of chirality bias also plays a crucial role in determining one global direction of rotation from opposing chiral collective motions at two interfaces.

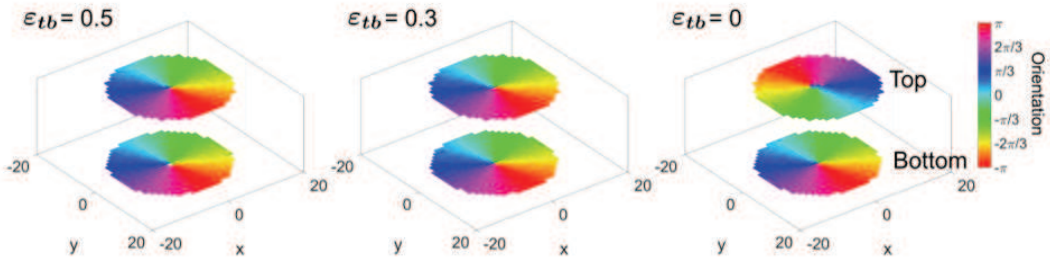

Figure 6.23: Numerical simulation of chirality selection in self-propelled particles without the chiral bias at the top interface. Because there is no chirality in the motion on the top interface, the CCW rotation occurs with a probability of 1/2. ε_{tb} represents the effective range of polar orientation alignment projected to the opposite interface. Collective motions between the top and bottom interfaces are fully correlated at $\varepsilon_{tb} = 0.5$, while at $\varepsilon_{tb} = 0$ they are uncorrelated.

References

[1] F. J. Ndlec, T. Surrey, A. C. Maggs, and S. Leibler, Self-organization of microtubules and motors. *Nature*, **389**, 305-308 (1997).

[2] Y. Sumino, K. H. Nagai, Y. Shitaka, D. Tanaka, K. Yoshikawa, H. Chaté, and K. Oiwa, Large-scale vortex lattice emerging from collectively moving microtubules. *Nature*, **483**, 448-452 (2012).

[3] I. H. Riedel, K. Kruse, and J. A. Howard, A Self-Organized Vortex Array of Hydrodynamically Entrained Sperm Cells. *Science*, **309**, 300-303 (2005).

[4] T. Vicsek and A. Zafeiris, Collective motion. *Physics Reports*, **517**, 71-140 (2012).

[5] M. C. Marchetti, J. F. Joanny, S. Ramaswamy, T. B. Liverpool, J. Prost, Madan Rao, and R. Aditi Simha, Hydrodynamic soft active matter. *Reviews of Modern Physics*, **85**, 1143 (2013).

[6] J. Palacci, S. Sacanna, A. P. Steinberg, D. J. Pine, and P. M. Chaikin, Living Crystals of Light-Activated Colloidal Surfers. *Science*, **339**, 936-940 (2013).

[7] A. Bricard, J.-B. Caussin, D. Das, C. Savoie, V. Chikkadi, K. Shitara, O. Chepizhko, F. Peruani, D. Saintillan, and D. Bartolo, Emergent vortices in populations of colloidal rollers. *Nature Communications*, **6**, 7470 (2015).

[8] J. Dessigne, O. Dauchot, and H. Chaté, Collective motion of vibrated polar disks. *Physical Review Letters*, **105**, 098001 (2010).

[9] N. J. Suematsu, S. Nakata, A. Awazu, and H. Nishimori, Collective behavior of inanimate boats. *Physical Review E*, **81**, 056210 (2010).

[10] T. Vicsek, A. Czirók, E. Ben-Jacob, I. Cohen, and O. Shochet, Novel Type of Phase Transition in a System of Self-Driven Particles. *Physical Review Letters*, **75**, 1226 (1995).

[11] H. Chaté and F. Ginelli, Collective motion of self-propelled particles interacting without cohesion. *Physical Review E*, **77**, 046113 (2008).

[12] J. Toner and Y. Tu, Flocks, herds, and schools: A quantitative theory of flocking. *Physical Review E*, **58**, 4828 (1998).

[13] F. Ginelli, F. Peruani, M. Bär, and H. Chaté, Large-Scale Collective Properties of Self-Propelled Rods. *Physical Review Letters*, **104**, 184502 (2010).

[14] F. Peruani, A. Deutsch, and M. Bär, A mean-field theory for self-propelled particles interacting by velocity alignment mechanisms. *European Physical Journal - Special Topics*, **157**, 111-122(2008).

[15] J. Toner and Y. Tu, Long-Range Order in a Two-Dimensional Dynamical XYModel: How Birds Fly Together. *Physical Review Letters*, **75**, 4326 (1995).

[16] J. Toner, Reanalysis of the hydrodynamic theory of fluid, polar-ordered flocks. *Physical Review E*, **86**, 031918 (2012).

[17] S. Ramaswamy, The Mechanics and Statistics of Active Matter. *Annual Review of Condensed Matter Physics*, **1** 323–345 (2010)

[18] N. D. Mermin and H. Wagner, Absence of Ferromagnetism or Antiferromagnetism in One- or Two-Dimensional Isotropic Heisenberg Models. *Physical Review Letters*, **17** (22), 1133 (1966).

[19] J. Iwasawa, D. Nishiguchi, and M Sano, Algebraic correlations and anomalous fluctuations in ordered flocks of Janus particles fueled by an AC electric field. *Physical Review Research* **3**, 043104 (2021).

[20] A. Bricard, J.-B. Caussin, N. Desreumaux, O. Dauchot, and D. Bartolo, Emergence of macroscopic directed motion in populations of motile colloids. *Nature*, **503**, 95-98 (2017).

[21] A. Chardac, S. Shankar, M. C. Marchetti, and D. Bartolo, Emergence of dynamic vortex glasses in disordered polar active fluids. *Proceedings of the National Academy of Sciences of the United States of America*, **118**(10), e2018218118 (2021).

[22] D. Nishiguchi, K. H. Nagai, H. Chaté, and M. Sano, Long-range nematic order and anomalous fluctuations in suspensions of swimming filamentous bacteria. *Physical Review E*, **95**, 020601 (2017).

[23] S. Tanida, K. Furuta, K. Nishikawa, T. Hiraiwa, H. Kojima, K. Oiwa, and M. Sano, Gliding filament system giving both global orientational order and clusters in collective motion. *Physical Review E*, **101**, 032607 (2020).

[24] M. Sano, 自ら動く物質における秩序とトポロジカル欠陥. *Nihon Butsuri Gakkaishi*, **72**, No.1 (2017).

[25] H. P. Zhang, A. Be'er, E.-L. Florin, and H. L. Swinney, Collective motion and density fluctuations in bacterial colonies. *Proceedings of the National Academy of Sciences of the United States of America*, **107**, 13626–13630 (2010).

[26] R. Suzuki and A. R. Bausch, The emergence and transient behaviour of collective motion in active filament systems. *Nature Communications*, **8**, 41 (2017).

[27] P. Guillamat, J. Ignés-Mullol, and F. Sagués, Taming active turbulence with patterned soft interfaces. *Nature Communications*, **8**, 564 (2017).

[28] C. Blanch-Mercader, P. Guillamat, A. Roux, and K. Kruse, Integer topological defects of cell monolayers: Mechanics and flows. *Physical Review E*, **103**, 012405 (2021).

[29] K. Kawaguchi, R. Kageyama, and M. Sano, Topological defects control collective dynamics in neural progenitor cell cultures. *Nature*. **545**, 327–331 (2017).

[30] V. Narayan, S. Ramaswamy, and N. Menon, Long-Lived Giant Number Fluctuations in a Swarming Granular Nematic. *Science*, **317**, 105-108 (2007).

[31] S. Ngo, A. Peshkov, I. S. Aranson, E. Bertin, F. Ginelli, and H. Chaté, Large-Scale Chaos and Fluctuations in Active Nematics. *Physical Review Letters*, **113**, 038302 (2014).

[32] B. Mahault, X.-c. Jiang, E. Bertin, Y.-q. Ma, A. Patelli, X.-q. Shi, and H. Chaté, Self-Propelled Particles with Velocity Reversals and Ferromagnetic Alignment: Active Matter Class with Second-Order Transition to Quasi-Long-Range Polar Order. *Physical Review Letters*, **120**, 258002 (2018).

[33] M. Bär, R. Groβmann, S. Heidenreich, and F. Peruani, Self-Propelled Rods: Insights and Perspectives for Active Matter. *Annual Review of Condensed Matter Physics*, **11**, 441-466 (2020).

[34] N. H. Mendelson, A. Bourque, K. Wilkening, K. R. Anderson, and J. C. Watkins, Organized Cell Swimming Motions in Bacillus subtilis Colonies: Patterns of Short-Lived Whirls and Jets. *Journal of Bacteriology*, **181**, 600-609 (1999).

[35] X.-L. Wu and A. Libchaber, Particle Diffusion in a Quasi-Two-Dimensional Bacterial Bath. *Physical Review Letters*, **84**, 3017 (2000).

[36] C. Dombrowski, L. Cisneros, S. Chatkaew, R. E Goldstein, and J. O. Kessler, Self-Concentration and Large-Scale Coherence in Bacterial Dynamics. *Physical Review Letters*, **93**, 098103 (2004).

[37] A. E. Patteson, A. Gopinath, and P. E. Arratia, The propagation of active-passive interfaces in bacterial swarms. *Nature Communications*, **9**, 5373 (2018).

[38] Y. Peng, Z. Liu, and X. Cheng, Imaging the emergence of bacterial turbulence: Phase diagram and transition kinetics. *Science Advances*, **7**, eabd1240 (2021).

[39] H. H. Wensink, J. Dunkel, S. Heidenreich, K. Drescher, R. E. Goldstein, H. Lowen, and J. M. Yeomans, Meso-scale turbulence in living fluids. *Proceedings of the National Academy of Sciences of the United States of America*, **109**, 14308-14313 (2012).

[40] A. Creppy, O. Praud, X. Druart, P. L. Kohnke, and F. Plouraboué, Turbulence of swarming sperm. *Physical Review E*, **92**, 032722 (2015).

[41] C. Blanch-Mercader, V. Yashunsky, S. Garcia, G. Duclos, L. Giomi, and P. Silberzan, Turbulent Dynamics of Epithelial Cell Cultures. *Physical Review Letters*, **120**, 208101 (2018).

[42] S.-Z. Lin, W.-Y. Zhang, D. Bi, B. Li, and X.-Q. Feng, Energetics of mesoscale cell turbulence in two-dimensional monolayers. *Communications Physics*, **4**, 21 (2021).

[43] T. Sanchez, D. T. N. Chen, S. J. DeCamp, M. Heymann and Z. Dogic, Spontaneous motion in hierarchically assembled active matter. *Nature*, **491**(7424), 431–434 (2012).

[44] B. Martínez-Prat, R. Alert, F. Meng, J. Ignés-Mullol, J.-F. Joanny, J. Casademunt, R. Golestanian, and F. Sagués, Scaling Regimes of Active Turbulence with External Dissipation. *Physical Review X*, **11**, 031065 (2021).

[45] K. Drescher, J. Dunkel, L. H. Cisneros, S. Ganguly, and R. E. Goldstein, Fluid dynamics and noise in bacterial cell-cell and cell-surface scattering. *Proceedings of the National Academy of Sciences of the United States of America*, **108**, 10940-10945(2011).

[46] J. S. Guasto, K. A. Johnson, and J. P. Gollub, Oscillatory Flows Induced by Microorganisms Swimming in Two Dimensions. *Physical Review Letters*, **105**, 168102 (2010).

[47] D. Saintillan and M. J. Shelley, Theory of active suspensions. Complex Fluids in Biological Systems (Springer, New York), 319–355 (2015).

[48] D. Saintillan and M. J. Shelley, Instabilities and Pattern Formation in Active Particle Suspensions: Kinetic Theory and Continuum Simulations. *Physical Review Letters*, **100**, 178103 (2008).

[49] D. Nishiguchi and M. Sano, Mesoscopic turbulence and local order in Janus particles self-propelling under an ac electric field. *Physical Review E*, **92**, 052309 (2015).

[50] I. S. Aranson, A. Sokolov, J. O. Kessler, and R. E. Goldstein, Model for dynamical coherence in thin films of self-propelled microorganisms. *Physical Review E*, **75**, 040901 (2007).

[51] C. W. Wolgemuth, Collective Swimming and the Dynamics of Bacterial Turbulence. *Biophysical Journal*, **95**, 1564-1574 (2008).

[52] R. Alert, J. Casademunt, and J.-F. Joanny, Active turbulence. *Annual Review of Condensed Matter Physics*, textbf13 (2022).

[53] J. Dunkel, S. Heidenreich, M. Bär, and R. E. Goldstein, Minimal continuum theories of structure formation in dense active fluids. *New Journal of Physics*, **15**, 045016 (2013).

[54] H. Reinken, S. H. L. Klapp, M. Bär, and S. Heidenreich, Derivation of a hydrodynamic theory for mesoscale dynamics in microswimmer suspensions. *Physical Review E*, **97**, 022613 (2018).

[55] V. Bratanov, F. Jenko, and E. Frey, New class of turbulence in active fluids. *Proceedings of the National Academy of Sciences of the United States of America*, **112**, 15048-15053 (2015).

[56] M. Linkmann, G. Boffetta, M. C. Marchetti, and B. Eckhardt, Phase transition to large scale coherent structures in two-dimensional active matter turbulence. *Physical Review Letters*, **122**, 214503 (2019).

[57] S. Liu, S. Shankar, M. C. Marchetti, and Y. Wu, Viscoelastic control of spatiotemporal order in bacterial active matter. *Nature*, **590**, 80-84 (2021).

[58] Y. Li, H. Zhai, S. Sanchez, D. B. Kearns, and Y. Wu, Noncontact Cohesive Swimming of Bacteria in Two-Dimensional Liquid Films. *Physical Review Letters*, **119**, 018101 (2017).

[59] S. Shankar, A. Souslov, M. J. Bowick, M. C. Marchetti, V. Vitelli, Topological active matter. arXiv:2010.00364 (2020).

[60] A. Doostmohammadi, J, Ignés-Mullol, J. M. Yeomans, and F. Sagués, Active nematics. *Nature Communications*, **9**, 3246 (2018).

[61] R. Alert, J.-F. Joanny, and J. Casademunt, Universal scaling of active nematic turbulence. *Nature Physics*, **16**, 682–688 (2020).

[62] L. Giomi, Geometry and Topology of Turbulence in Active Nematics. *Physical Review X*, **5**, 031003 (2015).

[63] H. Li, Xq. Shi, M. Huang, X. Chen, M. Xiao, C. Liu, H. Chaté, and H. P. Zhang, Data-driven quantitative modeling of bacterial active nematics. *Proceedings of the National Academy of Sciences of the United States of America*, **116**(3), 777-785 (2019).

[64] A. Sokolov, I. S. Aranson, J. O. Kessler, and R. E. Goldstein, Concentration Dependence of the Collective Dynamics of Swimming Bacteria. *Physical Review Letters*, **98**, 158102(2007).

[65] A. Sokolov and I. S. Aranson, Physical Properties of Collective Motion in Suspensions of Bacteria. *Physical Review Letters*, **109**, 248109(2012).

[66] S. Mukherjee, R. K. Singh, M. James, and S. S. Ray, Anomalous Diffusion and Lévy Walks Distinguish Active from Inertial Turbulence, *Physical Review Letters*, **127**, 118001 (2021).

[67] H. Wioland, F. G. Woodhouse, J. Dunkel, J. O. Kessler, and R. E. Goldstein, Confinement Stabilizes a Bacterial Suspension into a Spiral Vortex. *Physical Review Letters*, **110**, 268102 (2013).

[68] H. Wioland, F. G. Woodhouse, J. Dunkel, and R. E. Goldstein, Ferromagnetic and antiferromagnetic order in bacterial vortex lattices. *Nature Physics*, **12**, 341-345 (2016).

[69] D. Nishiguchi, I. S. Aranson, A. Snezhko, and A. Sokolov, Engineering bacterial vortex lattice via direct laser lithography. *Nature Communications*, **9**, 4486 (2018).

[70] H. Wioland, E. Lushi, and R. E. Goldstein, Directed collective motion of bacteria under channel confinement. *New Journal of Physics*, **18**, 075002(2016).

[71] H. Reinken, D. Nishiguchi, S. Heidenreich, A. Sokolov, M. Bär, S. H. L. Klapp, and I. S. Aranson, Organizing bacterial vortex lattices by periodic obstacle arrays. *Communications Physics*, **3**, 76 (2020).

[72] L. H. Cisneros, R. Cortez, C. Dombrowski, R. E. Goldstein, and J. O. Kessler, Fluid dynamics of self-propelled microorganisms, from individuals to concentrated populations. *Experiments in Fluids*, **43**, 737-753 (2007).

[73] A. Costanzo, R. Di Leonardo, G. Ruocco, and L. Angelani, Transport of self-propelling bacteria in micro-channel flow. *Journal of Physics: Condensed Matter*, **24**, 065101(2012).

[74] B. Ilkanaiv, D. B. Kearns, G. Ariel, and A. Be'er, Effect of Cell Aspect Ratio on Swarming Bacteria. *Physical Review Letters*, **118**, 158002(2017).

[75] A. E. Hamby, D. K. Vig, S. Safonova, and C. W. Wolgemuth, Swimming bacteria power microspin cycles. *Science Advances*, **4**, eaau0125 (2018).

[76] K. Beppu, Z. Izri, J. Gohya, K. Eto, M. Ichikawa, and Y. T. Maeda, Geometry-driven collective ordering of bacterial vortices. *Soft Matter*, **13**, 5038-5043 (2017).

[77] D. Lopez and E. Lauga, Dynamics of swimming bacteria at complex interfaces. *Physics of Fluids*, **26**, 071902 (2014)

[78] W. R. DiLuzio, L. Turner, M. Mayer, P.Garstecki, D. B. Weibel, H. C. Berg, and G. M. Whitesides, *Escherichia coli* swim on the right-hand side. *Nature*, **435**, 1271-1274 (2005).

[79] E. Lauga, W. R. DiLuzio, G. M. Whitesides, and H. A. Stone, Swimming in Circles: Motion of Bacteria near Solid Boundaries. *Biophysical Journal*, **90**, 400-412 (2006).

[80] B. Liebchen and D. Levis, Collective behavior of chiral active matter: Pattern formation and enhanced flocking. *Physical Review Letters*, **119**, 058002 (2017).

[81] H. Xu, J. Dauparas, D. Das, E. Lauga, and Y. Wu, Self-organization of swimmers drives long-range fluid transport in bacterial colonies. *Nature Communications*, **10**, 1792 (2019).

[82] V. Soni, E. S. Bililign, S. Magkiriadou, S. Sacanna, D. Bartolo, M. J. Shelley, W. T. M. Irvine, The odd free surface flows of a colloidal chiral fluid. *Nature Physics* **15**, 1188-1194 (2019).

[83] K. Dasbiswas, K. K. Mandadapu, and S. Vaikuntanathan, Topological localization in out-of-equilibrium dissipative systems. Proc. Natl. Acad. Sci. U.S.A. **115**(39) E9031-E9040 (2018).

[84] P. Liu, H. Zhu, Y. Zeng, Gu. Du, L. Ning, D. Wang, K. Chen, Y. Lu, N. Zheng, F. Ye, and M. Yang, Oscillating collective motion of active rotors in confinement. *Proceedings of the National Academy of Sciences of the United States of America*, **117**(22) 11901-11907 (2020).

[85] L. Yamauchi, T. Hayata, M. Uwamichi, T. Ozaway, and K. Kawaguchi, Chirality-driven edge flow and non-Hermitian topology in active nematic cells. arXiv:2008.10852 (2020).

[86] S. Bieri and J. Fröhlich, Physical principles underlying the quantum Hall effect. *Comptes Rendus Physique*, **12**, 332–346 (2011).

[87] L. Hall-Stoodley, J. W. Costerton and P. Stoodley, Bacterial biofilms: from the Natural environment to infectious diseases. *Nature Reviews Microbiology*, **2**, 95–108 (2004).

[88] E. A. Dubinsky, M. E. Conrad, R. Chakraborty, M. Bill, S. E. Borglin, J. T. Hollibaugh, O. U. Mason, Y. M. Piceno, F. C. Reid, W. T. Stringfellow, L. M. Tom, T. C. Hazen, G. .L Andersen, Succession of Hydrocarbon-Degrading Bacteria in the Aftermath of the Deepwater Horizon Oil Spill in the Gulf of Mexico. *Environmental Science & Technology*, **47**, 10860-10867 (2013).

[89] R. Di Leonardo, L. Angelani, D. Dell ' Arciprete, G. Ruocco, V. Iebba, S. Schippa, M. P. Conte, F. Mecarini, F. De Angelis, and E. Di Fabrizio, Bacterial ratchet motors. *Proceedings of the National Academy of Sciences of the United States of America*, **107**, 9541-9545 (2010).

[90] A. Sokolov, M. M. Apodaca, B. A. Grzybowski, and I. S. Aranson, Swimming bacteria power microscopic gears. *Proceedings of the National Academy of Sciences of the United States of America*, **107**, 969-974 (2010).

[91] N. Koumakis, A. Lepore, C. Maggi, and R. Di Leonardo, Targeted delivery of colloids by swimming bacteria. *Nature Communications* **4**, 2588 (2013).

[92] Y. Hu, X. Zhang, and W. Wang, Boundary conditions at the liquid-liquid interface in the presence of surfactants. *Langmuir*, **26**, 10693–10702 (2010).

[93] J. C. Conrad, Biophysical methods to quantify bacterial behaviors at oil-water interfaces. *Journal of Industrial Microbiology and Biotechnology*, **47**, 725–738 (2020).

[94] R. Jain and K. L. Sebastian, Diffusing diffusivity: Rotational diffusion in two and three dimensions. *Journal of Chemical Physics*, **146**, 214102 (2017).

[95] K.-T. Wu, J. B. Hishamunda, D. T. N. Chen, S. J. DeCamp, Y.-W. Chang, A. Fenandez-Nieves, S. Fraden, and Z. Dogic, Transition from turbulent to coherent flows in confined three-dimensional active fluids. *Science*, **355**, eaal1979 (2017).

[96] J. A. Gerde, E. G. Hammond, and P. J. White, Influence of polydimethylsiloxane on the oxygen concentration of oils at various temperatures. *Journal of the American Oil Chemists' Society*, **88**, 925–929 (2011).

[97] D. Banerjee, A. Souslov, A. G. Abanov, and V. Vitelli, Odd viscosity in chiral active fluids. *Nature Communications*, **8**, 1573 (2017).

[98] K. Sone and Y. Ashida, *Physical Review Letters*, **123**, 205502 (2019).

[99] K. Sone, Y. Ashida, and T. Sagawa, Exceptional non-Hermitian topological edge mode and its application to active matter. *Nature Communications* **11**, 5745 (2020).

[100] V. Yshunsky, D. J. G. Pearce, C. Blanch-Mercader, F. Ascione, L. Giomi, and P. Silberzan, Chiral edge currents in confined fibrosarcoma cells. arXiv:2010.15555 (2020).

[101] L. Q. Wan, K. Ronaldson, M. Park, G. Taylor, Y. Zhang, J. M. Gimble, and Go. Vunjak-Novakovic, Micropatterned mammalian cells exhibit phenotype-specific left-right asymmetry. *Proceedings of the National Academy of Sciences of the United States of America*, **108** (30) 12295-12300 (2011).

[102] T. Rahman, H. Zhang, J. Fan, and L. Q. Wan, Cell chirality in cardiovascular development and disease. *APL Bioengineering*, **4**, 031503 (2020).

[103] A. M. R. Kabir, D. Inoue, Y. Hamano, H. Mayama, K. Sada, and A. Kakugo, Biomolecular motor modulates mechanical property of microtubule. *Biomacromolecules*, **15**, 1797-1805 (2014).

[104] D. Inoue, B. Mahmot, A. M. R. Kabir, T. I. Farhana, K. Tokuraku, K. Sada, A. Konagaya, A. Kakugo, Depletion force induced collective motion of microtubules driven by kinesin. *Nanoscale*, **7**, 18054-18061 (2015).

[105] K. Beppu, Z. Izri, T. Sato, Y. Yamanishi, Y. Sumino and Y. T. Maeda, Edge current and pairing order transition in chiral bacterial vortices. *Proceedings of the National Academy of Sciences of the United States of America*, **118**(39), e2107461118 (2021).

[106] J. M. Moore, T. N. Thompson, M. A. Glaser, and M. D. Betterton, Collective motion of driven semiflexible filaments tuned by soft repulsion and stiffness. *Soft Matter*, **16**, 9436-9442 (2020).

[107] F. Afroze, D. Inoue, T. I. Farhana, T. Hiraiwa, R. Akiyama, A. M. R. Kabir, K. Sada, and A. Kakugo, Monopolar flocking of microtubules in collective motion. *Biochemical and Biophysical Research Communications*, **563**, 73-78 (2021).

[108] K. Kim, N. Yoshinaga, S. Bhattacharyya, H. Nakazawa, D. Umetsu, and W. Teizer, Large-scale chirality in an active layer of microtubules and kinesin motor proteins. *Soft Matter*, **14**, 3221-3231 (2018).

[109] V. Mirabet, P. Krupinski, O. Hamant, E. M. Meyerowitz, H. Jonsson, and A. Boudaoud, The self-organization of plant microtubules inside the cell volume yields their cortical localization, stable alignment, and sensitivity to external cues. *PLOS Computational Biology*, **14**, e1006011 (2018).

[110] R. Sakamoto, M. Tanabe, T. Hiraiwa, K. Suzuki, S. Ishiwata, Y. T. Maeda, and M. Miyazaki, Tug-of-war between actomyosin-driven antagonistic forces determines the positioning symmetry in cell-sized confinement. *Nature Communications*, **11**, 3063 (2020).

[111] K. Zieske and P. Schwille, Reconstitution of self-organizing protein gradients as spatial cues in cell-free systems. *Elife* **3**, e03949 (2014).

[112] J. Hardouin, J. Laurent, T. Lopez-Leon, J. Ignes-Mullol, and S. Francesc, Active microfluidic transport in two-dimensional handlebodies. *Soft Matter*, **16**, 9230-9241 (2020).

[113] R. E. Breier, R. L. B. Selinger, G. Ciccotti, S. Herminghaus, M. G. Mazza, Spontaneous chiral symmetry breaking in collective active motion. *Physical Review E* **93**, 022410 (2016).

[114] S. L. Porter, G. H. Wadhams, and J. P. Armitage, Signal processing in complex chemotaxis pathways. *Nature Reviews Microbiology*, **9**, 153-165 (2011).

[115] S. Takeuchi, W. R. DiLuzio, D. B. Weibel, and G. M. Whitesides, Controlling the Shape of Filamentous Cells of *Escherichia coli*. *Nano Letters*, **5**, 1819-1823 (2005).

[116] Z. Izri, D. Garenne, V. Noireaux, and Y. T. Maeda, Gene expression in on-chip membrane-bound artificial cells. *ACS Synthetic Biology* **8**, 1705-1712 (2019).

[117] J. A. Myers, B. S. Curtis, and W. R. Curtis, Improving accuracy of cell and chromophore concentration measurements using optical density. *BMC Biophysics*, **6**, 4 (2013).

Acknowledgements

I would like to express my deepest gratitude to my supervisor, Prof. Yusuke Maeda, not only for welcoming me into his laboratory but also for his professional guidance, supports, inspiration, and encouragement throughout my student years. He gave me enough freedom to pursue and develop my own research interests. Indeed, my works presented in this dissertation would not have been possible without his appetite, passion, and ceaseless energy for exploring questions, and his drive towards collaboration with the wider researcher's community.

I am greatly indebted to my assistant supervisor, Prof. Jun-ichi Fukuda, not only for reviewing my dissertation but also for his encouragement and teaching me the basics of the theory of liquid crystals associated with active matter, and to Prof. Yasuyuki Kimura for not only reviewing my dissertation but also providing invaluable guidance throughout my student years from 2013 to 2022.

My special thanks go to Dr. Ziane Izri for fruitful discussions and great support in developing our experimental system and writing our papers. He also kindly helped me in trouble at my first international conference. I appreciate the precious memories.

My gratitude also extends out to all my other collaborators, Kanta Eto for starting our research, Prof. Masatoshi Ichikawa for collaboration on the early stages of this work, Jun Goya for the assistance of analysis, Prof. Yutaka Sumino for fruitful discussions and assistance with the numerical simulations and the theoretical analysis, Prof. Yoko Yamanishi and Dr. Tasuku Sato for the technical assistance with the experiment, Shunya Araki for performing the experiments and analysis regarding confined active cytoskeletons, Dr. Arif Md. Rashedul Kabir,

and Prof. Akira Kakugo for providing us with materials of microtubules and kinesin motors, and having fruitful discussions with me.

My work was supported by a fellowship from the Japan Society for the Promotion of Science (grant no. 20J10039).

Of course, I am grateful to my friends of our laboratory, Dr. Tatsuya Fukuyama and Dr. Ryota Sakamoto, for encouragement and fruitful discourse for five years. I have a lot of fond memories of the time spent with them.

Lastly, I would like to express my sincere gratitude to my parents, brothers, and wife for always providing me with the love and support that has allowed me to achieve everything I have done not only during my student years but also throughout my life.

Publications

Original articles

- Kazusa Beppu, Ziane Izri, Jun Gohya, Kanta Eto, Masatoshi Ichikawa, and Yusuke T. Maeda, Geometry-driven collective ordering of bacterial vortices. *Soft Matter*, **13**, 5038-5043 (2017).

- Kazusa Beppu, Ziane Izri, Tasuku Sato, Yoko Yamanishi, Yutaka Sumino, and Yusuke T. Maeda, Edge current and pairing order transition in chiral bacterial vortices. *Proceedings of the National Academy of Sciences of the United States of America*, **118**(39), e2107461118 (2021).

- Shunya Araki*, Kazusa Beppu*, Arif Md. Rashedul Kabir, Akira Kakugo, and Yusuke T. Maeda, Controlling collective motion of kinesin-driven microtubules via patterning of topographic landscapes. *Nano Letters*, **21**, 10478–10485 (2021). (*equally contributed)

Review articles

- Kazusa Beppu*, Ziane Izri*, Yusuke T. Maeda and Ryota Sakamoto*, Geometric Effect for Biological Reactors and Biological Fluids. *Bioengineering*, **5**, 110 (2018).

- Yusuke T. Maeda and Kazusa Beppu, Ordered structure and geometric control of active matter in dense bacterial suspensions. *The Biophysical Society of Japan*, **60**, 013-018 (2020).